METEOROLOGICAL STUDIES OF CUT-OFF LOWS OVER AUSTRALIA WITH A VHF RADAR

By

Alireza Kazempour, M.Sc.

Thesis

submitted for the degree of

DOCTOR OF PHILOSOPHY

at the

UNIVERSITY OF ADELAIDE

(Department of Physics and Mathematical Physics)

November, 1998

This work contains no material which has been accepted for the award of any other degree or diploma in any university or other tertiary institution and, to the best of my knowledge and belief, contains no material previously published or written by another person, except where due reference has been made in the text.

I give consent to this copy of my thesis, when deposited in the University Library, being available for loan and photocopying.

Signed: dated: 17/11/1998

Alireza Kazempour, M.Sc.

Abstract

This thesis provides a thorough analysis of cut-off low phenomenon over Australia by using the VHF radar system, operating at a frequency of 54.1 MHz. The radar, operated by the Atmospheric Physics Group in the Department of Physics and Mathematical Physics at the University of Adelaide, provides an excellent tool for the investigation of such a phenomenon.

Among the severe weather phenomena over Australia, cut-off low systems and their impacts on the environment and economy are the important features. Comprehensive understanding of cut-off low necessitates the climatological behaviour as well as synoptic scale and mesoscale studies of some unique cases.

In the evolution of cut-off lows the vertical motion of the air is one of the most important parameters. In order to evaluate the long term vertical velocity at the Buckland Park site, the contamination of vertical velocity by folding a fraction of horizontal velocity into it due to a very slight tilt in the beam off-zenith direction, must be eliminated. This is done by determining the slope of VHF transmitting Co-Co antenna array by three different methods and the radial velocity data were corrected against the slope. The analysis of the long term vertical velocity is found to be appreciatively in good agreement with the Flatland VHF radar site in Illinois Colorado, USA found by *Nastrom and VanZandt* [1994].

The climatology of cut-off lows over South Australia, was determined using 20 years of data (i.e. 1974-1993). The impacts of the cut-off low such as: precipitation, thunderstorm and shower activities reveal its importance for the region.

Three unique cases were chosen for further studies. The studies involved synoptic scale discussion and mesoscale discussion. A common feature of these and the other cut-off low systems studied was the presence of the minor troughs

and minor ridges, where they manifested themselves in the cloud patterns, mean sea level pressure charts (MSLP) and VHF radar data analysis. These features were consistent with those observed by *Browning* [1990] and *Sanders and Bosard* [1985].

The key point about these studies is that without the high time and spatial resolution provided by the radar it would not be possible to see synoptic and mesoscale features in such detail. A limitation of the studies here has been the absence of wind data from below $2\,km$. The recent development of a VHF boundary layer radar will help to overcome this deficiency.

Acknowledgements

There are many people who deserve thanks for helping me to accomplish this work. First of all, I would like to thank my supervisors Dr. Robert A. Vincent and Dr. Peter T. May (from the Bureau of Meteorology Research Centre (BMRC) in Melbourne). Preparation of this thesis would have been impossible without their encouragement, advice, discussions, support, help and kindness. Words can't express my gratitude and appreciation to them. I thank Dr. Graham Elford for organizing Friday's discussions. I also thank Dr. Iain M. Reid for assuming the supervisory role during Dr. Vincent's absence.

I would especially like to acknowledge Dr. Alistair J. Blake and Dr. Rod Crewther. Their encouragement and support have been (and still are) invaluable for my family and me. Our sincerest gratitude to them.

I would like to thank Dr. David J. Low for his help in all aspects of VHF radar, Dr. David A. Holdsworth and Dr. Manual A. Cervera for their help in IDL programming. I would also like to thank my colleagues past and present who have been a pleasure to work with. These members of the Atmospheric Group include, in no particular order, Dr. Damian Murphy, Dr. Stephen Eckermann, Dr. Harish Chandra, Dr. Simon J. Allen, Dr. Trevor Harris, Dr. Drazen Lesicar, Dr. Brenton Vandepeer, Dr. Deepak Kanta Rajopadhyaya, Dr. Andrew Taylor, Dr. Drothy Gibson-Wild, Dr. Laurence Campbell, Dr. Bridget Hobbs, Florian Zink Karen Berkefeld, Scott Dullaway, Andrew MacKinnon, Stephen Grant, Jonathan Woithe, Rupa Vuthaluru, Sujata Kovalam, Daniel Badger, Dr. Lucas Christopher, and Thi Binh Minh Nguyen. I also thank Alex Didenko and Lesley Rutherford for their technical support. I also thank Neville Wild for his help and discussions about "Ceilometre". I hope I haven't forgotten anybody; if so, my

apologies, but thanks to you too.

I express my heartfelt appreciation to Dallas Kirby who has been always there to help me with Australian slangs and my English with smiling face, and Lyn Birchby who patiently, read my thesis twice (the most tedious job!!). They both have been (and still are!) nice and kind and helpful in all aspects to me that I will never forget. I owe them lots of gratitude.

Many thanks go to the other scientific, technical and administration members of the Physics and Mathematical Physics Department who have encouraged me, supported me, helped me or have been nice to me in any way.

Special thanks to Dr. Warwick Grace (currently working for "Airborne Research Australia"), Dr. Michael Vowles, Jenny Dichins, John Pethick, Robert Manson and Andrew Watson from the South Australian Regional Office of the Bureau of Meteorology for their invaluable support, discussions and help in all aspects of the meteorological parts of my study.

Thanks to: Frederik Jongejan, Deanna Nikolettos, Kevin Conduit and Beth Greenshields from the Australian Archives Centre for their assistance and preparation of meteorological charts during my long term tedious work there.

I wish to express my humble gratitude to Vivian Hope from the International Programs for her financial allowances and her countless help. She is always helpful. She has been always worried about us and has helped my family in so many ways. She has spent so much time with my family to ease our stress. Thanks Vivian for everything. I also thank Lisa ("White") Brown from the International programs who is always helpful and always with a smile.

My friends: Armin Ardekani, Setayesh Behin-Ain and Shahraam Afsharvahid, I wish to especially thank. Their help is too numerous to mention and is greatly appreciated. Thanks to Ali Imaanpur and Bahram Mojarrabi too.

Our lifestyle during the course of this program of study was supported by a scholarship from the Iranian Ministry of Culture and Higher Education (MCHE). My travel to BMRC in Melbourne was made possible under an Australian Academy of Science Travel Grant for Research in Climate and Atmospheric Sciences. I express my appreciation to these bodies for their contributions.

Outside science, I would like to thank Robyn Moore the director of Observatory Child Care Centre for accepting my son, Aria. Thanks also must go to, in no specific order, Lani, Rita, Michele, Lauren, Alicia and Gloria (from CCAST) for being so kind, patient and helpful and caring so much for Aria. We thank you all on his behalf.

Our sincerest thanks to my cousins Dr. Ali Hassanli and Nasrin Zamani whose companionship, friendship, helpfulness, emotional support and kindness made life easier for us during their stay in Australia. We have missed them so much! We also thank those other friends and their families who eased our stay in Adelaide. We thank them and missed them all.

A person who has a special place in our heart together with his family, is my cordial friend Dr. Davood Tahmasebi. Despite, his serious illness he has always been trying to help us financially or in any other possible ways. We count on him more than any one else on earth. He has been trying to hide his illness from us to prevent our heart break. We pray for him that he will be rid of that nasty illness very soon. He has been so nice to us and his help in so many ways too numerous to mention is greatly appreciated. He is continuously, so supportive. He is closer than our close relatives. He will always be in our heart. My pen is unable to fully describe his beauty. I can just say: Thanks Parviz!

At last, what acknowledgment would be complete without mention of one's loved ones? The support of one's loved ones goes a very long way towards keeping

one from becoming a total wreck, and so I thank my faithful wife, Sima, my charming daughter, Aisa and my wonderful son, Aria, for their continual love, support, encouragement, perseverance, bearing, tolerance and patience. During this long term project they haven't seen me much at home but without any complaint have made these years bearable for me. They have put up with the stress and pressure of my PhD. For this and many other things, I wish to thank them. I would like to express my heartfelt appreciation and gratitude to Sima especially, for being such a wonderful wife to me and such a good mother to our children, Aisa and Aria. She is so understanding and I am indebted to her. I get more energy to continue my work when I see them healthy, happy and joyful. Words just can't express my feelings, gratitude and appreciation to them. I would just say thanks for everything.

Finally, I would like to thank the rest of my family. Thanks to my brothers, my sisters, my brothers-in-law, my sisters-in-law, my nieces and my nephews for sending us encouraging letters, greeting cards, jokes and talking to us on the phone to make us happy. Our heartfelt appreciation and many thanks must go to them. I salute my lovely Mum and Dad. A big thankyou goes to them for their continued support throughout my life. I will never be able to repay the sacrifices of my parents. I just hope to be able to offer my own children whatever my parents offered to me. Thanks for everything, always.

This Thesis is dedicated to my lovely wife, Sima, my charming daughter, Aisa and my wonderful son, Aria, my dear Mum and my dear Dad.

Contents

Chapter 1

Introduction

1.1 Overview

The cut-off low is important considering the severe weather phenomena over Australian region. The evaluation of the importance of such a system and its impacts on the environment and economy have been our concern. Comprehensive understanding of cut-off low necessitates the climatological behaviour as well as synoptic scale and mesoscale studies of some unique cases.

The vertical motion of the air is one of the most important parameters in the evolution of the cut-off lows. The weather analysis in the Australian region has been based on the rawinsonde data and therefore it is focused on synoptic scales. The vertical velocity at the major meteorological centres is evaluated indirectly from divergence or vorticity equations through different models and consequently, suffers from poor temporal and spatial resolution.

An emerging technology that provides high temporal and spatial resolution wind data is the radar wind profiler. Wind profilers have been designed to measure the vertical velocity directly above the radar site. They measure the radial

velocity along the radar beam. The representativeness of the measurements of average vertical profiles of the vertical wind, in terms of actual vertical atmospheric motions is open to question. One possible complicating factor that can affect the accuracy of average vertical wind measurements arises from slight tilts of the pointing accuracy of the vertical beam resulting from the slope of ground under the transmitting antenna. Very slight inaccuracies in the vertical beam direction can severely contaminate the measurements. Although the land of transmitting Co-Co antenna array is normally flat, it may not be perfectly level resulting in some small bias in the vertical velocity. Correcting the radial velocity to be representative of air vertical velocity has been our concern.

The mechanism of apparent mean vertical velocity being weighted toward downward motion in a gravity wave [*Nastrom and VanZandt*, 1994] and determination of this bias in long term vertical velocity is also our interest.

During the last half of the century, satellites have allowed us to see and map the Earth's surface and its surrounding atmosphere. Detailed probing of smaller scale (*i.e.* mesoscale) phenomena, such as cut-off lows, requires high temporal and spatial resolution, and is beyond the capacity of remote measurements from space. These important studies can be achieved via ground-based measuring techniques, one of which is VHF Doppler radars or simply wind profilers. Regular radiosonde measurements from the meteorological upper-air network, have poor time-resolution for studying rapidly evolving meteorological phenomena. These are the areas in which this thesis is concerned.

It is worthwhile beginning with the characteristic of the Atmosphere itself and then proceeding with evolution and behaviour as well as techniques of measurements. The structure of this thesis is such that the introduction relevant to each topic is addressed in the appropriate chapter. Consequently, this overview

is necessarily brief.

1.2 Background

The term "RADAR", an acronym for RAdio Detection And Ranging, was devised by the United States Navy in November 1940. This code name was suggested by both Lieutenant-Commander S. M. Tucker and Lieutenant-Commander F. R. Furth who took steps to have it put into effect. A letter dated 19th November 1940, and signed by Admiral H. R. Stark, Chief of Naval operations, made the word official. It came into use quickly in 1943, and was officially adopted by the Allied Powers. Since the end of the Second World War, it has received general international acceptance [*Swords*, 1986].

Radars use ranges of frequencies which are divided into different bands as the following table:

Table 1.1: Radar Bands and their corresponding Frequencies and Wavelengths.

Band Code	Frequency Range	Wavelength
Medium (MF)	0.3 – 3 MHz	1000 – 100 m
High (HF)	3 – 30 MHz	100 – 10 m
Very High (VHF)	30 –300 MHz	10 –1 m
Ultra High (UHF)	300 – 3000 MHz	1 – 0.1 m
Super High (SHF)	3 – 30 GHz	10 – 1 cm
Extra High (EHF)	30 GHz and Higher	1 cm and Lower

The frequency (or wavelength) should be compatible with the size of the target. Too low a frequency (*i.e.* too large the wavelength), say, less than $100\,kHz$, yields an ambiguity in the detection of the target. The higher the frequency, the higher the resolution of the detected object will be. Production of very narrow beam widths, is another advantage of very high frequency radars. Now, depending on the size and type of targets to be detected, a variety of radars with

different frequencies are used worldwide. For instance, for atmospheric purposes, Doppler radars using the VHF and UHF bands are being used to detect clear air turbulence (CAT).

The available techniques reflect to a degree the evolution and development of experimental capabilities including those conducted from the ground and those conducted from space. Those conducted from the ground have the advantage of logistic simplicity, but provide data only at a single point of region of the global atmosphere. Those from orbit space provide the global coverage that ultimately becomes essential for many parameters.

Four categories of techniques can be usefully defined [Spencer, 1976]:

1. Ground-based measurements.
2. *In situ* measurements.
3. Remote measurements from aircraft, balloons, and rockets.
4. Remote measurements from space.

There are several ground-based techniques for measuring winds such as meteor radar for study of dynamics in the height range from 80 to 100 km and partial-reflection spaced antenna radar which can give information in the 55 to 105 km region. VHF radars can be used to measure motions from the troposphere to the lower stratosphere, and, given enough power, in the mesosphere and above. Atmospheric motions can also be measured by Lidar techniques following the movement of patterns of aerosols or Na, for example, or by Doppler techniques using Fabry-Perot interferometers. Acoustic methods (anomalous sound propagation) as well as UHF and VHF Boundary Layer radars have been used to

measure temperatures and winds.

In summary, it appears that there are several ground-based techniques that have the capability for relatively continuous and low-cost monitoring of constituent concentrations.

Radar investigations are based on the scattering of electromagnetic waves by fluctuations of the refractive index caused by turbulence. The signal-to-noise ratio is higher at longer wavelengths than at shorter wavelengths commonly used with weather radars [Spencer, 1976] for clear air measurements. The refractive index fluctuations are caused by electron density variations in the mesosphere and by temperature variations in the stratosphere. Individual gravity wave groups can be identified unambiguously because of their great amplitude. Thus, the radar provides a good opportunity to observe the vertical amplitude and phase variation of gravity waves which are generated in the troposphere and propagate at relatively high horizontal phase speeds through the middle atmosphere to thermospheric heights.

Radars operating in the Doppler mode, in the VHF or UHF bands, to obtain the backscattered signal from the middle atmosphere (10–110 km) are called "Mesosphere-Stratosphere-Troposphere (MST)" or "Stratosphere- Troposphere (ST)" radars. The atmospheric dynamics can be investigated by recording both the amplitude and phase of the reflected signal by MST/ST Doppler radars. The radial velocity of the scattering medium can then be determined from the Doppler shifted power spectrum of the returned signal. *Briggs*, [1968a,b] and *Röttger and Vincent*, [1978] showed that horizontal wind velocity in the troposphere can be determined by spaced-antenna (SA) techniques through the movement of the diffraction pattern observed on the ground, using a "full-correlation" analysis.

The Doppler radars operating in the SHF (super high frequency, 3-30 GHz)

band are called "Weather Radars" or "Centimeter Radars". They generally measure the radial speed of the hydrometeors rather than that of the clear-air. It has even been suggested that a powerful weather radar can detect clear-air echoes [*Doviak and Zrnic*, 1984].

1.3 The Atmosphere

The envelope of air surrounding the earth is bound to it more or less permanently by virtue of the earth's gravitational attraction. The earth's atmosphere extends from the solid or liquid surface of the earth to an indefinite height. The atmosphere may be subdivided vertically into a number of atmospheric layers, which will be discussed here.

1.3.1 Vertical Temperature Structure

In the 18th century it was assumed that temperature decreased with height through the whole atmosphere because it was known to do so in the lower atmosphere. The first high-altitude balloon measurements ruined this simple picture, showing a temperature increase above the tropopause into the stratosphere to about $55\,km$, above which the temperature started to decrease again. The upward temperature decrease in the troposphere is responsible for overturning (i.e. changing the atmosphere); hence its name, from the Greek prefix *tropos* (turn). The stratosphere is so called, because it tends to remain layered, or stratified, without rapid upward and downward mixing.

The *troposphere* contains the greater part of the mass ($\approx 90\%$ of the atmosphere. It is characterized by marked vertical motions, appreciable water vapour content, cloud, precipitation and other meteorological phenomena. As a result,

it is of great concern to meteorologists. In the troposphere, which contains all phenomena recognizable as weather, there is an average lapse rate (i.e. $-dT/dz$) of 6.5 $K\ km^{-1}$.

The *tropopause* is often spoken of as the level of the first significant temperature minimum in the atmosphere's vertical structure, but in fact the tropopause is not a continuous surface and there is often an overlap and abrupt change in height between two quite separate tropopauses. It has a height of approximately 18 km at the Equator, known as *tropical tropopause*, 13 km at midlatitutes and 8 km at polar regions, known as *polar tropopause*, with breaks occurring in the vicinity of jet-streams.

The *stratosphere* is the region above the troposphere. It extends from the tropopause to altitudes of about 50-60 km. In any particular locality, the temperature generally remains reasonably constant up to about 20 km and this is sometimes called the isothermal layer. The temperature then increases slowly to about 32 km, above which it rises rapidly. The stratosphere is almost free of clouds. The maximum temperature corresponds to the upper boundary of the stratosphere, the so called *stratopause*. The pressure at stratopause is only about 1 hPa. The warmth of this layer is derived from photo-chemical processes that take place as the result of the absorption of solar ultra-violet radiation (0.2 μ- 0.3 μ) by the minor constituent ozone. Consequently, the ozone causes the stratosphere.

The ozone layer, serves a highly important function for life on earth. This layer protects life from most of the high energy radiation from space, which is deadly to life.

The stratopause marks the lower limit of the *mesosphere*. The temperature generally decreases with height in the mesosphere until it reaches a value of about

–95°C at about 80 km which is the lowest in the upper atmosphere. This level, the top of the mesosphere, is called the *mesopause*, where the pressure has a value of about $10^{-6}\,hPa$.

The mesopause marks the end of what can be regarded as homogeneous atmosphere. Up to this level the gaseous composition of the atmosphere is nearly constant, except for variable amounts of water vapour and ozone. Sometimes the region below the mesopause is known as the *homosphere*. The homosphere therefore includes the *troposphere,* the *stratosphere* and the *mesosphere.*

Beyond the mesopause or homosphere there is the *thermosphere*, in which the nitrogen and oxygen of the atmosphere interact with short-wave solar radiation and dissociate into atoms and ions. During this process, the temperature rises in the higher layers to about 1000°C. The upper limit of the atmosphere is not exactly specified. The interactions between the top layers of the atmosphere and solar radiation reach their maximum at a height of about 1000 km (*i.e. exosphere*). The vertical temperature distribution through the layers of the atmosphere show two temperature maxima in addition to that at the earth's surface (Figure 1.1).

We have mentioned that it is important to study the various constituents of the atmosphere as a whole. However, almost all the clouds and weather that affect our daily lives occur in the troposphere. For this reason, we shall now direct most of our attention to atmospheric processes that occur in the troposphere.

1.3.2 Scales

There are different methods of scaling the atmospheric phenomena with spatial and temporal scales and ranges from *molecular* scale on which all atmospheric exchanges occur to the smallest scale of interest to meteorologists, *micrometeoro-*

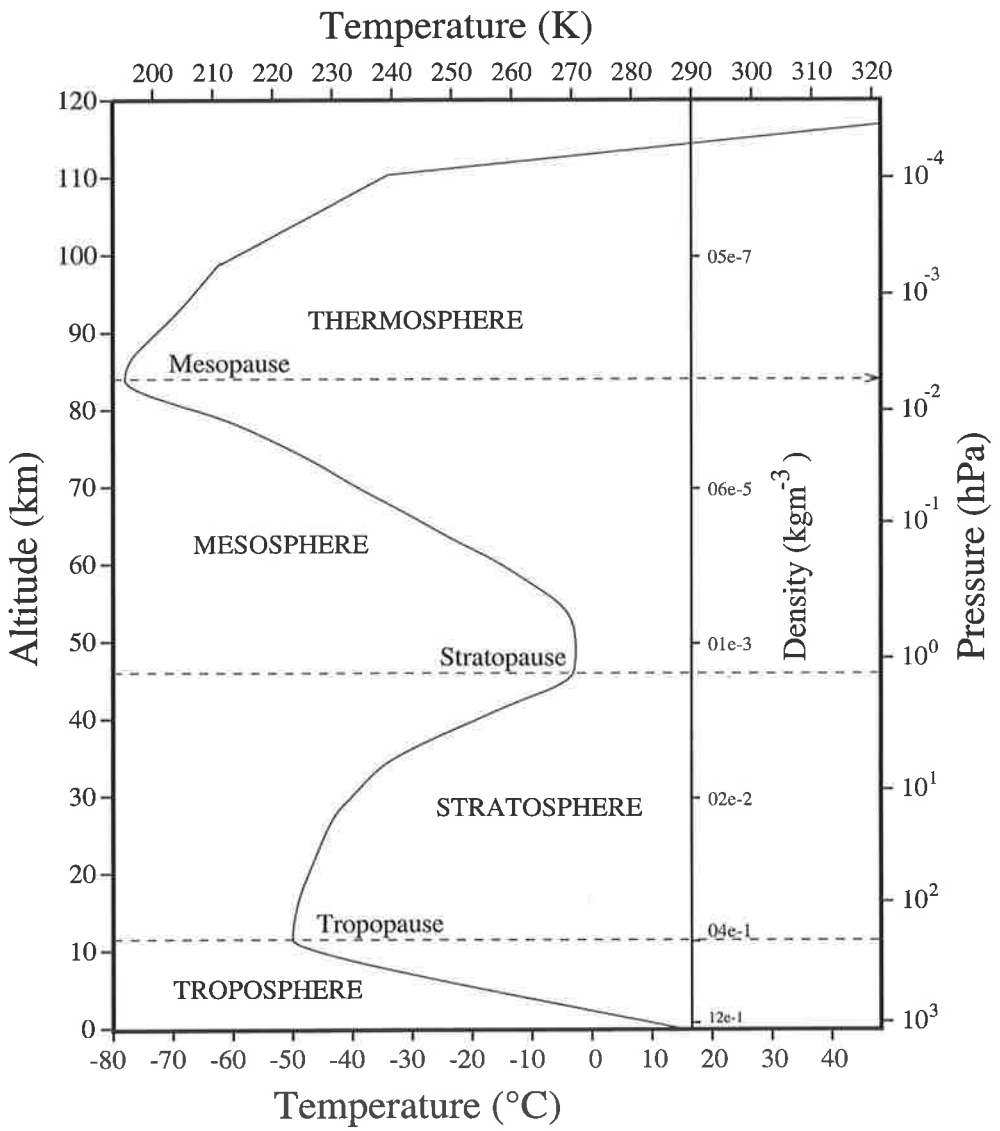

Figure 1.1: Vertical division of the atmosphere and a model temperature profile for mid-latitude equinox, and associated nomenclature, based on the U.S. standard atmosphere (1976) with a dimension added for atmospheric density.

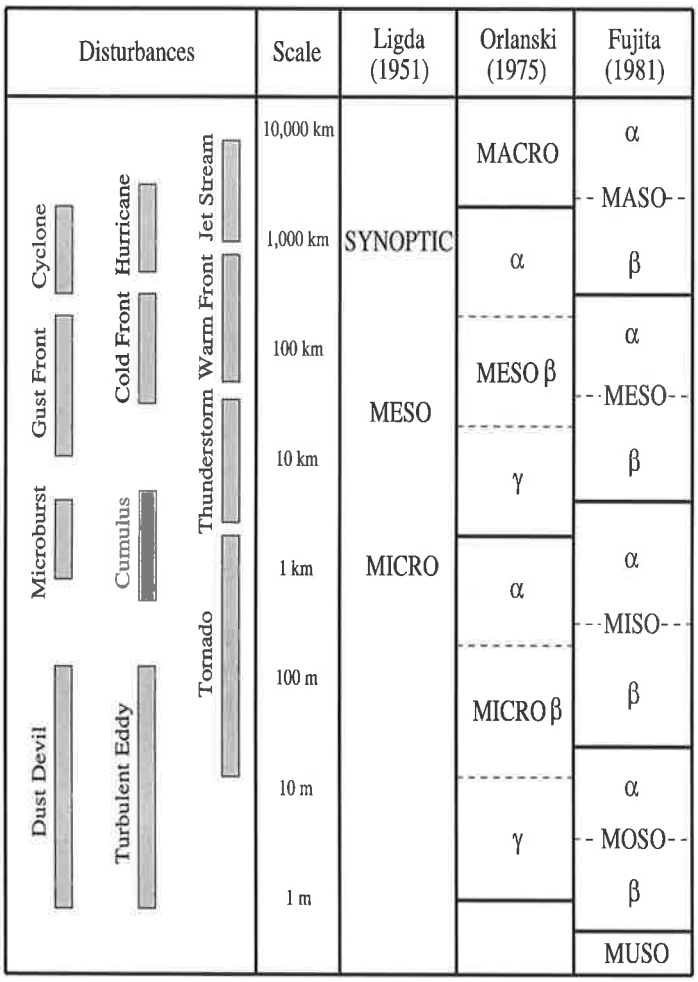

Figure 1.2: Horizontal scaled comparison of different atmospheric phenomena based on, *Ligda* [1951], *Orlanski* [1975] and *Fujita* [1981] (after Fujita [1986]).

logical scale, ending with *planetary* scales. A simplified model of scales proposed by *Ligda* [1951], *Orlanski* [1975] and *Fujita* [1981] are presented on Figure 1.2. In this thesis we have investigated in the mesoscale and synoptic scale region.

1.3.3 Thermodynamics of the Atmosphere

Motion in the atmosphere, thermodynamics, potential temperature, equivalent potential temperature and instability are some of the work presented in this thesis. So it is appropriate to introduce their definitions and terminologies. For thermodynamics and potential temperature, please see Appendix A.

1.3.3.1 Instability

A method of estimating the vertical instability is known as the *parcel method* in which, it is assumed that a parcel of air is displaced vertically from its initial position without mixing with the surrounding air. If the forces existing after displacement tend to return the parcel to its initial position, the atmosphere is said to be in *stable* equilibrium. On the other hand, if the parcel tends to be accelerated away from the initial position, the atmosphere is said to be in *unstable* equilibrium. Finally, if the net force is zero, *neutral* equilibrium prevails.

The atmospheric instability may be expressed in terms of the lapse-rate of potential temperatures. Taking logarithm of (Equation 1ϑ, *App.A*) and differentiating with respect to z, we find that:

$$\frac{1}{\theta}\frac{\partial\theta}{\partial z} = \frac{1}{T}\frac{\partial T}{\partial z} - \frac{R}{c_p}\frac{1}{p}\frac{\partial p}{\partial z}. \tag{1.1}$$

Applying the hydrostatic equation:

$$\partial p = -\rho g \partial z \tag{1.2}$$

and the equation of state, Equation A.9 , yields:

$$\frac{T}{\theta}\frac{\partial \theta}{\partial z} = \frac{\partial T}{\partial z} + \frac{g}{c_{pd}}. \tag{1.3}$$

By substituting for $-\partial T/\partial z = \gamma$, Environmental Lapse Rate, and $g/c_{pd} = \gamma_d$, Dry Adiabatic Lapse Rate, (*i.e.* 9.8 km^{-1}), the above equation becomes:

$$\frac{T}{\theta}\frac{\partial \theta}{\partial z} = \gamma_d - \gamma. \tag{1.4}$$

Hence the instability criteria may be written as follows:

- $(\partial\theta/\partial z) < 0$ (*i.e.* $\gamma < \gamma_d$ and θ increases with height) *stable.*
- $(\partial\theta/\partial z) = 0$ (*i.e.* $\gamma = \gamma_d$ and θ is constant with height) *neutral.*
- $(\partial\theta/\partial z) < 0$ (*i.e.* $\gamma > \gamma_d$ and θ decreases with height) *unstable.*

The treatment above has ignored the moisture effects, which is a reasonable assumption in the stratosphere and upper troposphere but not for the lower troposphere. Considering the moisture effects, for a pseudo-adiabatic process, the expression for Saturation Adiabatic Lapse Rate (SALR) will be:

$$\gamma_s = \gamma_d \left\{ \frac{1 + \frac{L r_s}{R_d T}}{1 + \frac{\epsilon L^2 r_s}{c_{pd} R_d T^2}} \right\} \tag{1.5}$$

where, L=latent (hidden) heat (Jkg^{-1}), r_s= saturation mixing ratio ($\mathrm{g\,kg}^{-1}$) and $\epsilon = M_v/M_d = 0.622$, where M_v and M_d are the molecular weights of water vapour

and dry air respectively.

The bracketed term is a function of the pressure and temperature and so, γ_s is not a constant but is always less than γ_d. However, it approaches γ_d as the pressure increases or the temperature decreases. The latter is the case of upper troposphere and stratosphere.

The additional terminology which sometimes is used to describe the vertical instability through thermodynamic diagrams (*i.e.* skewed T-log p), Figure 1.3, is given below. The word *absolutely* as used here implies the condition of stability or instability, regardless of moisture content, whereas, the word *conditionally* implies a dependence on moisture content.

(1) $\gamma < \gamma_s$ absolutely stable,

(2) $\gamma_d > \gamma > \gamma_s$ conditionally unstable

(3) $\gamma > \gamma_d$ absolutely unstable

The simplified illustration of the above terminology of instability criteria is shown in Figure 1.4.

Holton [1992], states that the vertical acceleration of the parcel of air will be:

$$\frac{\partial^2(\delta z)}{\partial t^2} = -N^2 \delta z \tag{1.6}$$

where,

$$N^2 = \frac{g}{\theta}\frac{\partial \theta}{\partial z} \tag{1.7}$$

is a measure of the static stability of the environment. Therefore, if N > 0 (*i.e.*

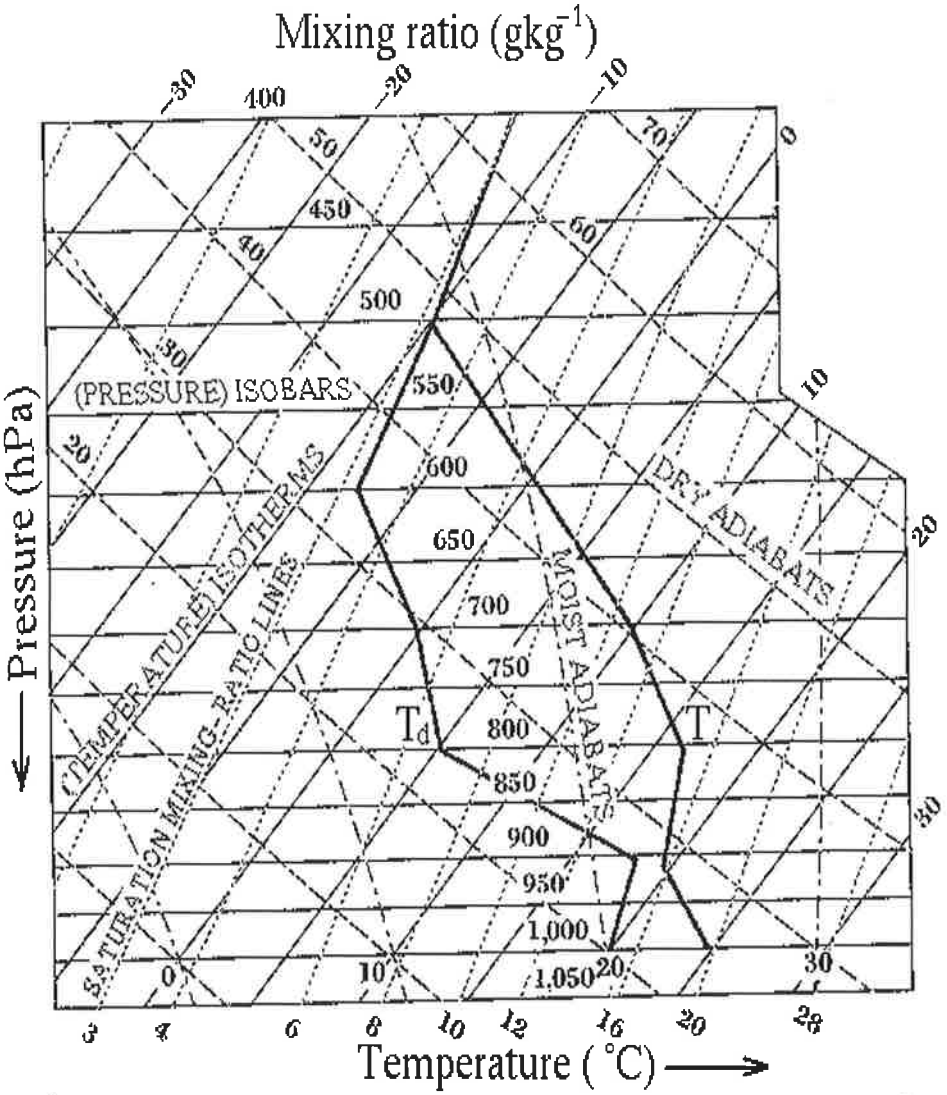

Figure 1.3: Example of a skew T-log p diagram. The background is an adiabatic chart. The right curve (T) is the plot of temperature, T(°C), and the left curve (T_d) is the plot of dew point temperature, T_d(°C), against pressure.

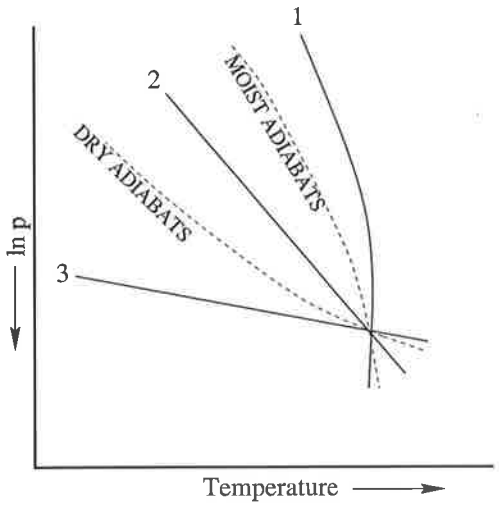

Figure 1.4: A simplified skeletal illustration of a skew T-log p diagram and *absolute stability* (1), *conditional instability* (2), and *absolute instability* (3) in relation to "Dry Adiabats" and "Moist Adiabats".

$(\partial\theta/\partial z) > 0$) the parcel will oscillate about its initial level with period:

$$\tau = 2\pi/N. \tag{1.8}$$

The corresponding frequency, N, is the buoyancy frequency (also often referred to as the Brunt-Väisälä frequency). If $N = 0$ (*i.e.* $(\partial\theta/\partial z) = 0$) the parcel will be at neutral equilibrium. On the other hand, if $N^2 < 0$ (*i.e.* $(\partial\theta/\partial z) < 0$, potential temperature decreasing with height) the displacement will increase exponentially in time.

In the case of dry air, the potential temperature, θ, is a useful, conserved quantity. The temperature which is conservative with respect to dry and pseudo-adiabatic processes is the *equivalent potential temperature*, θ_e (also known as pseudo-equivalent potential temperature). The equivalent potential temperature is defined [*Holton*, 1972] as the final temperature which a parcel of air attains when it is lifted dry adiabatically to its lifting condensation level, then further

up pseudo-wet adiabatically (with respect to water saturation) to a great height (dropping out condensed water as it is formed), then finally brought down dry adiabatically to $1000\,hPa$. The resultant latent heat is used to warm the parcel. *Bolton* [1980], following the work of *Betts and Dugan* [1973], *Betts and Miller* [1975] and *Simpson* [1978], recommended the following formula for computation of equivalent potential temperature for a water-saturation pseudo-adiabatic process:

$$\theta_e = \theta_m exp\left[\left(\frac{3.376}{T_L} - 0.00254\right) \times r\left(1 + 0.81 \times 10^{-3} r\right)\right] \tag{1.9}$$

where, r is the mixing ratio at the initial level; θ_m is the potential temperature for moist air as:

$$\theta_m = T\left(\frac{1000}{p}\right)^{0.2854\left(1-0.28\times10^{-3}r\right)} \tag{1.10}$$

and T_L is the absolute temperature at the lifting condensation level given by any of the following three formula:

$$T_L = \frac{1}{\frac{1}{T_D-56} + \frac{ln(T/T_D)}{800}} + 56 \tag{1.11}$$

where, T_D is the absolute dew point temperature (K).

$$T_L = \frac{1}{\frac{1}{T-55} - \frac{ln(U/100)}{2840}} + 55 \tag{1.12}$$

where, U is the relative humidity (%).

$$T_L = \frac{2840}{3.5lnT - lne - 4.805} + 55 \tag{1.13}$$

where, $e = \frac{p\times r}{622+r}$ is the water vapour pressure (hPa).

Bolton [1980] also recommended that the maximum error is $0.3\,K$, the main contribution to the error arising from neglect of variation of the specific heat of dry air (c_{pd}) with temperature and pressure, an error which also affects the value of the potential temperature (*i.e.* θ).

1.4 Observation systems

The measurement of meteorological parameters at the ground surface of the inhabited portion of the Earth is relatively easy and straightforward. The difficulty in obtaining the measurements arises when it comes to uninhabited areas such as, oceans, deserts, forests and polar regions. The Automatic Weather Stations (AWS) are able to measure some of the quantities in aforementioned areas. Upper-air measurements are relatively difficult because of the remote nature of such observations.

Essentially, there are two types of measurements one, *in situ* measurements, in which, the sensors are placed within the environment such as, balloon borne radiosondes, rocket sondes and aircraft measurements while, the other, remote sensing measurements, in which the effects of the environment on the passage of electromagnetic or sound waves are observed. The remote sensing methods can be fulfilled through the means of either, ground-based devices (*i.e.* Radars, Lidars and Sodars) or, space-based devices like satellites.

Balloon-borne radiosondes are used world wide at upper-air meteorological stations. Using this method, the atmospheric parameters such as, temperature, pressure and humidity are measured at the place (*i.e.* in situ measurement) with relatively high spatial resolution but, poor temporal (*i.e.* 12 hourly interval) resolution. The balloon is assumed to travel with the mean wind. The atmospheric

wind is measured by tracking the radiosonde transmissions via radio direction-finding. It can also be done by tracking a reflector which is suspended underneath the balloon with radar measuring the range, zenith angle and azimuth angle of the reflector. The accuracy of measurements decreases with height as the balloon's range increases. Sometimes, the measurements are done at 10 s of kilometers away from the initial surface spot as the upper high winds cause the balloon to drift.

Remote measurements of temperature and humidity from space are carried out by satellites equipped with Infra-Red (IR) and Visual (VI) sensors. There are mainly two types of meteorological satellites, the geostationary satellites and polar-orbiting satellites. The former, located at altitude of about 35000 km mainly over the Equator with relatively low horizontal resolution of about 5 km providing continuous global observations (processed half hourly) such as, GOES, GMS, and Meteosat. The latter, orbiting the Earth from about 850 km altitude through polar regions with higher horizontal resolution (*i.e.* 1 km). In the case of presence of clouds, the atmospheric winds can be measured by observing cloud drifts. Both systems have relatively low vertical resolution of the order of kilometers.

Among the ground-based remote sensing devices are the weather radars. Simply, the electromagnetic waves emitted from an antenna are interrupted for a predetermined period of time to permit a pulse of these waves to reach a target (*i.e.* hydrometeors) and return to the same antenna before the next pulse is transmitted. The range to the target is determined from measuring the transmission/reception time delay. The indicators are mainly two types, Plan-Position Indicator (PPI) or Range-Height Indicator (RHI) in which, the former is used for presentation quite similar to a map or chart, displaying the target in both range

and azimuth while, the latter displaying the target in range and height along the azimuth of the radar beam. The conventional weather radar can locate rain and indicate its intensity from the amplitude of the returned signal.

The wind profilers operating in UHF and VHF bands, detecting the returned signals from disturbed air with different refractive index, are being widely used. Horizontal and vertical wind velocities can be determined from the Doppler shift of the echoes.

As the result of the strong absorption and scattering of sound waves in the atmosphere and the fading out of the power, the acoustic radars (Sodars) are mainly used for observations of the boundary layer structure. They have a good vertical resolution. Since the acoustic wavelength and hence, the velocity, are temperature dependent, transmitting the acoustic wave simultaneously with the electromagnetic wave from radar (*e.g.* VHF radar), the temperature profile of the atmosphere can be constructed. This is done by varying the transmitted acoustic frequency and observing the altitude of enhancement of echoes via the Radio Acoustic Sounding System (RASS).

Pulsed Doppler Laser radars or simply Lidars, are designed based on the scattering (and hence, reflecting back) of light by aerosol particles (*e.g.* dust, salt particles, volcanic eruptions, etc). The principles of the wind measurement by Lidars are identical to that of wind profilers.

For more information about observation systems, the reader is referred to: *Hubert* [1979], *Hubert and Witney* [1971], *Homer* [1970], *Battan* [1973], *Doviak and Zrnic* [1984], *Skolnik* [1990], *Woodman and Guillen* [1974], *Golden et al.* [1986], *Väisälä* [1988], *Browning and Szejwach* [1994], *Matuura et al.* [1986], *May et al.* [1989a], *Hogg et al.* [1983] and *Bilbro et al.* [1984].

As the work presented here has utilised the wind profiler, this technique will

be discussed in the next chapter.

Chapter 2

Wind Profiler Technique

2.1 Introduction

This chapter gives a general overview of the coherent radar technique with special emphasis to mesosphere, stratosphere, troposphere (MST) radar operating in the VHF band. Some basic introduction to Doppler radar measurements and the radar equations are followed by the data analysis in terms of the correlation and spectrum analysis. The techniques for the measurement of wind velocities, namely, the different modes of the Doppler method as well as the spaced antenna (SA) method are surveyed. A brief discussion about comparisons of spaced antenna (SA) method with other wind measuring methods will bring the chapter to a close.

2.2 Measurement Techniques and Corresponding Altitude Observations

Briefly, to study the atmosphere, there are two groups of experimental techniques, the *remote sensing* techniques and the *in-situ* techniques. The advantages of the former, which senses the state of the atmosphere from a distance, is the significant time resolution while the latter has the advantage of measuring the parameters in a well-defined and predictable manner. Both have some disadvantages, the former generally suffers from some uncertainty, and the latter as well as having very poor time resolution, has measurements normally taken 10's of kilometers away from the launched spot.

There are two further distinctive types of remote sensing experiments, the passive experiments and the active experiments. The passive experiments are those which simply receive or monitor some state or constituent of the atmosphere like most satellite-borne apparatus, while active experiments are those which sound the atmosphere with some form of radiation. The radar and lidar experiments fall into the active category. Although, the passive experiments (e.g. satellite measurements) have the disadvantage of relatively poor height and time resolution, they are able to achieve excellent hemispheric coverage.

As well as being able to make measurements with excellent temporal and spatial resolution, the atmospheric radars are relatively inexpensive and can operate at remote areas unattended for long periods. The restriction of altitude coverage (i.e. generally, inability to sample at more than a small number of spatially separated locations), however, is a disadvantage of atmospheric radars.

Medium frequency (MF) and high frequency (HF) radars operate mainly at frequencies between 2 and 6 MHz and receive partial-reflection returns for the

roughly mesospheric region from below 60 *km* to 100 *km* [*Vandepeer and Reid*, 1995]. The pioneers of investigations of this region are *Gardner and Pawsey* [1953] and *Gregory* [1956]. The ionization and refractive index discontinuities with vertical scale of the order of half the radar wavelength causes the backscatter from turbulence and gravity waves. The range of altitudes observed by atmospheric radars is summarized in Figure 2.1

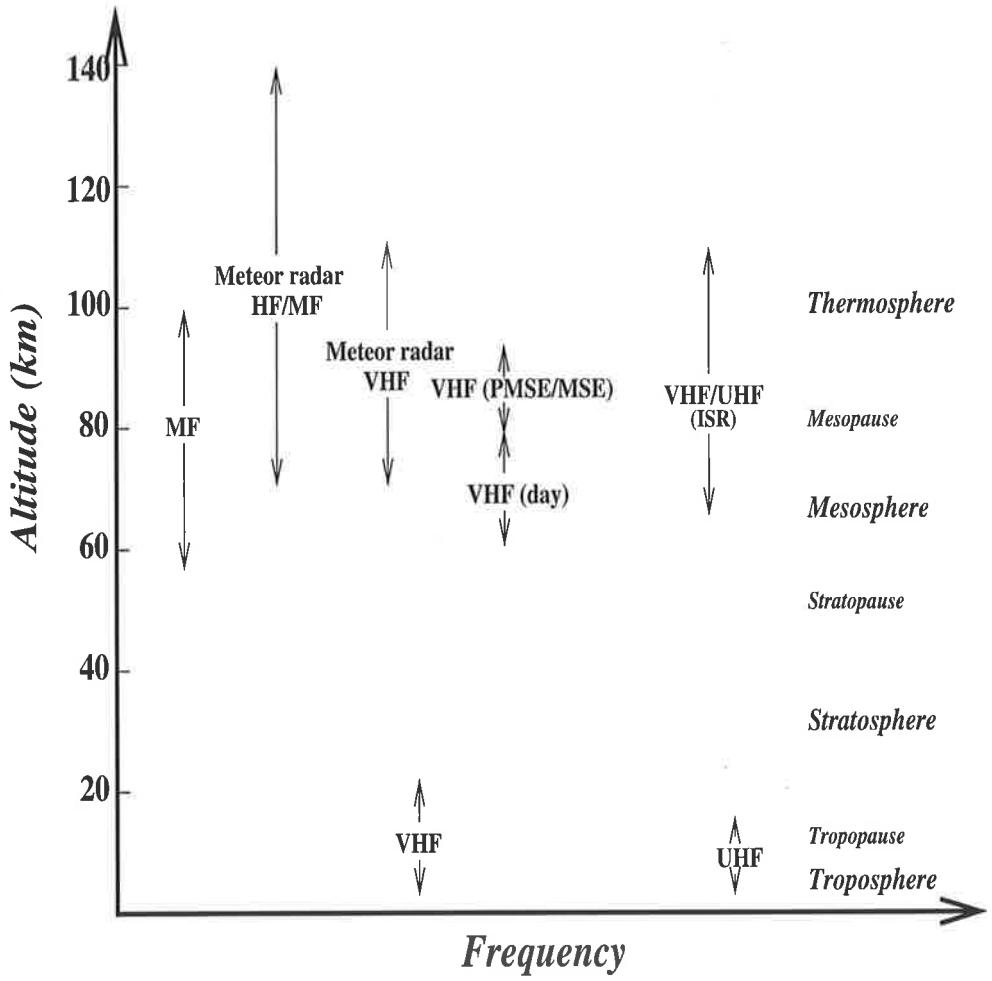

Figure 2.1: The altitude ranges observed by atmospheric radars (revised from *Vandepeer* [1993]).

Very high frequency (VHF) radars were first used in the late 60's and early

70's *(Flock and Balsley* [1967]; *Woodman and Guillen* [1974]).

MST radars make use of scattering and reflection from variations of humidity, temperature and electron density. Essentially, MST radars can observe the three dimensional wind vector, atmospheric reflectivity and stability, as well as morphology of turbulence and waves. The continuous measurements with MST radars offer very good quality and quantity of wind velocities [*Gage and Van-Zandt*, 1981]. MST radars operate at frequencies around $50\,MHz$ and are also called VHF radars (frequency band between $30\,MHz$ and $300\,MHz$). Typical peak powers of VHF radars are between $1\,kW$ and $1\,MW$. Range resolutions down to about 100 m and time resolutions down to some 10 second are possible. The antenna arrays with typical dimensions of $1000\,m^2$ to some $10{,}000\,m^2$ point close to the zenith direction. The basis of the so-called "MST radar technique", which is applicable to pulsed, coherent radars, has been described in detail by a number of authors such as: *Balsley* [1981], *Gossard and Strauch* [1983], *Röttger* [1984], and *Röttger and Larsen* [1990].

Ultra high frequency (UHF) radars operate at frequencies from 400 to 900 MHz. The "profilers" operating at the lower frequency are covering from $500\,m$ to $10\,km$. The "Boundary layer" radars operating at the higher frequencies are covering up to $4\,km$ with high spatial resolution. The backscatter for these radars results from water vapour, precipitation, and aerosols. The Doppler shift of the resulting power spectrum determines the wind velocity. The maximum observable height for the determination of the wind velocity is considered to be around $95\,km$ [*Hines et al.*, 1993].

2.3 Mechanisms of Scattering

Under suitable circumstances MST radars are capable of obtaining echoes from both thermal and non-thermal fluctuations in the atmospheric refractive index. In both cases the echoes are returned from structure in the medium with a scale along the beam comparable to one-half of the wavelength of the transmitted frequency. The thermal (or incoherent or Thomson) fluctuations arise from the statistical fluctuations of a medium in thermodynamic equilibrium, and non-thermal fluctuations are associated with either turbulent or laminar (coherent) structure.

Basically, all radar echoes arise from scattering or reflection from inhomogeneities in the atmospheric dielectric constant, ε, or index of refraction, n. These inhomogeneities result from the mixing produced by the action of turbulence and internal gravity waves, and are due to the existence of stable reflecting layers. The dielectric constant of free space is $\varepsilon_0 = (10^{-9}/36\,\pi\,F\,m^{-1})$. A relative dielectric constant can be defined by:

$$\varepsilon_r = \varepsilon/\varepsilon_0 \tag{2.1}$$

and the refractive index, n, is related to this dielectric constant by:

$$n = \sqrt{\mu_r \varepsilon_r} \tag{2.2}$$

where the relative permeability, μ_r, of air is approximately unity. The atmospheric refractive index for radio waves propagating through the lower and middle atmosphere is given by *Gage and Balsley* [1980] as:

$$n - 1 = \frac{3.73 \times 10^{-1} e}{T^2} + \frac{77.6 \times 10^{-6} P}{T} - \frac{N_e}{2N_c} \tag{2.3}$$

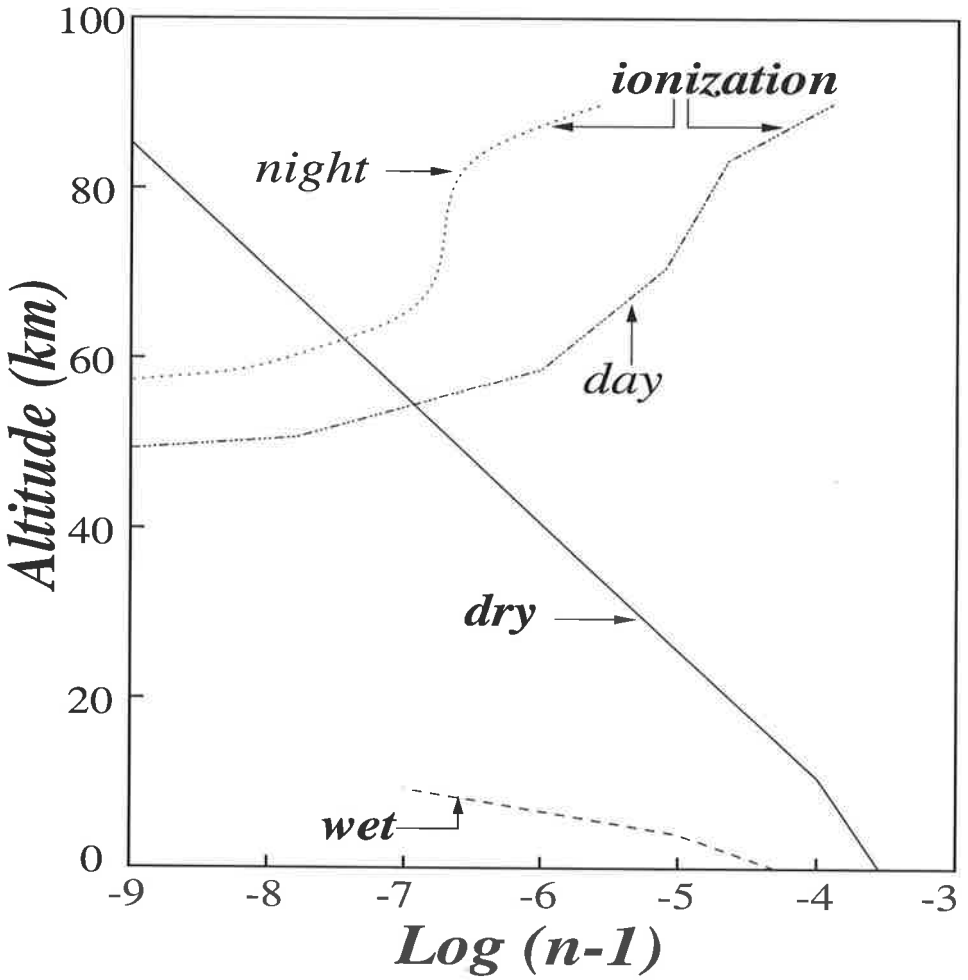

Figure 2.2: Typical altitude profiles of the wet, dry and ionization terms (adapted from *Sato* [1988]).

where, T is the absolute temperature (degrees Kelvin), e is the partial pressure of water vapour (hPa), P is the atmospheric pressure (hPa), N_e is the number density of free electrons (m^{-3}) and N_c is the critical plasma density (m^{-3})=$1.24\times10^{-2}f$ (MHz^2), in MKS units for the radio frequency, f. The three terms on the right-hand side of Equation 2.3 are referred to as the " wet", the "dry" and the "ionization" terms respectively. The refractive index equation is dominated by the wet term in the lower troposphere due to the relatively large

amount of water vapour present in that portion of the atmosphere. Above the tropopause, however, its influence is negligible. The dominance of the dry term begins from the mid-troposphere upwards into the stratosphere, where the effect of ionization begins to become significant. At these altitudes, the final term, the ionization term, dominates. This term undergoes the diurnal variation as a result of the ionization produced during the day and the recombination occurs during the night. The altitude dependence of each of these terms is illustrated in Figure 2.2.

The scatter observed by atmospheric radars can be separated into four distinct categories. The "Bragg scatter" or " turbulent scatter" results from variations in the refrative index with scale projected along the line of sight of the radar equal to one-half the radar wavelength distributed randomly throught the volume illustrated by the radar. A radar with operating wavelength λ_R obtains signal returns from irregularities whose outer scale, L_o, and inner scale, $l_o(= (v^3/\varepsilon_d)^{1/4}$, where v is kinetic viscosity of turbulence), fall in the range: $\lambda_{min} < \lambda_R/2 < \lambda_{max}$, where λ_{min} and λ_{max} are related to l_o and L_o, respectively. It is more precise to specify $C_1 2\pi l_o < \lambda_R/2 < C_2 2\pi L_o$ [*Balsley and Gage*, 1980], where C_1 and C_2 are constants of the order of unity and have empirical values of 0.94 and 0.75, respectively. "Fresnel scatter", or "diffuse reflection", [*Röttger,* 1989] occurs from collections of extended stable horizontal layers. Fresnel scatter produces much stronger and more coherent scattered signals. "Fresnel reflection" or "specular reflection", occurs from a single horizontally extended layer or sheet, which gives rise to backscattered signals. The returned signal may be quite strong and steady in amplitude and phase over relatively long periods. It is responsible for "slow fading" of radio signals. The Fresnel scatter, and Fresnel reflections are also known as partial reflections. The effects of these scattering mechanisms can be

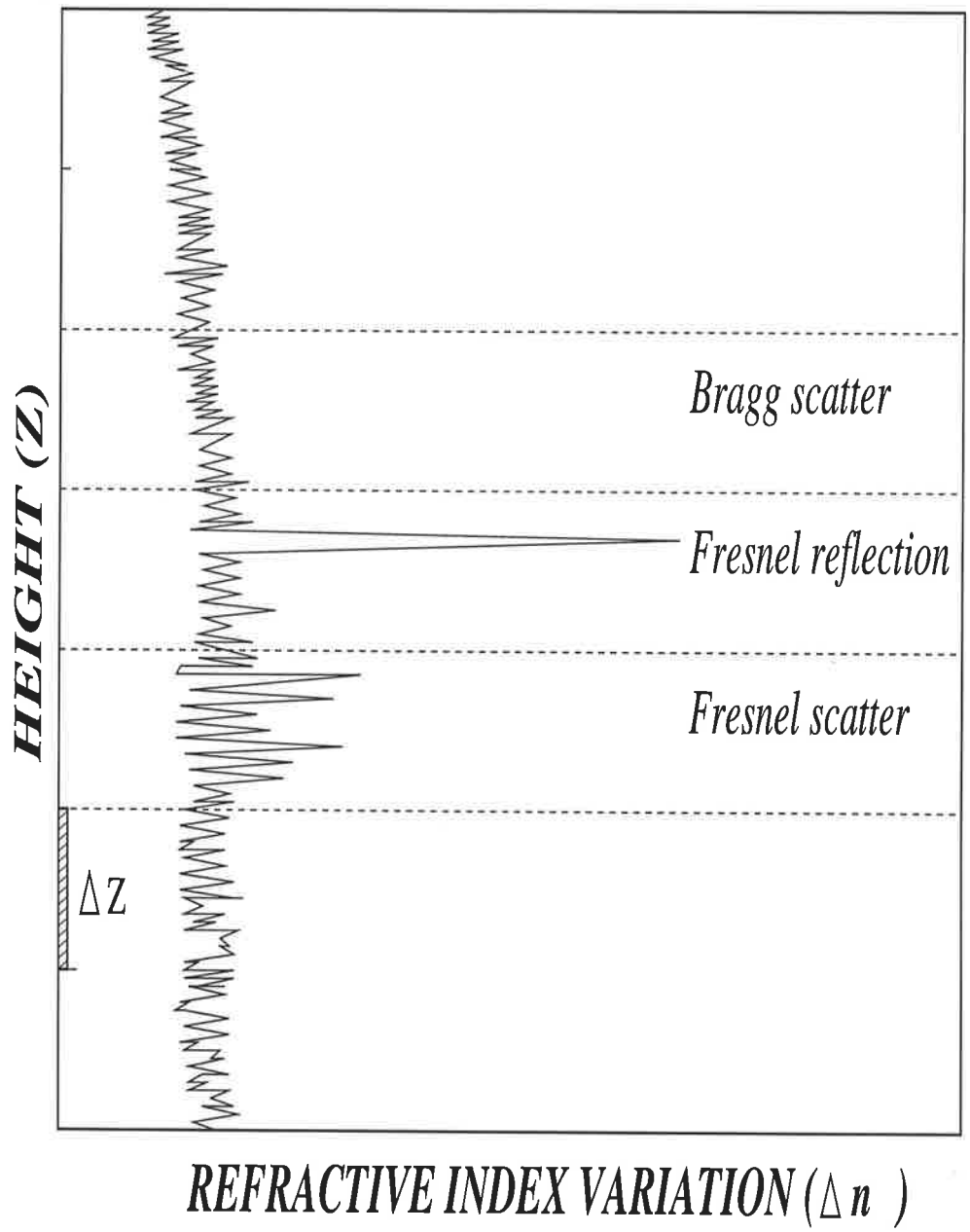

Figure 2.3: Effects of Bragg scatter, Fresnel reflection and scatter upon the atmospheric refractive index (adapted from *Röttger* [1989]).

distinguished by examining the returned power profile, as illustrated in Figure 2.3. An alternative (and much weaker) form of scatter arises when the incident electro-magnetic field interacts directly with free electrons which are forced to oscillate with the electric field. It is called "incoherent scatter" or "Thompson scatter" or "thermal scatter". The oscillating electrons re-radiate at a similar frequency to the incident radiation.

2.4 Atmospheric Pulsed Radar Theory

Consider a pulsed electromagnetic wave being transmitted at the time t_0 (see Figure 2.4) with the duration of Δt (the pulse width). The pulse travels in a nondispersive propagation medium (e.g. atmosphere) with the speed of light, c, and is backscattered from various ranges. The pulse shape is typically either smoothed trapezoid, triangular, boxcar or Gaussian shaped. The pulse reaches a range r_a after a time $t_a = r_a/c$. A target at r_a can scatter or reflect the signal in some directions. A small fraction of the signal returns to the location of the receiver (or transmitter) and is sampled after the time $t_1 = 2t_a = 2r_a/c$. For the monostatic radars (i.e. transmitter and receiver are at almost the same location), this yields the basic relationship:

$$r = ct/2 \tag{2.4}$$

enabling the range of any radar target to be determined by measuring the round-trip time, t. The returns sampled over the time interval t_1 to $t_1 + \Delta t$ originate from the range of heights indicated by the shaded region. This region is typically referred to as a "range gate" and is given by:

$$\Delta r = c\Delta t/2. \tag{2.5}$$

As echoes from the range between $r_a - \Delta r/2$ and r_a reach the receiver simultaneously at time t_1, the range Δr is called the "range resolution". The range resolution is increased by decreasing the pulse duration, Δt. The smaller the Δr, the better the detail along a profile can be resolved. The "bandwidth" of the receiving system, however, provides a lower limit for the pulse duration, and consequently, a lower limit for the range resolution, Δr. Figure 2.4 shows most of the echo power results from the range r_a, and minimum power is received from the range $r_a \pm \Delta r/2$. Accordingly, the resulting range weighting function of the single range gate centered around r_a is a triangle.

Radar pulses are normally transmitted periodically in order to sample the signal returns from each range gate with high temporal resolution. The transmission period is called interpulse period, t_{ipp}, in which, the reciprocal is denoted as pulse repetition frequency (PRF), $f_p = 1/t_{ipp}$. This leads to the definition of the "duty cycle" or "duty factor" of the transmitter as a ratio of the pulse duration to the interpulse period, $D = \Delta t/t_{ipp}$. The duty cycle is a measure of transmitter versus receiver activity (e.g. with the peak power of transmitter, P, the average power will be DP).

Pulse repetition puts a limit on the maximum range that can be observed without ambiguity due to " range aliasing". The effect is illustrated in figure 2.4, where echoes of the pulse from range r_a and the previous pulse from range r_b, are both received at time t_3, consequently, contributing to the echo power from that range. Echo power from the upper range is weak and obscured, while that of lower range is relatively strong and dominate. The maximum range that can

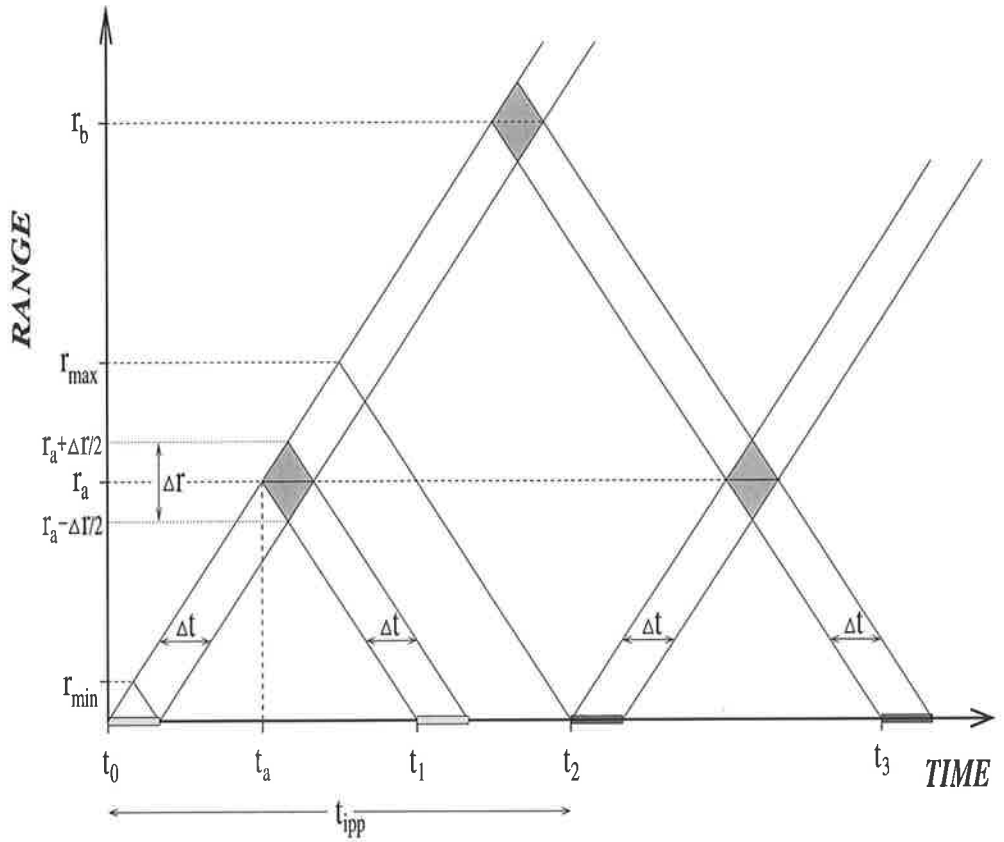

Figure 2.4: Range-time diagram of Doppler pulsed radar. Pulse echoes travel with a constant speed of c, from the scattering layers in the atmosphere. Δt is the pulse width, t_{ipp}, is the interpulse time between pulses. $t_{ipp} \gg \Delta t$ (after *Röttger* [1984]).

be observed without ambiguity, is a function of the interpulse period:

$$r_{max} = ct_{ipp}/2 = c/2f_p. \tag{2.6}$$

The pulse duration or pulse width determines the minimum detectable range as half the resolution, $r_{min} = \Delta r/2$, while, the pulse resolution, Δr, is chosen due to the instrumentally entailed transition between the transmission and the reception. The shorter the pulse width, the better the range resolution, and the

lower the PRF, the better the maximum range. However, the combination of low PRF and short pulses result in a very low duty cycle and average power, which reduces the maximum range. The short pulses have a greater band width and allow more background noise to enter the receiving system. The effect of range aliasing can be overcome by using "pulse coding", or by using a non-periodic t_{ipp}. Pulse coding [*Woodman, 1980; Röttger, 1984; Sulzer and Woodman, 1985*] involves assigning a unique "code" to each transmitted pulse so that the receiving system can distinguish the signal returns from each pulse.

2.5 Radar Equation for Scattering and Reflection

The returned power of echoes is very important in the design of radar systems. The relationship between transmitted power and received power is called the radar equation [*Tatarskii, 1971; Doviak and Zrnic, 1984; Sato, 1989*]. The radar equation operating at a wavelength λ for an isolated hard target at a range r with scattering cross-section, ς (perpendicular to the direction of incident beam) and also with transmitting power, P_t, from an antenna of effective aperture area A_e with gain $G = 4\pi A_e/\lambda^2$, shows the r^{-4} dependence of received power as:

$$P_r = \frac{GP_t}{4\pi r^2}\frac{\alpha A_e \varsigma}{4\pi r^2} \tag{2.7}$$

$$P_r = \frac{\alpha P_t A_e^2}{4\pi\lambda^2 r^4}\varsigma \tag{2.8}$$

where α is the efficiency factor (loss) for the system.

In the case of the isotropic volume scatter, the volume illuminated by the

radar beam increases with the square of the range. According to *Balsley and Gage* [1980], the radar equation reveals the r^{-2} dependence of received power as:

$$P_r = \frac{\alpha^2 P_t A_e \Delta r}{8\pi r^2} \eta \tag{2.9}$$

where the η is the volume reflectivity.

Gage and Balsley [1980] also determined r^{-2} dependency of received power of the radar equation from a single discontinuity by partial (Fresnel) reflection as:

$$P_r = \frac{\alpha^2 P_t A_e^2}{4\lambda^2 r^2} |\varrho|^2 \tag{2.10}$$

where ϱ is the amplitude reflection coefficient of the discontinuity. With the appropriate values for η and ϱ, the magnitude of the returned power is specified.

In real atmosphere, however, the range dependency of power returns is likely to lie somewhere between r^{-2} and r^{-4} that is, r^{-3} [*Doviak and Zrnic*, 1984].

2.6 Doppler Shift and Coherency

The transmitted pulse wave incident on the atmospheric scatterers or reflectors, forces molecular vibrations to occur at the same time as the electric and magnetic fields. In the case of stationary scatterers, or moving along a surface of constant range, r, the vibrations of molecules will be at the same frequency as the incident wave. For monostatic radars, if scatterers are moving toward the transmitter at velocity v, their vibration frequencies are higher by v/λ, since the target molecules experience more rapid fluctuations of electric and magnetic fields. The vibrating molecules generate electromagnetic fields radiating outward from the scatterers

and toward the transmitter with the increase of frequency of the magnitude of:

$$f_d = -2v_r/\lambda \tag{2.11}$$

where $v_r = dr/dt$ is the radial velocity, defined positive as the range increases away from the radar. This frequency change is called the "Doppler shift", which is higher (i.e. positive Doppler shift) if the target is moving towards the transmitter and lower (i.e. negative Doppler shift) if the target is receding. In the above formula, firstly, the target's electric vibrational frequency is increased by v_r/λ, and secondly, the frequency of its radiation field in the direction of the receiver is increased by v_r/λ.

The Doppler shift of the Equation 2.11 can be expressed as the rate of change of phase, ϕ, of the returned signal [*Low*, 1996] by:

$$f_d = \frac{1}{2\pi}\frac{d\phi}{dt} \tag{2.12}$$

since the radar signal is pulsed at a frequency $f_p = PRF$, the radar echo is sampled at a rate t_{ipp}, this yields the maximum Doppler frequency to be resolved by pulse-to-pulse analysis (Nyquist frequency) as $f_{d_{max}} = PRF/2 = f_p/2 = 1/2t_{ipp}$. From the Equations 2.11 and 2.6, the maximum unaliased measurable radial velocity can be derived as:

$$|v_r|_{max} = \frac{\lambda f_p}{4} = \frac{\lambda c}{8r_{max}}. \tag{2.13}$$

Equation 2.13 reveals that, the higher the PRF, the higher the maximum radial velocity observable and illustrates an important point in profiler design.

For MST radars operating in the lower VHF band around 50 MHz, the radial

velocities with quasi-vertical radar beams, do not exceed several $10\,m\,s^{-1}$ and the Doppler frequency will barely exceed $10\,Hz$. Applying a large enough PRF (i.e. PRF $> 1\,KHz$), the radar echo will be heavily oversampled, that is, its phase and amplitude does vary little from pulse to pulse. This is called the "coherency" of radar echo, in contrast to an "incoherency" of radar echo, which randomly changes in phase and amplitude from one pulse to the next. This coherency in the echoes allows us to improve the signal quality by simply adding together a number, n_c, of sequential samples. This coherent averaging reduces the total noise power by removing high-frequency components from the signal, as well as deduce some obvious experimental advantages. The "sampling rate" which is defined by f_p/n_c, determines the time resolution of echo measurements. By substituting the f_p/n_c into Equation 2.13, the largest radial velocity measurable is given:

$$|v_r|_{max} = \frac{\lambda f_p}{4n_c}. \tag{2.14}$$

The degree of coherent averaging is an important factor in radar experiments, and its selection is determined by the nature of the turbulent irregularities being observed.

2.7 Data Analysis Techniques

There are two ways of analysing the raw data, sampled time series of electromagnetic field variations at the receiving antenna system on the ground; the frequency domain and the time domain. Each has advantages and disadvantages. A brief discussion of each will follow, as in the three case studies of cut-off lows discussed in this thesis, the raw data analysis of two of the most recent ones (i.e. 1995) are

carried out in the frequency domain and the other (i.e. 1992) in time domain by David J. Low at the University of Adelaide.

2.7.1 Frequency Domain Analysis

In the frequency domain, the pulse-to-pulse time-varying echo strength time series is reduced, which is the most important aspect of this technique. In order to avoid ambiguity in the Doppler shift arising from Fourier transform of a single discrete wave form, the returns from each transmitted pulse are mixed with sine and cosine phase-locked signals from a local oscillator. The Fourier transform of the resultant signals, which are called the "in-phase" and "quadrature" components, respectively, give the complex time series, z_i.

Figure 2.5 illustrates a typical power spectrum. The central frequency corresponds to the transmitted signal with Doppler shifted frequencies on either side. A positive Doppler shift corresponds to motion towards the antenna while, a negative Doppler shift corresponds to motion away from the profiler. The noise power $<N>$, or equivalently the average background signal level $\overline{N}$, is one of the four basic quantities (moments) measurable from the power spectrum. The mathematical details can be found in the reviews by *Zrnic* [1979], *Doviak and Zrnic* [1984] and *Woodman* [1985]. The area under the peak above the noise level, the signal power $<P>$, is another moment and the mean Doppler shift, f_d, which can be converted to a velocity using Equation 2.11 being the other moment. Finally, the width W_f of the peak, which is related to the degree of turbulence in the sampled volume [*Hocking*, 1983a], is the last measurable moment. The central peak, which is the reflections from stationary targets, caused by sidelobes of the beam, is called "ground clutter". Other contaminations such as: aliasing, interference, ocean wave echoes, or mixed scattering with reflection modes, and their

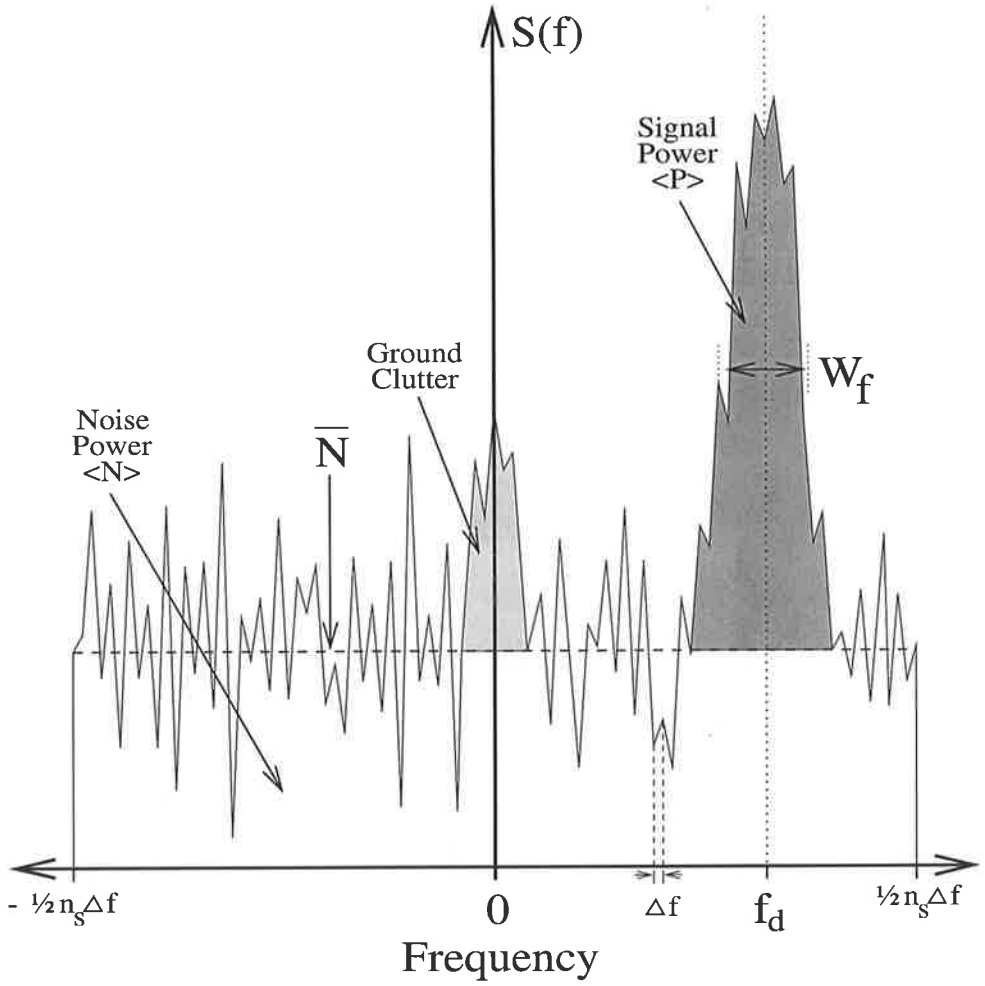

Figure 2.5: A typical power spectrum and measurement parameters (revised from *Low* [1996]).

eliminations are discussed by *Röttger* [1980a], *Rastogi and Holt* [1981], *Rastogi and Röttger* [1982], *Hocking* [1983a], and *Hocking* [1983b]. The signal-to-noise ratio (SNR) defined by $<P>/<N>$ is an important derived parameter. Analysis in frequency domain allows the identification of multimodal spectra such as: combined clear-air and precipitation echoes, as well as the removal of spectral artifact.

2.7.2 Time Domain Analysis

According to the Wiener-Khinchine theorem, the power spectrum and autocorrelation function of a sampled signal contain similar information about the lower spectral moments, distributed over frequency in the power spectrum, and concentrated in the small lags of the autocorrelation function [*Woodman and Guillen*, 1974; *Bowhill*, 1983]. The m-th lag value of the autocorrelation function of the N-point complex time series Z_i defined by:

$$R(m) = \frac{1}{N-m} \sum_{k=0}^{N-m-1} Z_k^{\star} Z_{k+m} \tag{2.15}$$

where $\star$ denotes cojugation. There is a direct relationship between the n-th classical spectral moment, M_n, and the n-th derivative of the autocorrelation function at zero lag:

$$M_n = R^{[n]}(0)/(2\pi j)^n. \tag{2.16}$$

Figure 2.6 illustrates a typical autocorrelation function, displayed as amplitude ρ and phase ϕ components as a function of the lag τ. The random background noise appears as a "spike" of size N in amplitude at zero lag. Ground clutter produces almost constant amplitude platform(c), where the expected (pseudo) Gaussian is superimposed. The interpolated zero-lag value of this Gaussian corrected for clutter, is a direct measure of the signal power P, while its width W_τ is a measure of the echo lifetime. According to *Hocking* [1983b] and *May* [1988], it is advisable to set the time series length, n_s, to a value between 25 and 50 times the autocorrelation width to reduce the effects of small-scale temporal variability, whilst retaining a representative data record. Eventually, the mean frequency shift is given by the slope of the autocorrelation phase through Equa-

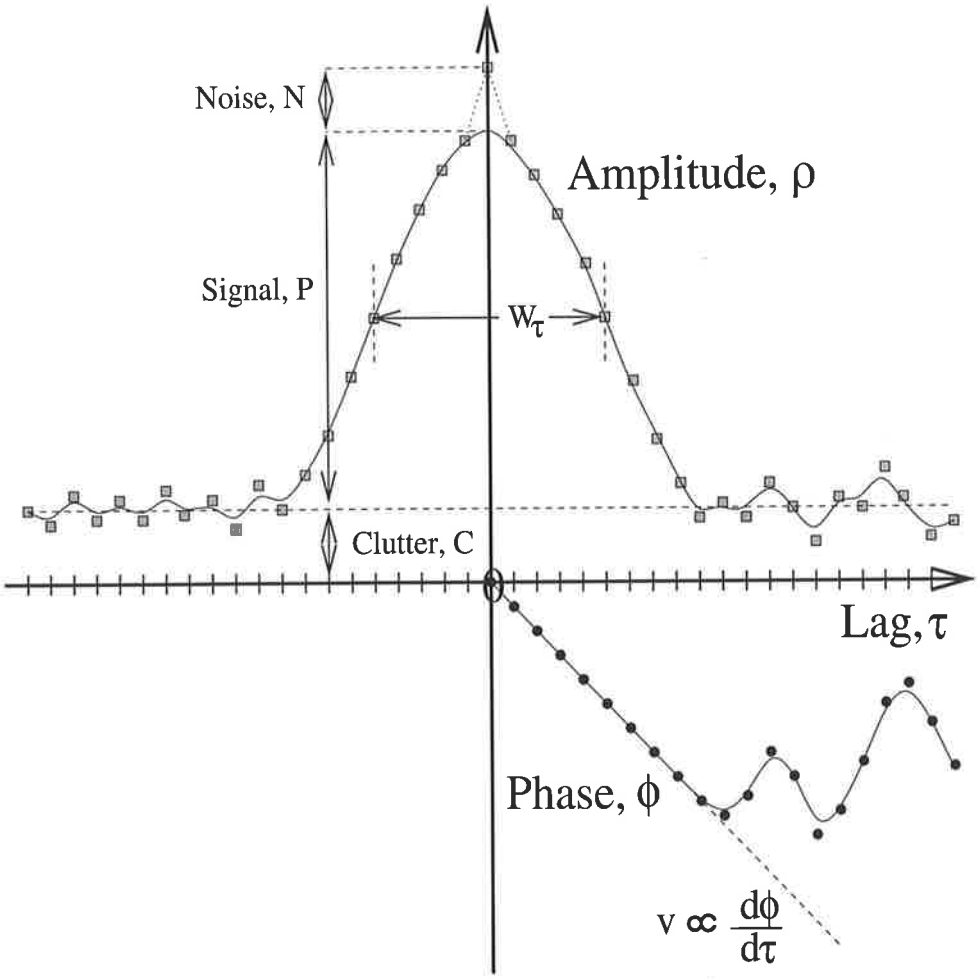

Figure 2.6: A typical autocorrelation function and measurement parameters (adapted from *Low* [1996]).

tion 2.12. The Doppler velocity is thus derived by applying Equation 2.11. The SNR is defined by P/N and is usually expressed in decibel (dB) units by taking $10log_{10}(P/N)$.

Woodman [1985] gives a detailed evaluation of the signal power and Doppler velocity from the zero and first lag values of ρ and ϕ respectively through the single delay autocorrelation approach.

2.8 The Measurement of Winds

The main task of VHF/UHF radars is the measurement of the three-dimensional wind field of the atmosphere. For radars working at vertical beam mode, the Fresnel reflection is the main mechanism, whereas, for those working off-zenith beam mode, the scattering from irregularities generated by isotropic turbulence is an essential mechanism. *Gage and Green* [1978] were the first to point out the importance of Fresnel reflection for the VHF radars that was confirmed later by *Röttger and Liu* [1978] and *Röttger and Vincent* [1978], who observed the enhancement in the returned signal power.

By measuring the Doppler frequency of Bragg scatter echoes, the wind velocity vector can be determined [*Wilson and Miller*, 1972; *Gage and Balsley*, 1978]. This method is usually referred to as the Doppler method. The other method uses a vertical-beam antenna for transmission and at least three horizontally spaced, vertical-beam receiving antennas. The echoes, which in the low VHF band are typically a result of Fresnel scatter or reflection, are cross-correlated to determine the wind velocity [*Briggs*, 1977; *Röttger and Vincent*, 1978] in the technique known as the spaced antenna (SA) method. These two methods are described in more detail in the next section and appendix A, respectively. Both methods are based on the same physical mechanism (Taylor hypothesis), in principle. Namely, echoes scattered or reflected from moving irregularities in different directions show a different Doppler shift, which is measured with the Doppler method to deduce the velocity. Fading signal amplitudes or a drifting diffraction pattern at the ground will result from the interference pattern of echo amplitudes from moving scatterers or particular reflecting regions located in different directions. The fading pattern is measured with the spaced antenna method in order to deduce

the velocity. The other techniques of wind measurements will not be reviewed here.

2.8.1 Doppler Technique

The radial velocity of scatterers can be measured through autocorrelation or spectral analysis. *May et al.*, [1989b] and *May and Strauch* [1989] discussed the accuracy of various estimators for the Doppler shift in the estimation of winds. With the Doppler method the Doppler shift of the backscattered radar echoes is measured over a set of beam directions. Complex autocovariance of spectral analysis, and further digital processing yield the radial velocities in different beam-pointing directions. These line-of-sight velocities are then used to calculate the three orthogonal wind components. The method is a simplified version of the well-known velocity-azimuth display (VAD) method. With the assumption of the uniform wind field, for a constant zenith angle, radial velocity will vary sinusoidally with azimuth angle. Fourier analysis of the radial velocity taken at several azimuths yields the three-components of wind field. However, profiling radars usually observe the vertical velocity with better accuracy by using a vertical beam. Using one vertical and four or more off-vertical beams enables us to calculate the divergence of the wind field *Clark et al.*, [1986]. More accurate estimates of the vertical velocity can be obtained by keeping the azimuth constant and changing the elevation angle. This is known as the velocity-elevation display (VED) technique. Extension to multiple azimuth angles enables us to measure the full three-dimensional wind field. The measurement of the aspect sensitivity of scatterers, which is a measure of atmospheric stability and thus allows the detection of a stable layer (e.g. the tropopause), is also achieved by the VED method.

The most widely applied method is Doppler beam swinging (DBS) where, the echoed Doppler-shifted frequency is measured with a narrow beam pointed in different directions. Equations 2.12 and 2.14 yield [*Röttger*, 1984]:

$$V_r = \frac{\lambda}{4\pi}\frac{\delta\phi}{\delta t}. \tag{2.17}$$

According to *Woodman and Guillen* [1974], the mean rate of change of phase for the scatterers is:

$$\frac{d\Delta\phi}{dt} = \frac{1}{2\pi\delta t} tan^{-1}\left[\frac{Im\left(\rho\left(\delta t\right)\right)}{Re\left(\rho\left(\delta t\right)\right)}\right] \tag{2.18}$$

where $\rho(\delta t)$ is the autocovariance function of the complex time series at time shift δt, Im and Re stand for imaginary and real parts of the complex quantity respectively. Fourier transform of the power spectrum of a time series which is the autocovariance function [*Bracewell,* 1986], is found from:

$$\rho\left(\delta t\right) = \sum_{i=1}^{n} P\left(f_j\right) e^{2\pi i f_j \delta t} \tag{2.19}$$

where $f_j = (j-1)/T$ and T is the data length of the time series.

Substituting Equations 2.18 and 2.19 in Equation 2.17 with the assumption that the term inside the brackets is much less than unity, yields:

$$V_r \approx \frac{\lambda}{2}\frac{\sum_{i=1}^{n} f_j P\left(f_j\right)}{\sum_{i=1}^{n} P\left(f_j\right)}. \tag{2.20}$$

The vertical velocity (beam vertical) and horizontal wind (beam off-vertical) can be deduced from Equation 2.20. The strong aspect sensitivity of the scatterers at VHF band ($\sim 50\,MHz$), can cause the effective pointing beam direction to be

smaller than the physical direction. As mentioned by *Strauch* [1983] and *Vincent* [1984], there is an optimum beam pointing angle. The recommended off-vertical pointing angle for radars operating at VHF band, is $10° - 15°$. The significant sidelobe signals have to be rejected from the analysis.

Comparisons of Doppler wind measurements with rawinsondes have been carried out with almost all existing radars. A fair to good agreement has always been reported [*Fukao et al.*, 1982; *Larsen*, 1983a]. *Frisch et al.*, [1986] compared wind velocities measured with a VHF and a UHF wind profiler and found an almost one-to-one correlation. *Fukao et al.*, [1982] came to the conclusion that 430 MHz, as well as 50 MHz Doppler radar measurements of winds provide more accurate, and more frequent wind profiles than do conventional rawinsondes. Furthermore, the radars can measure the vertical velocities, providing more important additional data than the indirect methods, which are typically used to derive the vertical velocities from radiosonde data. *Larsen* [1983b] noted that an MST radar can provide synoptically meaningful data and that the Doppler radar measurements produce data of a quality that is at least comparable to the estimates of accuracy for radiosonde data.

2.8.1.1 Comparisons of Spaced Antenna Method with other Wind Measurements

Vincent and Röttger [1980] first showed that spaced antenna (SA)[1] winds in the lower atmosphere are in good agreement with radiosonde winds.

Comparison of SA wind estimates with a number of other techniques have been done to assure accuracy. Comparisons of upper atmospheric wind have been made with rocket sounding by *Vincent et al.* [1977], with meteor drift by

[1]The spaced antenna (SA) technique is discussed in appendix A.

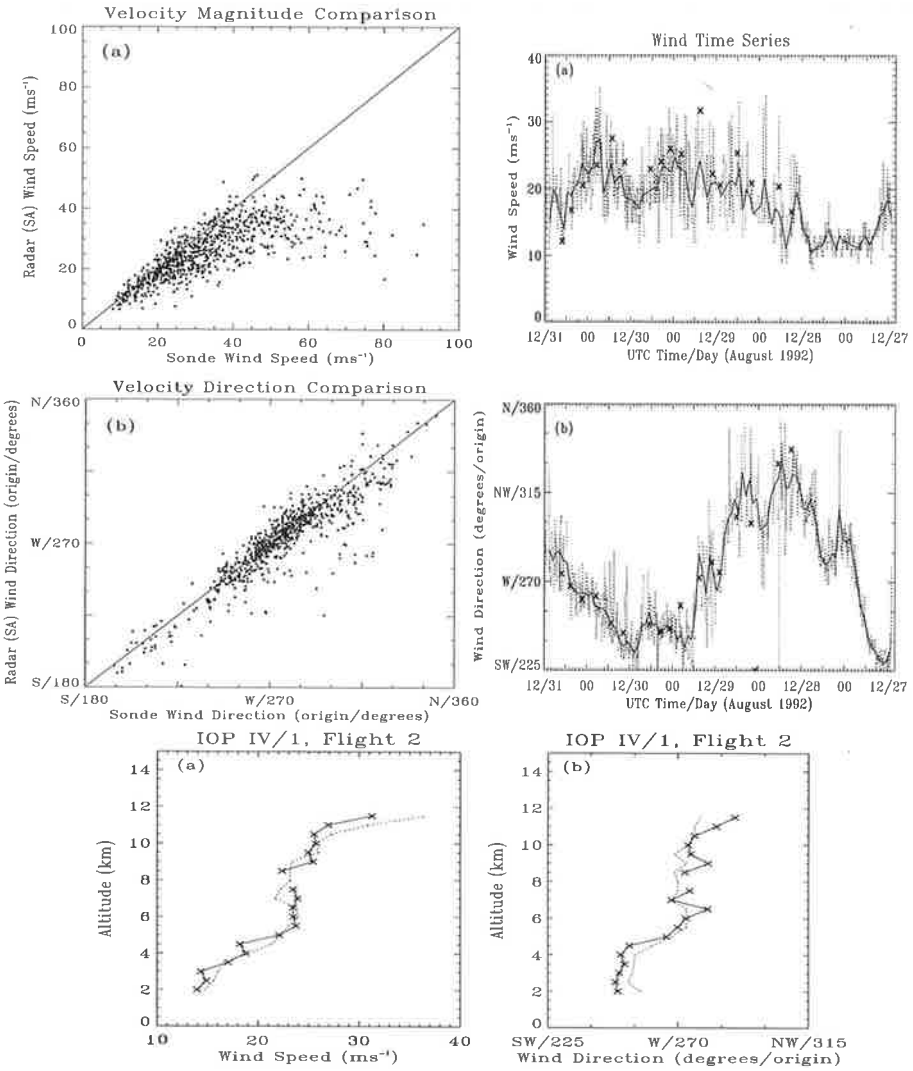

Figure 2.7: A comparison of SA winds with MARWINsonde: (top-left) wind magnitude and (middle-left) wind direction. Time series of wind speed (top-right) and wind direction (middle-right) at $3\,km$ height . Sonde measurements are marked by $\times$'s, raw SA winds by dotted lines and two-hourly average SA winds by solid lines. Altitude profiles of wind speed (bottom-left) and wind direction (bottom-right) for profiler (solid line, $\times$'s) and MARWINsonde (dotted line). (adapted from *Low* [1996]).

Cervera and Reid [1995] and with Doppler beam swinging (DBS) by *Reid* [1988]; *Röttger and Czechowsky* [1980] and *Van Baelen et al.*, [1990]. The comparisons with all three techniques, SA, DBS and radiosonde have been made by *Vincent et al.,* [1987] and also with interferometric winds by *Sheppard et al.*, [1993]; *Holdsworth and Reid* [1995b] and *Vandepeer and Reid* [1995]. All comparisons have shown a good agreement, although *Holdsworth and Reid* [1995a,b] quoted a slight underestimation (~ 5) from a modeling perspective.

A comprehensive comparison of all aspects of SA wind and a large number of co-located radiosonde (MARWINsonde) for minimizing the effects of spatial variation during the South Australian Frontal Experiment campaign (SAFEx), has been carried out by *Low* [1996]. He pointed out that the wind *direction* returned by the radar is in excellent agreement with the sonde measurements (Figure 2.7, top-left), while the spaced antenna wind *magnitude* shows a distinct "levelling out" around $30\,m\,s^{-1}$ (Figure 2.7, middle-left). He mentioned that, the previous comparisons by *Vincent et al.*, [1987] have generally been made in conditions of low or moderate winds. In high winds, however, radiosondes can travel hundreds of kilometres laterally from their launch site, making precise comparison with ground-based sensors difficult. He also added, the traces of the behaviour displayed in Figure 2.7 can be seen in Figure 5 of *Vincent et al.*, [1987] and Figure B.3 of *Rajopadhyaya* [1994].

Figure 2.7 (top-right and middle-right) shows a comparison of spaced antenna and MARWINsonde winds as a *time series* at $3\,km$ height for about four days during the SAFEx campaign [*Low*, 1996]. It shows that, the agreement between the sonde and radar is generally excellent, given the bounds of inherent variability.

Finally, an example of *altitude* profile comparison is displayed in Figure 2.7 (bottom-left and bottom-right), which again displays excellent agreement [*Low*, 1996].

Chapter 3

Buckland Park VHF Radar

3.1 Introduction

In the atmosphere the presence of turbulence will cause the refractive index to fluctuate around its mean value, both in time and in space. These fluctuations will in principle produce scattering of radio waves, which is observable with a radar sensitive enough to detect the very weak echoes.

It is known that it is technically feasible to construct radars which can utilize those very weak echoes. This is accomplished by combining sufficiently large antennas with high transmitter powers and sophisticated signal averaging techniques, as well as appropriate choice of operating frequency. The need for high gain antennas and short pulses (to achieve the required height resolution) suggests the use of high radio frequency. It is known that if the atmospheric density fluctuations are Fourier analysed, then the strength of the radar echo is proportional to the magnitude of density fluctuations having a scale equal to half the radar wavelength. The higher the radar frequency, the smaller the spatial scale and it is high likely to be damped or not present at all, due to the effects

of viscous dissipation. The choice of the half-wavelength of a radar is essential in the so-called "inertial range" of the turbulence spectrum, where viscosity is not important. The frequency variation of galactic and man-made noise are also important in choosing the radar frequency. The frequency near $50\,MHz$ is the frequency of most existing radars which are designed to measure the atmospheric wind fields and turbulence. With the above frequency, the "see" spatial scales in the atmospheric structure will be of the order of $3\,m$. The effectiveness of a radar depends on the product of the mean power transmitted and the area of the antenna array. By varying the angle of the radar beam the strength of the echoes can be studied as a function of off-vertical angle, in which, the strongest echoes are sometimes found to be those for the beam directed vertically upwards.

In the past two decades radars have become powerful tools for studying the properties of the lower, middle and upper atmosphere. These systems might be a replacement of existing wind measuring instruments and methods. The VHF wind profiling radar system has a variety of applications in atmospheric research and meteorology such as:

- Vertical structure of winds for synoptic studies of the troposphere and stratosphere.
- Measurement of atmospheric stability and turbulence.
- Measurement of small scale phenomena.
- Studies of frontal structure.
- Studies of short-waves.
- Tropospheric/Stratospheric exchange.

- Studies of atmospheric wave generation, propagation and dissipation.
- Studies of gravity waves.

The time resolution of the profiler technology is as high as a few minutes and height resolutions as high as a few hundred meters for wind measurements. The system can provide a cost effective replacement for balloon-borne wind measuring instrumentation, allowing continuous tropospheric wind observations at remote sites.

3.2 Hardware and Operating Parameters

The 54.1 *MHz* Buckland Park VHF radar (34°37′ S, 138°29′ E) is situated some 35 *km* north of Adelaide (34°55′ S, 138°35′ E) on a flat coastal plain and about 50 *km* from significant orography, Mountain Lofty (517 *m* height). It is located adjacent to the 2 *MHz* MF radar [*Briggs et. al.*, 1969]. The first result appeared in *Vincent et. al.*, [1987]. The VHF radar was initially designed to study tropospheric winds and dynamics however, its versatility enables it to be used for a variety of meteor experiments.

The VHF radar antenna consists of collinear coaxial (Co-Co) array which can be used for both transmission and reception. The array is approximately 90 *m* square and consists of 32 dipole rows. There are two sets of sixteen North-South rows, each of 48 dipoles producing a beam with a half-power half-width of about 1.6°. Phasing the rows of antennas tilts the beam in an Eastward or Westward direction. There are three other sets of antennas, called Yagi antennas, each of sixteen 3-element antennas located adjacent to the main array (i.e. Co-Co array) allowing spaced antenna (SA) measurements of the full three dimensional wind

field. These Yagis are used for reception only. A site plan for VHF spaced antenna radar system is shown in Figure 3.1. For more details, the reader is referred to *Vincent et. al.*, [1987].

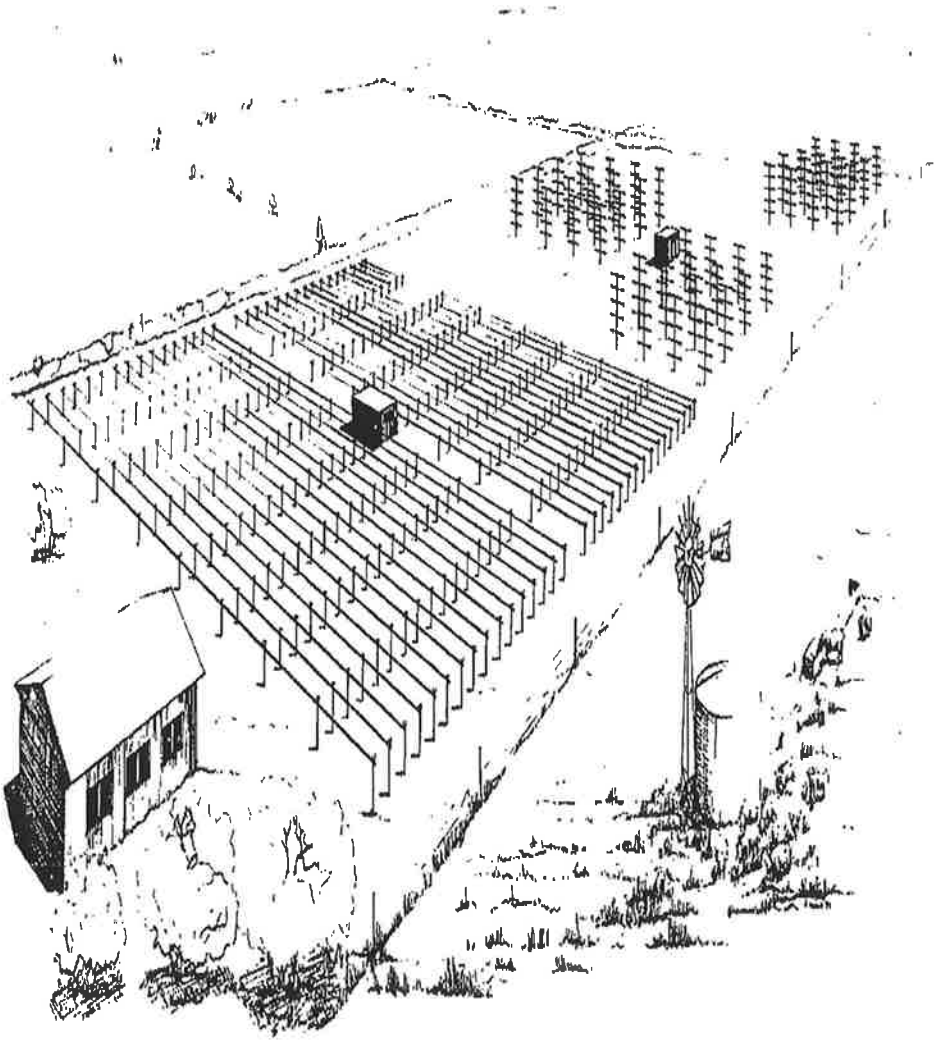

Figure 3.1: A site plan for a VHF Spaced Antenna radar system based on the Adelaide VHF radar (adapted from *Vincent and Reid* [1994]).

During 1992/93 the power and time resolution of the VHF radar was up-

graded. The transmitted peak power was increased from $4\,kW$ to $32\,kW$ and the time resolution of the receiving system was reduced from $16\,ms$ to $1\,ms$ which is very important in short duration echo detection. Typical operating parameters of the VHF radar are summarised in Table 3.1.

The operating mode of the profiler usually consists of a five minute cycle, alternating one vertical Doppler retrieval (64 seconds of data collection, plus analysis time) with one spaced antenna run (128 seconds of data collection plus analysis). This situation of cycles enables the estimations of vertical velocity from the narrow Doppler beam, together with the estimations of horizontal wind from the enhanced returned power of the SA method. As during the experiments there were only three receiving channels available, the simultaneous measurements were not possible. There were three channels (i.e. Rx0, Rx1 and Rx2). Channel Rx0 was switching between reception on the large Co-Co array for Doppler measurements and Yagi array for SA measurements. The switching was performed through a simple logic chip setup in a box called logic box. For details of antenna switching control and the Co-Co array polar diagram model, the reader is referred to Appendix A and Appendix B of *Low* [1996] respectively.

3.3 The Co-Co Antenna Array

The VHF array consists of 32 rows of Co-Co antennas, each of a length of $52\,\Omega$ coaxial cable with the inner and outer conductors interchanged every half wavelength [*Wheeler,* 1956; *Balsley and Ecklund*, 1972]. As they are relatively cheap to built and easy to maintain, Co-Co arrays are widely used. However, they are less efficient than Yagi arrays. Due to the loss of signal in the coaxial cable used for the Co-Co rows and feeders, the efficiency of the VHF Co-Co array is only

Table 3.1: Typical operational parameters of the Buckland Park VHF radar in Doppler (DBS) and spaced antenna (SA) modes, appropriate to the 1992 case study of 6-9/10/92 (adapted from *Low* [1996]).

Radar system:	Monostatic DBS/bistatic SA pulse radar
Operational frequency:	54.1 MHz ($\lambda = 5.55\,m$)
Transmission antenna (Tx):	Coaxial-collinear dipole array (32 rows of 48 $\lambda/2$ elements)
Tx antenna area:	7900 m^2
Tx antenna efficiency:	≈ 0.3
Tx beamwidth:	1.6° half-power half-width
Beam steerability (ψ, χ):	Vertical (0°,0°), East (86°,11°), West (266°,11°)
Peak Tx power:	16 kW (from eight, 2 kW solid-state Tx modules)
DBS reception (Rx):	On Co-Co array, parameters as above
Pulse length:	6.7 μs
Range resolution:	1000 m, but oversampled every 500 m
Range coverage:	2.0–19.5 km inclusive (36 range gates)
PRF:	4096 Hz
Average Tx power:	440 W (2.7% duty cycle)
Coherent integrations:	1024 points
Effective sample rate:	4 Hz (intersample period 0.25 seconds)
Record length:	64 seconds (256 points)
Maximum unaliased velocity:	22.2 ms^{-1}
SA reception (Rx):	3 Yagi arrays of sixteen 0.7λ-spaced 3-element Yagi antennas
SA Rx effective area:	$\approx 150\,m^2$ (each Yagi array)
SA Rx spacing:	50 m equilateral triangle, at 176° and 236° from Yagi array Rx0
SA Rx beamwidth:	9° half-power half-width
Pulse length:	6.7 μs
Range resolution:	1000 m, but oversampled every 500 m
Range coverage:	2.0–14.5 km inclusive (26 range gates)
PRF:	8192 Hz
Average Tx power:	880 W (5.4% duty cycle)
Coherent integrations:	1024 points in hardware, then 4 points in software
Effective sample rate:	2 Hz (intersample period 0.5 seconds)
Record length:	128 seconds (256 points)

30% while, that of Yagi's with the similar aperture is about 80% (estimated). Each row is centre fed and has 23 inner/outer interchanges either side of the centre feed. Thus, each Co-Co antenna row contains 48 half wavelength dipoles, making a total of 1536 dipoles. Taking into account the propagation velocity of the signal in the coaxial cable, each element of it is cut to 0.67 of a wavelength, giving a physical length of 88.7 m to the antenna. The array is constructed on an area of accurately leveled ground of 90 m by 90 m. The rows are separated by half a wavelength with the exception of the two centre ones which are three times that distance (i.e. 1.5 wavelength) apart; the area where transmitting caravan is located. Thus the distance between the two end rows is then 88.7 m, giving a square array of 88.7 m^2. Figure 3.2 illustrates the schematic ground plan of the VHF radar system at Buckland Park, South Australia.

The Co-Co array is suspended a quarter of a wavelength above the ground. Copper wire with a spacing of $\lambda/12$ strung out on the ground, parallel to the Co-Co antennas, produces a ground plane that is independent of the reflectivity of the ground, which is necessary to maximize the efficiency of the array.

The center feeds to the Co-Co antenna have 70 pF fixed capacitors across the inputs together with small lengths of coaxial cable or "capacitive tuning stubs" in parallel with the 70 pF capacitors. Fine tuning of each of the antennas is provided by trimming the stubs to the required length. The balanced impedance for each antenna should be 50 Ω with zero phase. In order to get the vertically directed beam, the electric length of the parallel feeder cables to each of the rows of antennas should be of integral wavelength. If the beam is required to be tilted in either an Eastward of Westward direction, phasing cables of the appropriate length are introduced to successively delaying the signal to or from each row. Relays controlled by a micro processor are used to switch the phasing cables in

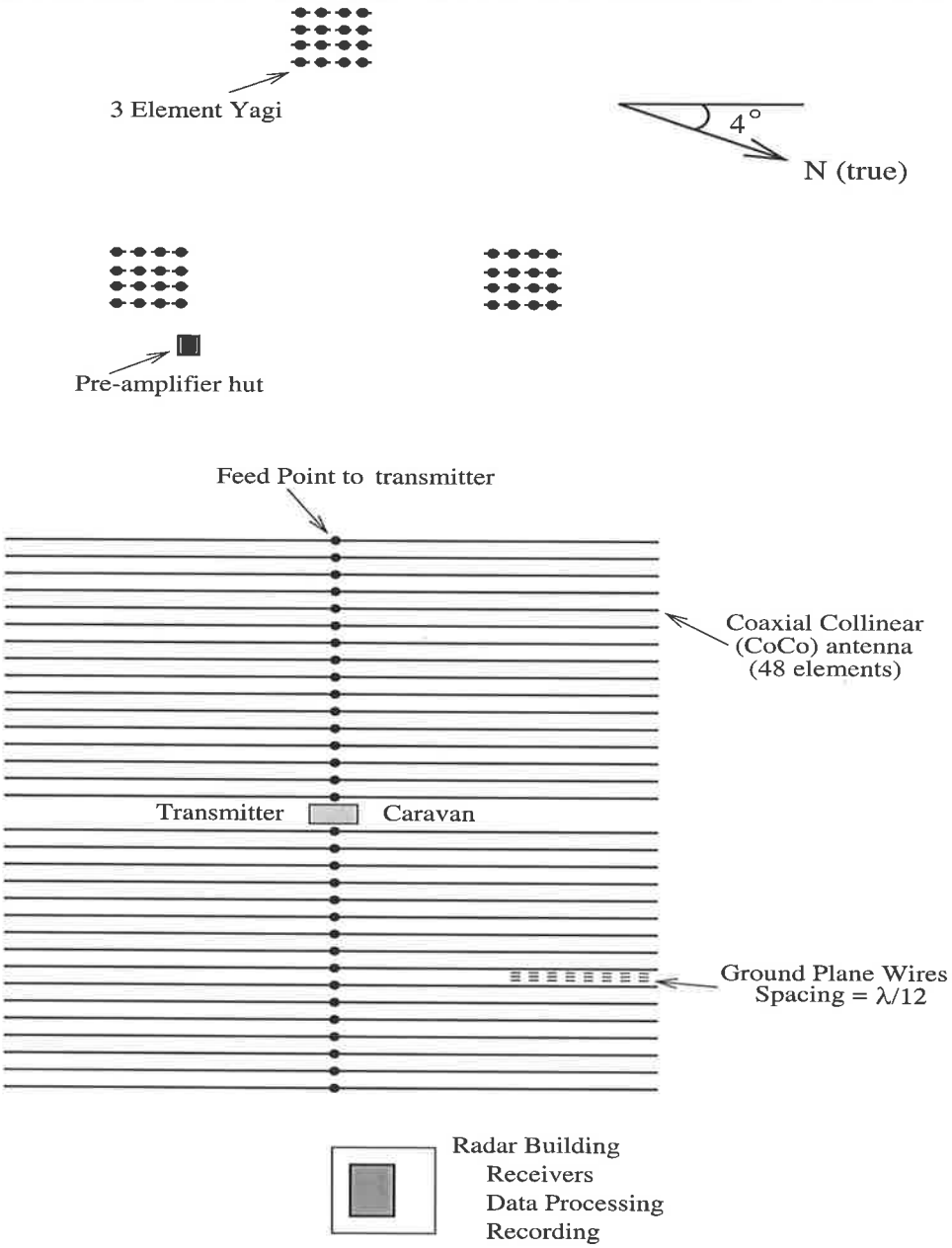

Figure 3.2: A schematic ground plan of the 54.1 *MHz* VHF radar system at Buckland Park (34°37′ S, 138°29′ E), South Australia.

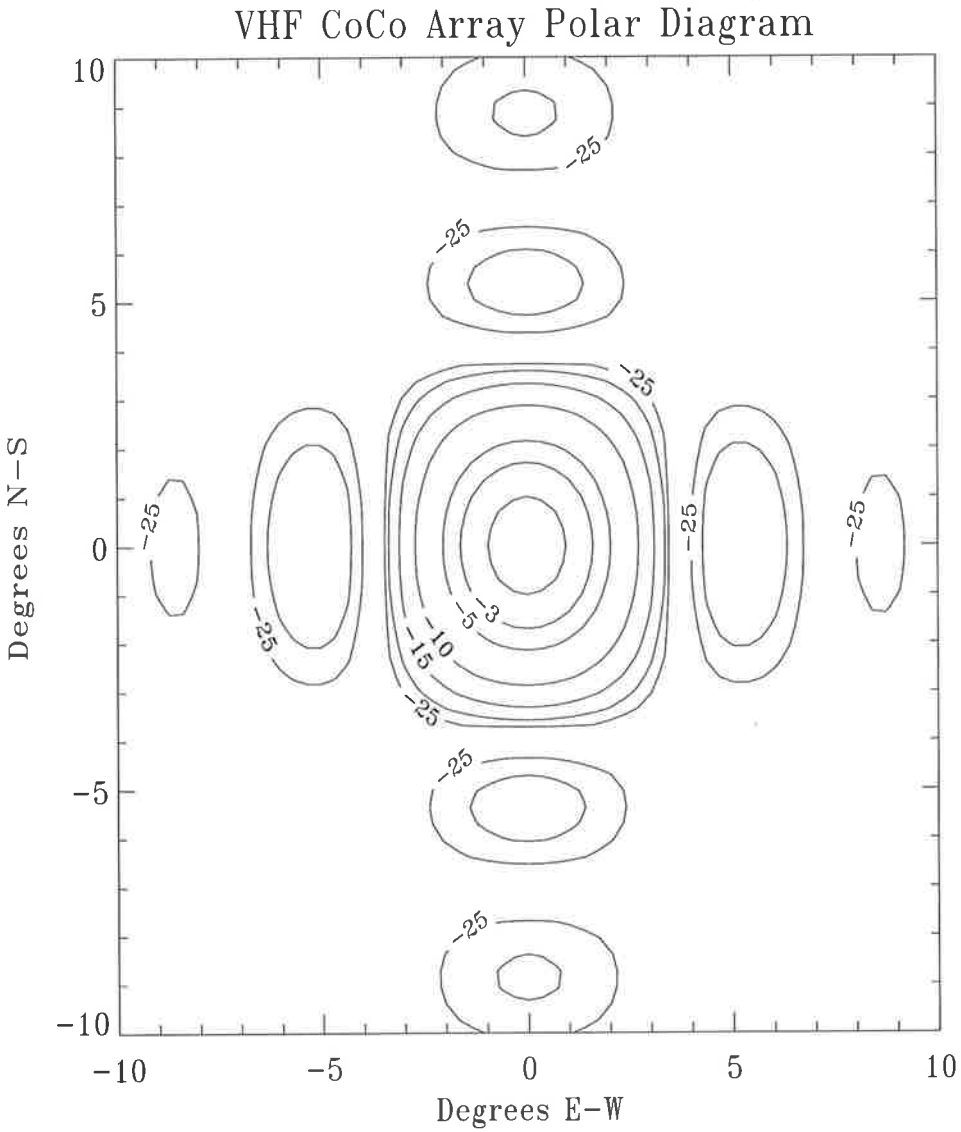

Figure 3.3: A contour diagram of the VHF Co-Co antenna polar diagram. Contours are plotted at -1 *dB*, -3 *dB*, -5 *dB*, and every 5 *dB* thereafter to -25 *dB*. The half-power(-3 *dB*) half-widths are about 1.6° in the East-West plane, and about 1.7° in the North-South plane. (adapted from *Low* [1996]).

or out, or to switch the direction of the phase delay so that the beam may be vertically directed or tilted, East or West. The simple geometry implies that the phase delay δ required between adjacent rows separated by $l = \lambda/2$, to produce a beam at zenith angle α is given by:

$$\delta = \frac{2\pi}{\lambda} l sin\alpha = \pi sin\alpha \tag{3.1}$$

where λ is the wavelength.

For example if a beam tilt of 30°is needed, then cables of length $\lambda/4$, $\lambda/2$, $3\lambda/4$, and λ are used to give successive 90° phase differences to each Co-Co antenna.

The receiving antennas for the spaced antenna technique are three spaced arrays each consisting of sixteen, 5-element Yagis. The Yagis are of an inexpensive commercial type sold for television reception. The arrangement of the receiving antennas is shown in the upper part of Figure 3.2. Signals from the three arrays are fed to a small hut containing preamplifiers and then by underground coaxial cables to the main radar building at the east end of the site. This building contains the receivers, and all the computing, recording and control equipment. Coherent averaging of several successive received pulses is used to improve the signal to noise ratio (SNR).

A polar diagram of the vertical beam, a contour diagram of the ideal array, with no phase errors, is shown in Figure 3.3. The half-power half-width is about 1.6° in the East-West plane, and about 1.7° in the North-South plane. The East-West width is slightly narrower than the North-South width since losses along the coaxial-collinear rows are more severe than losses in the transmission lines to each row.

3.4 The Transmitting and Receiving Systems.

The Buckland Park VHF pulse transmitter is housed in a small building at the center of the Co-Co transmitting array. It was upgraded in three stages during 1992 and 1993, from 4 kW to the design specification of 32 kW. There are 16 channels, each capable of supplying 2 kW of power to an East and West pair of rows of the Co-Co array. The pulse repetition frequency (PRF) and pulse width of the output power may be independently selected. Tables 3.2 and 3.3 list the available values which may be selected for both parameters. All combinations of PRF and pulse width can be selected without any reduction in pulse power. The transmitting system is modular in design, a single channel comprises a power amplifier (PA) module, exciter and a transmit/receive (T/R) switch. The T/R switches isolate the transmitting system from the receiving system. They employ state of the art solid state pin diodes to enable extremely fast switching (less than 1 μs). This is very important for the investigation of the lower atmosphere, where very short duration pulses and hence, high range resolutions are needed.

Table 3.2: Available pulse repetition frequency (PRF) of the VHF radar transmitting system.

PRF (Hz)
256
512
1024
2048
4096
8192

The Buckland Park VHF receiving and data acquisition system is housed in the main VHF radar building at the east end of the site. This building contains

Table 3.3: Available pulse width of the VHF radar transmitting system.

Pulse Width (μs)	Range resolution
1.3	0.20 km
2.4	0.36 km
3.5	0.53 km
6.7	1.01 km
12.8	1.92 km

the receivers, and all the computing, recording and control equipment. The receiving system holds 3 receiving channels, each with in-phase and in-quadrature outputs, and 6 digitizing channels and 6 coherent averagers. The three receiving channels are required for studies of the troposphere. Data are transferred via direct memory access (DMA) to an IBM compatible PC for analysis and storage. The usual operation of the radar is in one of two modes:

- Doppler Mode: Receiver 0 (Rx0) connected to the Co-Co array, Rx1 and Rx2 are not used. The radar in this mode is used for either tropospheric research (vertical beam) or meteor observations (East or West pointing beam).

- Spaced Antenna Mode: Rx0, Rx1 and Rx2 are each connected to one of the spaced Yagi arrays. Transmission is on the Co-Co array with a vertical beam. This mode is used to study atmospheric winds using Full Correlation Analysis (FCA) of spaced antenna data [*Briggs*, 1984].

For further detail of Buckland Park transmitting and receiving systems, the reader is referred to *Cervera* [1996].

Although the transmitting Co-Co antenna array ground is flat at Buckland Park, it is not perfectly level. Looking to vertical velocity, there is some small bias. We will try to evaluate the slope of ground-level and antenna-level to correct

this bias in vertical velocity measurements in the next step.

Chapter 4

ST Radar Studies of Vertical Motion

The vertical motion of the air is one of the most important parameters in meteorology. Wind profilers have been designed to measure the vertical velocity above the radar site, directly. The horizontal spacing of the radiosonde sites being about $300\,km \sim 400\,km$ puts limits on indirect estimates of $\overline{w}$ to relatively large-scale features. Wind profiling radars though, offer the unique capability of measuring the high temporal (almost continuous), as well as spatial resolution vertical velocity of the air.

Wind-profiling Doppler radars measure the radial component of motion in the atmosphere along the radar beam. The representativeness of the measurements of average vertical profiles of the vertical wind, in terms of actual vertical atmospheric motions is open to question. One possible complicating factor that can affect the accuracy of average vertical wind measurements arises from slight tilts of the pointing accuracy of the vertical beam resulting from slope of the ground under the transmitting antenna. Very slight inaccuracies in the vertical beam

direction can severely contaminate the measurements. For example, assuming a typical mean horizontal wind of 15 $m\,s^{-1}$, a mere 0.05 degree off-vertical skew of the vertical beam adds a $1.3\,cm\,s^{-1}$ component of the horizontal wind to the observed vertical velocity. Under some conditions, such a skew would heavily compromise the accuracy of mean vertical velocity measurements. However, the beam tilt of a few hundredths of a degree does not appreciatively affect instantaneous vertical velocity values. With the increasing use of profiler wind data, it is important to evaluate the feasibility of making useful mean vertical velocity measurements by assessing the impact of off-vertical beam on the measurements.

4.1 Buckland Park VHF Co-Co Antenna Array Slope

In order to have a transmitted beam pointing close to the zenith with uniformly phased antenna elements, the ground should be as flat and level as possible. The maximum slope across the transmitting array was approximately found to be less than 0.1 degrees from horizontal, with the low side on the south-east corner [*May*, 1986]. It was decided to determine the slope of the antenna more precisely and in different ways. Consequently, three different methods have been applied for determination as follows: ***(i) The height measurements of ground and the antenna level***, ***(ii) determination of gradient a plane surface fitted to the surface data*** and ***(iii) correlation of*** $\overline{w}$ ***with*** $\overline{u}$ ***and*** $\overline{v}$.

4.1.1 The First Method

The height of the ground and antenna level for 30 different positions of array, where the Co-Co lines meet each other in Figure 4.2, were measured by using the visible hose and water method. At first, the heights were measured with reference to the centre point of the array and then recalculated based on the lowest point. Figure 4.1 shows the sketch of the antenna array positions with the slope of different sides. The slope across the transmitting array was found to be approximately 0.176 degrees from the horizontal, with the low side on the south-west corner.

4.1.2 The Second Method

In this method the data obtained from the first method were surface plotted and the best plane surface was fitted to the data surface. Consequently, the gradient of the plane surface was found. In this way, the azimuth angle (ϕ) from north measured clockwise, is also determined.

The left hand plot of the Figure 4.2 shows the surface plot and the contour (gpm) plot of the ground level of the Co-Co antenna array while, the right hand plot with the best plane fitted to the surface, as well as a contour (gpm) plot of the plane surface. As it is shown, the highest point of the ground underneath the Co-Co array occurs midpoint on the northern side. The zenith angle (θ) is around 0.158 degrees and the azimuth angle is about 209 degrees. Obviously the ground plane has a slope towards south-west.

The left hand plot of the Figure 4.3 shows the surface and contour (gpm) plots of the level of the Co-Co antenna array, while, the right hand side shows the best plane fitted to the surface, as well as contour (gpm) plot of the plane

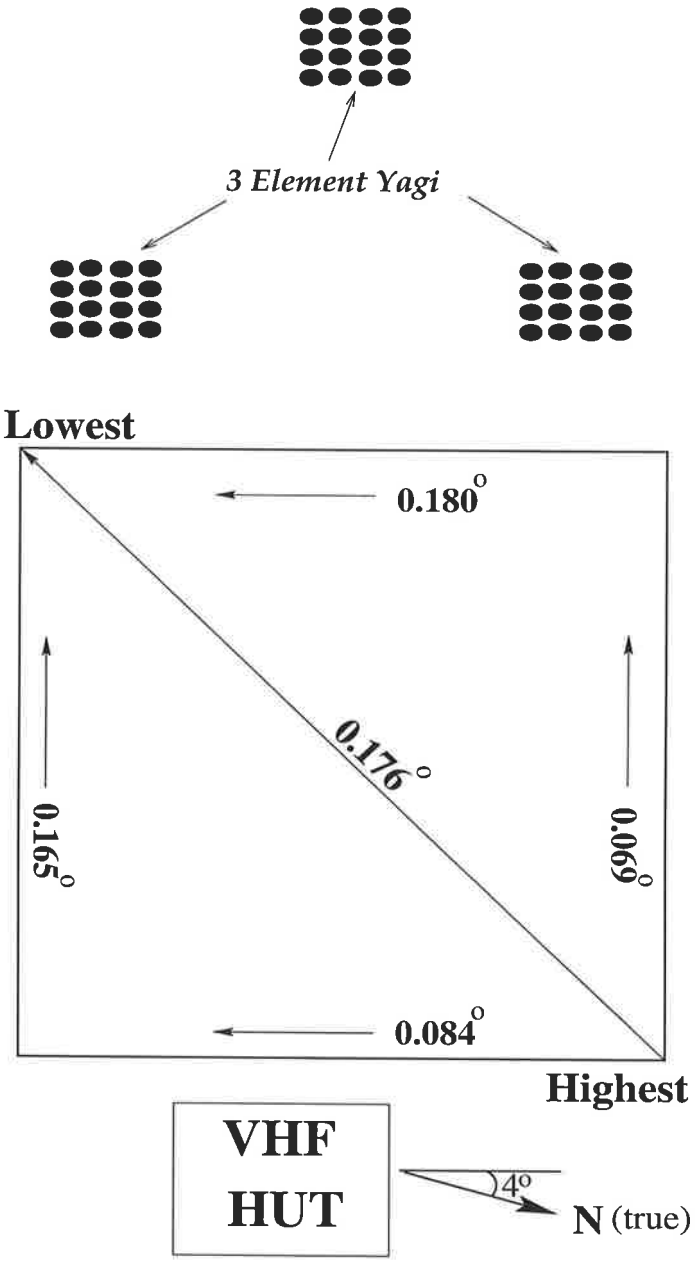

Figure 4.1: Diagram showing the slope of the Buckland Park VHF Co-Co antenna array level in different directions.

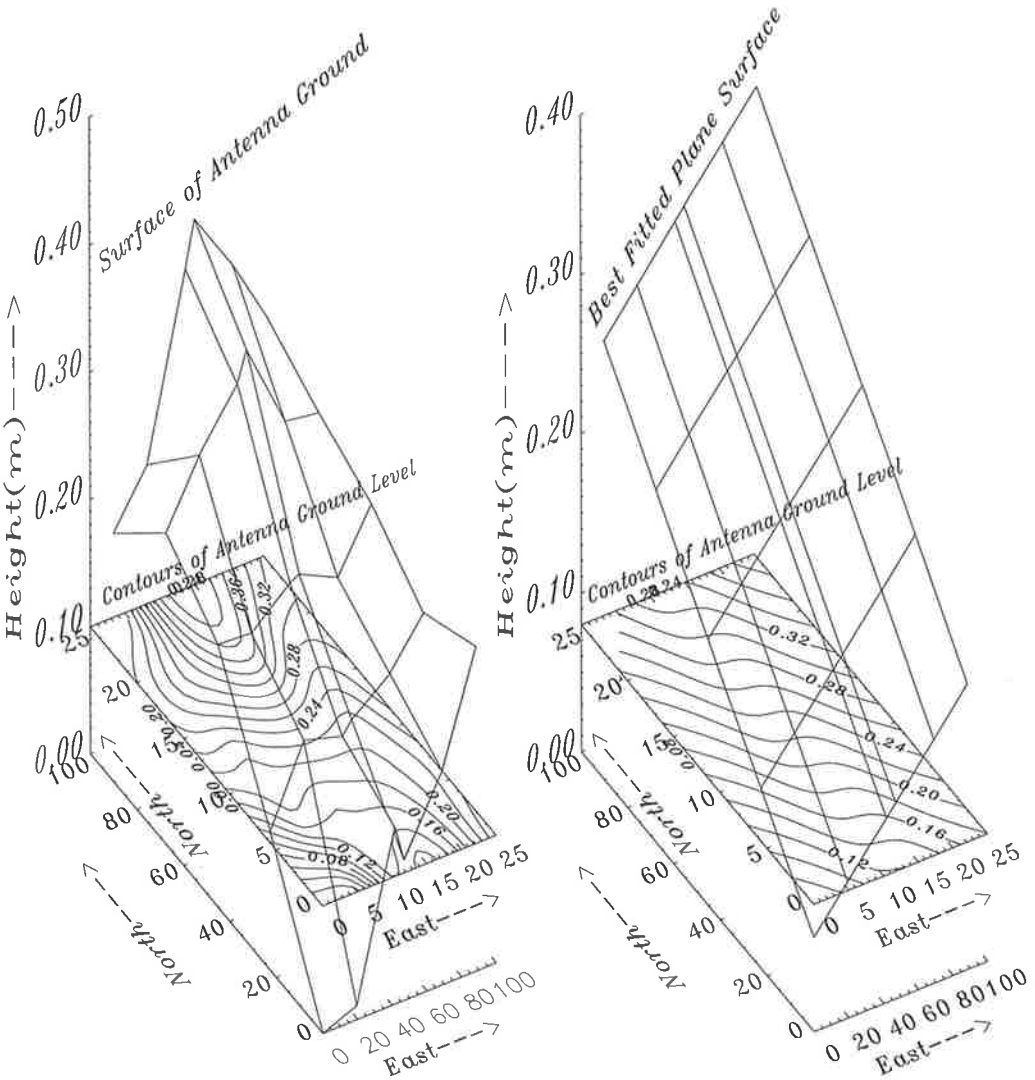

Figure 4.2: Surface plot of the ground level of the Co-Co antenna array and the corresponding contour (gpm) plot (left). The best fitted plane surface to the ground level and the corresponding contour (gpm) plot of the surface (right). The zenith angle (θ) and the azimuth angle (ϕ) are approximately 0.158 and 209 degrees respectively.

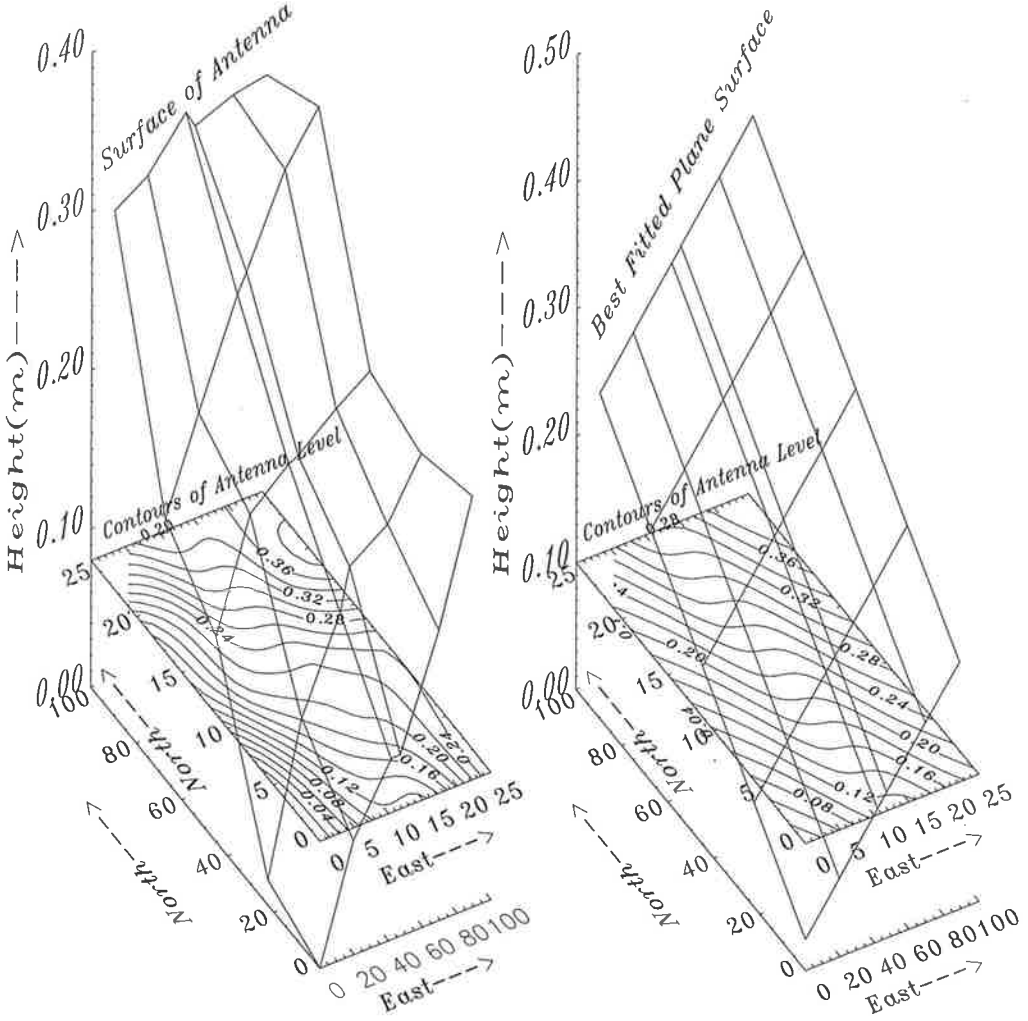

Figure 4.3: Surface plot of the antenna level of the Co-Co array and the corresponding contour (gpm) plot (left). The best fitted plane surface to the antenna level and the corresponding contour (gpm) plot of the surface (right). The zenith angle (θ) and the azimuth angle (ϕ) are approximately 0.184 and 216 degrees respectively.

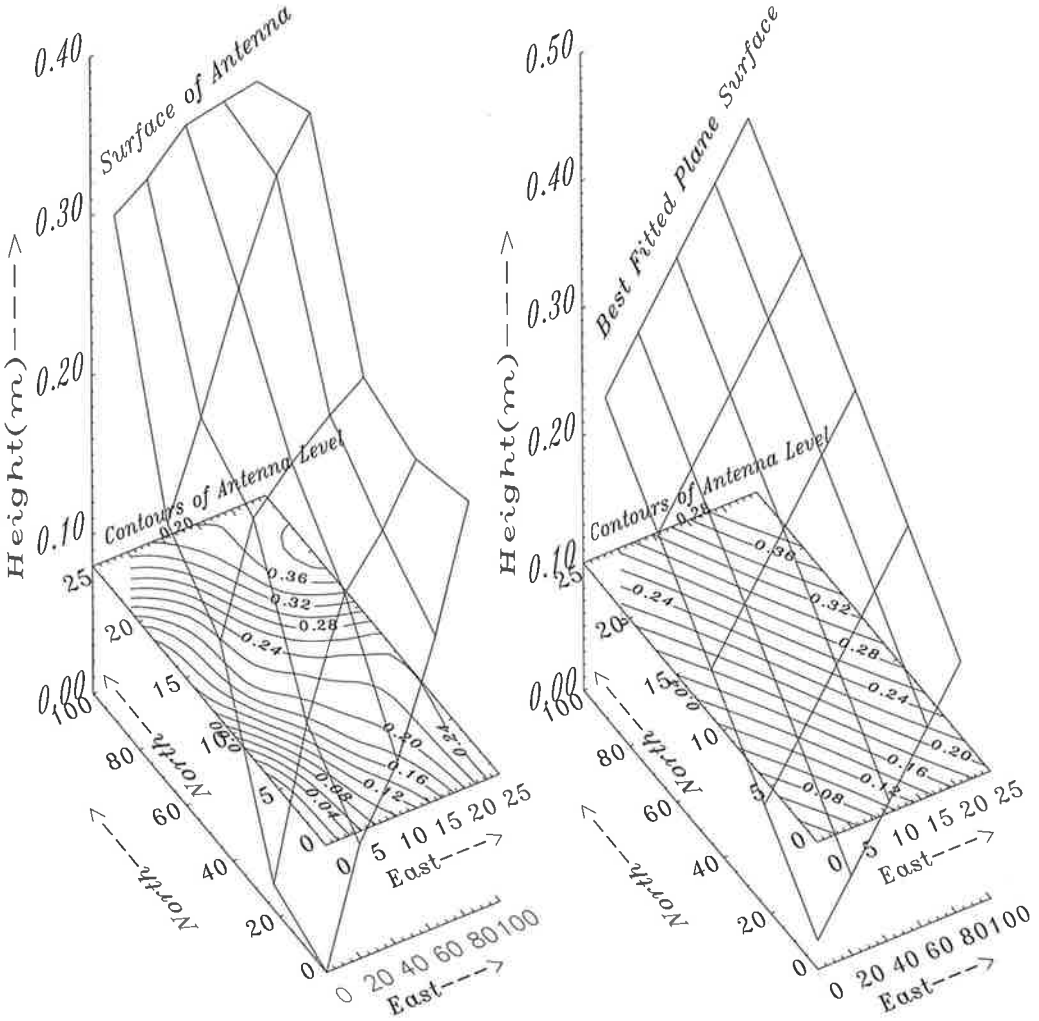

Figure 4.4: Surface plot of the antenna level of the Co-Co array (disregarding the Transmitting Hut gap between the east and west portion of the array) and the corresponding contour (gpm) plot (left). The best fitted plane surface to the aforementioned antenna level and the corresponding contour (gpm) plot of the surface (right). The zenith angle (θ) and the azimuth angle (ϕ) are approximately 0.188 and 219 degrees respectively.

surface. As it is shown, the northeast corner is the highest point of the Co-Co array. Similarly, the southwest corner is the lowest point. The zenith angle (θ) is around 0.154 degrees and the azimuth angle is about 216 degrees. Obviously the antenna plane also has the slope towards south-west.

Figure 4.4 is the same as Figure 4.3, but disregarding the Transmitting Hut gap between the east and west portion of the array. In this case, the contours of the fitted surface to the antenna surface are parallel, showing the slope towards south-west with the zenith (θ) and azimuth (ϕ) angles of 0.188 and 219 degrees, respectively.

The surface plots and contour plots of each side of the array (east and west) separately with fitted surface and relevant contour (not presented), show almost the same results.

The result of this method is consistent with the first method. The zenith (θ) angle lies around 0.18 degrees while, the azimuth (ϕ) angle is about 210 degrees.

4.1.3 The Third Method

Assuming the transmitting beam along off-vertical to be V_r, in Figure 4.5 with the angle θ from zenith and angle ϕ clockwise from north, thus:

$$V_r = wcos(\theta) + V_H sin(\theta) \tag{4.1}$$

and

$$V_H = usin(\phi) + vcos(\phi) \tag{4.2}$$

therefore,

$$V_r = wcos(\theta) + usin(\phi)sin(\theta) + vcos(\phi)sin(\theta). \tag{4.3}$$

Plotting the radial wind, V_r,versus zonal wind, u, gives the slope of u, which is $sin(\phi)sin(\theta)$. Likewise, plotting the radial wind, V_r, versus the meridional wind, v, gives the slope of v, which is $cos(\phi)sin(\theta)$. The angles θ and ϕ can be easily determined from the slope of u and v.

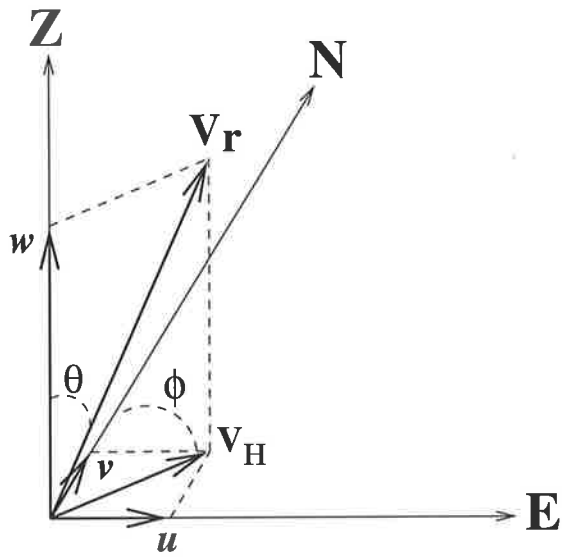

Figure 4.5: Three dimensional geometry of probable beam direction.

The slope of the line of best fit to scatter plots of all the available winds data ($\simeq$ 5405 hours) from 1991-1995, zonal versus radial (Figure 4.6) and meridional versus radial (Figure 4.8), reveals the zenith and azimuth angles. To show the slope clearly, the radial wind is scaled in $cm\,s^{-1}$ in the plots. The scatter plots for different heights up to $14.5\,km$ are shown in Figures 4.7 to 4.9. As is shown in Figure 4.10 (top), the slope of u and v with the appropriate errorbars at different heights, tends towards 0° with height from possessing the negative values at the lower troposphere. Consequently, the bottom figures of Figure 4.10 show the zenith and azimuth angles of the beam at different heights which is consistent with the overall zenith angle of approximately 0.18° and azimuth angle of approximately 210°, derived from the scatter plots of Figures 4.6 and 4.8.

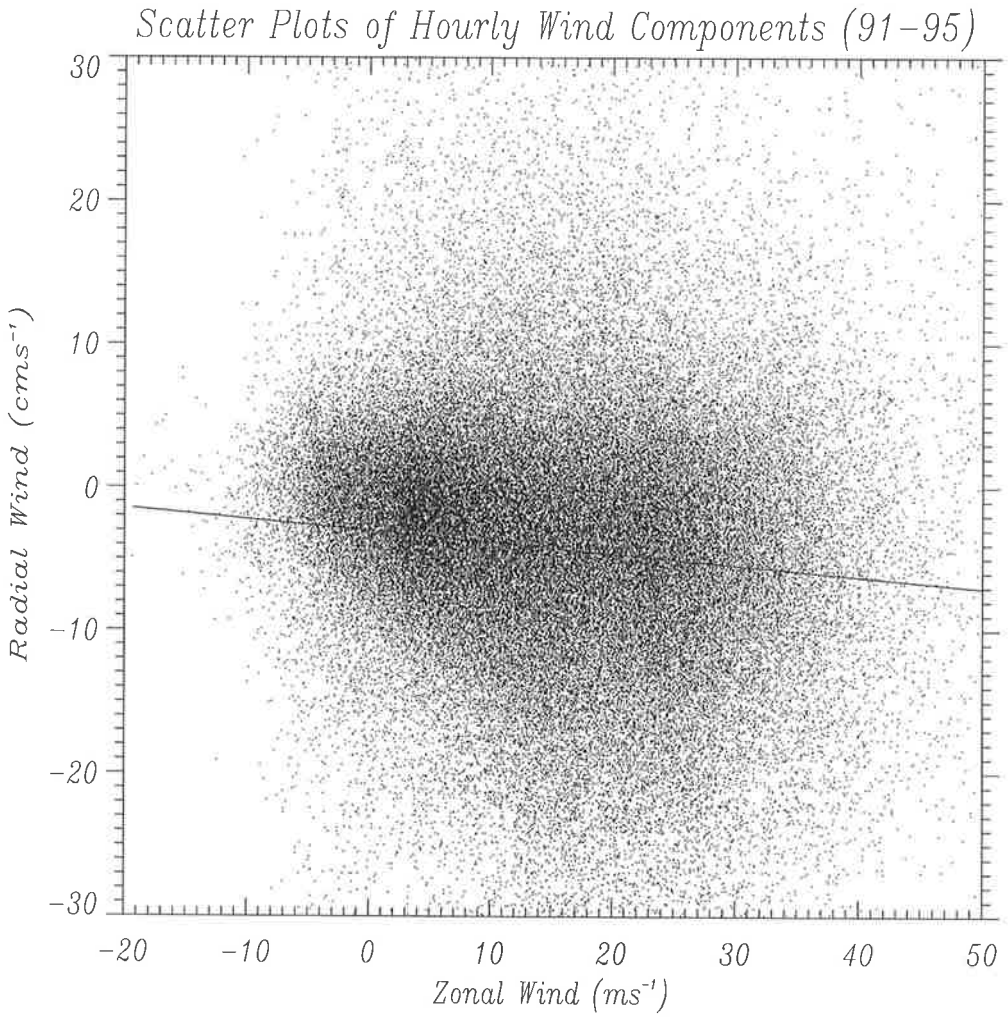

Figure 4.6: Scatter plots of about 5405 hourly zonal wind versus radial wind for years 1991-1995. To manifest the slope clearly, the radial wind is scaled in $cm\,s^{-1}$. The line of best fit shows the slope of the zonal wind.

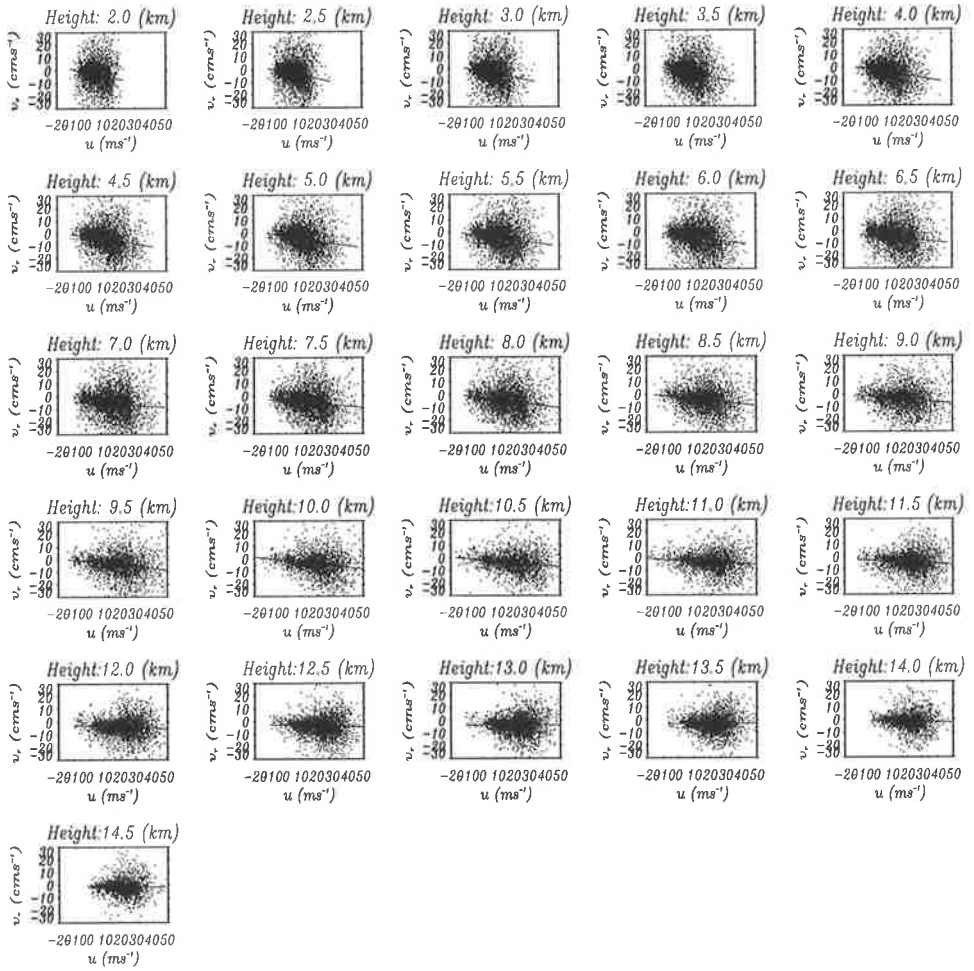

Figure 4.7: Scatter plots of about 5405 hourly zonal wind ($m\,s^{-1}$) versus radial wind ($cm\,s^{-1}$) for different heights. The line of best fit shows the slope of zonal wind at nominal heights.

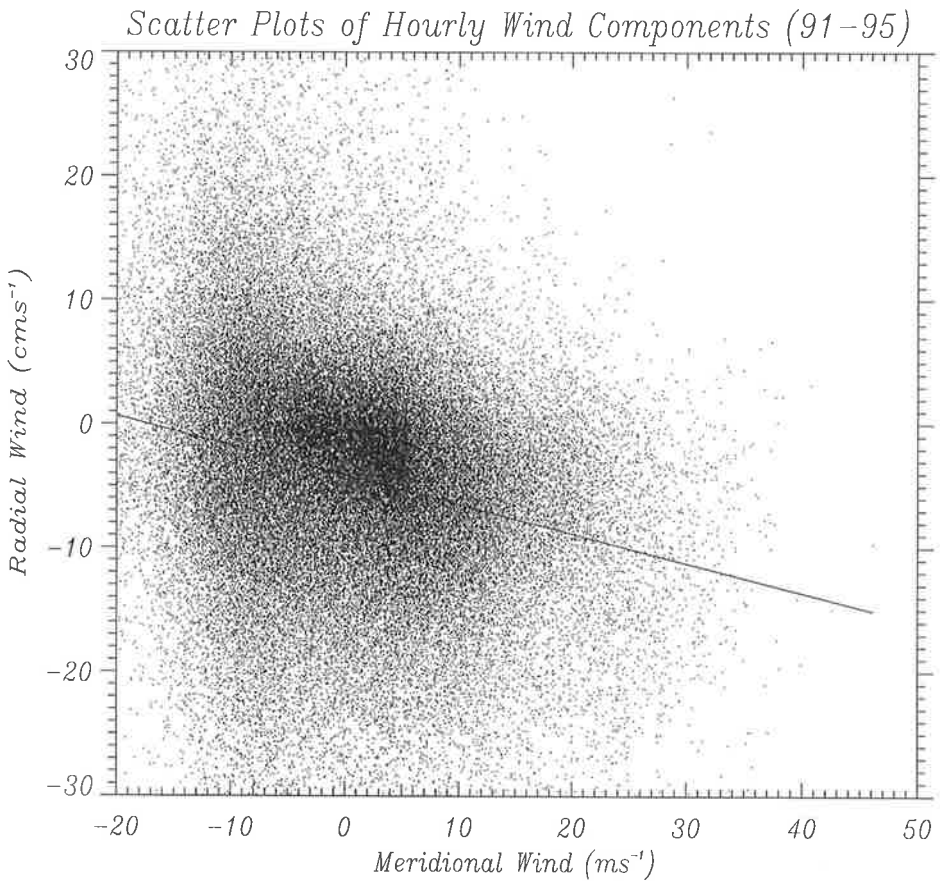

Figure 4.8: Scatter plots of about 5405 hourly meridional wind versus radial wind for years 1991-1995. To manifest the slope clearly, the radial wind is scaled in $cm\,s^{-1}$. The line of best fit shows the slope of the meridional wind.

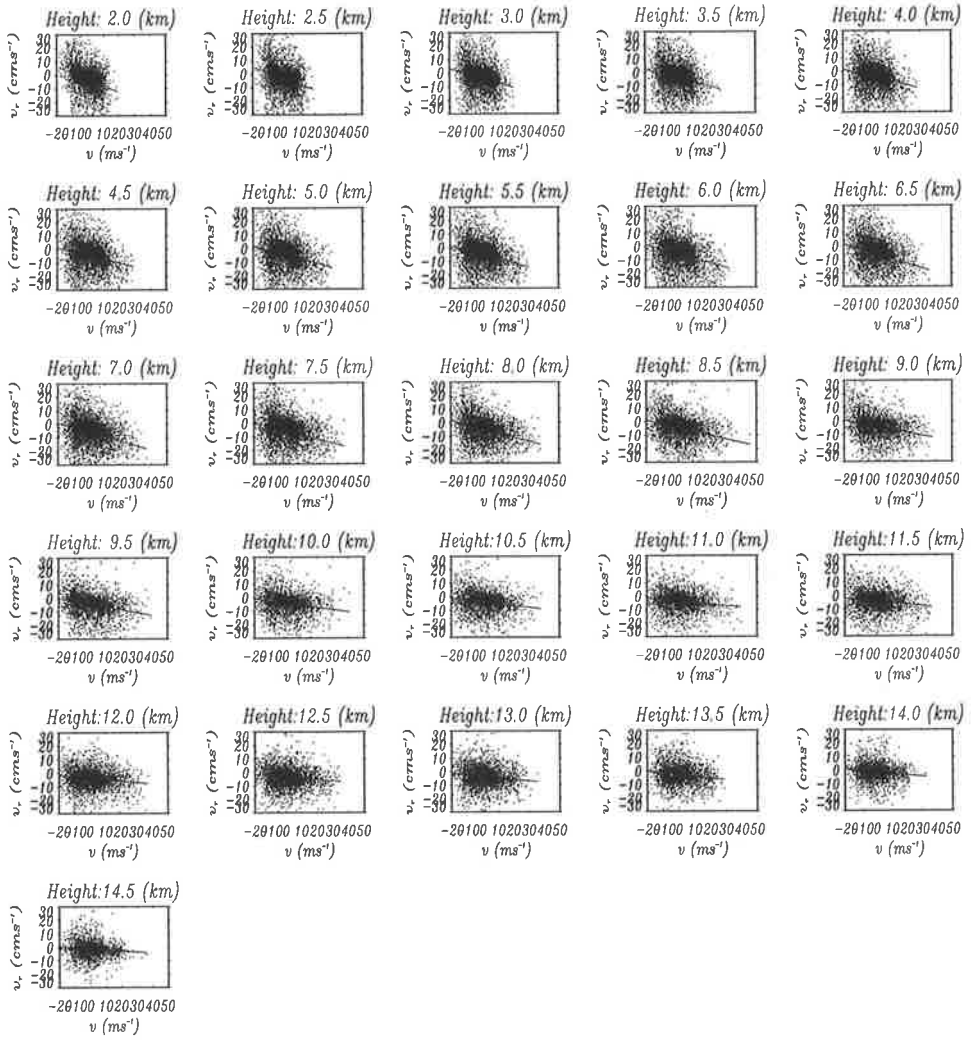

Figure 4.9: Scatter plots of about 5405 hourly meridional wind ($m\,s^{-1}$) versus radial wind ($cm\,s^{-1}$) for different heights. The line of best fit shows the slope of the meridional wind at nominal heights.

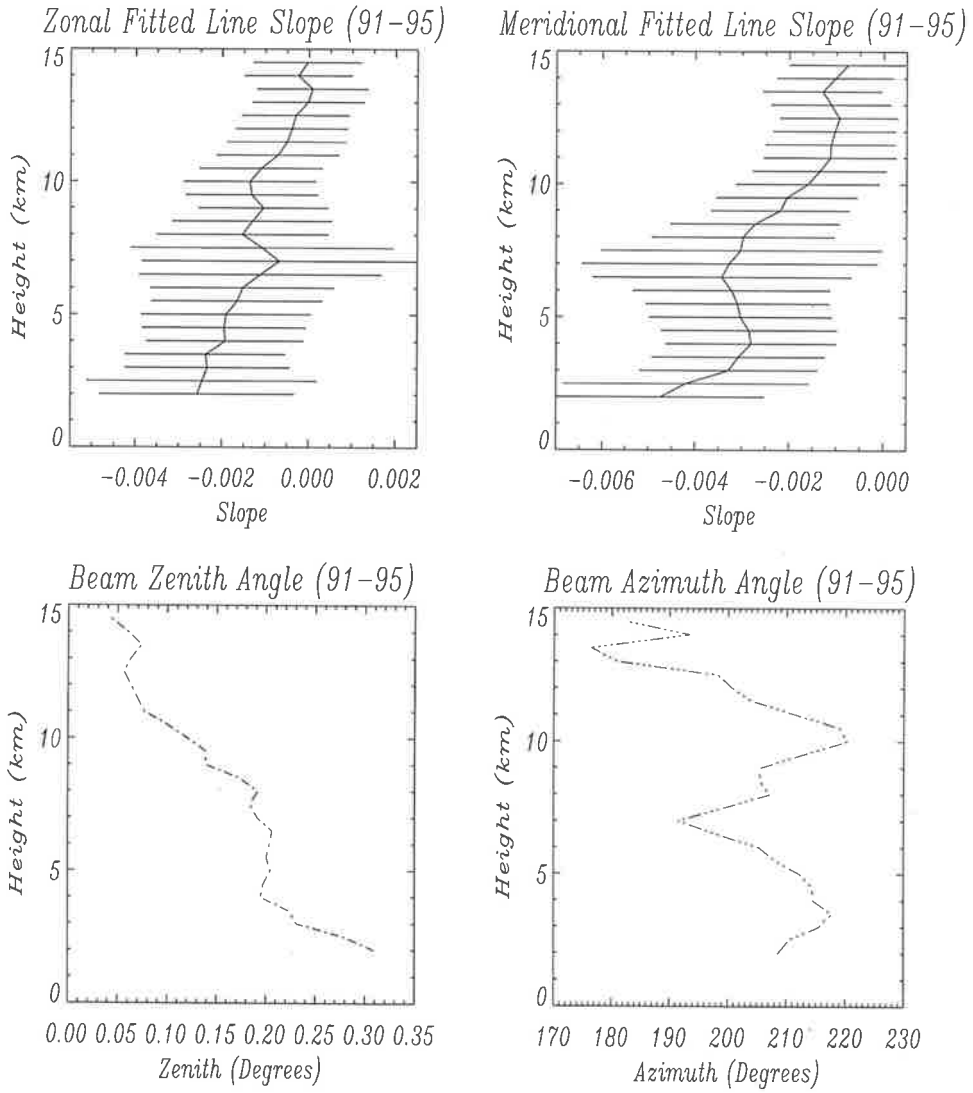

Figure 4.10: The slope of zonal wind with the errorbars at different heights (top-left) for years 1991-1995. The slope of meridional wind with the errorbars at different heights (top-right) for the same times. Beam zenith angles at different heights (bottom-left) and beam azimuth angles at different heights (bottom-right) for the same period.

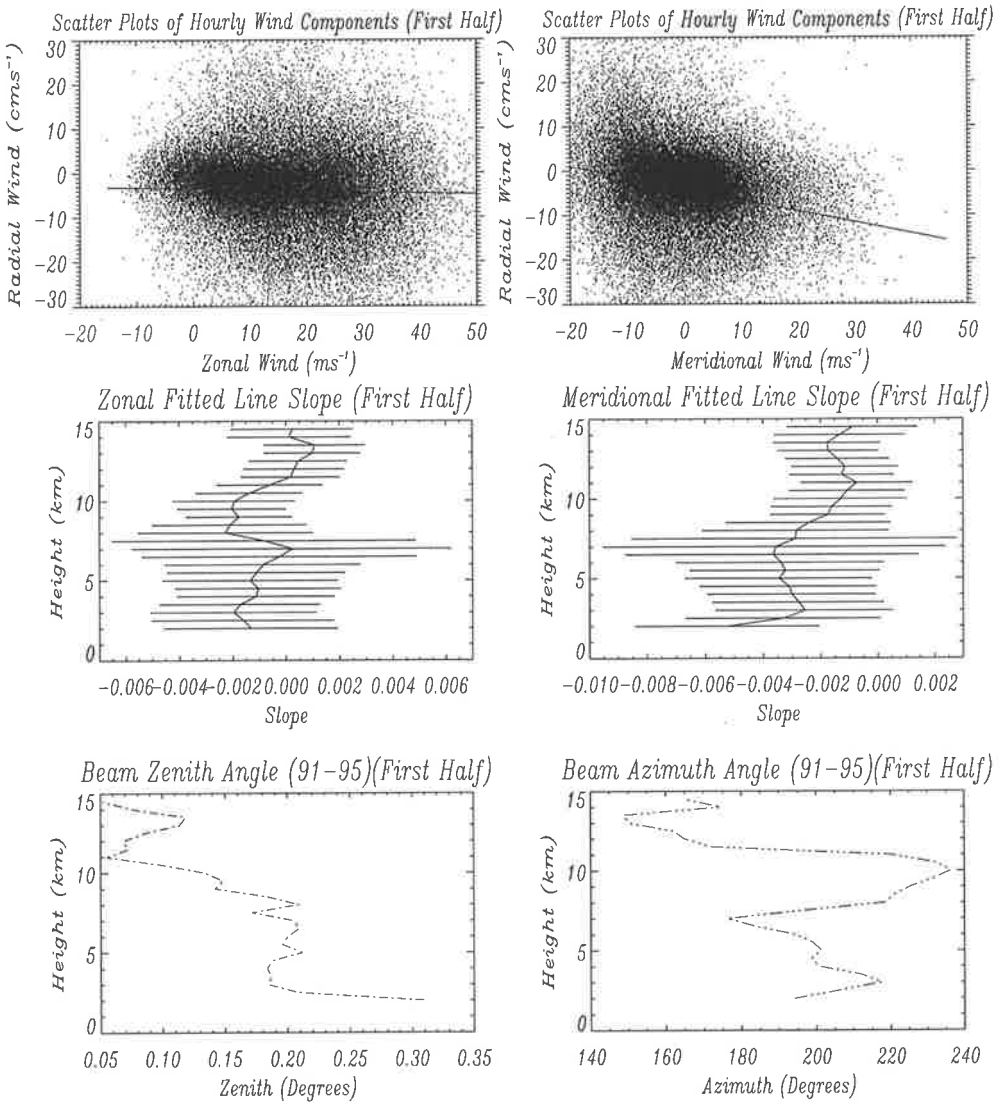

Figure 4.11: Scatter plots of zonal wind (top-left), slope of zonal wind at different heights (middle-left) with the corresponding zenith angle (bottom-left) for the first half of the data from 1991-1995. Scatter plots of meridional wind (top-right), slope of meridional wind at different heights (middle-right) with the corresponding azimuth angle (bottom-right) for the same period.

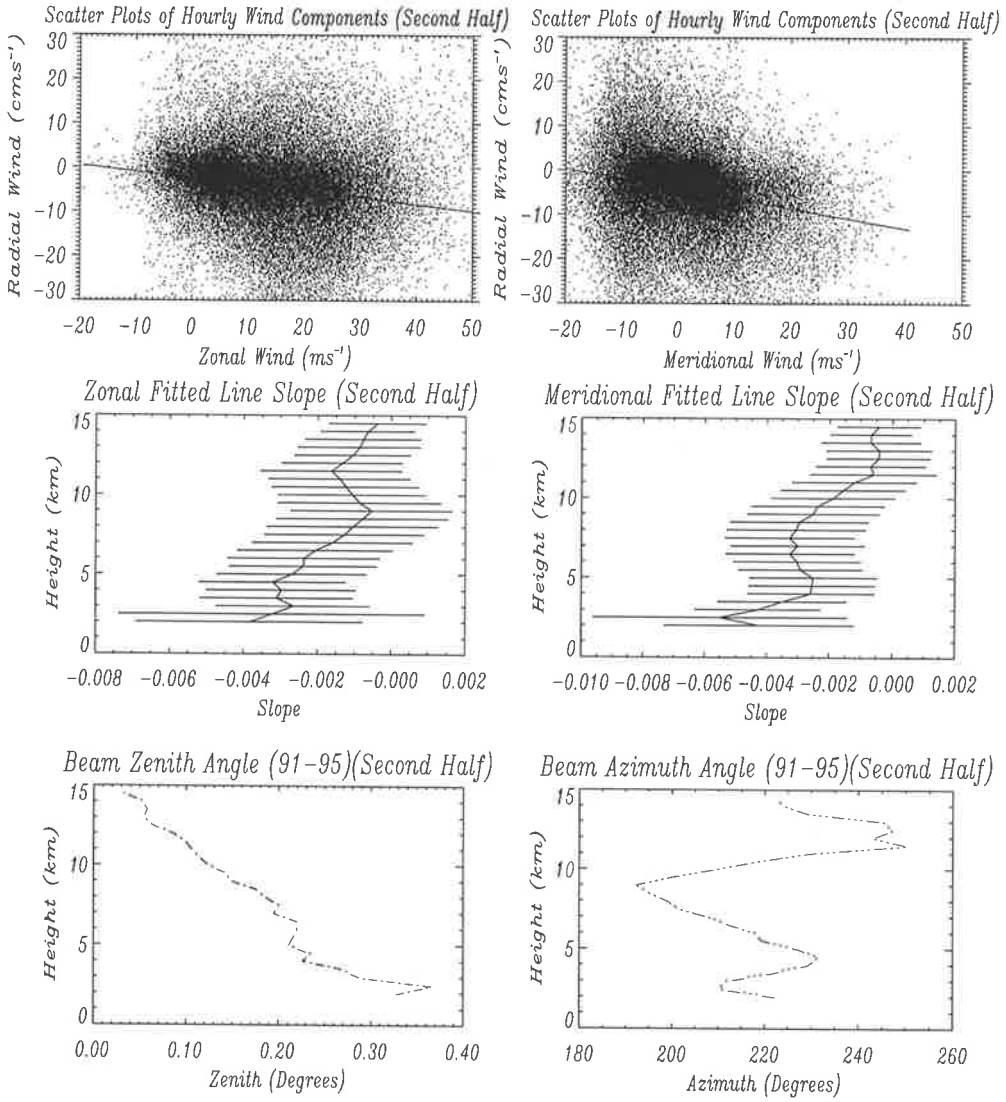

Figure 4.12: Scatter plots of zonal wind (top-left), slope of zonal wind at different heights (middle-left) with the corresponding zenith angle (bottom-left) for the second half of the data from 1991-1995. Scatter plots of meridional wind (top-right), slope of meridional wind at different heights (middle-right) with the corresponding azimuth angle (bottom-right) for the same period.

The data were divided in two and the above procedure was applied for both halves and the results are shown in Figures 4.11 and 4.12. The resultant angles were almost the same as above.

Noting that echoes from rain droplets may have contaminated the data below $5\,km$, the data above $5\,km$ were extracted and analysed (Figure 4.13). Again a zenith angle of 0.18° and azimuth angle of 210° appear dominant.

Separate analysis of wet-seasons (May-Sep) of years 1991-1995, Figure 4.14, and dry-seasons (Nov-Apr), Figure 4.15, reveals the same results as before.

To check the possible effects of precipitation on the beam slope, the precipitation and non-precipitation events have been extracted from the available data of years 1991-1995. The results were consistent with the previous studies (Figures 4.16 & 4.17).

Finally, the analysis for different seasons, Figures 4.18, 4.19, 4.20 and 4.21, accompanied by that of different months during the years of 1991-1995 (not presented), show approximately the same results.

From Equation 4.3, the vertical velocity of the air (w) can be derived as:

$$w = V_r/cos(\theta) - usin(\phi)tan(\theta) - vcos(\phi)tan(\theta). \tag{4.4}$$

The available data using Equation 4.4 were corrected assuming $\theta = 0.18°$ and $\phi = 210°$. This time the Scatter plots of zonal wind (u) and meridional wind (v) versus vertical velocity, Figure 4.22, reveal the slope of u vs w and v vs w to be in the order of 10^{-5} , which is small enough to be assumed as 0°. Similar analysis for wet-seasons (Figure 4.23), dry-seasons (Figure 4.24), precipitation periods (Figure 4.25) and non-precipitation periods (Figure 4.26), also shows the relevant slopes for u vs w and v vs w to be in the order of $10^{-5}$to 10^{-6}, verifying

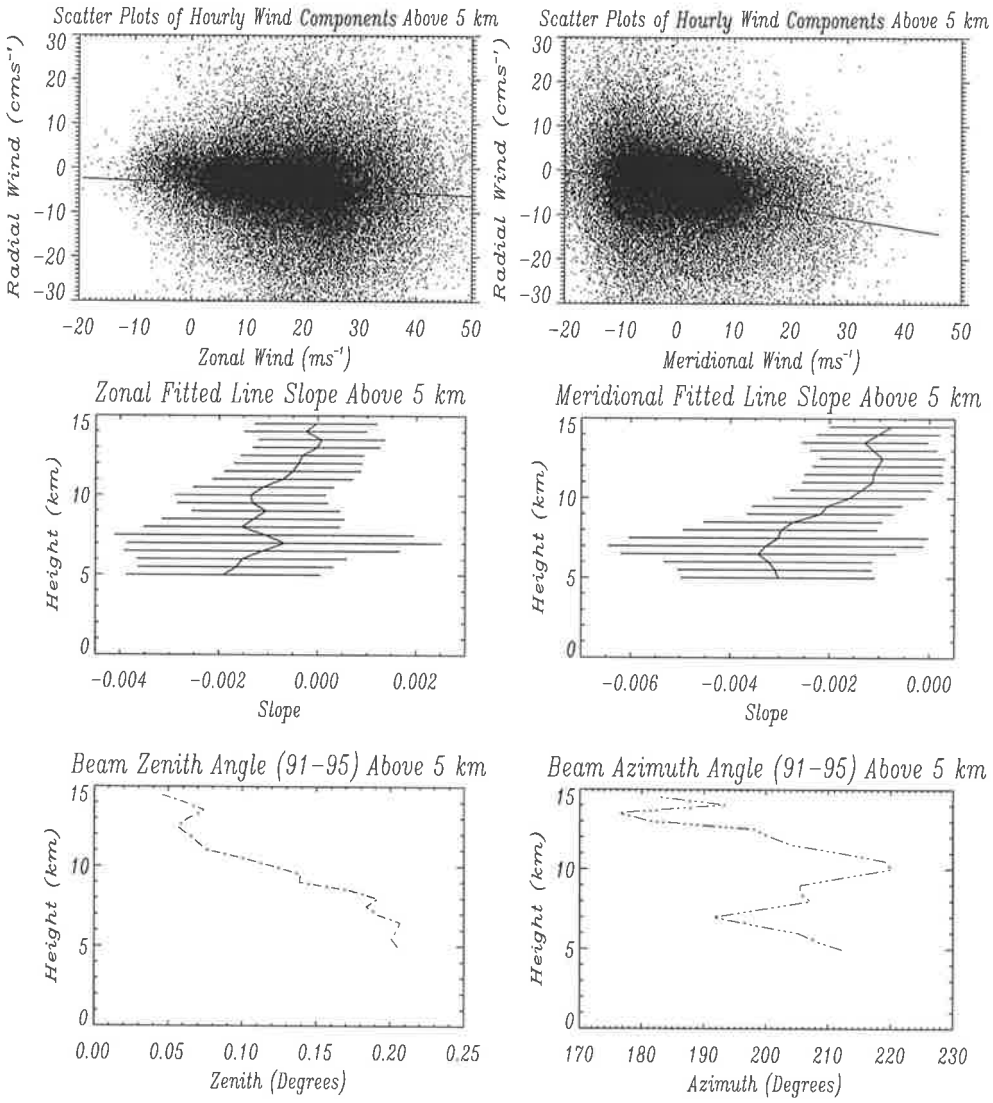

Figure 4.13: Scatter plots of zonal wind (top-left), slope of zonal wind at different heights (middle-left) with the corresponding zenith angle (bottom-left) for the all data from 1991-1995 above 5 km. Scatter plots of meridional wind (top-right), slope of meridional wind at different heights (middle-right) with the corresponding azimuth angle (bottom-right) for the same period.

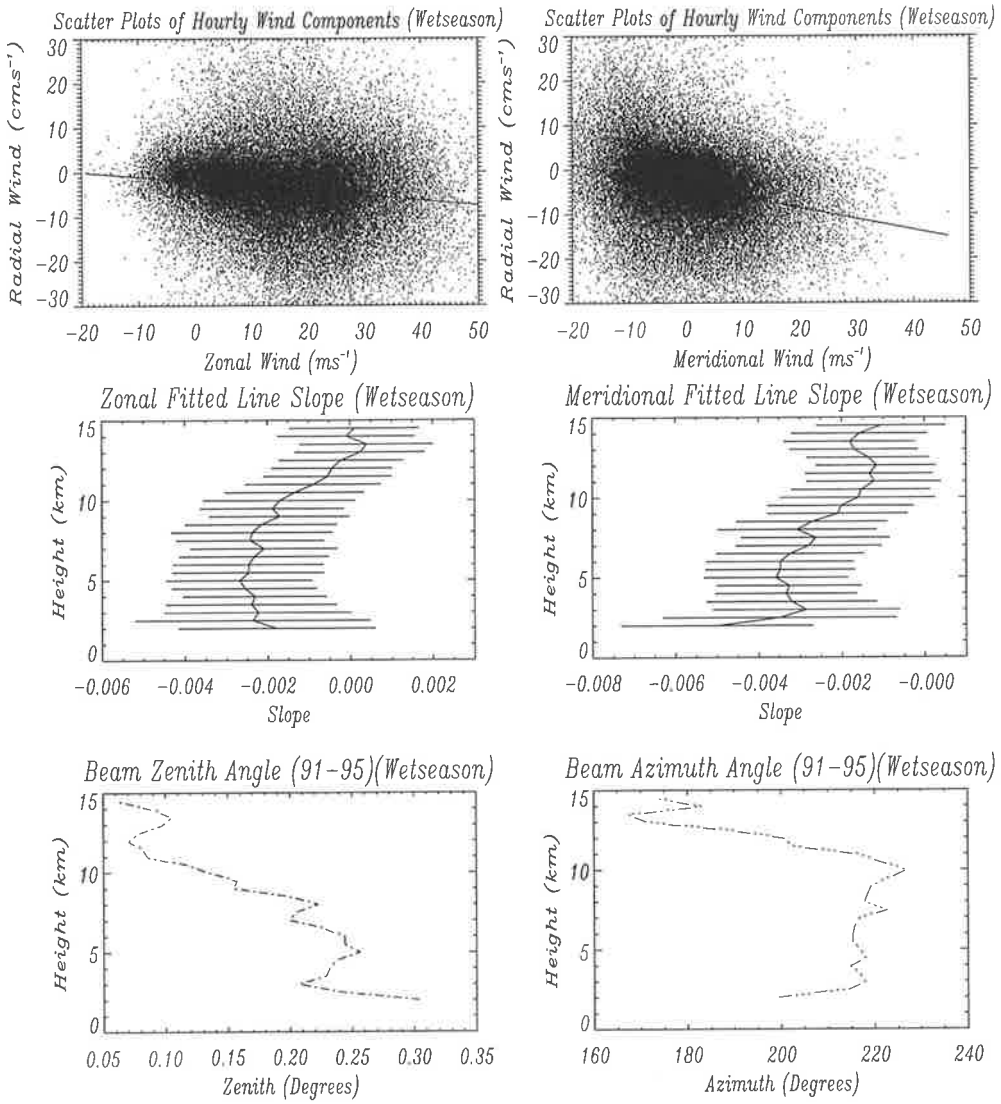

Figure 4.14: Scatter plots of zonal wind (top-left), slope of zonal wind at different heights (middle-left) with the corresponding zenith angle (bottom-left) for the wet-seasons (May-Sep) of the data from 1991-1995. Scatter plots of meridional wind (top-right), slope of meridional wind at different heights (middle-right) with the corresponding azimuth angle (bottom-right) for the same period.

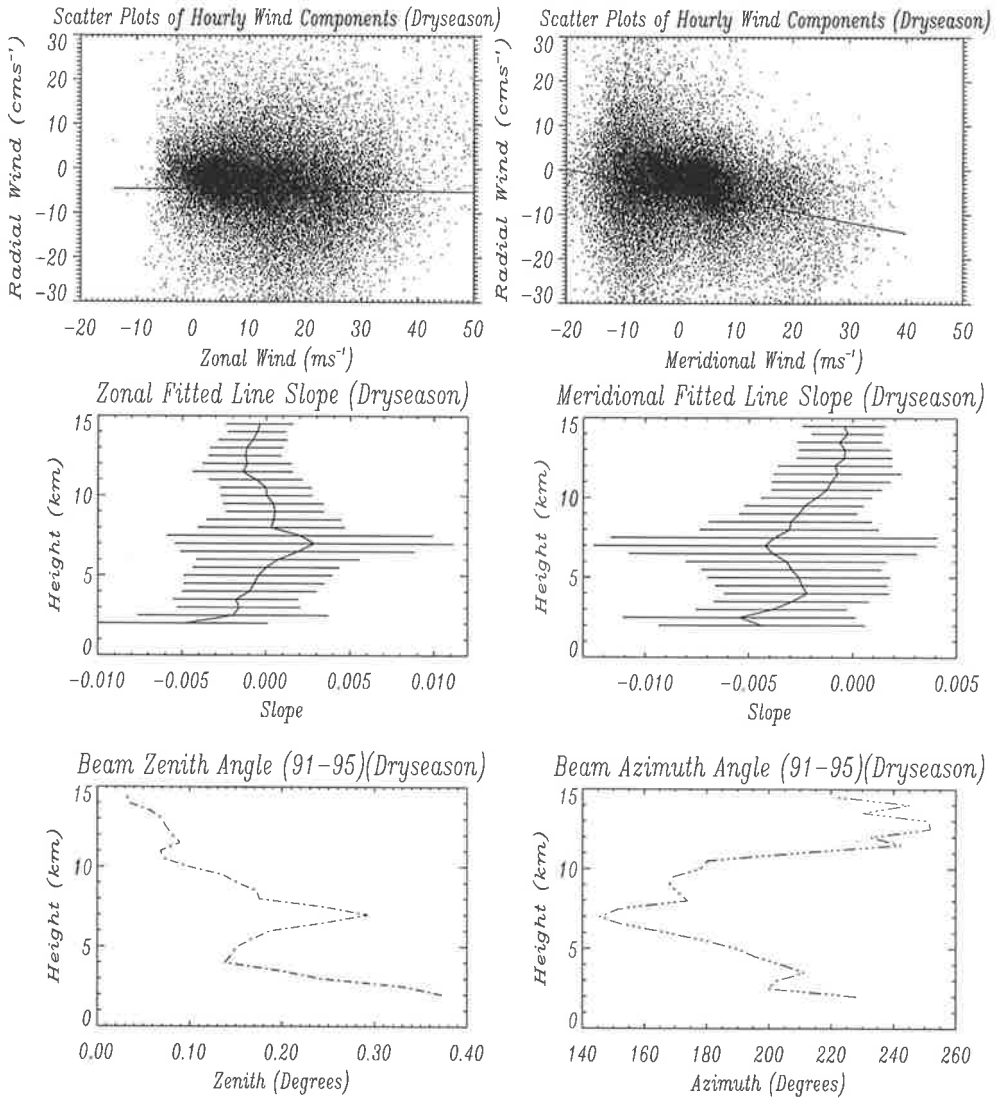

Figure 4.15: Scatter plots of zonal wind (top-left), slope of zonal wind at different heights (middle-left) with the corresponding zenith angle (bottom-left) for the dry-seasons (Nov-Apr) of the data from 1991-1995. Scatter plots of meridional wind (top-right), slope of meridional wind at different heights (middle-right) with the corresponding azimuth angle (bottom-right) for the same period.

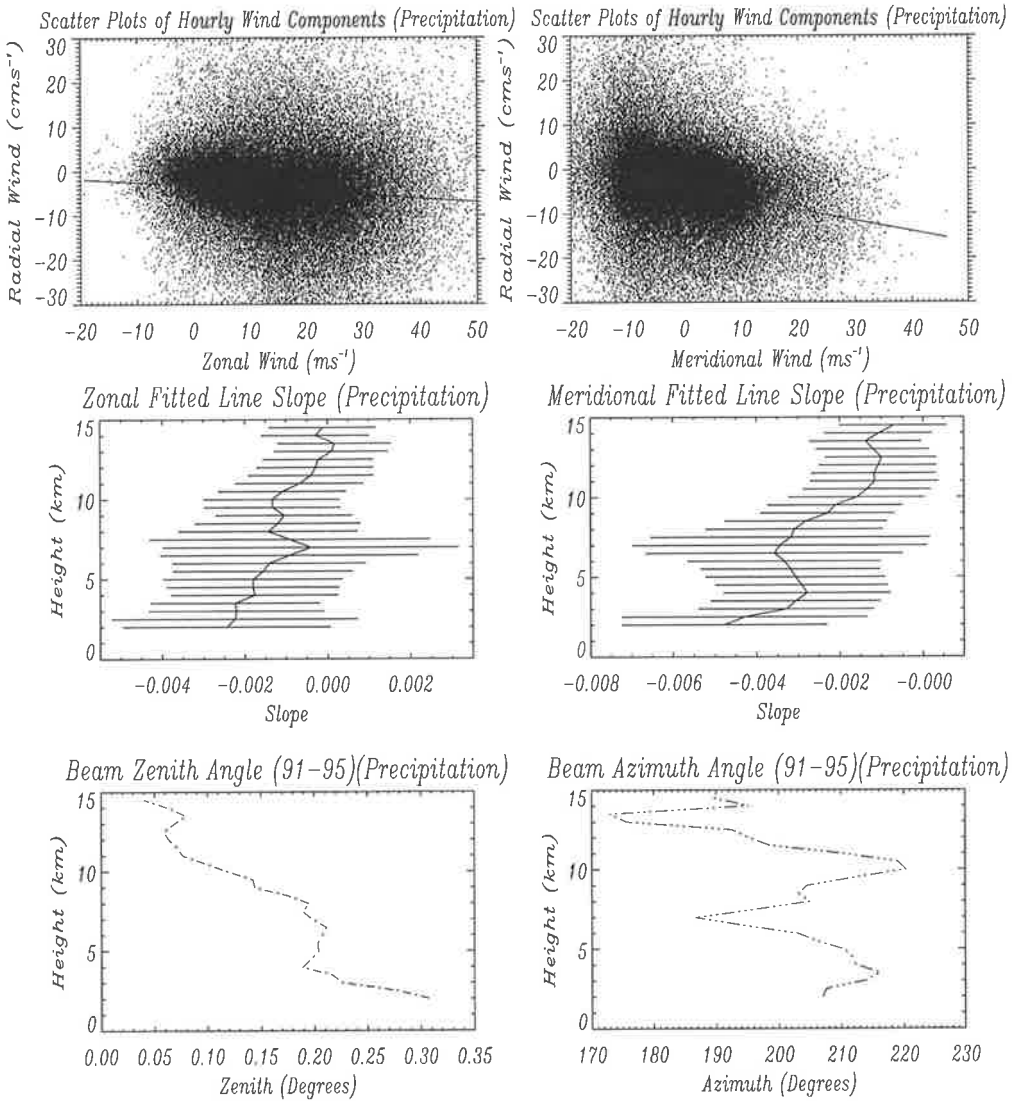

Figure 4.16: Scatter plots of zonal wind (top-left), slope of zonal wind at different heights (middle-left) with the corresponding zenith angle (bottom-left) for the precipitation periods of years 1991-1995. Scatter plots of meridional wind (top-right), slope of meridional wind at different heights (middle-right) with the corresponding azimuth angle (bottom-right) for the same period.

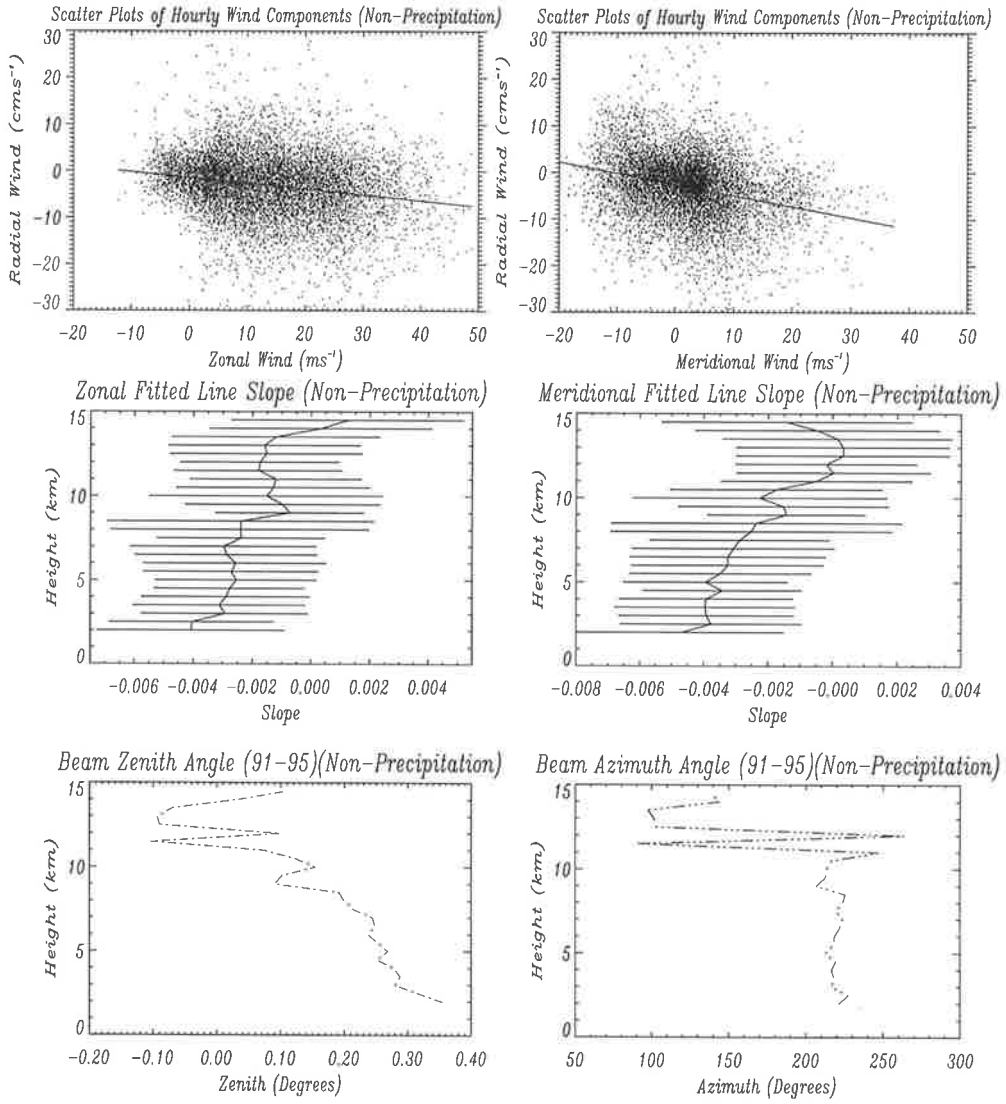

Figure 4.17: Scatter plots of zonal wind (top-left), slope of zonal wind at different heights (middle-left) with the corresponding zenith angle (bottom-left) for the precipitation periods of years 1991-1995. Scatter plots of meridional wind (top-right), slope of meridional wind at different heights (middle-right) with the corresponding azimuth angle (bottom-right) for the same period.

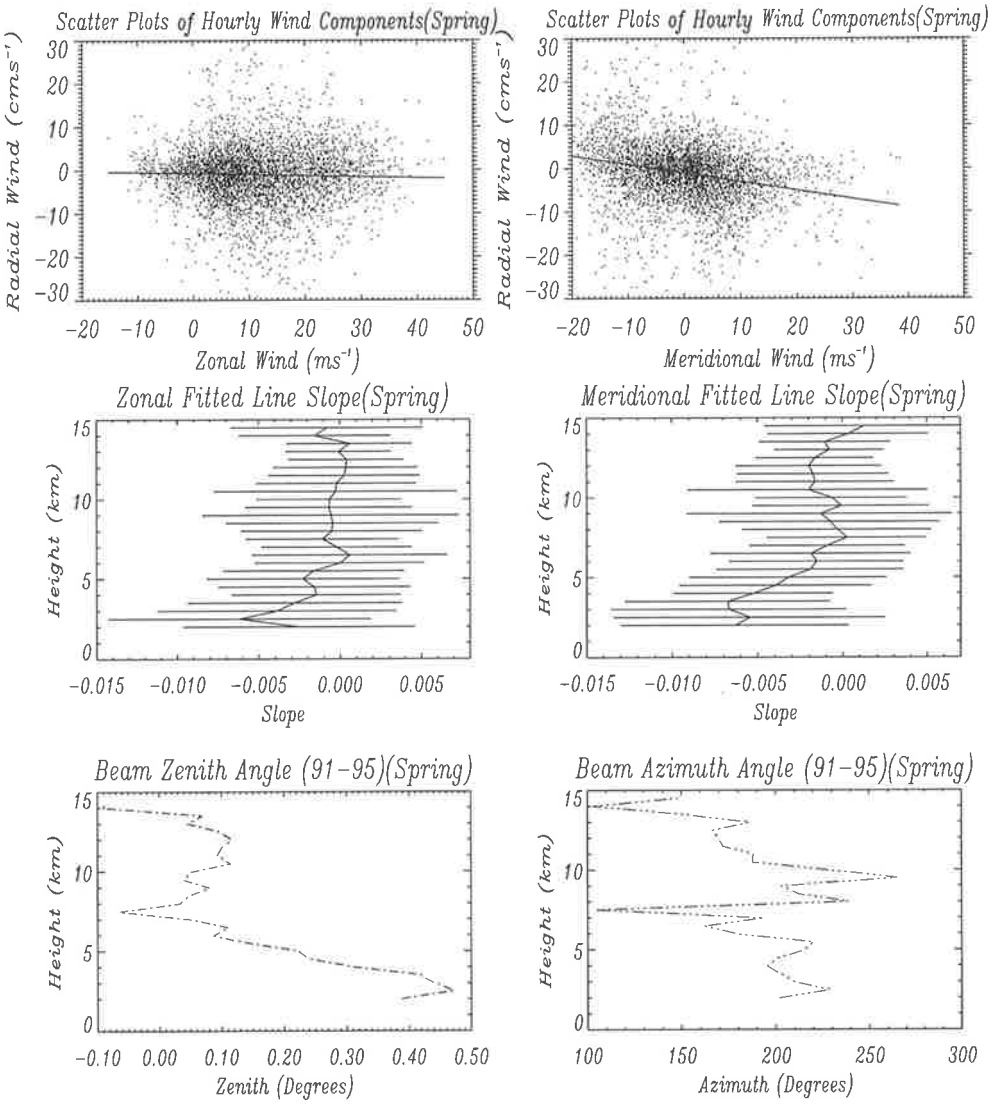

Figure 4.18: Scatter plots of zonal wind (top-left), slope of zonal wind at different heights (middle-left) with the corresponding zenith angle (bottom-left) for the spring seasons of years 1991-1995. Scatter plots of meridional wind (top-right), slope of meridional wind at different heights (middle-right) with the corresponding azimuth angle (bottom-right) for the same period.

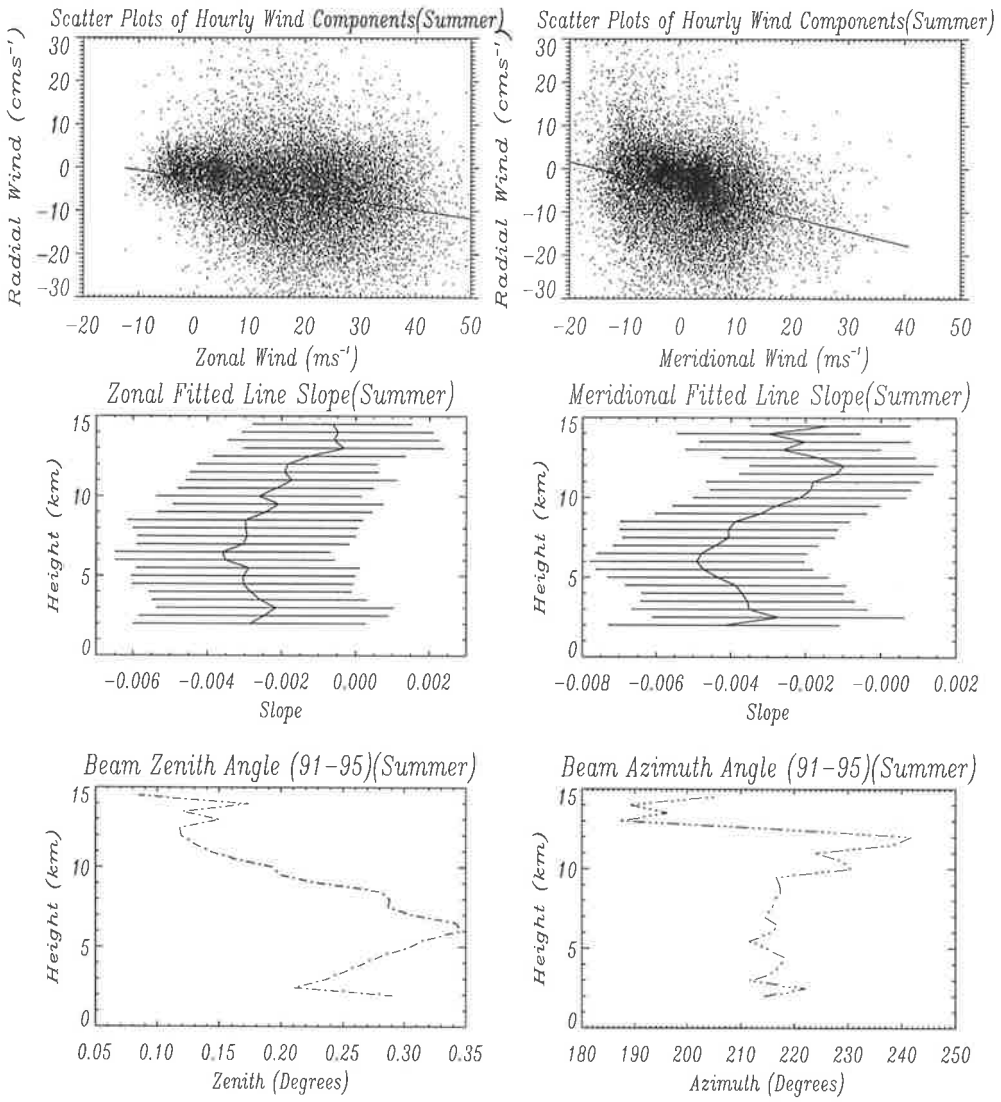

Figure 4.19: Scatter plots of zonal wind (top-left), slope of zonal wind at different heights (middle-left) with the corresponding zenith angle (bottom-left) for the summer seasons of years 1991-1995. Scatter plots of meridional wind (top-right), slope of meridional wind at different heights (middle-right) with the corresponding azimuth angle (bottom-right) for the same period.

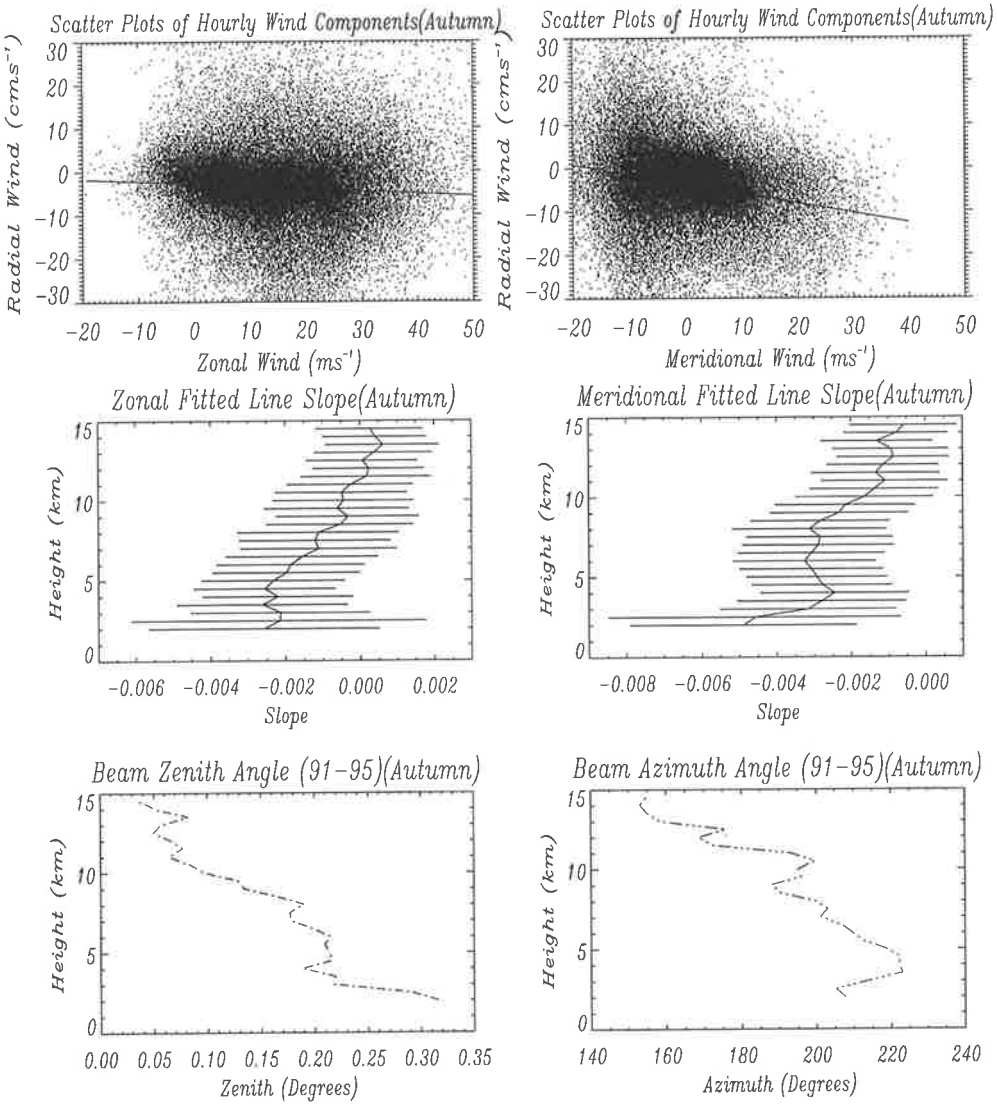

Figure 4.20: Scatter plots of zonal wind (top-left), slope of zonal wind at different heights (middle-left) with the corresponding zenith angle (bottom-left) for the autumn seasons of years 1991-1995. Scatter plots of meridional wind (top-right), slope of meridional wind at different heights (middle-right) with the corresponding azimuth angle (bottom-right) for the same period.

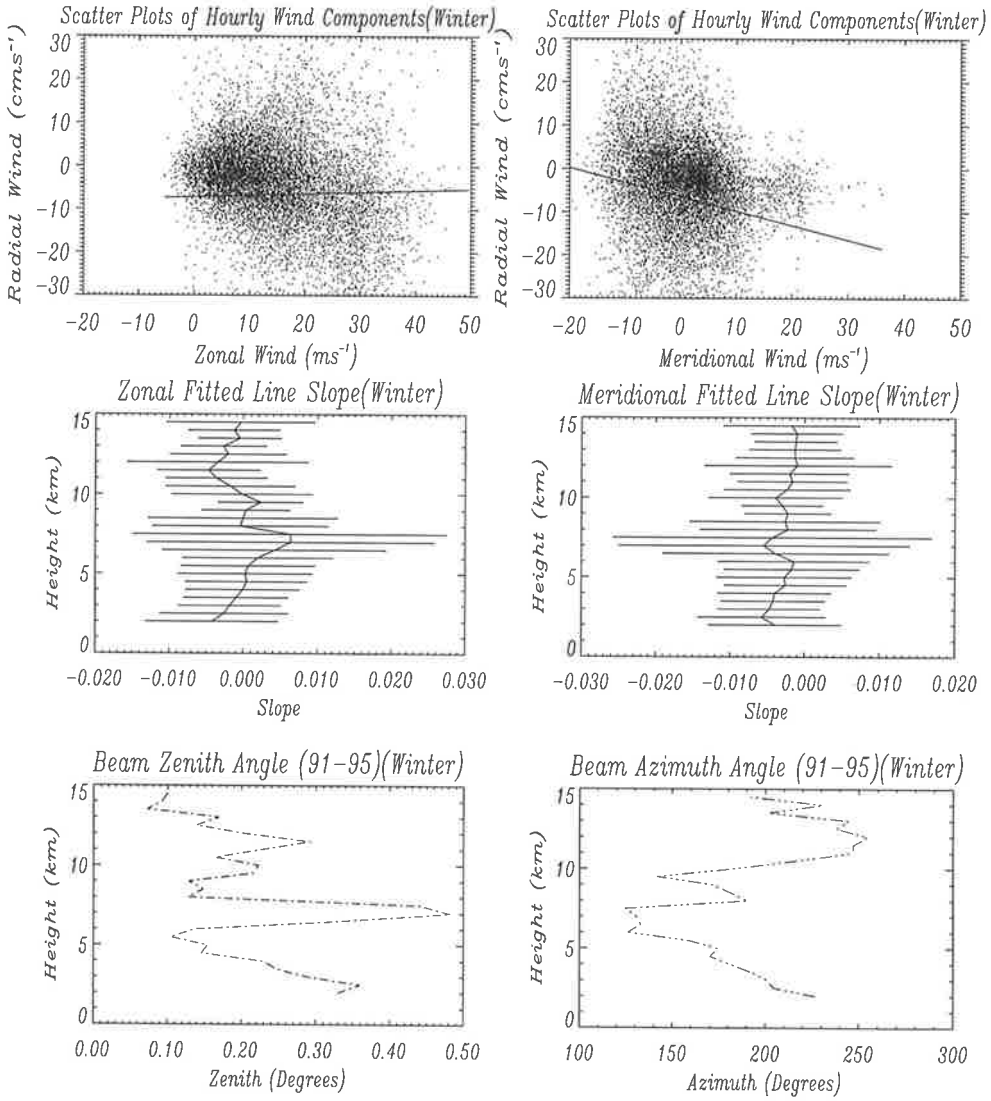

Figure 4.21: Scatter plots of zonal wind (top-left), slope of zonal wind at different heights (middle-left) with the corresponding zenith angle (bottom-left) for the winter seasons of years 1991-1995. Scatter plots of meridional wind (top-right), slope of meridional wind at different heights (middle-right) with the corresponding azimuth angle (bottom-right) for the same period.

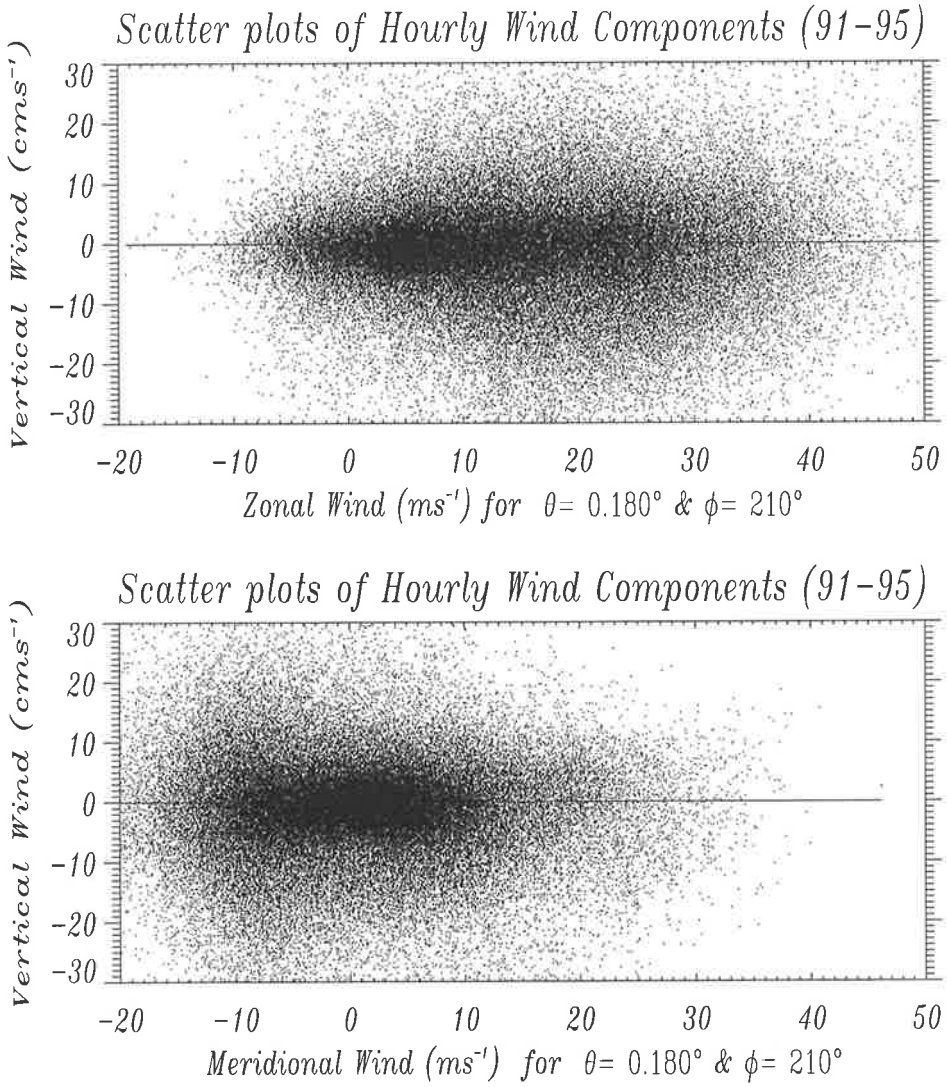

Figure 4.22: Scatter plots of zonal wind ($m\,s^{-1}$) (top) and meridional wind ($m\,s^{-1}$) (bottom), versus vertical velocity ($cm\,s^{-1}$) after correction of data for zenith angle of 0.18° and azimuth angle of 210° for the years of 1991-1995.

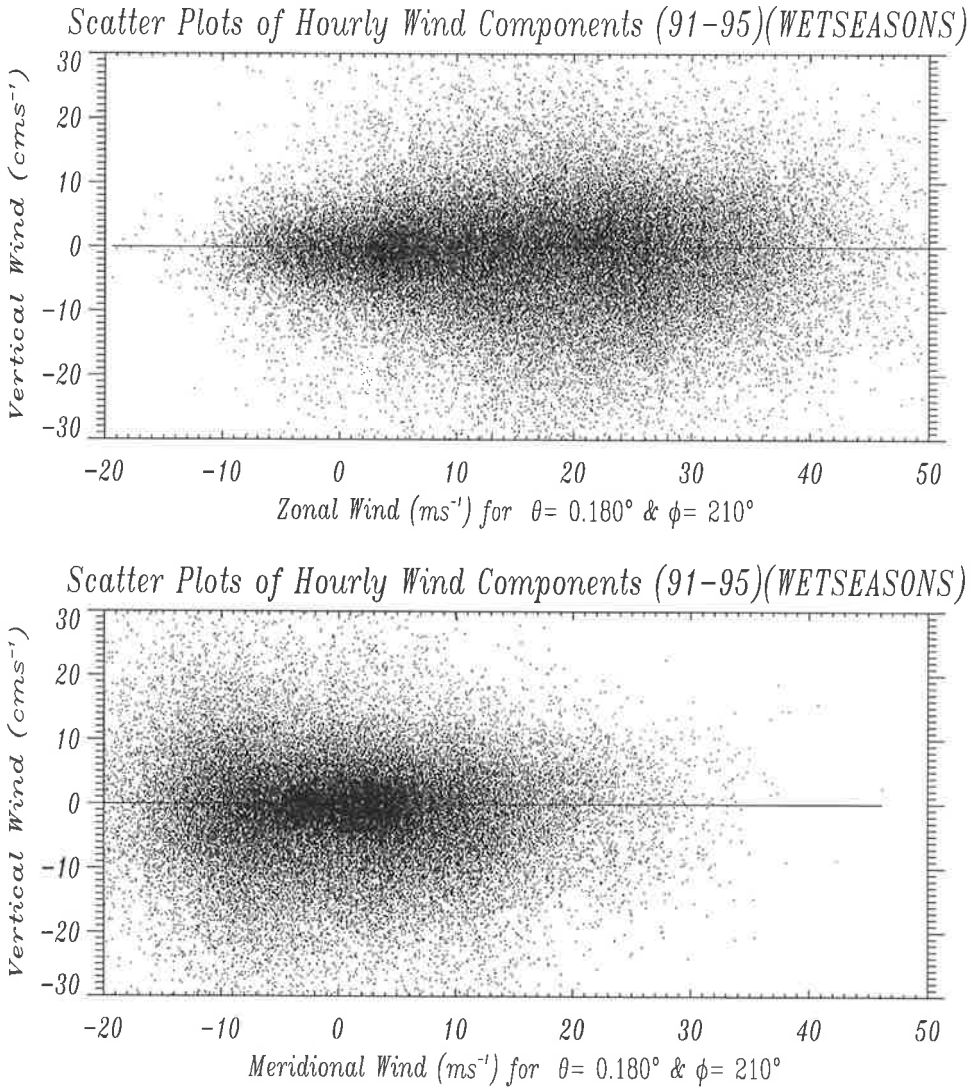

Figure 4.23: Scatter plots of zonal wind ($m\,s^{-1}$) (top) and meridional wind ($m\,s^{-1}$) (bottom), versus vertical velocity ($cm\,s^{-1}$) after correction of data for zenith angle of 0.18° and azimuth angle of 210° for the wet-seasons (May-Sep) of the years 1991-1995.

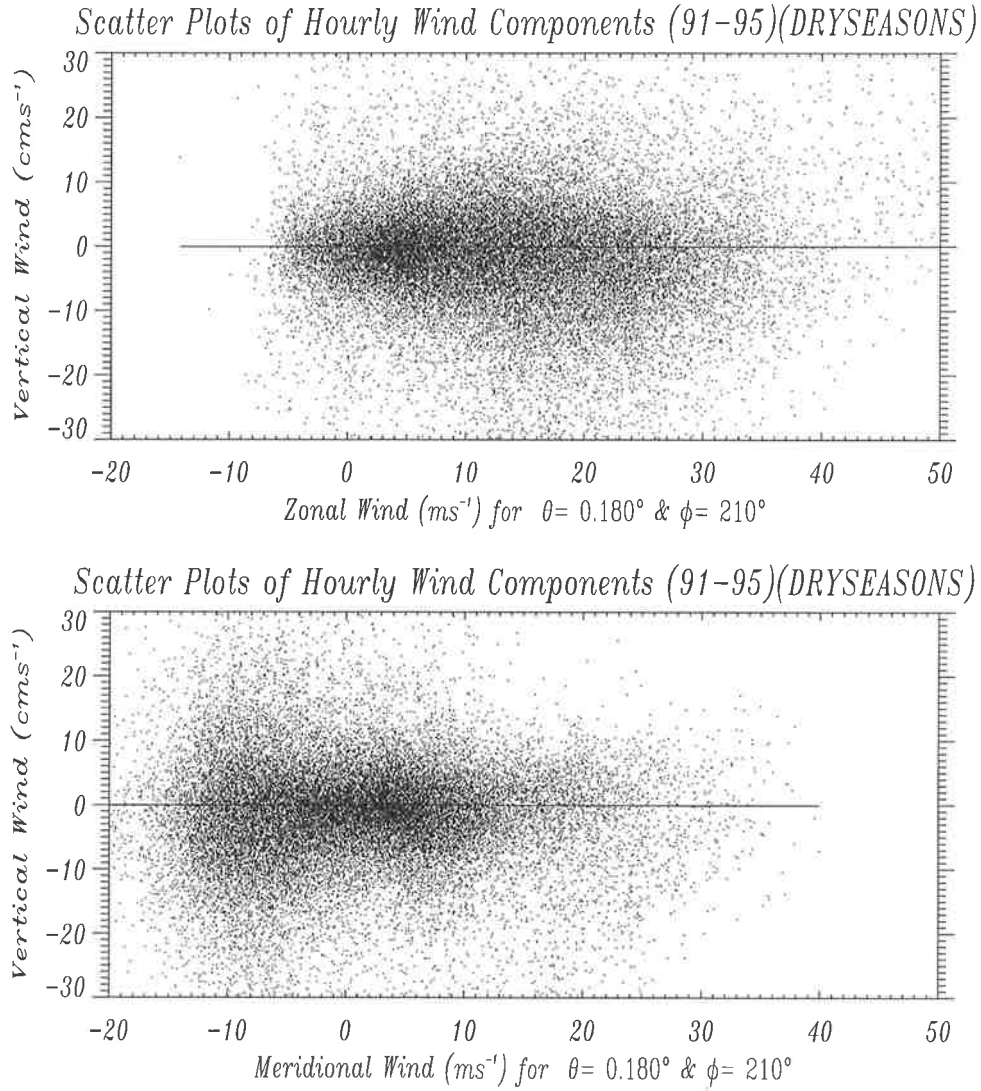

Figure 4.24: Scatter plots of zonal wind ($m\,s^{-1}$) (top) and meridional wind ($m\,s^{-1}$) (bottom), versus vertical velocity ($cm\,s^{-1}$) after correction of data for zenith angle of 0.18° and azimuth angle of 210° for the dry-seasons (Nov-Apr) of the years 1991-1995.

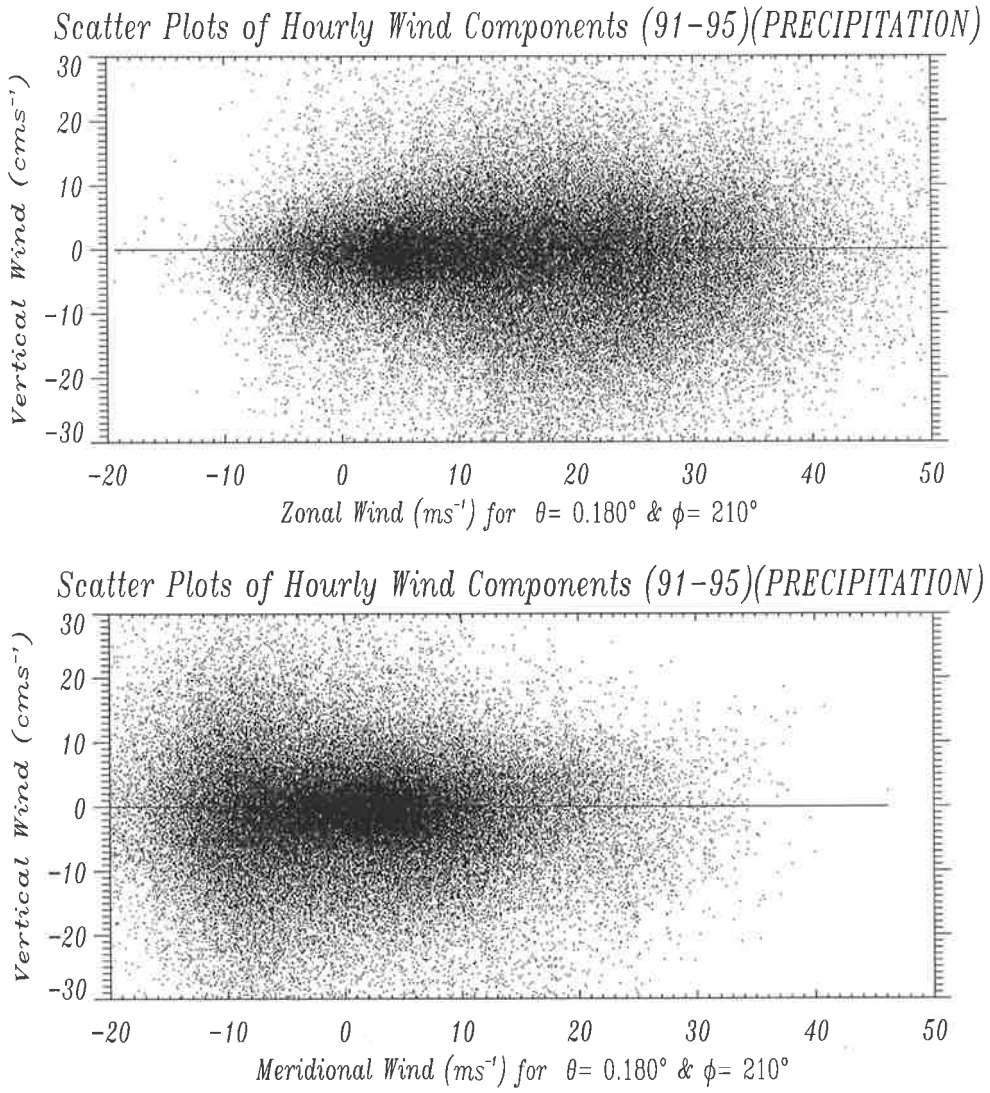

Figure 4.25: Scatter plots of zonal wind ($m\,s^{-1}$) (top) and meridional wind ($m\,s^{-1}$) (bottom), versus vertical velocity ($cm\,s^{-1}$) after correction of data for zenith angle of 0.18° and azimuth angle of 210° for the precipitation periods of the years 1991-1995.

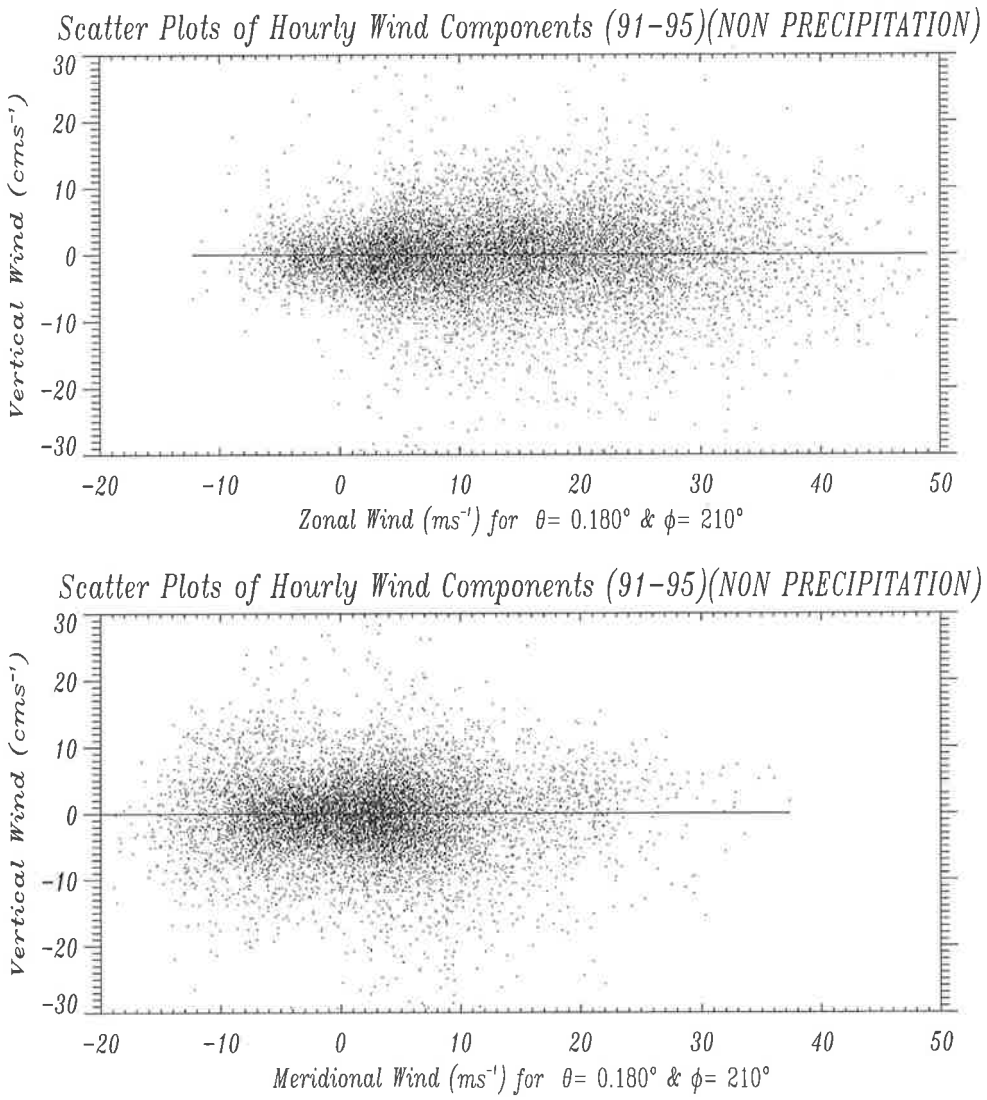

Figure 4.26: Scatter plots of zonal wind ($m\,s^{-1}$) (top) and meridional wind ($m\,s^{-1}$) (bottom), versus vertical velocity ($cm\,s^{-1}$) after correction of data for zenith angle of 0.18° and azimuth angle of 210° for the non-precipitation periods of the years 1991-1995.

the infinitesimal slope. This means that $\theta = 0.18°$ and $\phi = 210°$are confirmed.

In order to investigate for other possible angles, the data were corrected against randomly chosen zenith and azimuth angles. The corresponding slopes were determined. Based on Figure 4.27, it is clear that the minimum slope of u and v ($\simeq 0.000°$) is met at zenith angle of 0.18° and azimuth angle of 210°. Figure 4.27 also clearly shows the predominance of south-westerly winds over Adelaide's tropospheric region.

The zenith angle of **0.18°** and azimuth angle of **210°** which are consistent for three different methods were chosen for the Buckland Park VHF Co-Co array antenna slope. The data obtained from the aforementioned radar should be corrected with the above angles through the Equation 4.4 to avoid the unrealistic widespread subsidence as a result of folding a fraction of predominant south-westerly wind over Adelaide into a slightly south-westward-pointing beam.

4.1.4 Comparison of Corrected and Uncorrected Data

In order to see the importance of the correction of data for the antenna slope, a cut-off low event for 24-26 July 1995 was chosen. The hourly mean vertical velocity for this case of a cut-off low with severe frontal structure and horizontal cyclonic wind shear has been contoured both raw (uncorrected) and corrected versus antenna slope. They are illustrated in Figure 4.28 & 4.29 respectively. As it is shown in Figure 4.29, the regions of upward motion are more pronounced and the meteorological pattern is quite clear whereas, the pattern in Figure 4.28 is not as clear. The case studies will be discussed in more detail later.

A comparison of raw data and corrected data through the above technique (i.e. Equation 4.4) is also done by *Low* [1996] for a set of data from 1200 UTC on 27th August 1992 to 1200 UTC on 31st August 1992. He has pointed out that

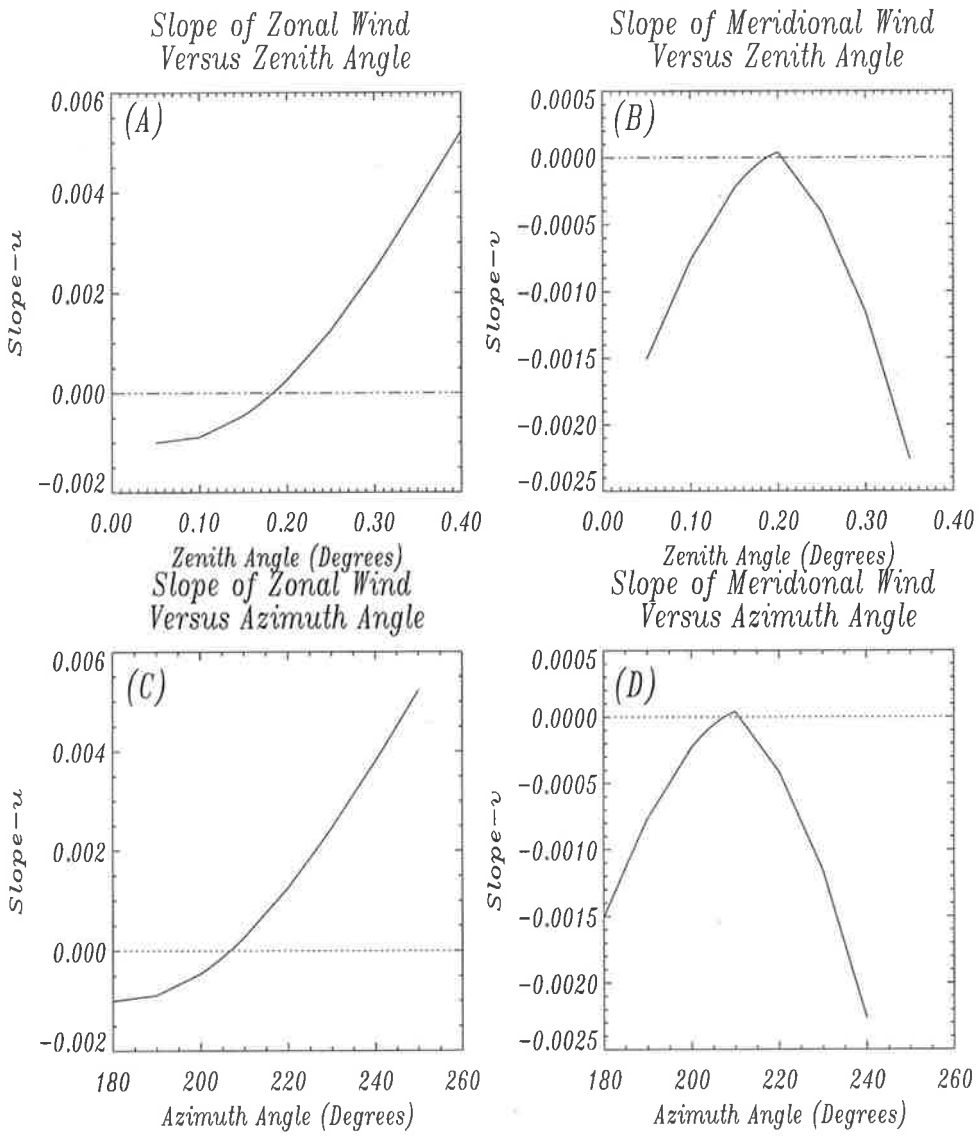

Figure 4.27: Graphs of slope of zonal wind versus zenith angle (A) and versus azimuth angle (C). Slope of meridional wind versus zenith angle (B) and versus azimuth angle (D). The slopes meet zero at about zenith angle of 0.18° and azimuth angle of 210° .

in broad terms, the correction has balanced regions of ascent and descent, rather than the unrealistic widespread subsidence seen in raw vertical beam retrievals.

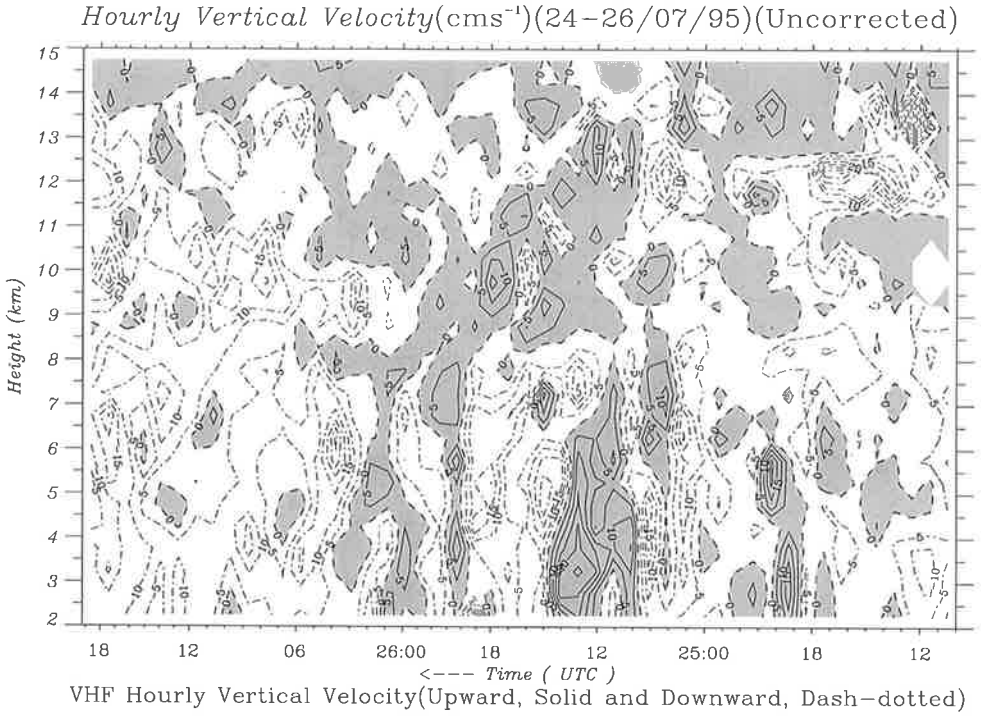

Figure 4.28: Contours of hourly vertical velocity ($cm\,s^{-1}$) for 24-26 July 1995 without any correction. The upward motions are solid and downward motions are dashed. Time is from right to left in UTC.

The blank area in Figure 4.29 is as a result of missing data of the horizontal component of the wind. By instalment and operation of a new RDAS (Radar Data Acquisition System), the missing data is minimised and the relevant contours will be even more clear and informative.

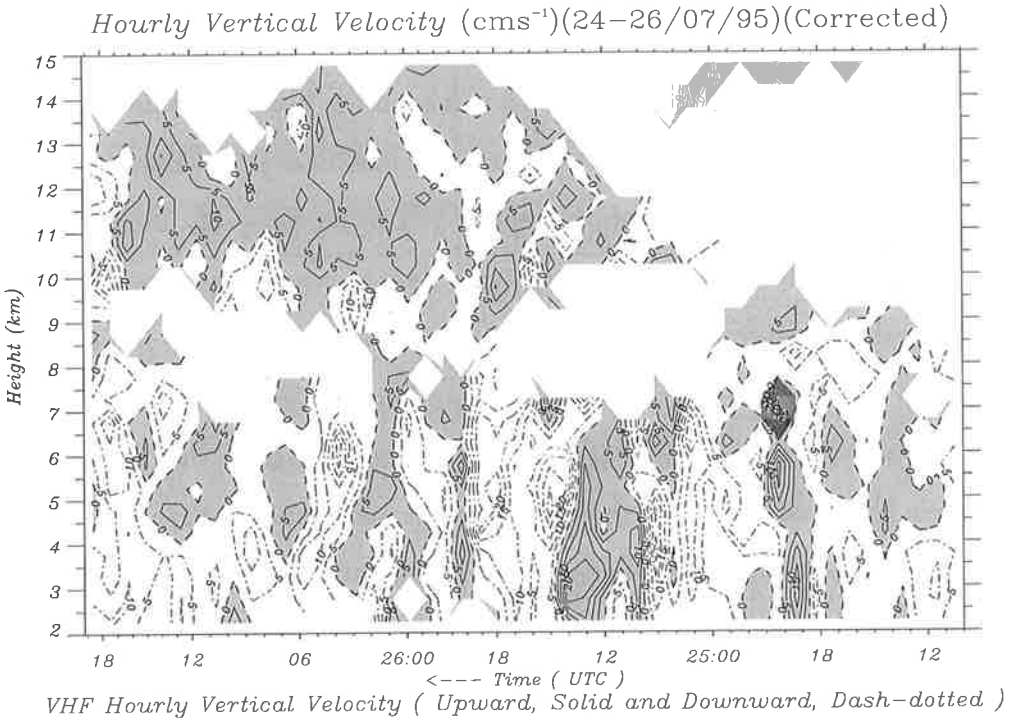

Figure 4.29: Contours of hourly vertical velocity ($cm\ s^{-1}$) for 24-26 July 1995 with correction versus antenna slope. The upward motions are solid and downward motions are dashed. Time is from right to left in UTC.

4.2 Long Term Mean Vertical Motion Observed by Buckland Park VHF Radar

4.2.1 Background

Long term mean vertical motions in the troposphere and lower stratosphere for sites in mountainous areas have been reported to have values of several centimeters per second downward. They have often been attributed to the effect of quasi-stationary lee waves. *Nastrom and VanZandt* [1994] conducted research with a VHF radar at a site in central U.S.A. far from any mountains, called Flatland ($40.5°N$, $88.5°W$). They again showed mean vertical velocity, $\overline{w}$, with the value of several centimeters per second downward through the troposphere, when averaged over periods ranging from hours to months, rather than nearly zero as expected. They reviewed some of the suggestions that have previously been advanced to explain these observations and found that each is inconsistent with the observations in some respect, except that of quasi-horizontal flow along gently sloping isentropic surfaces. It was found that flow along tilted isentropes in the midtroposphere (near $5.6\,km$) could account for only about 1-2 $cm\,s^{-1}$.

Comparison of monthly mean vertical motions during the times of clear or cloudy skies by *Nastrom et al.*, [1990b], disproved that the $\overline{w} \neq 0$ was related to clouds as the results were the same. Since the intensity of convective activity changed both with season and with time of day in midlatitudes, observations indicated that $\overline{w} \neq 0$ was not attributable to convection.

The suggestion that non-zero mean vertical velocity is not due to tilted refractivity surfaces as discussed by *Palmer et al.*, [1991] was proven by *Tsuda et at.*, [1988]. They used oblique beams (i.e. 15°) with off-zenith angles much big-

ger than any reflecting surfaces. Further *McAfee et al.*, [1993] and *Weber et al.*, [1992] found high correlation between the $\overline{w}$ values measured by $50\,MHz$ and $404\,MHz$ radars. Their results were also inconsistent with effects from the tilted refractivity surfaces as hypothesized by *Palmer et al.*, [1991].

The biases of wind measurement, due to horizontal shears as discussed by *Kudeki et al.*, [1993] seem an unlikely mechanism for $\overline{w} \neq 0$ since they would grow with height rather than go to zero at the tropopause, as observed.

Rejecting other hypotheses, then gravity wave effects will be almost the only cause of non-zero mean vertical motions. Radar reflectivity is proportional to static stability [*Gage,* 1990]. The apparent mean vertical velocity in the sampling volume is then weighted toward downward motions in a gravity wave with downward phase propagation or upward energy propagation.

Nastrom and VanZandt [1994], developed a model for the apparent vertical velocity due to the mechanism of apparent mean velocity being weighted toward downward motion in a gravity wave. Their model predicted a relationship between the energy density of vertical velocity and $\overline{w}$. For the horizontal homogeneity they found:

$$\overline{w} = \frac{m}{\nu}\widehat{w}^2 \tag{4.5}$$

where m is the wavenumber, ν is the frequency and $\widehat{w}$ is the gravity wave amplitude.

It is noteworthy that $\overline{w}$ is independent of the radar operating parameters, $Z = 2n\pi/m$ (i.e. vertical range resolution) where, n is an integer and $T = 2n\pi/\nu$ (i.e. observation time interval). *Nastrom and VanZandt* [1994], extended the analysis to a spectrum of waves and found:

$$\sigma_w^2 = \frac{\widehat{w}^2}{2} \tag{4.6}$$

where σ_w^2 is the variance of the vertical velocity, w.

These relations predict a correlation between mean observed vertical velocity in radar observations, $\overline{w}$, and the gravity wave amplitude for a monochromatic wave (i.e. Equation 4.5) or the variance of vertical velocity, σ_w^2, for a spectrum of waves (i.e. Equation 4.6). These predictions have been tested using observations from the Buckland Park VHF radar. Buckland Park, like Flatland, is located in a very flat plane and ideal for this comparison.

4.2.2 Data Sources

In order to investigate the correlation between mean observed vertical velocity in radar observations and the variance of vertical velocity for a spectrum of waves, all available Buckland Park VHF radar data from 1991 to 1995 with 5 minutes interval were concatenated and the reliable data (i.e. data with signal to noise ratio greater than $-3\,\mathrm{dB}$) were selected for further analysis. The data were equivalant to 5404 hours of continous data.

4.2.3 Data Analysis Method

To eliminate the effect of the slight tilt of the radar beam from vertical direction due to the slope of the Co-Co array's ground level and the array's antenna level, the data were corrected using Equation 4.4 by different windowing. Different windowing gives us the opportunity to choose a method of acquiring the most reliable data.

First, every set of vertical velocity data were corrected versus the corresponding set of horizontal components of wind (i.e. with 5 minute window) and then hourly averaged, Figure 4.30.

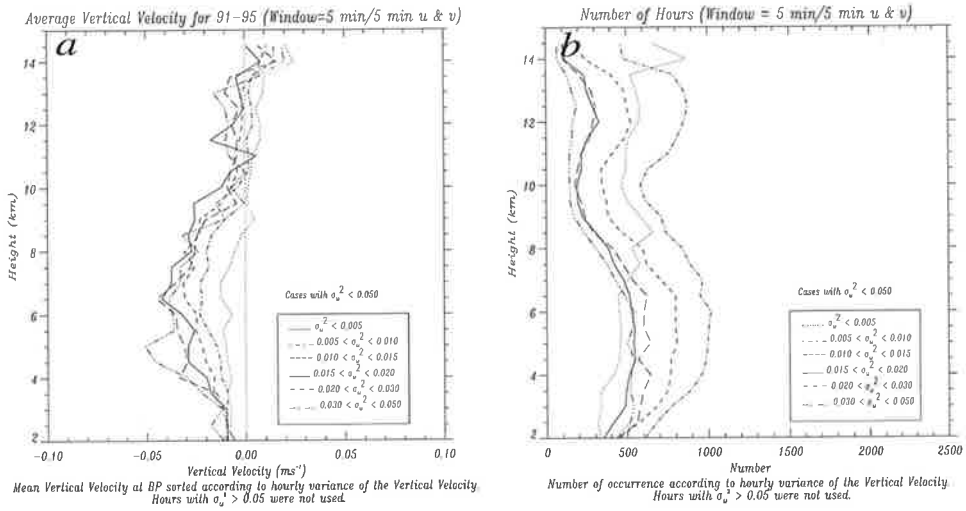

Figure 4.30: Mean vertical velocity (a), and number of hourly occurrences (b), at Buckland Park VHF radar for 1991-1995 with 5 minute window, sorted according to hourly variance of the vertical velocity. Hours with $\sigma_w^2 > 0.05\ m^2\,s^{-2}$ were not used.

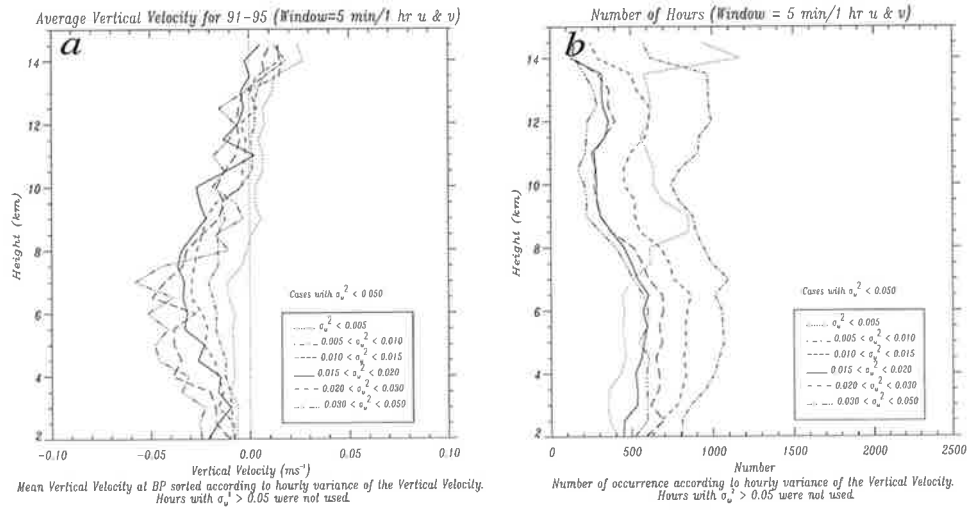

Figure 4.31: Mean vertical velocity (a), and number of hourly occurrences (b), at Buckland Park VHF radar for 1991-1995 with 5 minute $w/1$ hour u and v window, sorted according to hourly variance of the vertical velocity. Hours with $\sigma_w^2 > 0.05\ m^2\,s^{-2}$ were not used.

Second, every set of vertical velocity data were corrected versus the corresponding hourly-averaged components of wind (i.e. 1 hour window) and then hourly averaged, Figure 4.31.

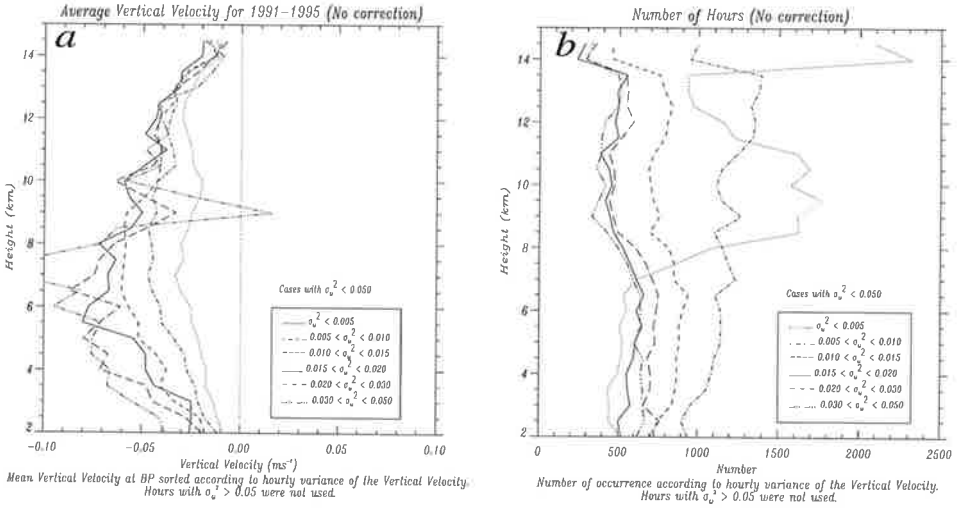

Figure 4.32: Mean vertical velocity (a), and number of hourly occurrences (b), at Buckland Park VHF radar for 1991-1995 without any corrections, sorted according to hourly variance of the vertical velocity. Hours with $\sigma_w^2 > 0.05\ m^2\,s^{-2}$ were not used.

Finally, they were compared with the non-corrected hourly averaged vertical velocity, Figure 4.32.

Apart from almost identical results irrespective of which way the data were corrected and averaged, the 5-minute/ 5-minute window has the advantage of simplicity and is therefore chosen as the primary method for further analysis.

The mean and the variance of vertical velocity were computed for each hour at each level; the means were then sorted into bins depending on their associated variance, and the mean of each bin is plotted in the above figures.

4.2.4 Correlation of Mean Vertical Velocity with Vertical Velocity Variance

Correlation between mean observed vertical velocity in radar observations, $\overline{w}$, and the variance of vertical velocity σ_w^2 for the spectrum of gravity waves is predicted by Equations4.5 and 4.6. This prediction has been tested using observations from the Buckland Park VHF radar. As Buckland Park is located relatively far from significant orographic features, the data used should not include any orographic effects. Figures 4.30a, 4.31a & 4.32a show vertical profiles of $\overline{w}$ as a function of hourly σ_w^2 for the data available from 1991 to 1995, inclusively. It is clearly shown in these figures that, as σ_w^2 increases the magnitude of $\overline{w}$ increases throughout the troposphere for small σ_w^2. Below about 7 km the largest values of σ_w^2, greater than about 0.020 $m^2\,s^{-2}$ apparently represent cases where falling precipitation contaminated the observations [*Pauley, et al.*, 1994]. Above this level, there is no apparent correlation between σ_w^2 and $\overline{w}$ when $\sigma_w^2 > 0.020\ m^2\,s^{-2}$, perhaps signaling a breakdown of linear theory in the case of large amplitudes [*Nastrom and VanZandt,* 1994].

The number of hourly data available as a function of height for different bins of vertical velocity variances are shown in Figures 4.30b, 4.31b & 4.32b. The number of events decreases with increasing vertical velocity variance throughout the troposphere and lower stratosphere, with the exception of very low variances (i.e. $\sigma_w^2 < 0.005\ m^2\,s^{-2}$). The periods of very large variances are associated with active features such as fronts and squall lines, jet-streams, short-wave troughs and intense gravity wave activity such as in baroclinic storms. The number of hours of data for all bins of σ_w^2 falls off slightly above about 7 km and then shows a small secondary peak in the lower stratosphere. This peak is due to specular

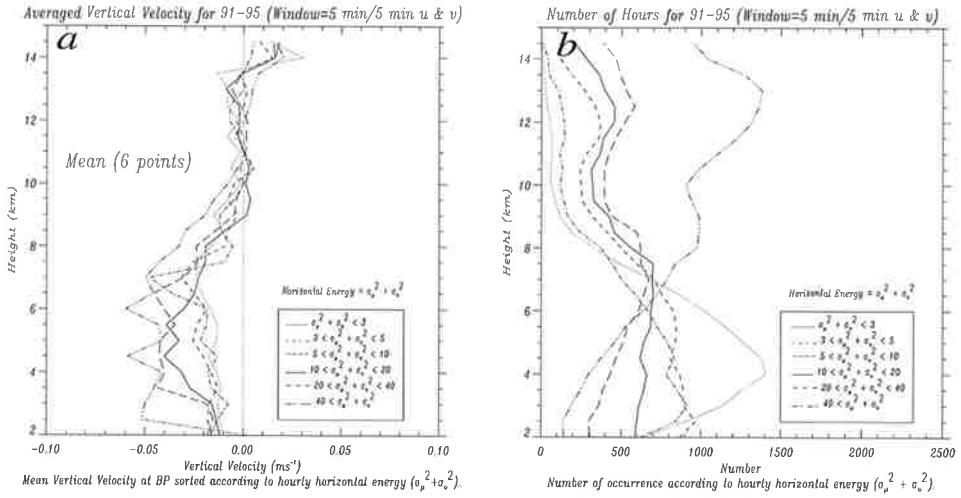

Figure 4.33: Mean vertical velocity (a), and the number of hourly occurrences (b), at Buckland Park VHF radar for 1991-1995 with a 5-minute window, sorted according to hourly horizontal energy. This analysis was carried out by running the data through the 6 point mean.

reflections [*Nastrom and VanZandt*, 1994].

The same analysis as vertical variance (i.e. σ_w^2) has been carried out with respect to total horizontal variances (i.e. $\sigma_u^2 + \sigma_v^2$). Vertical profiles of $\overline{w}$ versus height and sorted according to various bins of horizontal energy with different methods of corrections are plotted in Figures 4.33a, 4.34a & 4.35a. Similarly, as the horizontal energy increases, the magnitude of $\overline{w}$ increases throughout the troposphere beyond which they merge together around $0\, cm\, s^{-1}$. Periods of very large horizontal energy associated with intense gravity wave activity, where the mean vertical velocity is reflecting, weighted toward downward motion with upward energy propagation.

The number of hourly data available as a function of horizontal energy are plotted in Figures 4.33b, 4.34b & 4.35b. The number of events decreases with increasing horizontal energy in the troposphere beyond which the number of high horizontal energy (i.e. $\sigma_u^2 + \sigma_v^2 > 40\ m^2\, s^{-2}$) increases perhaps, due to strong

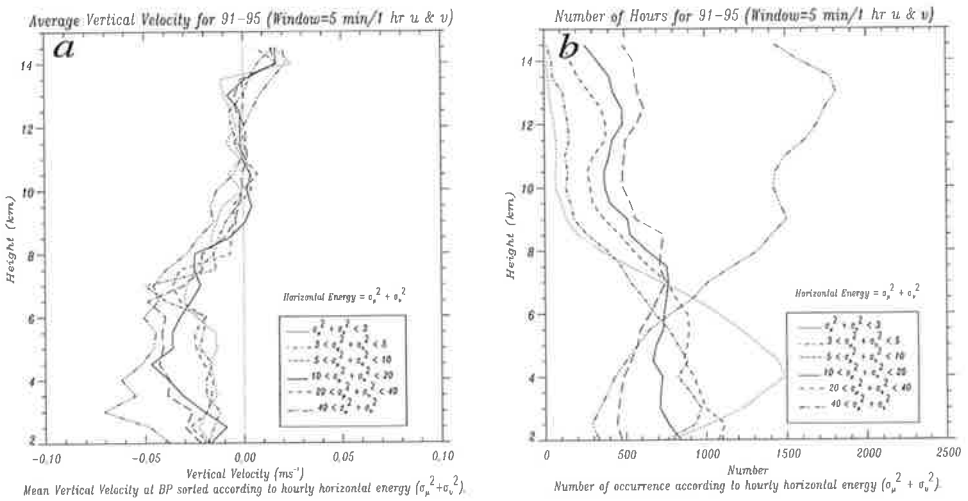

Figure 4.34: Mean vertical velocity (a), and the number of hourly occurrences (b), at Buckland Park VHF radar for 1991-1995 with a 5-minute $w/1$ hour u and v window, sorted according to hourly horizontal energy.

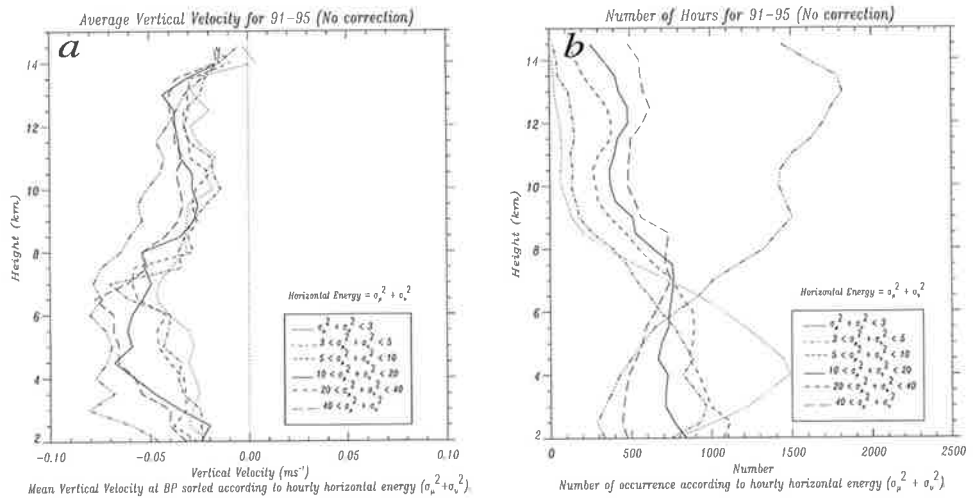

Figure 4.35: Mean vertical velocity (a), and the number of hourly occurrences (b), at Buckland Park VHF radar for 1991-1995 without any corrections, sorted according to hourly horizontal energy.

stratospheric biannual horizontal wind.

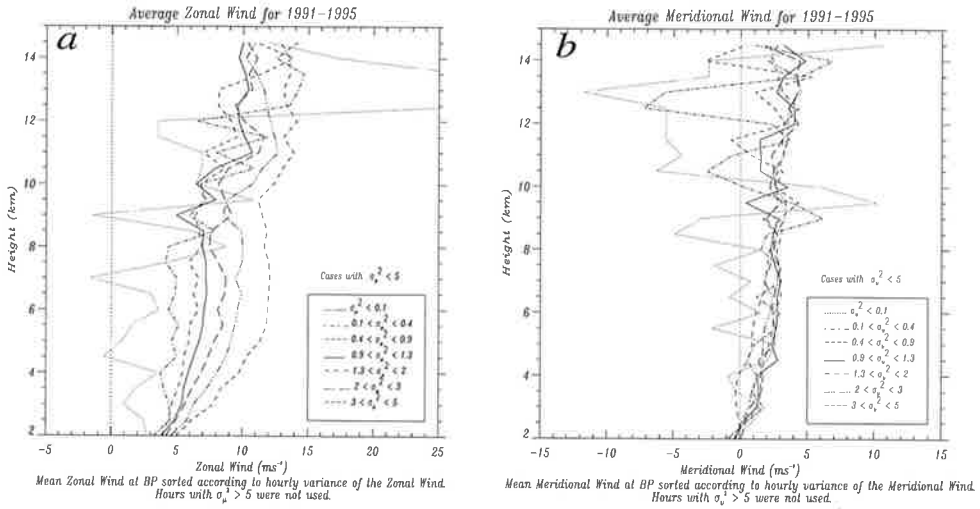

Figure 4.36: Mean zonal wind (a), and meridional wind (b) at Buckland Park VHF radar for 1991-1995, sorted according to hourly σ_u^2 and hourly σ_v^2, respectively.

Zonal wind and meridional wind as a function of their hourly variances (i.e. zonal wind variance, σ_u^2, and meridional wind variance, σ_v^2) for the available data have been shown in Figure 4.36a & 4.36b. Clearly, as σ_u^2 increases, the magnitude of $\overline{u}$ increases throughout the troposphere and lower stratosphere. The predominance of high velocity stratospheric westerly wind with very low variance seems to be as a result of biannual horizontal wind in that region. The predominance of high westerlies are self-evident from Figure 4.36a. Unlike zonal profiles, the meridional winds are uncorrelated with their hourly variances (i.e. σ_v^2). The weak southerlies through the troposphere and lower stratosphere are perceptible from Figure 4.36b.

4.2.5 Long Term Mean Vertical Velocity

Vertical velocity of the air is the most important factor in now casting and forecasting in meteorology. The VHF radar measures the vertical velocity directly. To check its reliability, this research has investigated 5 years (1991-1995) of available data. Figures 4.36a & 4.36b distinctly reveal the steadiness of southwesterlies over the VHF radar. A small portion of this prevailing wind is folding into vertical velocity as a result of the antenna tilt toward southwest. To eliminate this phenomenon, the available data have been corrected using Equation 4.4.

To investigate the effect of precipitation on radar detection as an apparent downward vertical velocity, the available data were split into two groups of "dry-season" (November-April) and "wetseason" (May-September) and analysed separately. The results are shown in Figure 4.37a & 4.37b, respectively. The results show a contradiction to the expectation of having stronger mean downward vertical velocity during the wetseasons.

In order to be more accurate, the data were split into two groups of non-precipitation and precipitation periods and analysed separately (Figure 4.37c & 4.37d). To choose the non-precipitation and precipitation periods, the South Australian stations data received from the Bureau of Meteorology were used as well as the regional meteorological daily analysed charts. The results show consistency with the expectation, as the magnitude of $\overline{w}$ is higher during the precipitation periods. Although, there is no contamination of precipitation during the non-precipitation periods, the long term $\overline{w}$ still implies a considerable downward motion.

Eventually, analysis of all available data are illustrated in Figure 4.38. As the results show, the long term mean vertical velocity, $\overline{w}$, is about $-4\ cm\,s^{-1}$ at mid-troposphere, tending toward $0\ cm\,s^{-1}$ near the tropopause and possessing

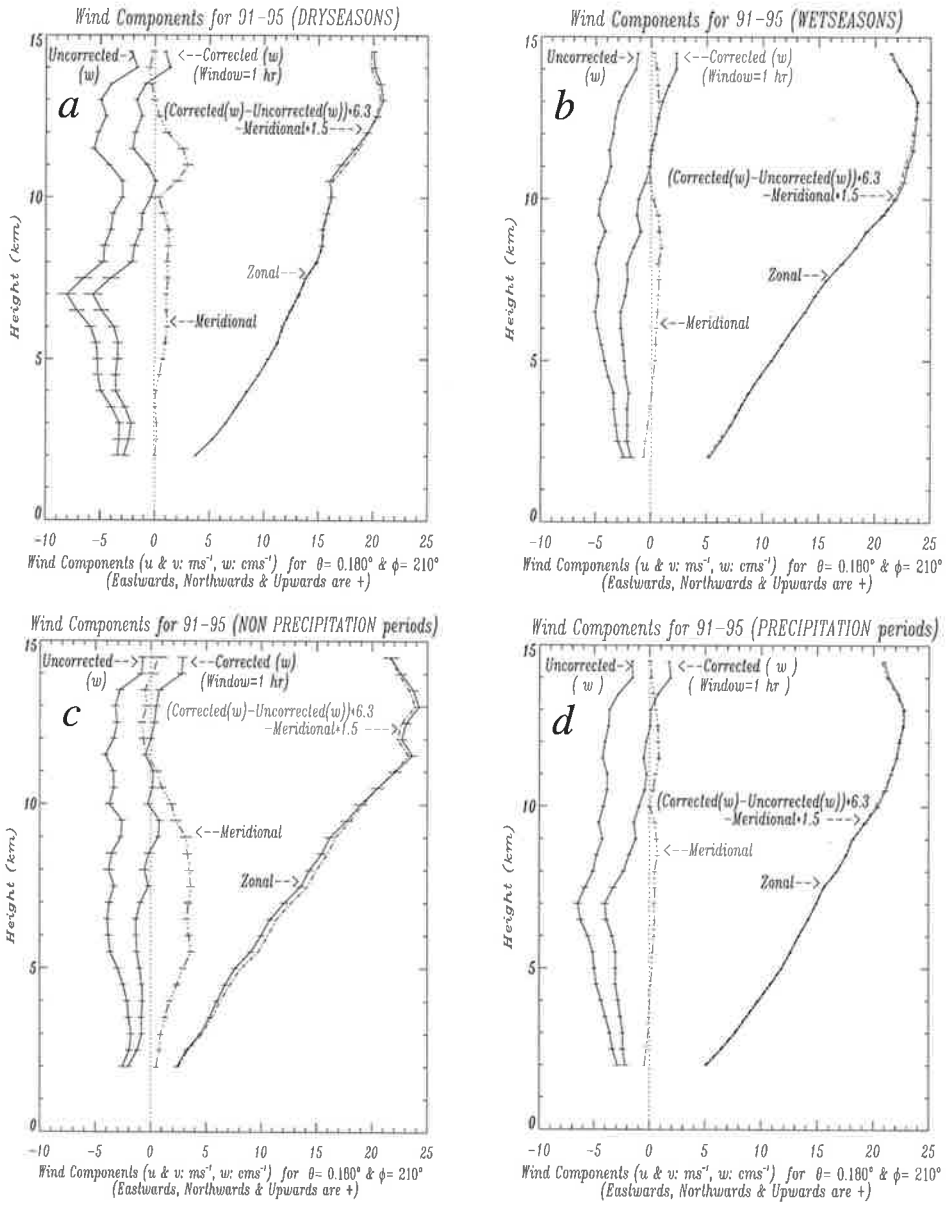

Figure 4.37: Long term mean wind components of 1991-1995 for, a:) dryseasons (Nov-Apr), b:) wetseasons (May-Sep), c:) non-precipitation periods and d:) precipitation periods. The vertical velocity has been corrected based on $\theta = 0.180°$ and $\phi = 210°$. The zonal and meridional winds are in $m\,s^{-1}$ and vertical velocity in $cm\,s^{-1}$. Eastwards, northwards and upwards are positive.

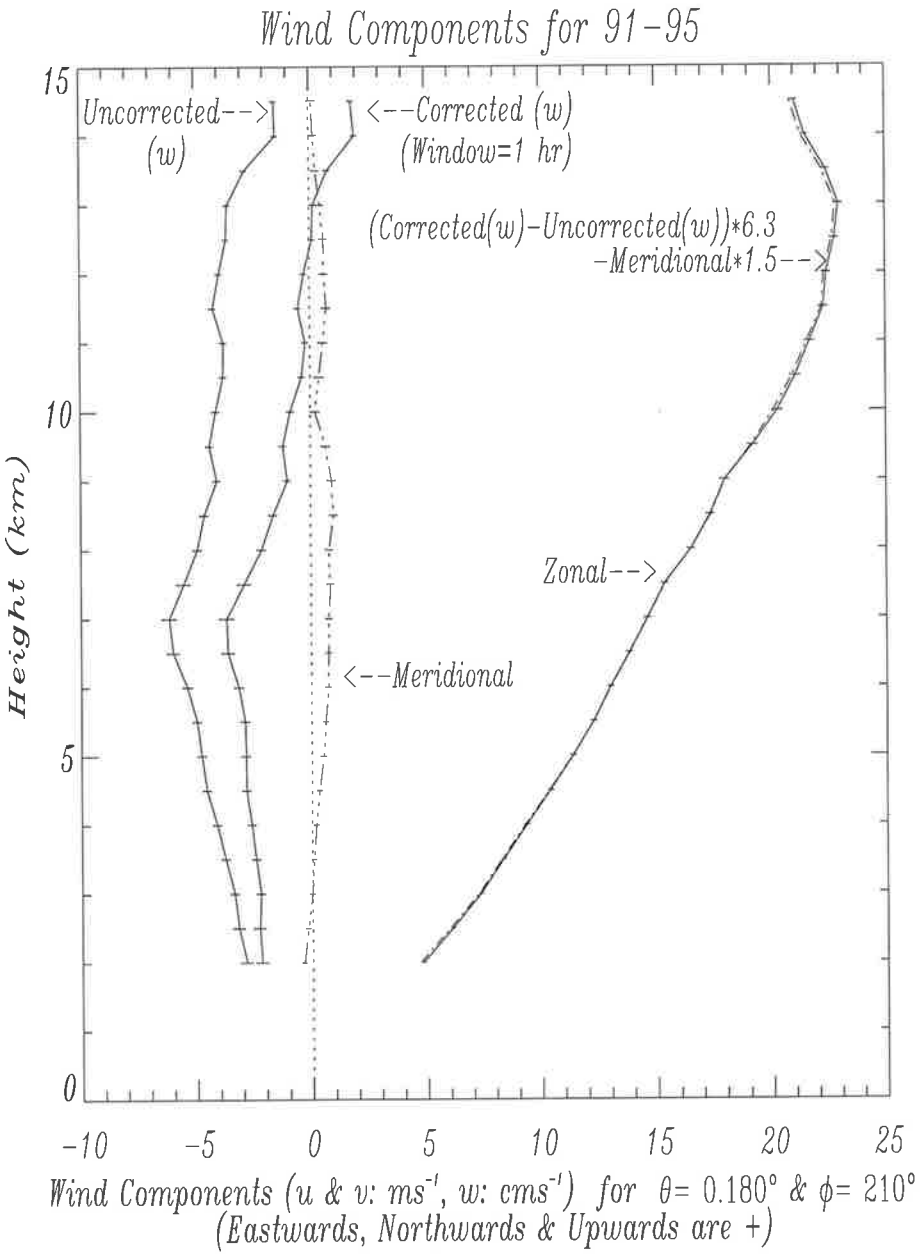

Figure 4.38: Long term mean wind components of 1991-1995. The vertical velocity has been corrected based on $\theta = 0.180°$ and $\phi = 210°$. The zonal and meridional winds are in $m\,s^{-1}$ and vertical velocity in $cm\,s^{-1}$. Eastwards, northwards and upwards are positive.

slightly positive characteristics farther away.

Nastrom and VanZandt [1994] found that the value of $\overline{w}$ was consistently near $-4\,cm\,s^{-1}$ in the troposphere during all hours of the day and during all seasons and approached zero near the tropopause. This investigation for Buckland Park VHF radar reveals the same results for an even longer period.

In addition to the mathematical relationship between the instantaneous radial velocity, V_r, vertical velocity, w, zonal wind, u, and meridional wind, v, as in Equation 4.4, an experimental relationship between the long term means of $\overline{V_r}$, $\overline{w}$, $\overline{u}$, and $\overline{v}$ was found to be as follows:

$$((\overline{w})(cm\,s^{-1}) - (\overline{V_r})(cm\,s^{-1})) * 6.3 - ((\overline{v})(m\,s^{-1})) * 1.5 = (\overline{u})(m\,s^{-1}) \qquad (4.7)$$

This experimental relationship has been shown in Figures 4.37 and 4.38. In the case of using the same scales for horizontal and vertical components of wind, the above coefficients have to be changed accordingly.

4.3 Summary

Long-term averaging of vertical velocity is important for the evaluation of characteristics of radar systems and for determining the properties of the atmosphere. VHF radars have been designed to measure the radial component of the air motion along the radar beam, but the representativeness of these profiles in terms of actual vertical atmospheric motions has been questioned. An important potential complicating factor lies in the pointing accuracy of the vertical beam [*e.g. Huaman and Balsley*, 1996]. Slight inaccuracies in the vertical beam direction can severely compromise the measurements, as discussed in section 4.1.4. However,

this does not appreciably affect instantaneous vertical velocity values. In order to evaluate the vertical beam tilt, three different methods were applied. The results of the different methods were all consistent. A zenith angle of 0.18° and azimuth angle of 210° were derived for the Buckland Park Co-Co transmitting antenna array slope, and these correction factors applied to the evaluation of the long-term vertical motion.

Different mechanisms have been proposed in the past to be responsible for the contamination of vertical velocity. *Nastrom and VanZandt* [1994] tested a number of these mechanisms and disproved that they were the cause of $\overline{w} \neq 0$ in troposphere, although the Fresnel tilting process outlined by *Larsen and Röttger* [1991] is important in short-term measurements at mid-latitudes. *Nastrom and VanZandt* [1994] proposed that the non-zero long-term mean vertical velocity arises from the scattering process itself. They suggested that the effects of vertically propagating gravity waves can account for most of the apparent mean downward motions measured with VHF radars. Gravity waves modulate the static stability of the atmosphere, an important feature in the radar reflectivity. The modulation is such that it enhances the reflectivity and hence, echo strength at the phase of the wave where the (reversible) downward wave velocity is greater.

We need to compare our results with the studies described by *Nastrom and VanZandt* [1994] for midlatitudes. They used measurements at the Flatland radar site, which is similar to the Buckland Park radar site in having no orographic effects. The apparent $\overline{w} \neq 0$ for the Buckland Park site, after correction for slight beam tilt, was found to be approximately -4 $cm\,s^{-1}$ at mid-troposphere tending towards -0 $cm\,s^{-1}$ near tropopause and possessing slightly positive values higher up. The results for dry-season, wet-season, non-precipitation periods, precipitation periods, below 5 km, above 5 km etc. were checked and it was

shown that the results could not be explained by precipitation effects.

In agreement with *Nastrom and VanZandt* [1994], we found a strong correlation between the apparent mean vertical velocity and mean variances of vertical velocity: The stronger the hourly averaged mean variance, the more negative the observed mean vertical winds. More extensive analysis for radars as a range of latitudes has been carried out by *Shimomai and Balsley* [1998] suggesting the effects are a mid-latitude phenomena. It should be pointed out that such large downward motions are not observed at lower latitude profiler sites [*Balsley et al.*, 1988; *Gage et al.*, 1991; *Shimonai and Balsley*, 1998]. The results presented in this work are in a good agreement with this recent result and extended the finding to the mid-latitude of the southern hemisphere.

Chapter 5

Cyclones

5.1 Introduction and History

Contemporary studies of cyclones during the 19th and early 20th centuries, based on the emerging thermodynamical-physical principles and fragmentary observations, established many significant features of cyclones [*Kutzbach*, 1979]. Elements of earlier investigations, together with new insights from observations and theory, were assimilated into the grand concept of the polar front theory of cyclones and general circulation. Erik Palmen's scientific career encompassed the era during which theory and observations were brought together in a coherent conception of global atmosphere [*Newton*, 1990]. Among the researchers of the early days Carl-Gustaf Rossby was one of the most outstanding personalities, certainly the best-known leader of such activities for a number of years [*Riehl*, 1990]. He had written an extensive monograph [*Rossby*, 1941] on the general circulation just before the onset of war.

As documented by *Kutzbach* [1979], a considerable knowledge of cyclone structure and behavior existed prior to World War I and many relevant thermodynamic

and dynamic principles were understood. *Kutzbach* [1979] documents the interest of the leading European and American meteorologists of the 19th and early 20th centuries in description of the weather and airflow associated with cyclones and identification of the physical processes that contribute to their development. The "thermal theory of cyclones" appeared based on the work of *Espy* in the 19th century. He believed that the decrease of surface pressure in storms is related primarily to the release of latent heat in the ascending air near the storm center. By the early 20th century, the dynamical perspective of cyclogenesis was led by the theoretical work of *Margules and Bjerknes* and the observational studies of *Dines*.

The importance of dynamical processes provided a basis for the polar front theory of cyclogenesis which was developed by the Bergen school in Norway [*Bjerknes and Solberg*, 1922] and instigated the discussions about the importance of dynamic and thermodynamic processes in extratropical storms. According to *Brunt* [1930], observational studies in the 1920's supported the importance of both, dynamic processes associated with low-level fronts and the existence of a strong upper-level current, for the development of cyclones. He did not rule out the importance of boundary layer heating and latent heat release.

Rapid advances in the understanding of cyclogenesis occurred from the 1920s to the 1950s. The reduction of the surface pressure was shown to be provided by the divergence caused by the upper-level trough/ridge systems, while low-level convergence contributed to the vorticity increase that marked the rapid spin-up of cyclones [*Bjerknes and Holmboe*, 1944]. The vorticity advection and thermal advection patterns as key factors in cyclogenesis were focused by synopticians [*Petterssen*, 1956]. The emphasis of dynamics, baroclinic instability, diabatic processes [*Sutcliffe*, 1947 and *Petterssen*, 1956] and latent heat [*Palmen*, 1951;

Krishnamurti, 1968 and *Johnson and Downey*, 1976], in the rapid deepening of cyclones and the vertical extension of the vortex from the lower to middle troposphere was the synopticians' concern at the time.

The meteorological community still finds itself involved in a vigorous debate concerning the relative importance of latent heat release, boundary-layer processes and dynamical processes in the development of cyclones.

It is about three decades since meteorological satellites have been introduced into meteorology. More cyclone structure behavior has been revealed since cloud patterns have been seen in visible (VI) and infrared (IR) images by the early polar-orbiting satellites. Cloud systems in cyclones over oceans have been adequately documented from the viewing of the entire globe by satellite images.

Because of special importance of rapidly intensifying storms and some difficulties of predicting them [*Sanders*, 1987], explosive cyclogenesis (defined roughly as deepening in excess of $24\,hPa$ in 24 hours [*Sanders and Gyakum,* 1980]) has attracted much attention in the past decade. They showed that rapidly deepening storms are primarily maritime, cold season events and that they occur usually somewhat downstream of a $500\,hPa$ trough within or poleward of maximum westerlies and within or ahead of planetary scale troughs. They also occur predominantly near the region of strong sea surface temperature (SST) gradients. *Sanders and Gyakum* [1980] concluded that explosive cyclones are baroclinic events. Cyclones display remarkable case-to-case variability, especially during the initial development phase. They are born in a variety of ways, but their appearance at death is remarkably similar.

5.2 The Potential Vorticity

The potential vorticity (PV) introduced by *Rossby* [1940] and *Ertel* [1942], is mainly used in the form:

$$P = \frac{1}{\rho}\zeta_a.\nabla\theta \tag{5.1}$$

where P is potential vorticity, ρ is density, ζ_a is absolute vorticity and θ is isopotential.

With the hydrostatic approximation, the PV is:

$$P \simeq -g\zeta_{a\theta}\partial\theta/\partial p \tag{5.2}$$

where

$$\zeta_{a\theta} = f + \left(\frac{\partial v}{\partial x}\right)_\theta - \left(\frac{\partial u}{\partial y}\right)_\theta \tag{5.3}$$

and $f = 2\Omega sin\phi$, is the Coriolis parameter.

For a frictionless, adiabatic process P is materially conserved. As discussed by *Charney and Stern* [1962], quasi geostrophic potential vorticity, q, is a quantity whose behavior on a horizontal surface approximates that of P on an isentropic surface.

Figure 5.1 illustrates the climatological distribution of P and θ in the atmosphere below $100\,hPa$. Isentropic surfaces such as that with $\theta = 330K$ have PV values rising from 0 PVU (PVU=$10^{-6}\,K\,m^{-2}\,kg^{-1}\,s^{-1}$) near the equator to slightly greater than $1\,PVU$ near the tropopause following the rapid transition to stratospheric values. In the case of adiabatic and frictionless motion, the P contours will be advected on each isentropic surface. Likewise, θ contours are advected on a P surface. Poleward of 25° latitude, the P=$2\,PVU$ surface corresponds

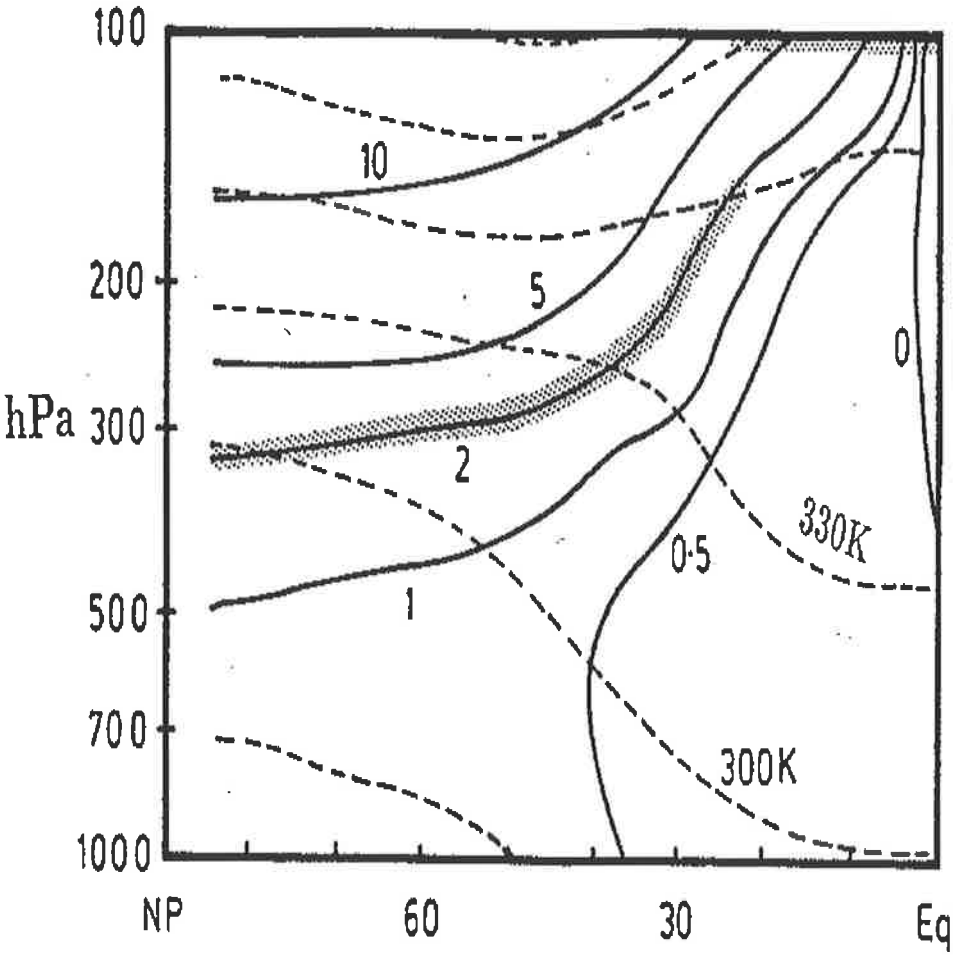

Figure 5.1: A summary of the climatological P and θ distribution below 100 hPa in the Northern Hemisphere winter. The dashed contours are those of θ, drawn every 30 K. Values of P are given in terms of the unit PVU=$10^{-6}\,K\,m^{-2}\,kg^{-1}\,s^{-1}$, and contours are drawn at 0, 0.5, 1, 2, 5 and 10. The "dynamical" tropopause specified by 2 PVU, is indicated by stippling. (Adapted from *Hoskins* [1990])

to the "dynamic" tropopause.

Generally, a positive P anomaly or a positive lower boundary θ anomaly both correspond to cyclonic circulation in the northern hemisphere. The static stability is enhanced at the level of the anomaly and reduced above and below. Neutral Rossby waves are possible on a P gradient on a θ surface, equivalently, a θ gradient on a P surface. The tropopause is an example of such a region.

5.3 Organization of Cloud and Precipitation

During the past three decades, the availability of imagery from satellite and radars has transformed the ability to observe clouds and precipitation. The patterns of cloud and precipitation in cyclones can be interpreted dynamically using relative-flow isentropic analysis and conceptual models. The imagery has drawn attention to many synoptic-scale and mesoscale features not explained by the classical model.

The geometry and dynamics of small scale concentrated flows from within the air masses that come together and interact in the cyclone, determine the cloud and precipitation distributions, as well as the structure and evolution of the cyclone. It is helpful to carry out analyses of these concentrated airflows within either moist (θ_w) or dry (θ) isentropic surfaces according to whether the flow is saturated or not, rather than traditional isobaric surfaces which intersects the flows as they ascend or descend through them. To a good approximation θ_w is conserved for moist flow and θ is conserved for dry flow within cyclones.

5.3.1 The Warm Conveyor Belt

There is a baroclinic slantwise motion producing the elongated band of cloud that forms along the boundary of a major confluence zone at the leading edge of the trough. Warm air enters the cloud belt from the convective boundary layer at its equator-ward end. As this air travels along the axis of the cloud belt it ascends into the middle and upper troposphere, producing low and medium-level cloud and thus a belt of upper-level cirrus. According to *Harrold* [1973], this most important cloud and precipitation-generating airflow is referred to as the warm conveyor belt (WCB). Large quantities of heat, moisture and westerly momentum are conveyed poleward and upward within this relatively narrow flow. Figure 5.2 illustrates a Northern Hemispheric well-defined cloud belt associated with WCBs, in that the western and poleward edge tends to be quite sharp and to consist of high cloud. Most of the cloud on the less well defined right edge is at middle and lower levels. Towards its poleward end the WCB flow turns anticyclonically as it overtakes and ascends the cold air ahead of the surface warm front, WW, in Figure 5.2. The WCBs are mainly saturated flows of high wet-bulb potential temperature, rising from the lower troposphere at their equatorward and into the upper troposphere at their poleward end.

Recent detailed analyses by *Hemler* [1987] using wind profiler data have confirmed that the WCB generally corresponds to a belt of relatively strong winds.

Although the main component of motion within the WCB is indeed parallel to the cold front, the relatively small and partly ageostrophic component perpendicular to the front has an important bearing on the frontal structure [*Browning*, 1990]. According to *Browning* [1986], there are "rearward-sloping ascent" and "forward-sloping ascent" configuration of WCB corresponding to the classical ana-cold front and kata-cold front, respectively.

Figure 5.2: Infrared (IR) image from a NOAA satellite at 1550 UTC 2 September 1987, showing an elongated belt of cloud (WW) associated with a major warm conveyor belt. The belt of cloud labeled PP is associated with the cold conveyor belt. (*Courtesy of University of Dundee.*)

5.3.2 The Cold Conveyor Belt

Another well-defined cloud and precipitation-producing flow is the cold conveyor belt (CCB) [*Carlson*, 1980]. Originating in the anticyclonic low-level flow to the east-poleward of a cyclone, the air in the CCB travels westward just ahead of the surface warm front, undercutting the WCB. At first, the air in the CCB subsides and is very dry, so that the precipitation from WCB evaporates on falling into it. As the air travels westward toward the cyclone center, the CCB begins to ascend, reaching into middle troposphere near the apex of the warm sector. When the CCB emerges beneath the western edge of the WCB, it may either ascend antcyclonically and merge with the WCB, or part of it descend cyclonically around the cyclone center. An example of the resulting cloud pattern is shown in Figure 5.2, in which the cloud band associated with the polar air trough, CCB, is labeled PP and that of WCB is labeled WW.

A partially schematic isentropic relative flow analysis for a cyclone is shown in figure 5.3. The western boundary of the WCB is represented by a hatched double line labeled LSW, LSW. The double-shafted arrow represents the relative flow within the WCB as it ascends from 600 to 300 hPa (isobars shown dashed). In the cold air behind the WCB solid streamlines depict descending flow on a dry isentropic surface (dot-dashed isobars). The CCB protruding into this region is represented by dashed streamlines ascending from 700 hPa (isobars shown dotted where the flow is beneath the WCB) to 400 hPa (dashed isobar). The CCB cloud (F), where it protrudes to the west of the WCB, is represented by a hatched double line labeled CC, CC, CC. A separate area of boundary layer stratus is denoted by the unshaded scalloped boundary. The cloud associated with the CCB is mainly confined to low and medium levels, with tops significantly lower than those associated with the WCB; the cloud tops, however, become higher in

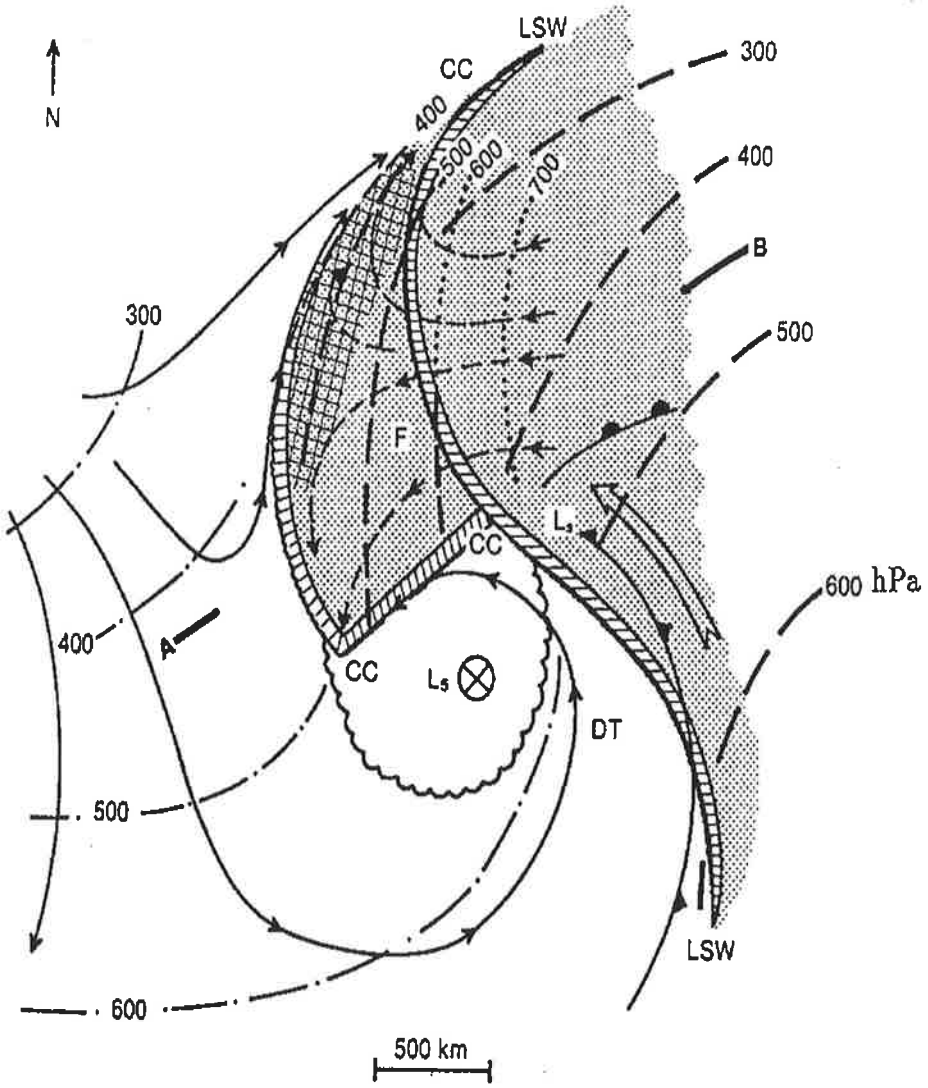

Figure 5.3: Partially schematic isentropic relative flow analysis for a cyclone, showing a CCB flow emerging beneath the western boundary of a WCB [*Carlson*, 1987]. The symbols L_s and L_5 denote the locations of the cyclone center at the surface and $500\,hPa$, respectively, and the encircled cross shows the location of the $500\,hPa$ vorticity maximum. Surface fronts are shown conventionally. Other details are described in the text (adapted from *Browning* [1990]).

the cross-hatched western part of the CCB where the ascending cloudy air flow approaches a confluent asymptote.

5.3.3 Precipitation Associated with WCB and CCB

The broad zones of frontal precipitation usually contain mesoscale banded features embedded within them. Two categories have been described: wide rainbands with shallow convective cells in middle or upper troposphere and narrow rainbands confined to lower troposphere. The former typically 50 km wide, are associated with enhanced slantwise ascent perhaps due to conditional symmetric instability giving moderate-to-heavy rain over the region. The latter, only about 3 km across, are associated with upright line convection at the sharp surface cold front, probably forced by a density current. The dry air with low wet-bulb potential temperature, θ_w, originating behind the cold front also plays an important role in determining the pattern of cloud and precipitation. It often overruns the WCB to form a shallow moist zone and potential instability.

One of the first detailed observational data sets showing the mesoscale circulations associated with wide upper tropospheric rainbands was obtained by *Heymsfield* [1979]. His observations apply to warm frontal rainbands and he summarized his results as in Figure 5.4. Each rainband is associated with a transverse circulation 100 km wide and 3 km deep situated in the WCB above the warm frontal zone.

5.3.4 Comma Cloud

A pattern of development, often seen in satellite pictures, involves cyclogenesis in cold air masses rearward of the polar front and poleward of the jet axis. The

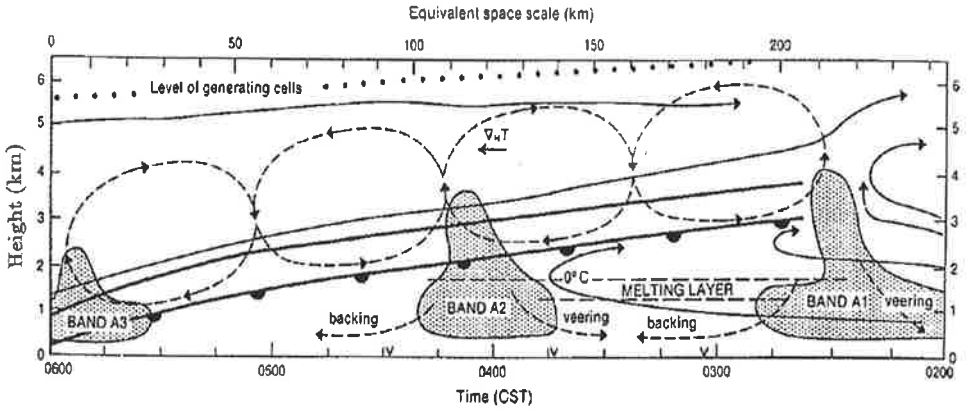

Figure 5.4: Schematic cross section through a warm front containing three warm frontal rainbands (A1, A2, A3). The top and bottom of the warm frontal zone are represented by thick solid lines. The large-scale flow relative to the front is represented by thin solid streamlines. The secondary circulations associated with the rainbands (axes of bands are normal to the plane of the diagram) are represented by dashed streamlines [*Heymsfield*, 1979].

disturbances are first seen in satellite imagery as a region of enhanced cumulus convection. Subsequently, the convective elements spread and merge, and a more or less solid comma-shaped cloud mass emerges. The final shape is not unlike that of many developing frontal cyclones, but typically the cold air systems are smaller in dimension. A satellite picture of such a system is shown in Figure 5.5. The area of cloud associated with the emerging CCB constitutes the head of a comma cloud pattern in Figure 5.3.

When a vorticity maximum in the polar air approaches a cold front, a variety of cloud systems may develop. Depending on how close it approaches, it may generate a comma cloud pattern entirely within the cold air or a wave on the cold frontal cloud band [*Browning*, 1990].

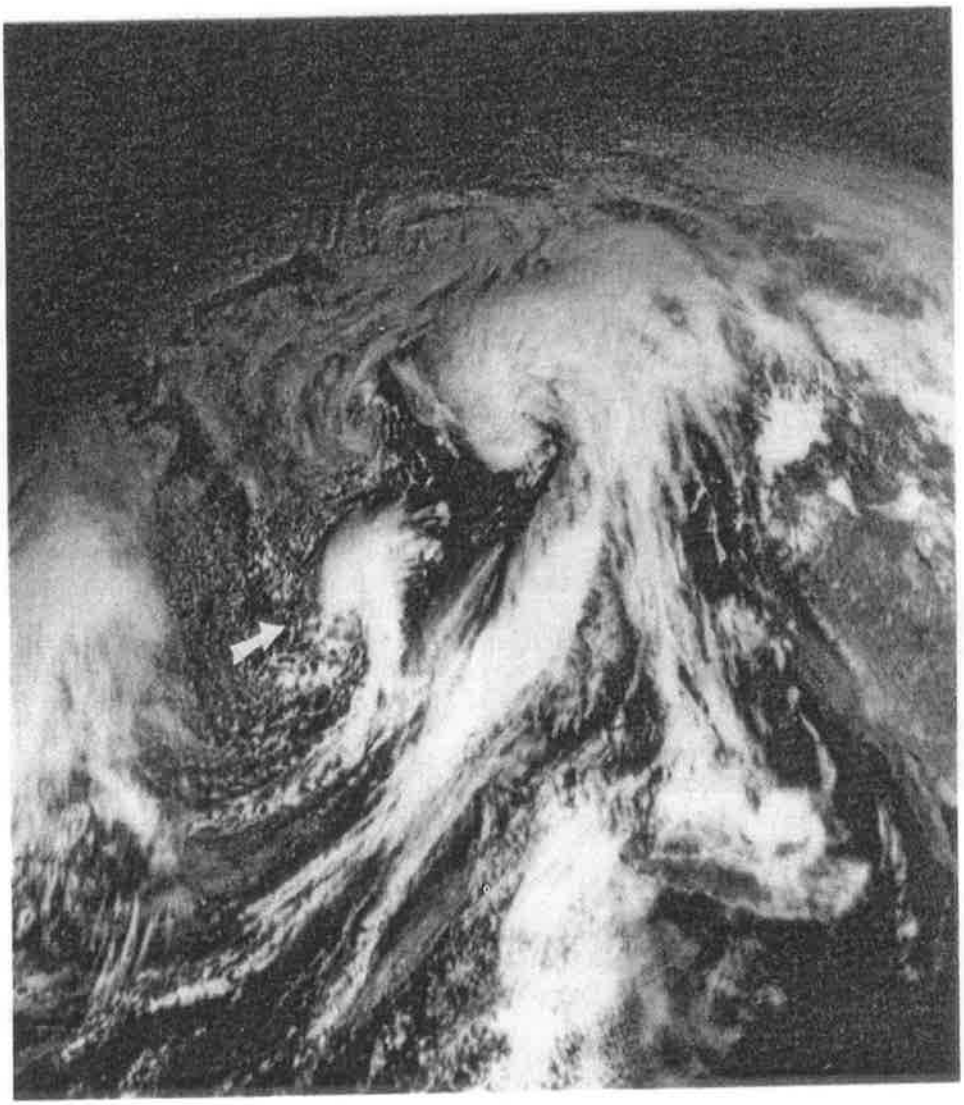

Figure 5.5: Example of comma-shaped cloud pattern (indicated by arrow) in a polar air mass [*Reed* , 1979].

5.3.5 Some Aspects of Cloud and Precipitation Over Australia

The aspects of the cloud and precipitation distribution over Australia has been discussed by *Wilson and Stern* [1985], *Garratt et al.*, [1985] and *Ryan and Wilson* [1985]. In their studies of the summertime cool change of southeastern Australia, two observational programs, each of one month duration, were conducted in the area in early summer of 1980 and 1981. As a consequence of continental effects, the WCB was found to have a relatively low moisture content.

The Southern Hemispheric subsynoptic and mesoscale model is consistent with the models developed for the Northern Hemisphere. The Northern Hemisphere studies carry several obvious implications for summertime frontal systems in southern Australia. Firstly, the moist warm flow associated with the prefrontal low-level jet in the Northern Hemisphere would be replaced by a hot, dry flow with possible effects on the intensity of "line convection" (*Browning and Harrold* [1970]; *Hobbs et al.*, [1980]) and on reduced rainfall arising from that convection. The air comprising this prefrontal high θ_w flow has an initially low relative humidity and the observed middle level cloud base is relatively high at $700\,hPa$ over southern Australia. Frictional convergence ahead of the surface cold front would be affected more by the presence of the coastline at these latitudes, 35°S-40°S, than at 50°N-55°N, because of the deeper and more frequently occurring convective boundary layer over land.

In the Australian region numerous investigations relating to cut-off lows have been carried out. *May* et al., [1990] studied the structure of cold fronts over southern Australia using the both VHF radar data and rawinsonde observations. Their studies confirmed the presence of deep, direct, vertical circulations across

the front as developed in theoretical models. *Eckermann and Vincent* [1992] specifically studied different aspects of gravity-waves produced by cold fronts over South Australia by using VHF radar observations. *Frederiksen and Frederiksen* [1993] concluded that the three-dimensional instability theory is able to generate analogs of a wide variety of Southern Hemisphere observed fluctuations, including those associated with cyclogenesis, blocking and low frequency teleconnection patterns. *Hopkins and Holland* [1997] studied the Australian East-Coast cyclones and found a strong linear correlation between the Southern Oscillation Index and heavy-rain events and East-Coast cyclones. *May* et al., [1994] used wind profiler observation to analyse Tropical Storm Flo (1990) as it passed within 115 km of the experimental site on Saipan. They resolved details of the circulation and precipitation structure of the storm and its rainbands. *Mills and Wu Bao-Jun* [1995] comprehensively studied the Cudlee Creek' flash flood of 29th August 1992. They concluded that the passage of the comma-head cloud over the Adelaide Hills produced intense localised rainfall and flash-flooding in the Torrens River system. Also in an in-depth investigation *Griffiths et al.*, [1998] studied the Cudlee Creek Cut-off low, especially with regards to the mesoscale analysis. *May* [1996] studied the organization of convection in the rainbands of a slow-moving, weak, tropical cyclone Laurence, which passed near Darwin, Australia, in December 1990.

5.4 Typical Synoptic Structure of Cut-off Low

In the normal sequence of events, a cyclone develops at the surface and gradually builds to higher levels as the occlusion process takes place.

Quite frequently however, cyclone development may commence in the upper levels. They may develop along with low level formation or sometimes develop

independently. These more or less independent developments in the middle and upper troposphere are called cut-off cyclones and are frequently seen on synoptic charts.

The unstable behaviour of a progressive upper wave in a baroclinic wind current is closely connected with the development of cyclones at the earth's surface. Growth of wave amplitude finally leads to wave degeneration in which warm cut-off highs shift polewards, and cold cut-off lows move equatorwards.

The behaviour of upper waves as they change from a stable progression to an unstable development is schematically illustrated in Figure 5.6 in which, a thermal trough is seen at the rear of a weak contour trough (stage A). The thermal advection at the rear intensifies the contour trough which in turn intensifies the thermal advection further (stage B). In stage C, the warm air from the west begins to merge with the warm air to the east of the trough. A ridge of high pressure builds across the trough thus cutting off the cold air to the equatorward and so causing a closed low. In stage D, a ribbon of isotherms is established to the poleward of the cut-off low which attains thermal symmetry.

It should be noted that these unstable processes not only occur in the horizontal plane but that they are three-dimensional processes. This three-dimensional development has to be explored by analysis of isobaric maps at several levels, and by the use of vertical cross sections placed in such a way as to picture the structure change during the development. Both analysis techniques applied together allow a three dimensional understanding of unstable wave-development processes in time and space.

An interesting feature of the cut-off low is that as the low is formed the tropopause is also depressed and finally forms a tropopause ring or tropopause funnel over it. Rising motions with cloud and rain occurs in the core of the cut-off

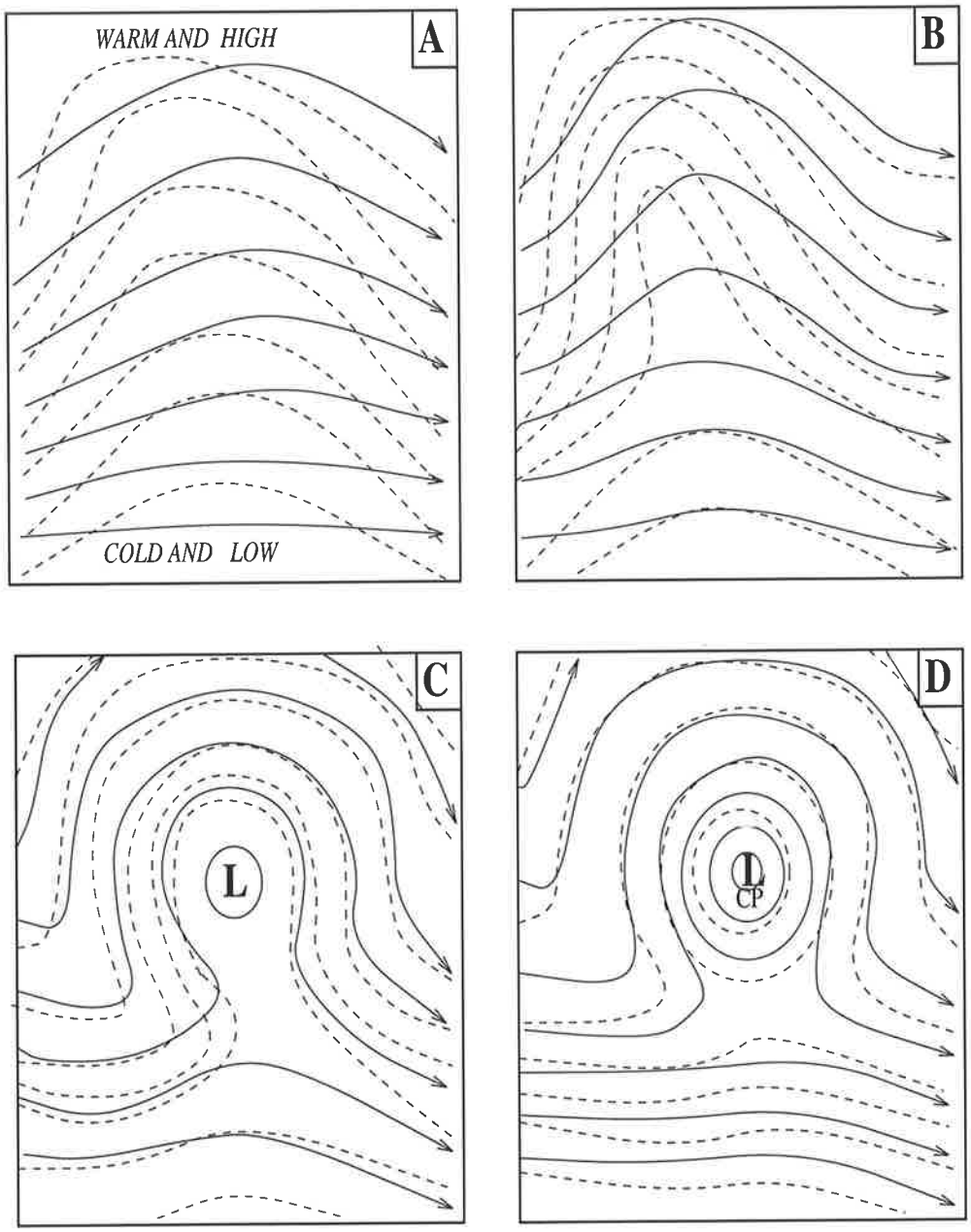

Figure 5.6: Typical features of the development of a Cut-off Low for Southern Hemisphere. Contours (solid) and isotherms (dashed) of an isobaric surface in the middle troposphere (say, 500 hPa) during the development of a Cut-off Low. CP stands for cold pool and L stands for low.

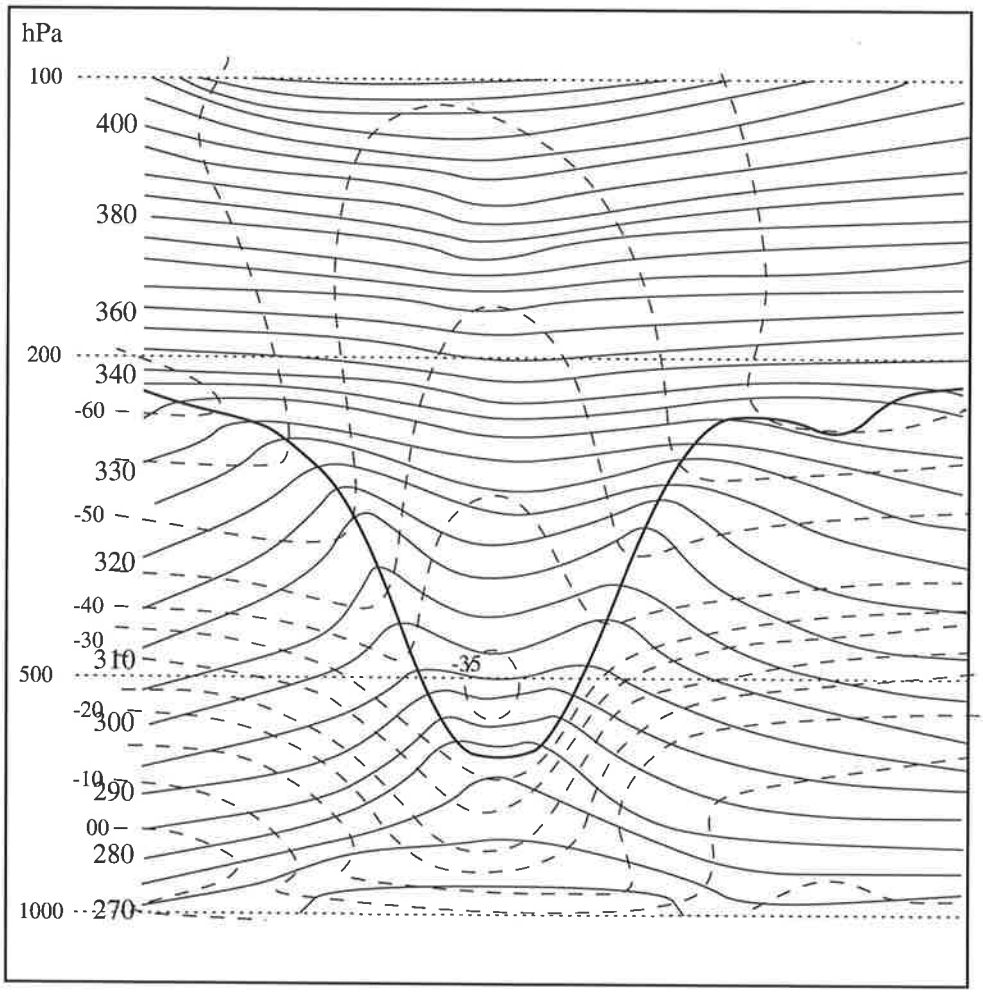

Figure 5.7: Idealized sketch of the vertical cross section of a Cut-off Low. Heavy line corresponds to tropopause, dashed lines are isotherms at 5 °C intervals, solid lines are isentropes (K).

low with sinking motions polewards of the low centre. Figure 5.7 schematically illustrates an idealized vertical cross-section of a cut-off low and its associated tropopause funnel.

5.5 Scope

The vertical motion of the air is the most important factor in the analysis, now casting and forecasting in meteorology. The instantaneous (or relatively short time averaged) vertical motion is crucial in the analysis of cut-off lows. Wind profilers are capable of measuring the vertical motion directly. Indirectly estimated vertical motion through different means of analysis are too temporal and horizontal averaged to be used for mesoscale structures.

As a matter of fact, wind profilers measure the radial velocity rather than vertical velocity. To be assured about the representativeness of radial velocity as a vertical velocity, the slope of the transmitting antenna array is essential. For this reason, we decided to determine the accurate slope of the Buckland Park transmitting Co-Co antenna array to be able to correct the radial velocity at a later stage. In the next chapter we investigate antenna slope and then long term vertical velocity of air to verify whether there is any bias in weighting the upward and downward gravity wave energy propagation similar to that of *Nastrom and VanZandt* [1994] for the Flatland wind profiler.

Chapter 6

Climatology of Cut-off Low over Australia

6.1 Introduction.

The climatology of cut-off lows in South Australia and its impact in all aspects is very important, as in the study undertaken for 20 years (i.e. 1974-1993), 62.5% of the cut-off lows have passed over South Australia. Significantly, high proportions of precipitation, thunderstorm, shower and hail in South Australia are also due to cut-off lows in this region.

The World Meteorological Organization's (WMO) defined the cut-off process as a sequence of events by which a cold low, originally within the westerlies, becomes displaced equatorward in the atmosphere; and it frequently produces, or is part of the production of, a blocking situation. A cold low (cold pool) which has become displaced out of the basic westerly current and lies to the equatorward of this current, is called a cut-off low (COL).

A region, or "pool", of relatively cold air surrounded by warmer air is called

the cold pool; the opposite of a warm pool. Cold pool is usually applied to cold air of appreciable vertical cxtcnt that has been isolated in lower latitudes as part of the formation of a cut-off low.

The COLs over Australia are classified depending on the place of their appearance on the meteorological synoptic charts. In the case of appearance from north or northwest, they are classified as Low Latitude origin Cut-off Lows (LLCOL). If they appear from south or southwest then they are classified as High Latitude origin Cut-off Lows (HLCOL).

The LLCOLs are mainly from recurved tropical cyclones or heat lows or West Coast dips. As tropical cyclones move from ocean to land mainly over Western Australia, they lose their energy supply of latent heat and weaken, turning into cut-off lows. Some of them, which reach South Australia, have many common features. There are some cases in which East Coast tropical cyclones recurve westwards and then turn into cut-off lows.

During the hot season, there is a heat low spread over the northern part of the Australian continent. As the upper troughs extend to lower latitudes, they intensify the heat lows and force them to move south-east-ward across the continent as a cut-off low which also sometimes passes over South Australia.

The HLCOLs are associated with cyclogenesis through baroclinic processes [*Reed,* 1990].

The aim of the study of the climatology of cut-off lows among the others, was to evaluate the importance of such a system and its impact in the South Australian region from the point of:

Association with the severe weather ,

High potential of precipitation,

Relatively low movement,

Damage to environment,

Influence on economy.

The flash-flood of the "Cudlee Creek" on 29th August 1992, an intense extra-tropical cyclone, passed south of Adelaide, South Australia, was an example of a cut-off low with associated impacts on the region.

The lack of investigation in these fields in the region was another reason for choosing the cut-off low for further study.

6.2 Typical Synoptic Structure

As the name of cut-off low indicates, they are equatorward extensions of cold troughs which become cut off from their source regions and remain as a cold low well to the equatorward of the polar trough system.

An interesting feature of the cut-off low is that as the low is formed the tropopause is also depressed and finally forms a tropopause ring or tropopause funnel over it. Rising motions with cloud and rain occurs in the core of the cut-off low with sinking motions to its poleward side.

The unstable behavior of a progressive upper wave in a baroclinic wind current is closely connected with the development of cyclones at the earth's surface. Growth of wave amplitude finally leads to wave degeneration in which warm cut-off highs shift polewards, and cold cut-off lows move equatorwards.

The behavior of upper waves as they change from a stable progression to unstable development was discussed in chapter 5.

6.3 Methodology

In order to study the climatology of cut-off lows, two sources of data were studied:

a) Twenty years (1974-1993) of South Australian 3-hourly synoptic charts and 12-hourly four standard levels of upper air charts (i.e. $800\,hPa$, $700\,hPa$, $500\,hPa$ and $300\,hPa$ levels) which had been archived, were manually inspected at the Bureau of Meteorology and South Australian Archives (Tables 6.1 & 6.2). These were used to plot the origin, paths, monthly variations, seasonal variations and annual variations, and to generate statistics of cut-off lows themselves.

b) To generate statistics of some phenomena associated with cut-off lows which could be distractive and hazardous to life and impact on the economy of the region, such as: *Precipitation*, *Thunderstorm*, *Shower* and *Hail*, the 20-year contemporaneous hourly observations of the 4 main stations (i.e. Woomera, Ceduna, Adelaide Airport and Mt. Gambier) were analysed. The synchronous 3-hourly observations of the 21 other stations (Table 6.3) in the Card 7 format supplied by the Bureau of Meteorology Research Center (BMRC) in Melbourne, were also added to the analysis.

6.4 Origins

During the period of study (1974-1993), 208 cases of cut-off lows which passed over Australia were found from the meteorological synoptic charts. They included 140 cases of LLCOLs and 68 cases of HLCOLS (Tables 6.1 & 6.2).

Depending on the statistical study of COL behavior, they will be discussed as "*Monthly and Seasonal characteristics*" and "*Yearly variability*".

Table 6.1: Monthly Cut-off Lows for 20 years, from 1974 to 1993.

		JAN	FEB	MAR	APR	MAY	JUN	JUL	AUG	SEP	OCT	NOV	DEC	Freq.
COLOA	Freq.	14	11	16	16	21	16	18	19	15	19	29	14	208
	Rel.Freq.	0.07	0.05	0.08	0.08	0.10	0.08	0.09	0.09	0.07	0.09	0.14	0.07	1.000
	Ave.	0.70	0.55	0.80	0.80	1.05	0.80	0.90	0.95	0.75	0.95	1.45	0.70	10.4
LLCOLOA	Freq.	13	10	14	13	11	5	7	8	8	17	22	12	140
	Rel.Freq.	0.09	0.07	0.10	0.09	0.08	0.04	0.05	0.06	0.06	0.12	0.16	0.09	1.000
	Ave.	0.65	0.50	0.70	0.65	0.55	0.25	0.35	0.40	0.40	0.85	1.10	0.60	7
HLCOLOA	Freq.	1	1	2	3	10	11	11	11	7	2	7	2	68
	Rel.Freq.	0.01	0.01	0.03	0.04	0.15	0.16	0.16	0.16	0.10	0.03	0.10	0.03	1.000
	Ave.	0.05	0.05	0.10	0.15	0.50	0.55	0.55	0.55	0.35	0.10	0.35	0.10	3.4
COLOSA	Freq.	6	4	7	7	13	10	11	13	12	17	20	10	130
	Rel.Freq.	0.05	0.03	0.05	0.05	0.10	0.08	0.08	0.10	0.09	0.13	0.15	0.08	1.000
	Ave.	0.30	0.20	0.35	0.35	0.65	0.50	0.55	0.65	0.60	0.85	1.00	0.50	6.5
LLCOLOSA	Freq.	5	3	6	5	6	2	3	5	5	16	15	8	79
	Rel.Freq.	0.06	0.04	0.08	0.06	0.08	0.03	0.04	0.06	0.06	0.20	0.19	0.10	1.000
	Ave.	0.25	0.15	0.30	0.25	0.30	0.10	0.15	0.25	0.25	0.80	0.75	0.40	3.95
HLCOLOSA	Freq.	1	1	1	2	7	8	8	8	7	1	5	2	51
	Rel.Freq.	0.02	0.02	0.02	0.04	0.14	0.16	0.16	0.16	0.14	0.02	0.10	0.04	1.000
	Ave.	0.05	0.05	0.05	0.10	0.35	0.40	0.40	0.40	0.35	0.05	0.25	0.10	2.55

Table 6.2: Yearly Cut-off Lows for 20 years, from 1974 to 1993.

		1974	1975	1976	1977	1978	1979	1980	1981	1982	1983	1984	1985	1986	1987	1988	1989	1990	1991	1992	1993	Freq.
COLOA	Freq.	11	15	13	10	19	9	9	8	6	12	12	15	5	9	9	7	10	6	15	8	208
	Rel.Freq.	0.05	0.07	0.06	0.05	0.09	0.04	0.04	0.04	0.03	0.06	0.06	0.07	0.02	0.04	0.04	0.03	0.05	0.03	0.07	0.04	1.000
	Ave.	0.92	1.25	1.08	0.83	1.58	0.75	0.75	0.67	0.5	1	1	1.25	0.42	0.75	0.75	0.58	0.83	0.5	1.25	0.67	17.3
LLCOLOA	Freq.	10	11	7	5	11	5	5	3	3	8	9	9	3	7	6	6	9	5	11	7	140
	Rel.Freq.	0.07	0.08	0.05	0.04	0.08	0.04	0.04	0.02	0.02	0.06	0.06	0.06	0.02	0.05	0.04	0.04	0.06	0.04	0.08	0.05	1.000
	Ave.	0.83	0.92	0.58	0.42	0.92	0.42	0.42	0.25	0.25	0.67	0.75	0.75	0.25	0.58	0.5	0.5	0.75	0.42	0.92	0.58	11.7
HLCOLOA	Freq.	1	4	6	5	8	4	4	5	3	4	3	6	2	2	3	1	1	1	4	1	68
	Rel.Freq.	0.01	0.06	0.09	0.07	0.12	0.06	0.06	0.07	0.04	0.06	0.04	0.09	0.03	0.03	0.04	0.01	0.01	0.01	0.06	0.01	1.000
	Ave.	0.08	0.33	0.5	0.42	0.67	0.33	0.33	0.42	0.25	0.33	0.25	0.5	0.17	0.17	0.25	0.08	0.08	0.08	0.33	0.08	5.67
COLOSA	Freq.	5	8	5	5	12	7	7	7	4	8	8	10	5	6	6	4	2	5	12	4	130
	Rel.Freq.	0.04	0.06	0.04	0.04	0.09	0.05	0.05	0.05	0.03	0.06	0.06	0.08	0.04	0.05	0.05	0.03	0.02	0.04	0.09	0.03	1.000
	Ave.	0.42	0.67	0.42	0.42	1	0.58	0.5	0.58	0.25	0.58	0.5	0.67	0.42	0.42	0.5	0.33	0.08	0.42	0.92	0.33	10.8
LLCOLOSA	Freq.	4	7	2	3	5	5	3	2	2	5	5	6	3	4	3	3	1	4	8	4	79
	Rel.Freq.	0.05	0.09	0.03	0.04	0.06	0.06	0.04	0.03	0.03	0.06	0.06	0.08	0.04	0.05	0.04	0.04	0.01	0.05	0.1	0.05	1.000
	Ave.	0.33	0.58	0.17	0.25	0.42	0.42	0.25	0.17	0.17	0.42	0.42	0.5	0.25	0.33	0.25	0.25	0.08	0.33	0.67	0.33	6.58
HLCOLOSA	Freq.	1	1	3	2	7	2	4	5	2	3	3	4	2	2	3	1	1	1	4	0	51
	Rel.Freq.	0.02	0.02	0.06	0.04	0.14	0.04	0.08	0.1	0.04	0.06	0.06	0.08	0.04	0.04	0.06	0.02	0.02	0.02	0.08	0	1.000
	Ave.	0.08	0.08	0.25	0.17	0.58	0.17	0.33	0.42	0.17	0.25	0.25	0.33	0.17	0.17	0.25	0.08	0.08	0.08	0.33	0	4.25

6.5 Monthly and Seasonal Characteristics

Cut-off low's behaviour may be subject to change monthly or seasonally. Knowledge of their monthly and seasonal variabilities is essential in the climatology of cut-off lows.

Approximately, 130 of the 208 cut-off lows studied passed over South Australia. Their seasonal distributions are shown in Figure 6.1. As it is shown, they correlate very well with the overall Australian statistics and one can be the sample of the other. There are two peaks; the higher peak occurs in November and the smaller one in May. According to Figure 6.2, the LLCOLs are responsible for the November maximum and HLCOLs are responsible for the May maximum.

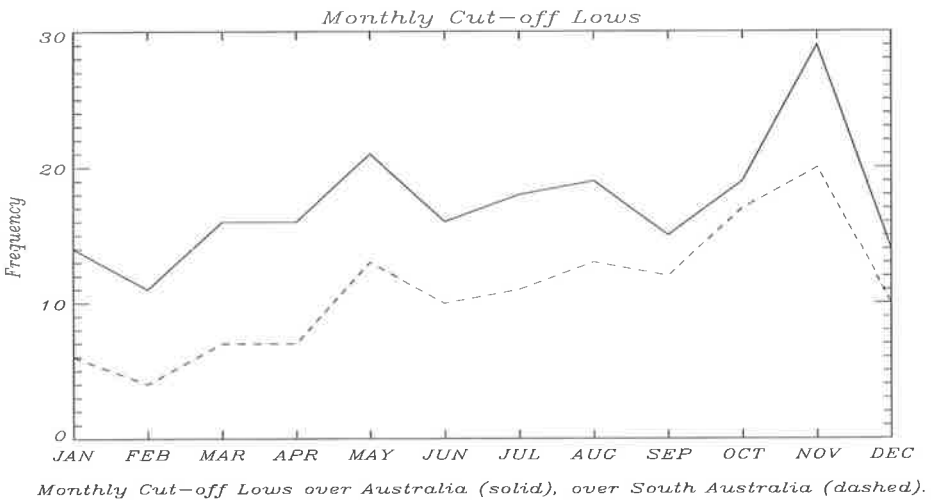

Figure 6.1: Monthly Cut-off Lows over Australia (solid) and over South Australia (dashed) for 20 years of data (1974-1993).

Separating the two types of COLs from each other, the extraordinary similarity can be seen between the sets of the same type of COLs over Australia and South Australia. This similarity occurs even in those COLs which pass through other states of Australia rather than the South Australia (Figures 6.1 & 6.4).

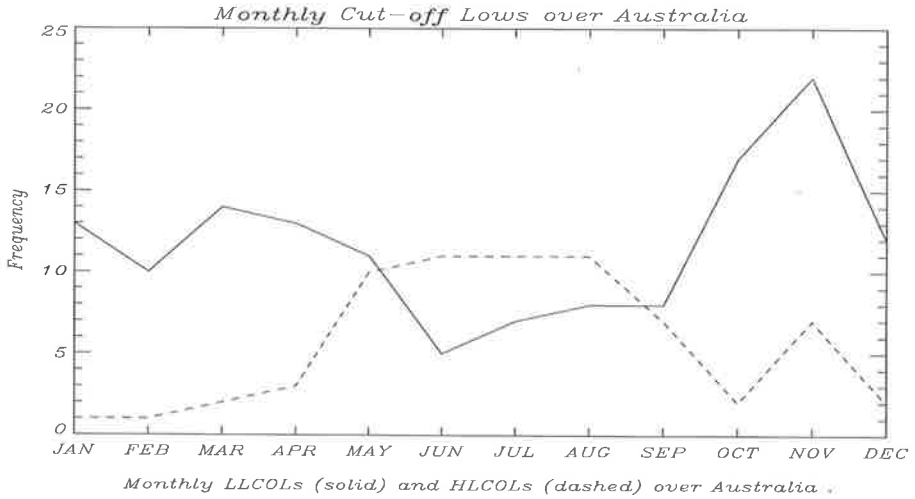

Figure 6.2: Monthly Low Latitude origin Cut-off Lows (solid) and High Latitude origin Cut-off Lows (dashed) over Australia for 20 years of data (1974-1993).

Figures 6.2 and 6.3 show that there is a maximum season of HLCOLs in winter (i.e. May - August) and minimum in summer, whereas maximum LLCOLs occur in summer (i.e. November - March) and minimum in winter.

The November maximum coincides with the onset of the cyclone season over north west of Australia, as well as the increase in the strength of the continental heat low.

The May maximum is associated with the northward movement of storm tracks during the winter.

6.6 Year to Year Variability

Yearly variabilities of COLs over Australia and South Australia are also important features in the climatology of cut-off lows.

The number of COLs each year between 1974 and 1993 over Australia and South Australia are shown in Figure 6.4. There is a very strong correlation

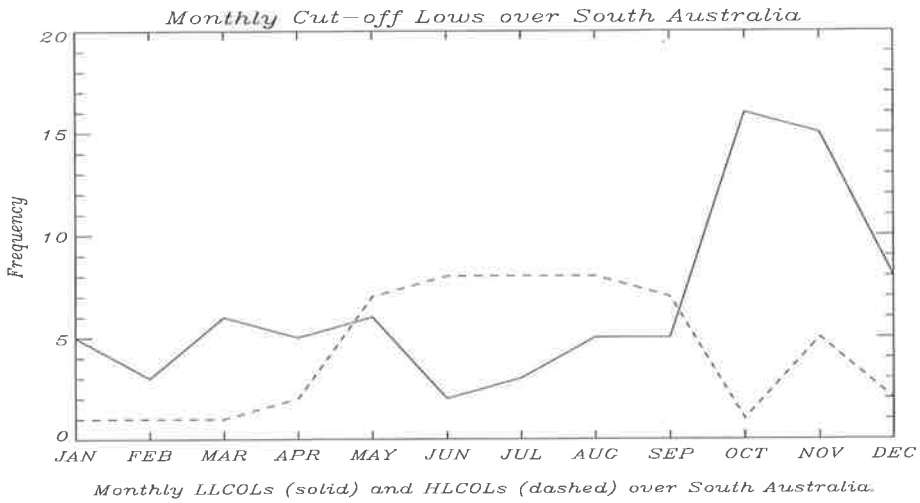

Figure 6.3: Monthly Low Latitude origin of Cut-off Lows (solid) and High Latitude origin of Cut-off Lows (dashed) over South Australia for 20 years of data (1974-1993).

between both curves. There appears to be a periodical peak of about 7 years (i.e. 1978 - 1985 - 1992) in both time series.

The predominance of LLCOLs over the whole period except 1981 in which the HLCOLs are more than that of LLCOLs is shown in Figure 6.5.

Almost the same results for COLs over South Australia are revealed in Figure 6.6.

The SOI is defined as:

$SOI = 10{*}mean(MSLP_{Tahiti(17.37S,149.27W)} - MSLP_{Darwin(12.24S,130.50E)})$ where SOI stands for Southern Oscillation Index, MSLP stands for mean sea level pressure.

Negative SOI refers to "ElNino" and positive SOI represents "LaNina".

Plots of COLs (scaled by a factor 10, in order to be recognized) and the Southern Oscillation Index (SOI) is shown in Figure 6.7. It is clear that they correlate in such a way that as the heat island in Pacific Ocean moves towards

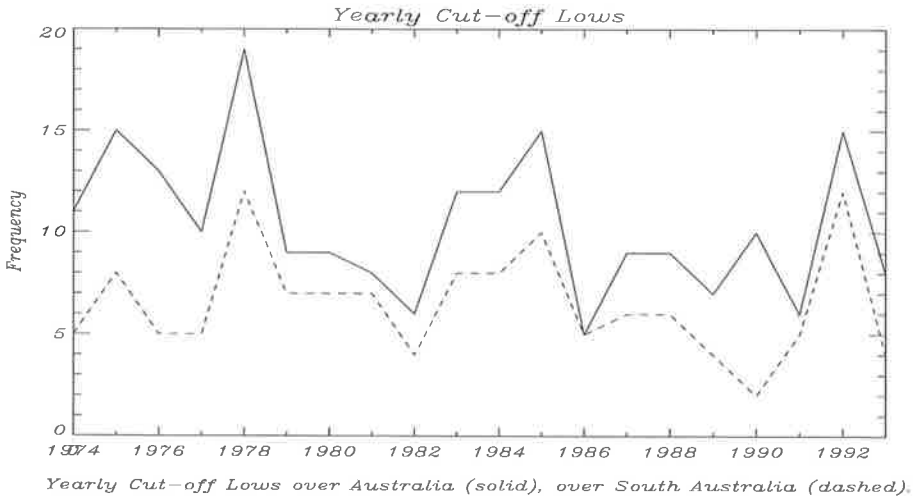

Figure 6.4: Yearly Cut-off Lows over Australia (solid) and over South Australia (dashed).

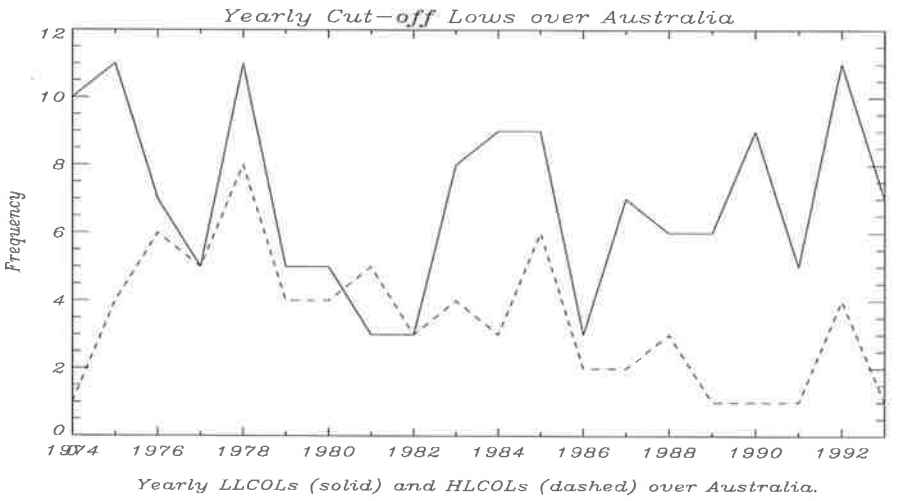

Figure 6.5: Yearly Low Latitude origin Cut-off Lows (solid) and High Latitude origin Cut-off Lows (dashed) over Australia.

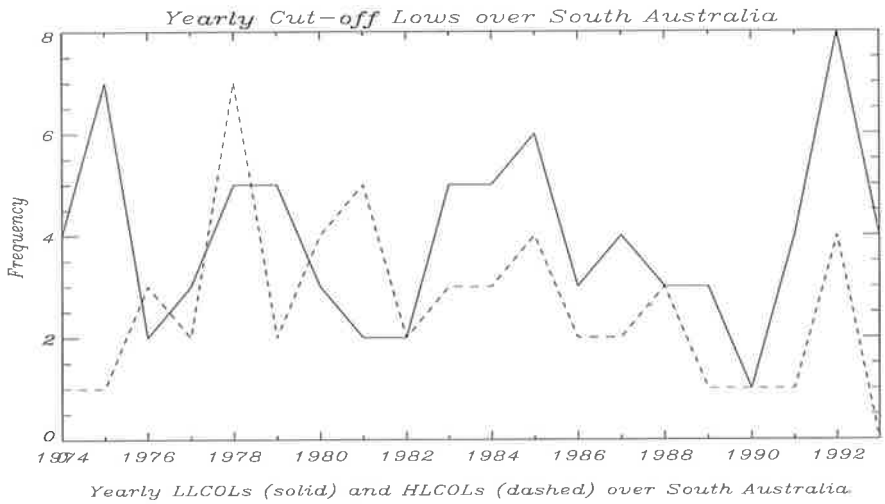

Figure 6.6: Yearly Low Latitude origin of Cut-off Lows (solid) and High Latitude origin of Cut-off Lows (dashed) over South Australia.

west, it brings along heat and moisture which in turn, increases and intensifies the LLO of COL.

Correlation of SOI without the lag with COL over Australia is 0.25, with LLO of COLs 0.27 and with the HLO of COLs over Australia is 0.06, demonstrating that low latitude origin of cut-off lows have better correlation with SOI. The heat island in the Pacific Ocean is located adjacent to the equator. Moving the heat island toward west (i.e. LaNina), brings heat and moisture toward low latitude regions of Australia and has very low effects on high latitudes. Furthermore, the Australian monsoon is weak during ElNino events and very active during LaNina years and feeding into the low latitude origin cut-off lows.

As Figure 6.8 shows, the peak of almost all curves occur within about a month of peak SOI. This overlaps the uncertainty from averaging and smoothing (5 points smoothing) of data. As a result, it can be concluded that the onset of positive SOI (i.e. LaNina) and cut-off lows (mainly, LLO) over Australia coincide.

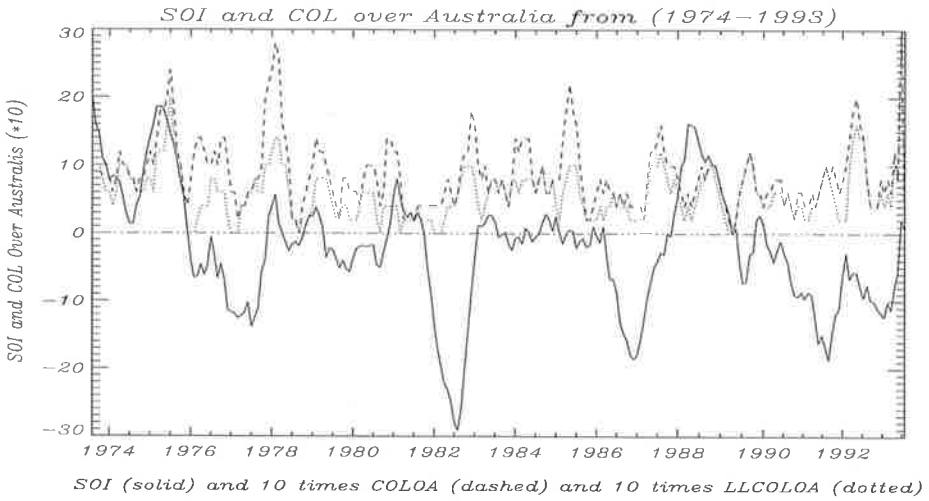

Figure 6.7: Southern Oscillation Index (solid) and 10 times Cut-off Lows over Australia (dashed) as well as, 10 times Low Latitude origin Cut-off Lows over Australia (dotted).

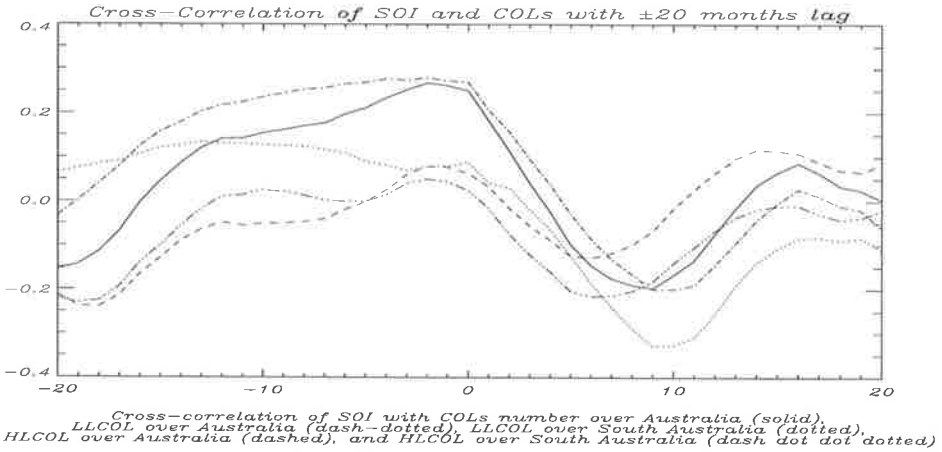

Figure 6.8: Cross-correlation of Southern Oscillation Index with Cut-off Lows over Australia (solid), Low Latitude origin Cut-off Lows over Australia (dash-dotted), Low Latitude origin Cut-off Lows over South Australia (dotted), High Latitude origin Cut-off Lows over Australia (dashed), and High Latitude origin Cut-off Lows over South Australia (dash dot dot dotted).

6.7 The Cut-off Low Tracks

Figure 6.9 illustrates the tracks of LLCOLs over Australia. The LLO of COLs mainly originate from north and northwest. There are a few unusual tracks which originate from northeast associated with east coast cyclones as well. These are mainly tropical cyclones which detour towards south and southwest and are driven to the continent.

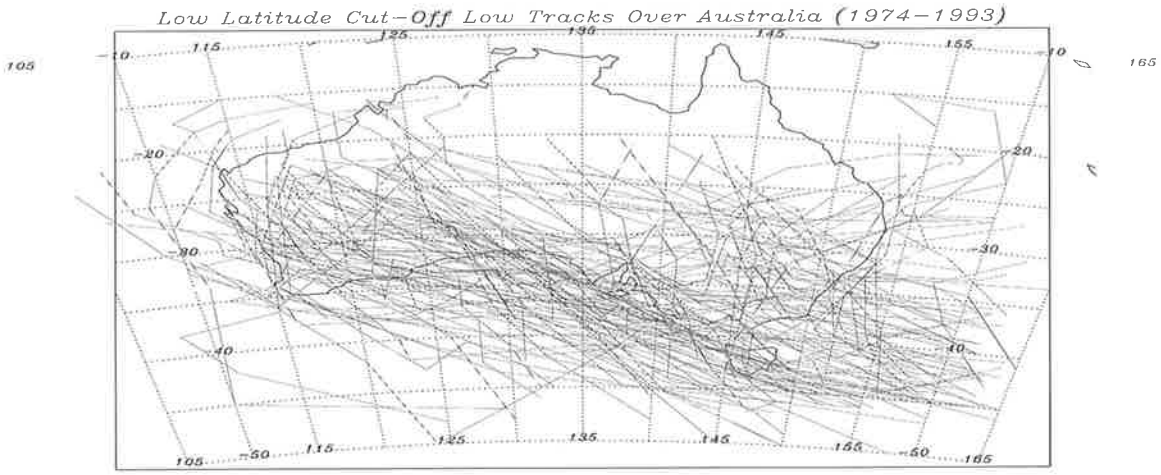

Figure 6.9: Low Latitude origin Cut-off Low Tracks over Australia for 20 years from 1974 to 1993.

Figure 6.10 shows the tracks of HLCOLs over Australia. As can be seen, they origin from south and south west, rise to lower latitudes and then recurve eastwards or southeastwards, covering mainly the southern parts of the Australian continent.

Figure 6.11 illustrates the yearly COL tracks which in turn supports the yearly maxima and types which were discussed earlier.

Approximately, 62% of COLs pass through South Australia. This includes 56% of LLO and 75% of HLO of COLs. This makes South Australia very significantly affected by COLs. This means that the Buckland Park VHF radar in

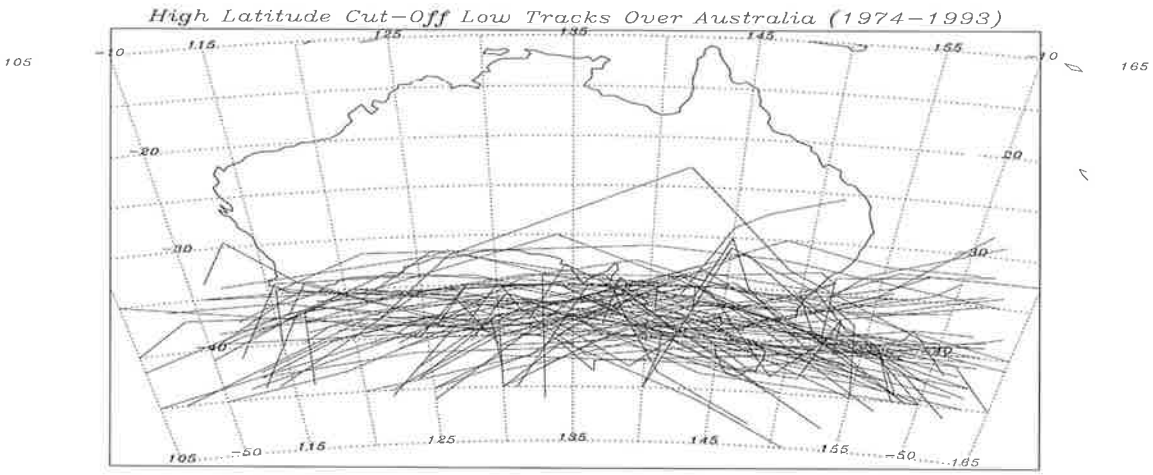

Figure 6.10: High Latitude origin Cut-off Low Tracks over Australia for 20 years from 1974 to 1993.

conjunction with the Boundary Layer radar can be very important means for the forecasters in helping them allocate, distinguish and consequently, forecast the COL systems. This will be discussed later on.

6.8 The Cut-off Low Speed

The parent systems of surface cut-off lows move fast, as long as the contours are not closed on upper air charts. As the warm air rotates around the cold pool, the movement slows down. the movement of COLs speeds up as the closed contours on upper air charts open up. Figure 6.12 shows the histogram of the speed of the COLS passing over South Australia, between latitudes of 26° S and 38° S and longitudes of 129° E and 141° E, with the mean of $9.4\,m\,s^{-1}$ and median of $8.7\,m\,s^{-1}$.

The high speeds refer to the movement of COLs before being closed and after being opened in the upper atmosphere, while low speeds refer to the movement

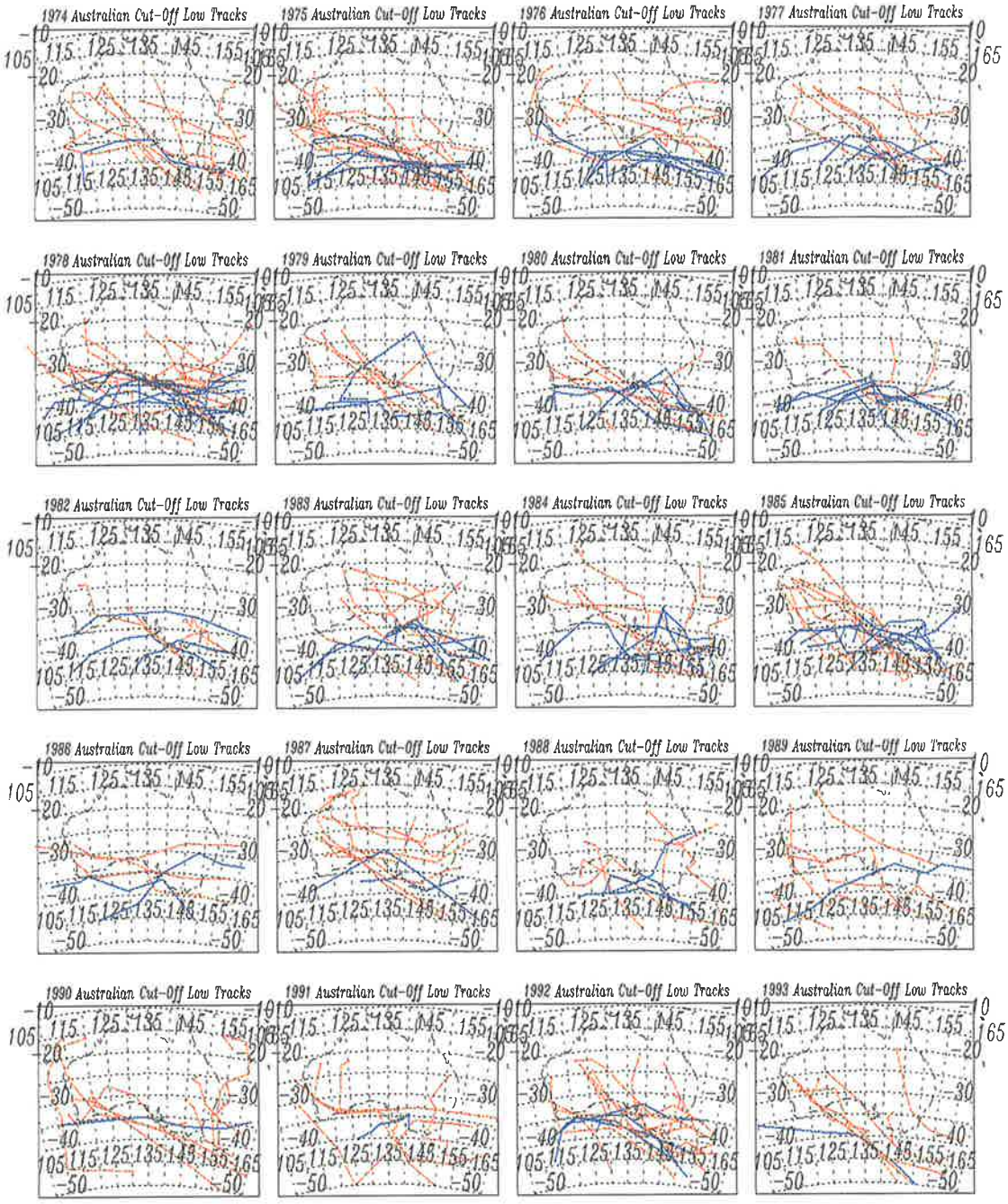

Figure 6.11: Yearly Australian Cut-off Low Tracks. High Latitude origin Cut-off Lows in blue and Low Latitude origin Cut-off Lows in red.

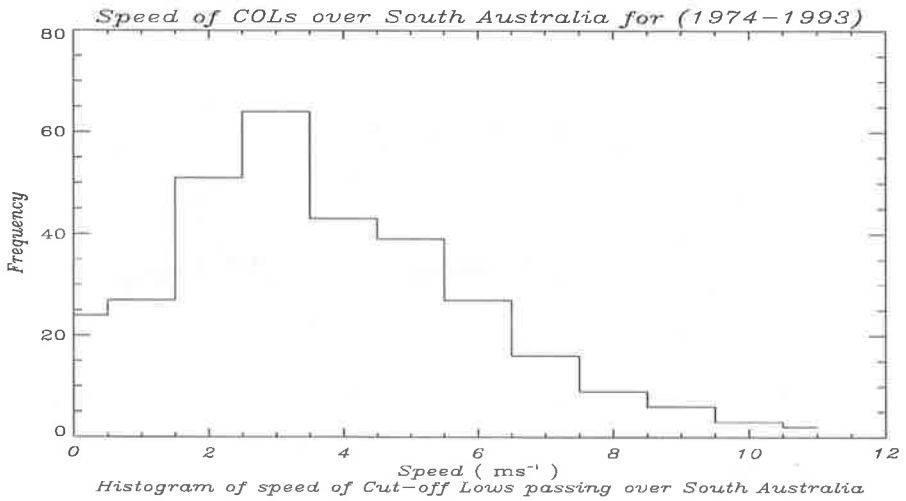

Figure 6.12: Histogram of speed of Cut-off lows passing over South Australia between latitudes of 26° S and 38° S and longitudes of 129° E and 141° E.

of COLs when the pattern is closed..

6.9 Synoptic Structure

Inspection of 20 years of mean sea level (MSL) charts and upper air Meteorological charts (i.e. 800 hPa, 700 hPa, 500 hPa and 300 hPa) revealed that:

- a) In almost all cases an upper level cut-off low with closed contours accompanies a surface system.
- b) The surface cut-off low is intensified as far as the vertical axis of COL tilts backwards towards the west.
- c) There is no change of intensification while the vertical axis of COL is vertical.
- d) The surface COL is weakened as the vertical axis tends towards the east and passes the MSL surface center.

- e) If the upper closed low is located to the south west of a surface low, it will drag the surface COL towards the higher latitudes and by intensifying the surface COL, the upper one will also be intensified.

- f) There is almost always a closed cold isotherm (cold pool) in the 500 hPa COLs. As the cold pool migrates from the COL center, the COL starts to be opened up.

- g) The COL will move faster as it opens up and becomes a trough.

6.10 Impacts of Cut-off Low

Impacts of COLs on the South Australian region have been investigated by analyzing 20 year (1974-1993) 3-hourly synoptic data from 25 major South Australian stations for *Precipitation* (PPTN), *Thunderstorm, Shower* and *Hail* by a variety of statistical approaches such as: *yearly average*, *yearly COL average* and *COL percentage.*

The stations and their related information are shown in Table 6.3. Their locations are shown in Figure 6.13.

6.10.1 Precipitation

Precipitation is any or all of the forms of water particles, whether liquid or solid, that fall from the atmosphere and reach the ground, including drizzle, rain, snow, snow pellets, snow grains, ice crystals, ice pellets, and hail and is distinguished from cloud, fog, dew, rim, frost and virga [*Huschke*, 1970].

Precipitation (PPTN) of the region is under the influence of two types of cut-off lows from High Latitudes and Low Latitudes. As it is shown in Figure 6.14,

Table 6.3: South Australian stations and their information.

No.	Station Name	Regional No.	WMO No.	Latitude(S)	Longitude(E)	Elevation
01	Adelaide Ap.	023034	94675	34.95	138.53	6.0(M)
02	Arkaroola	017099	94676	30.31	139.33	340.0(M)
03	Birdsville	017081	94482	25.90	139.35	43.0(M)
04	Cape Borda	022801	94805	35.75	136.60	145.0(M)
05	Ceduna AMO	018012	94653	32.13	133.72	23.0(M)
06	Coober Pedy	016007	95458	29.04	134.72	215.0(M)
07	Cook	018110	94649	30.62	130.42	121.0(M)
08	Hawker	019017	94673	31.89	138.42	315.0(M)
09	Keith	025507	94816	36.10	140.35	29.0(M)
10	Kingscote	022807	95807	35.71	137.52	5.0(M)
11	Kyancutta	018044	94657	33.13	135.57	58.0(M)
12	Lameroo	025509	94688	35.33	140.52	99.0(M)
13	Maitland	022008	94665	34.38	137.68	186.0(M)
14	Marla	016085	94477	27.30	133.62	322.0(M)
15	Marree	017031	94480	29.65	138.05	50.0(M)
16	Moomba	017096	94481	28.10	140.20	39.0(M)
17	Mt. Barker	023733	94806	35.05	138.51	330.0(M)
18	Mt. Gambier	026021	94821	37.82	140.77	65.0(M)
19	Pt. Lincoln	018070	95661	34.60	135.88	6.0(M)
20	Pt. Augusta	019066	94666	32.53	137.78	4.0(M)
21	Pt. Pirie	021043	94669	33.19	138.01	4.0(M)
22	Renmark	024016	94687	34.17	140.75	20.1(M)
23	Snowtown	021046	94670	33.78	138.22	103.0(M)
24	Whyalla Ap.	018103	95664	33.06	137.52	10.0(M)
25	Woomera	016001	94659	31.15	136.82	165.0(M)

there is a PPTN maxima around the York Peninsula which is influenced by the two types of COLs, as well as being influenced by moisture from Spencer Gulf and Saint Vincent Gulf.

The highest rate of PPTN belongs to Mt. Gambier, where an orographic effect is mostly responsible. Low latitude cut-off maxima in the far north of the state, around Marla, produces the third maxima there.

Figure 6.15 supports the idea of COL responsibility for PPTN maxima in the far north. The far south of the state, around Mt. Gambier, is less affected by COL. The York Peninsula region is the area within the region most affected by COLs, as this area is under the passage of both types of cut-off lows.

The highest percentage of cut-off low precipitation takes place on York Peninsula where both types of cut-off lows pass through.The maxima at the far north shows that the area is mostly affected by low latitude origin of cut-off lows and a high proportion of PPTN belongs to COL. The far south is the least affected by COLs (Figure 6.16).

Comparison of Figure 6.14 with Figures 6.17 and 6.18, which are the yearly *mean* PPTN and yearly *median* PPTN, respectively, obtained from Regional Meteorological Center (RMC), reveals the strong similarity between them. The regions of highest precipitation are almost identical in these three charts, verifying the analysis.

6.10.2 Thunderstorm

In general, thunderstorm (sometimes called electric storm) is a local storm invariably produced by a cumulonimbus cloud, and always accompanied by lightning and thunder, usually with strong gusts of wind, heavy rain, and sometimes with hail. These storms are of short duration, seldom over two hours for any one storm

[*Huschke*, 1970].

To extract Thunderstorm events from the 3-hourly synoptic reports of stations, the numbers: 13, 17, 29, 91, 92, 93, 94, 95, 96, 97, 98 and 99 from the present weather, "ww", of WMO synoptic codes as well as, number 9 from past weather"W1" and "W2" of the same code which were representative of thunderstorm, were chosen.

Figure 6.19 shows the maxima over the far north, which is due mainly to the passage of Low Latitude cut-off lows, and the central and far south of the state.

According to Figure 6.20, the contribution of COL thunderstorm in the far north is greater than elsewhere. Figure 6.21 reveals the highest percentage of COL thunderstorms in the center of the state and around York Peninsula due to the passage of both COLs.

6.10.3 Shower

Showers (also known as precipitation from a convective cloud) are characterized by the suddenness with which they start and stop, by the rapid changes of intensity, and usually by rapid changes in the appearance of the sky, in the form of "rain showers", "snow showers" and "sleet showers" [*Huschke*, 1970].

To analyse the number of showers from the 3-hourly synoptic reports of stations, the numbers: 25, 27, 80, 81, 82, 83, 84, 85, 86, 87, 88, 89 and 90 from the present weather, "ww", of WMO synoptic codes as well as, number 8 from "W1" and "W2" of the same code which were representative of shower, were chosen.

The region of highest number of showers is mostly along the shore. The high rate of showers at Adelaide area in Figure 6.22, is due to the passage of both types of COLs.

The maxima at Mt. Gambier is obviously due to orographic effect as there is

not much contribution of COLs there. Relatively high rates of showers in the far north is due to the passage of low latitude origin of COLs. Figures 1.23 and 1.24 support the idea of the passage of COLs over the region.

6.10.4 Hail

Hail, precipitation in the form of balls or irregular lumps of ice having a diameter of $5\,mm$ or more (smaller particles of similar origin may be classed as either "ice pellets" or "snow pellets"), is always produced by convective clouds, and nearly always cumulonimbus clouds [*Huschke*, 1970].

To depict the number of hail events from the 3-hourly synoptic reports of stations, the numbers: 25, 27, 80, 81, 82, 83, 84, 85, 86, 87, 88, 89 and 90 from the present weather, "ww", of WMO synoptic codes which were representative of hail, were chosen.

The highest rate of number of events of hail occurs in the southern part of the state in the mountainous region, where the temperature is lowered as the air is forced to lift over the mountains Figure 6.25.

The average and percentage of COL hail in Figures 6.26 and 6.27 are not reliable as the number of events are very small during the COL events and non COL events.

6.11 Summary

The surface cut-off lows over Australia for a period of 20 years from 1974 to 1993 has been investigated. The results show that there are two types of cut-off lows passing through Australia, one which is called low latitude origin cut-off low (LLCOL), originates mainly over the northwestern part of the continent and

then passes across Australia, the second called high latitude origin cut-off low (HLCOL) comes mainly over the southwestern part of the continent and passes through.

The correlation between SOI and COL over Australia is 0.25. The South Australian region is under the effect of both types of COLs. The Northern part is affected by LLCOLs while the Central part and especially around the York Peninsula region and Adelaide is affected by both LLCOLs and HLCOLs. The fact that more than 15% of precipitation and thunderstorm activity and 8% of shower activity 'in Adelaide is due to COLs, makes the COL very important for the economy of the region.

In almost all cases an upper level COL with closed contour have accompanied the surface system.The surface COLs were intensified as far as, its core tilted towards west, weakened while its core tilted towards east and consequently, no change as vertical. Almost always there were a cold pool in the $500\,hPa$ COL centers and as it migrated from the center, the COL were opened up and moved away faster.

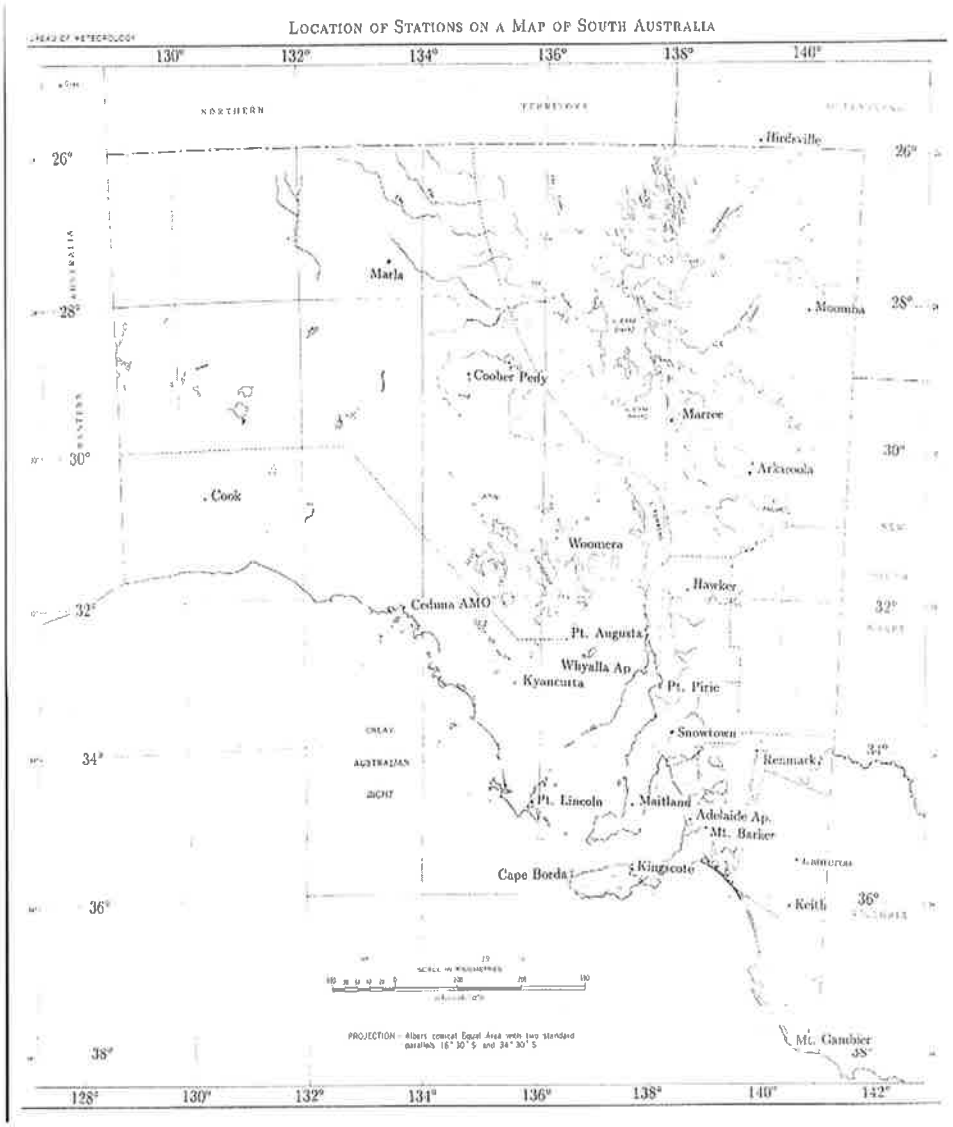

Figure 6.13: Locations of the South Australian stations whose data have been used for this report.

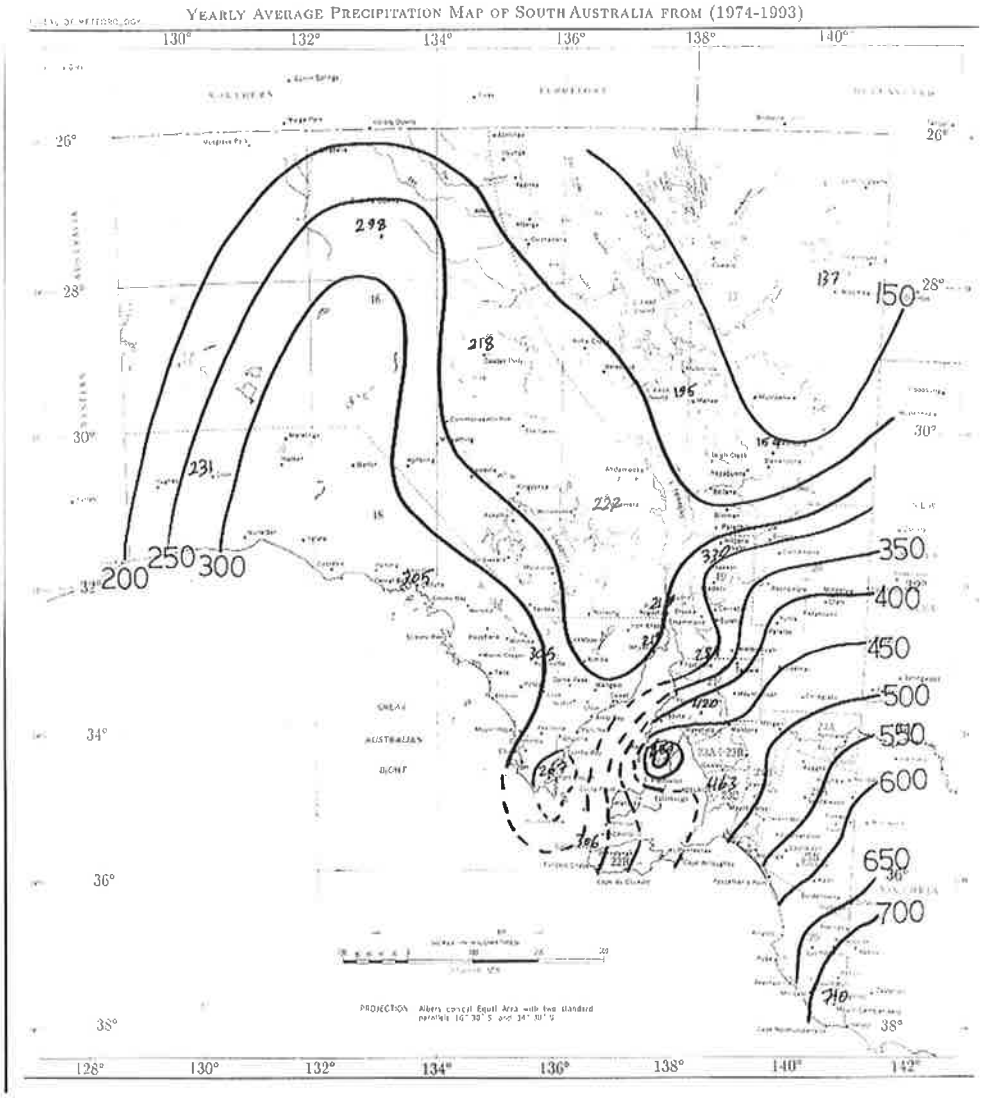

Figure 6.14: Yearly Average Precipitation Map of South Australia from 1974-1993.

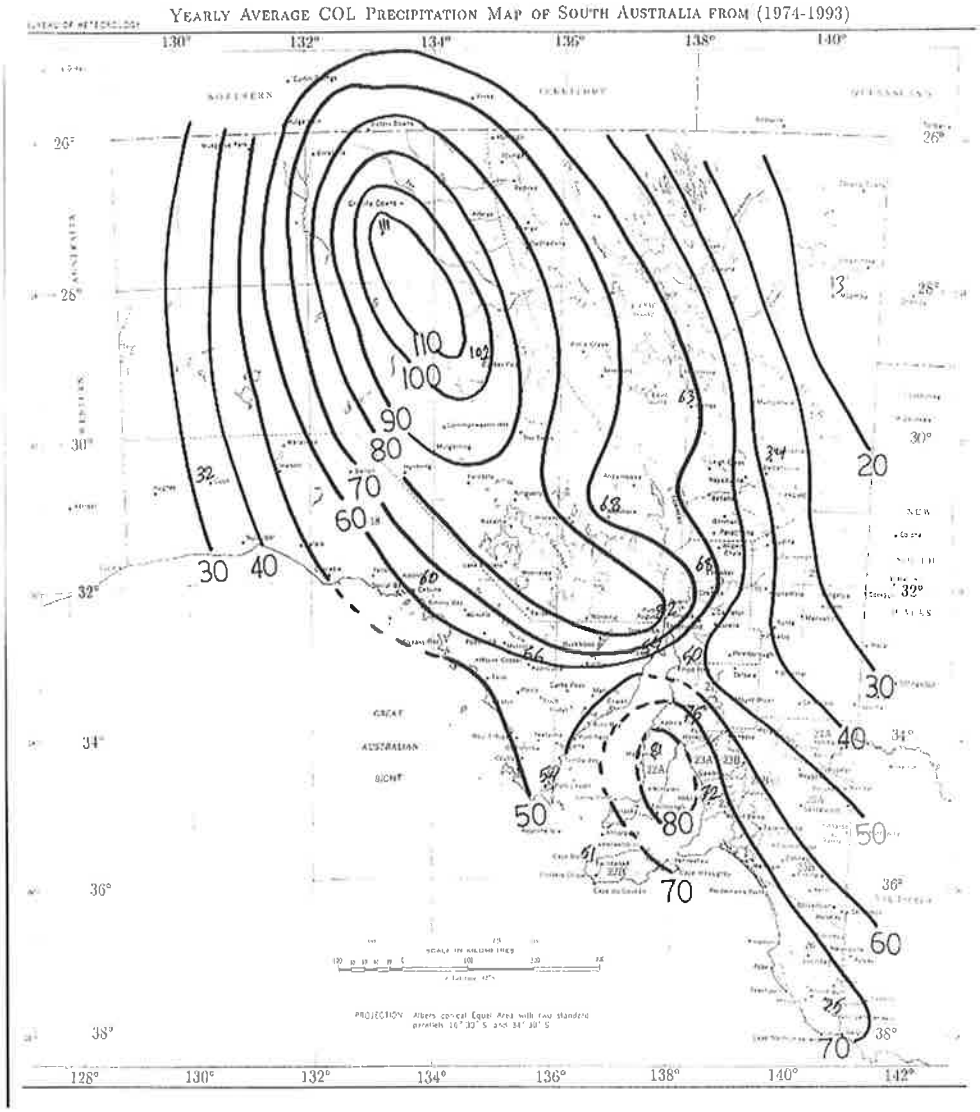

Figure 6.15: Yearly Cut-off Low Precipitation Map of South Australia from 1974-1993.

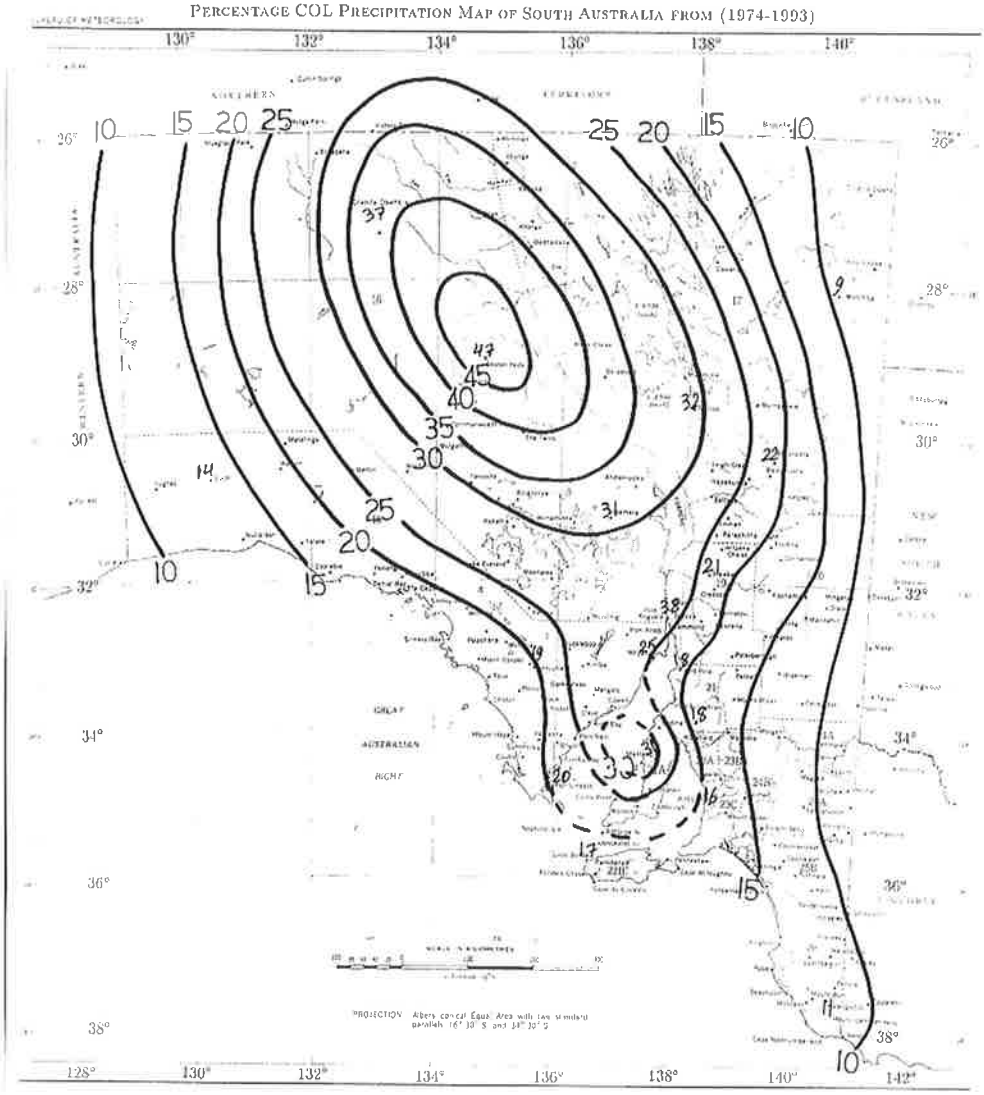

Figure 6.16: Percentage Cut-off Low Precipitation Map of South Australia from 1974-1993.

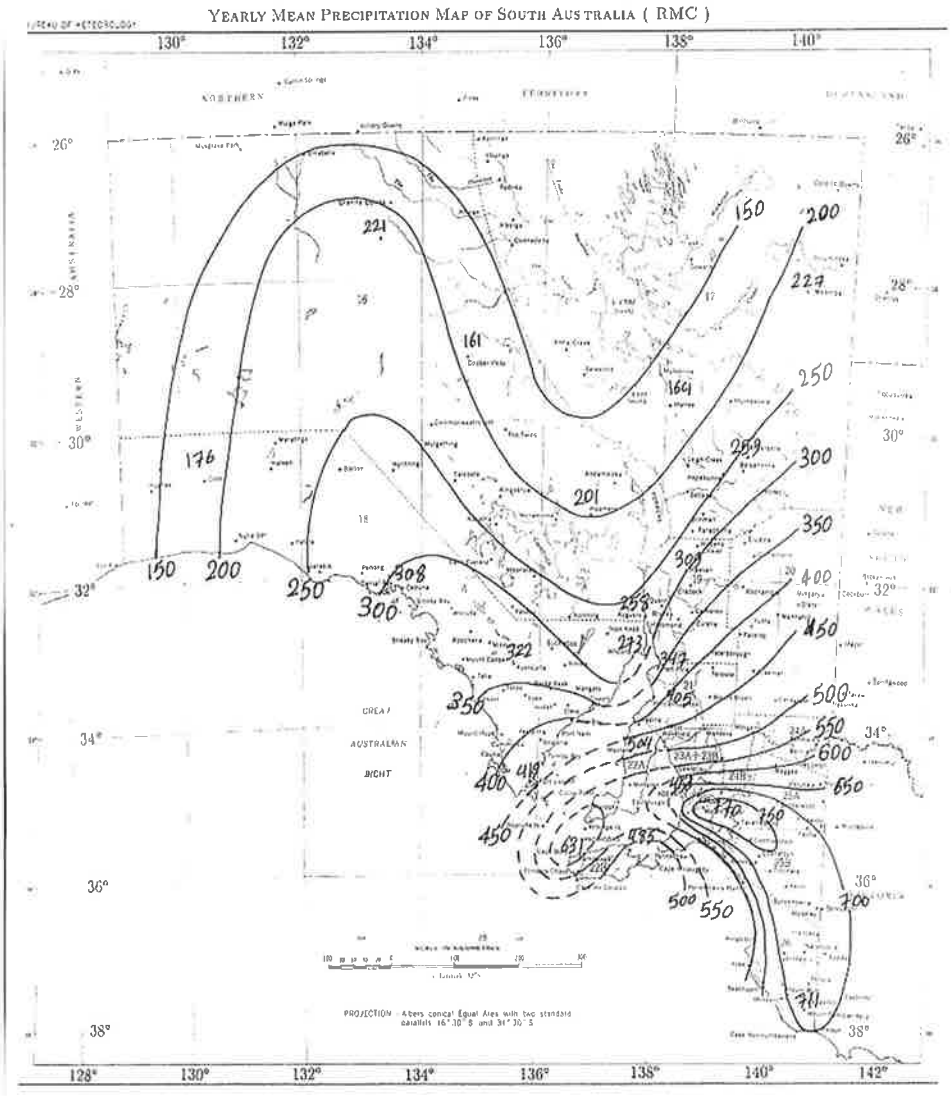

Figure 6.17: Yearly Mean Precipitation Map of South Australia from the Regional Meteorological Centre (RMC).

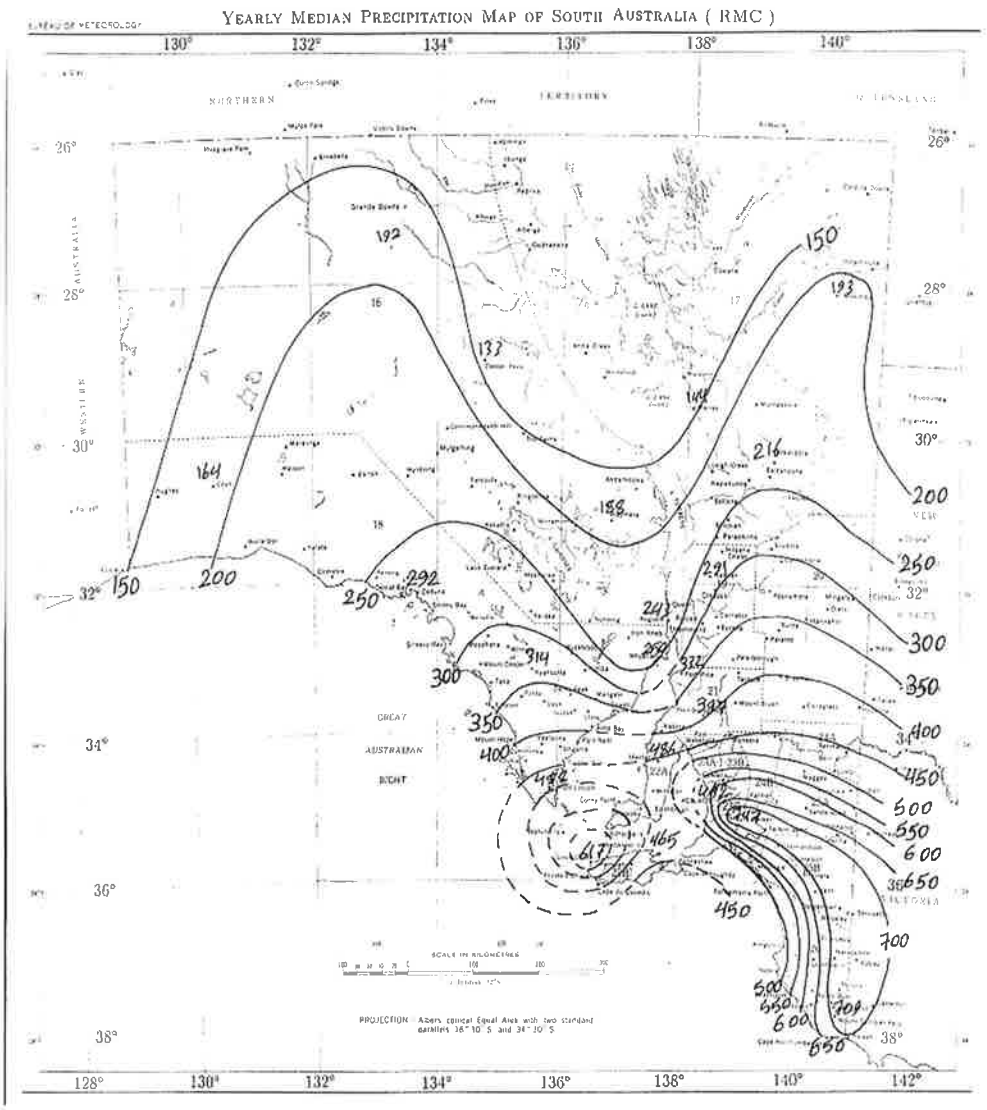

Figure 6.18: Yearly Median Precipitation Map of South Australia from the Regional Meteorological Centre (RMC).

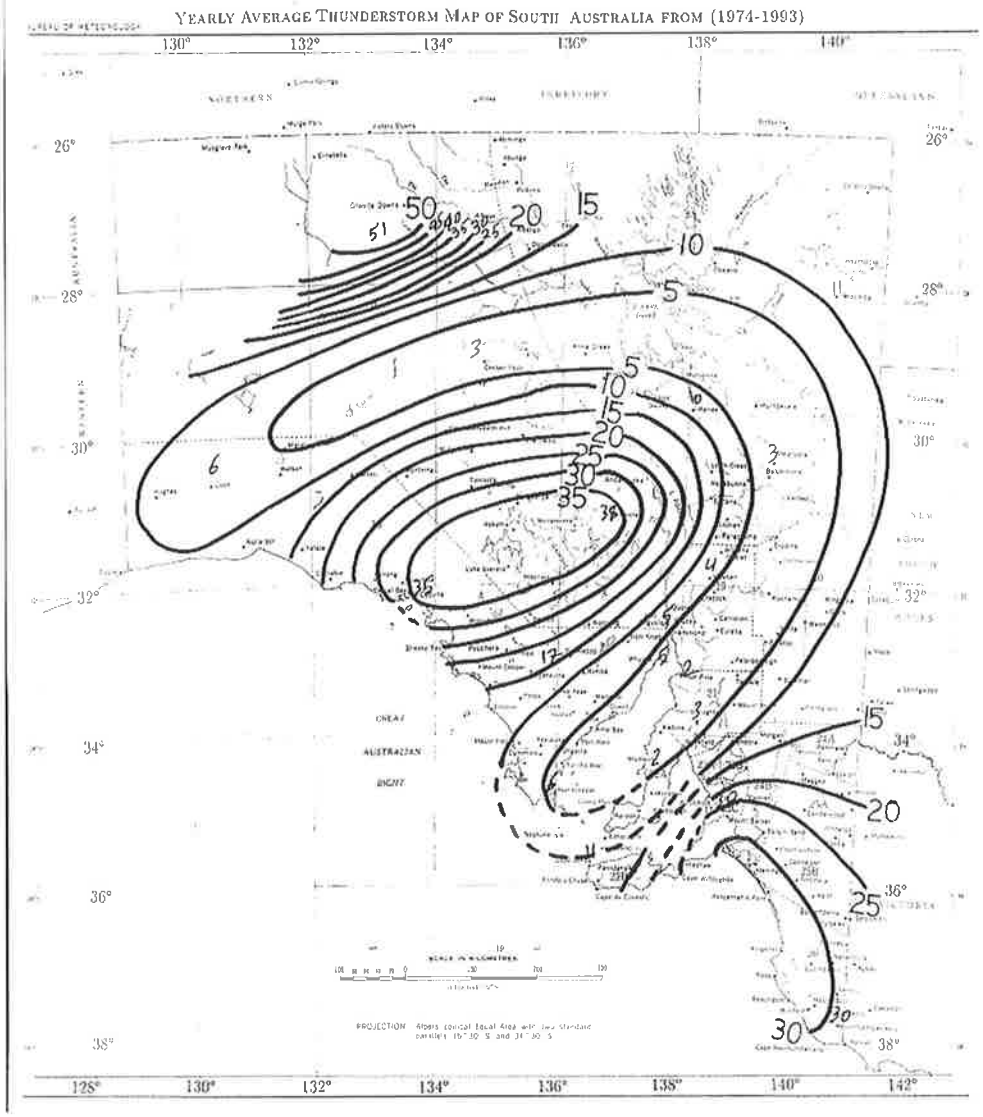

Figure 6.19: Yearly Average Thunderstorm Map of South Australia from 1974-1993.

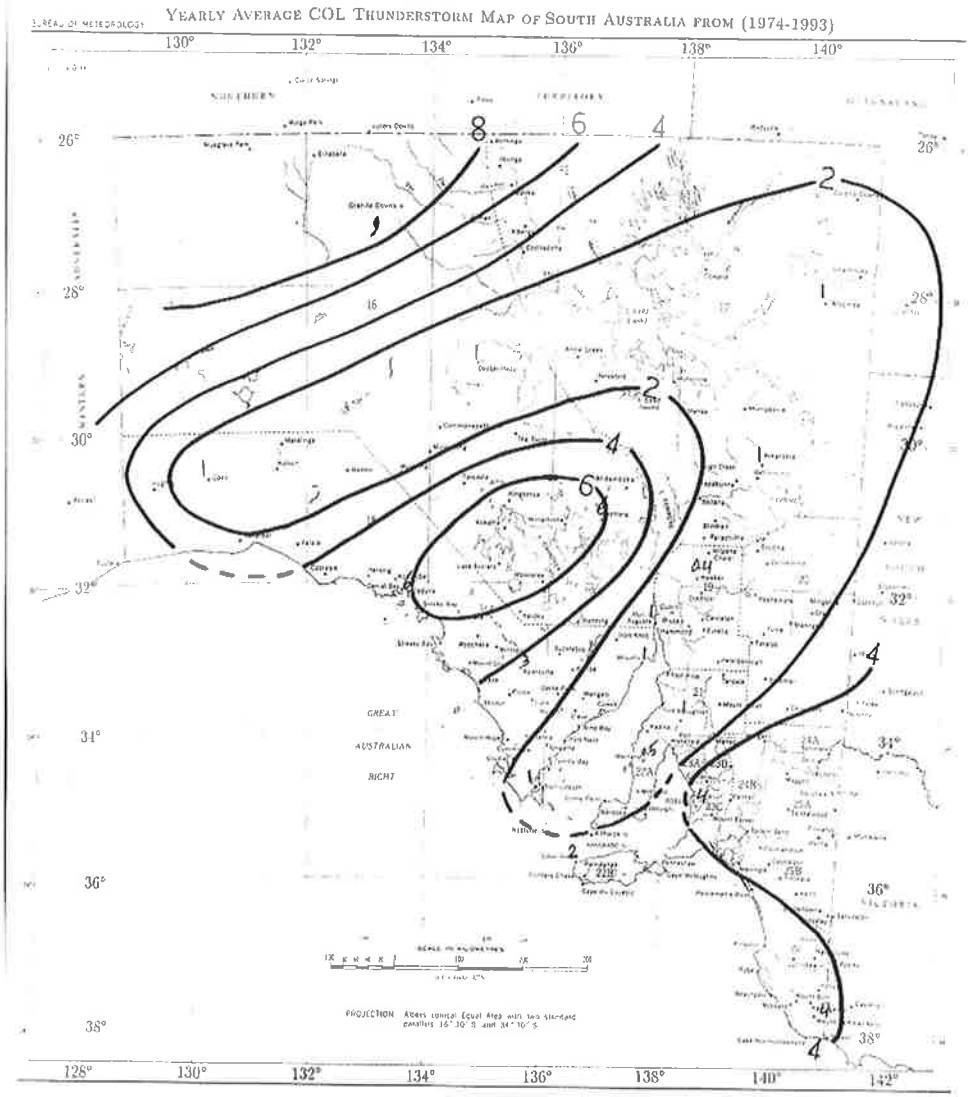

Figure 6.20: Yearly Average Cut-off Low Thunderstorm Map of South Australia from 1974-1993.

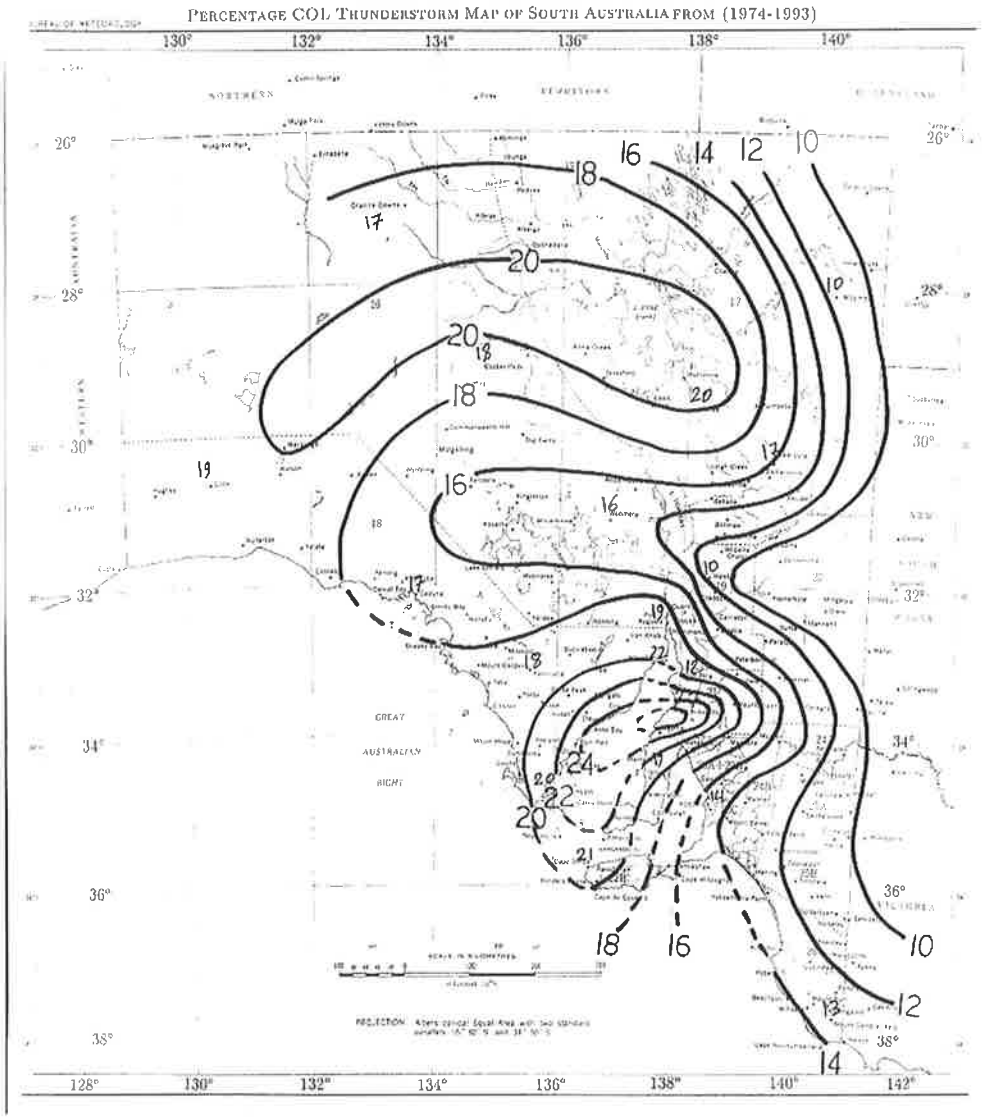

Figure 6.21: Percentage Cut-off Low Thunderstorm Map of South Australia from 1974-1993.

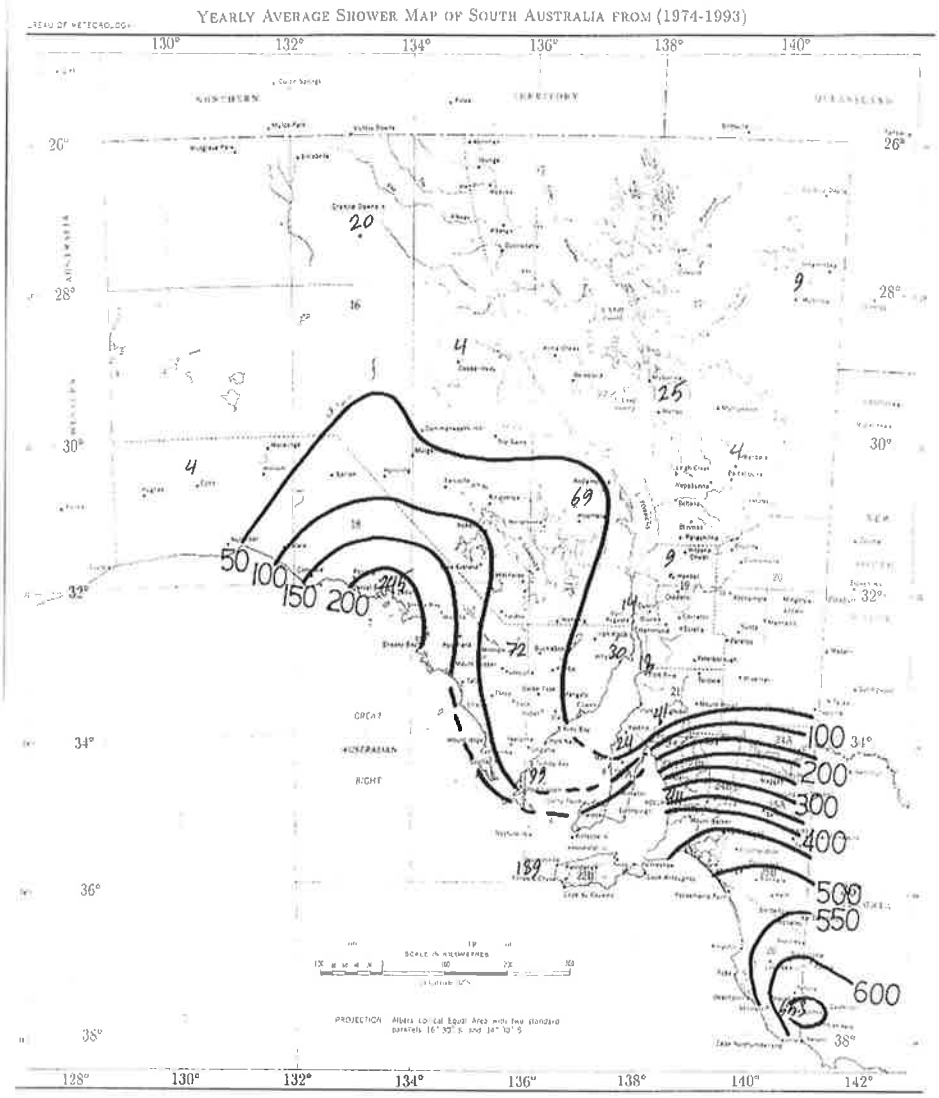

Figure 6.22: Yearly Average Shower Map of South Australia from 1974-1993.

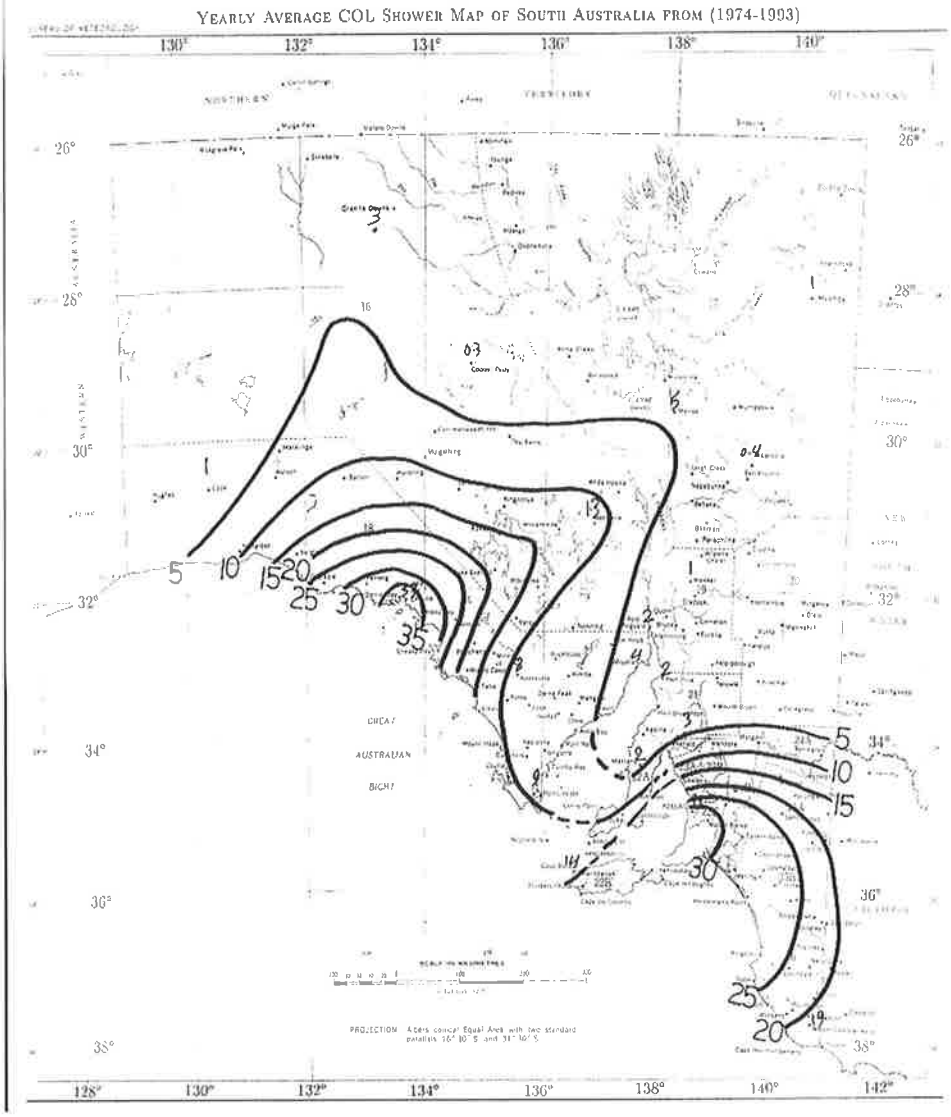

Figure 6.23: Yearly Average Cut-off Low Shower Map of South Australia from 1974-1993.

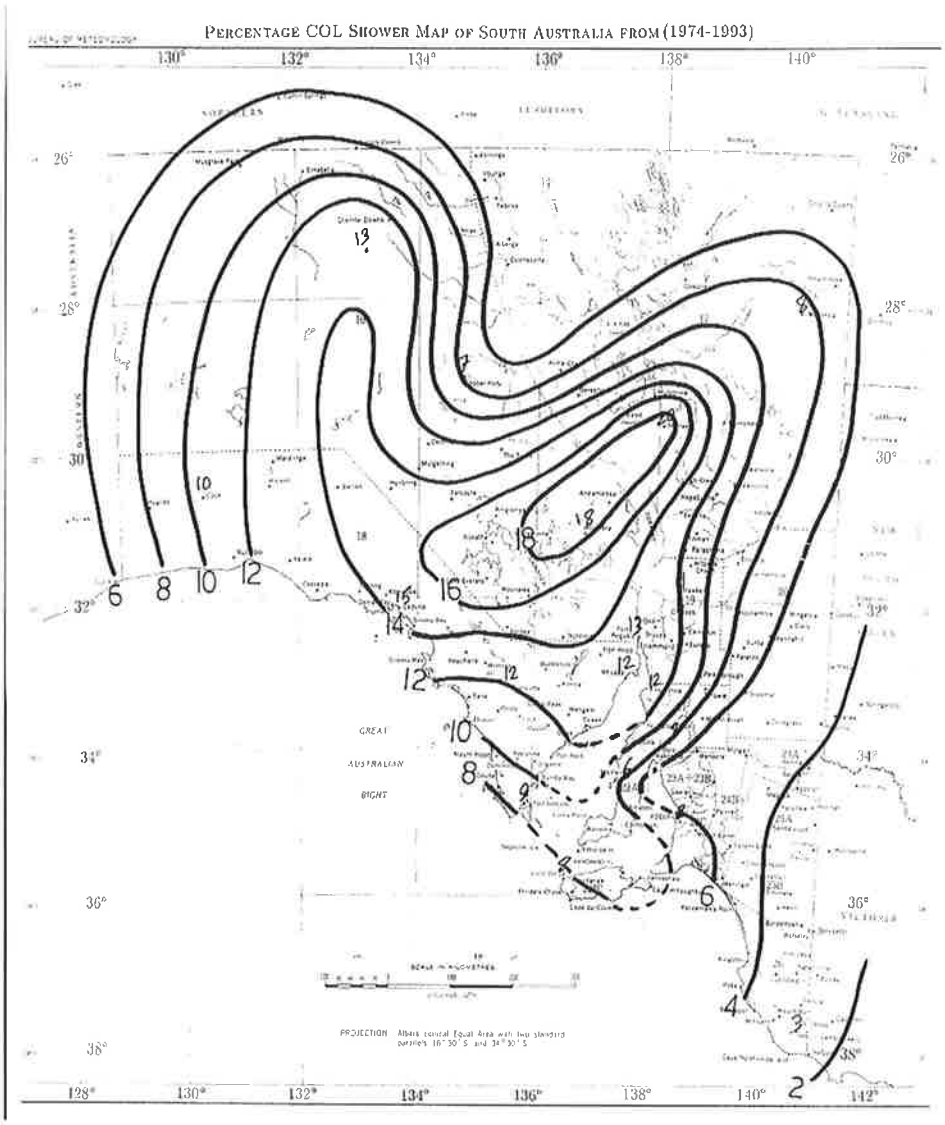

Figure 6.24: Percentage Cut-off Low Shower Map of South Australia from 1974-1993.

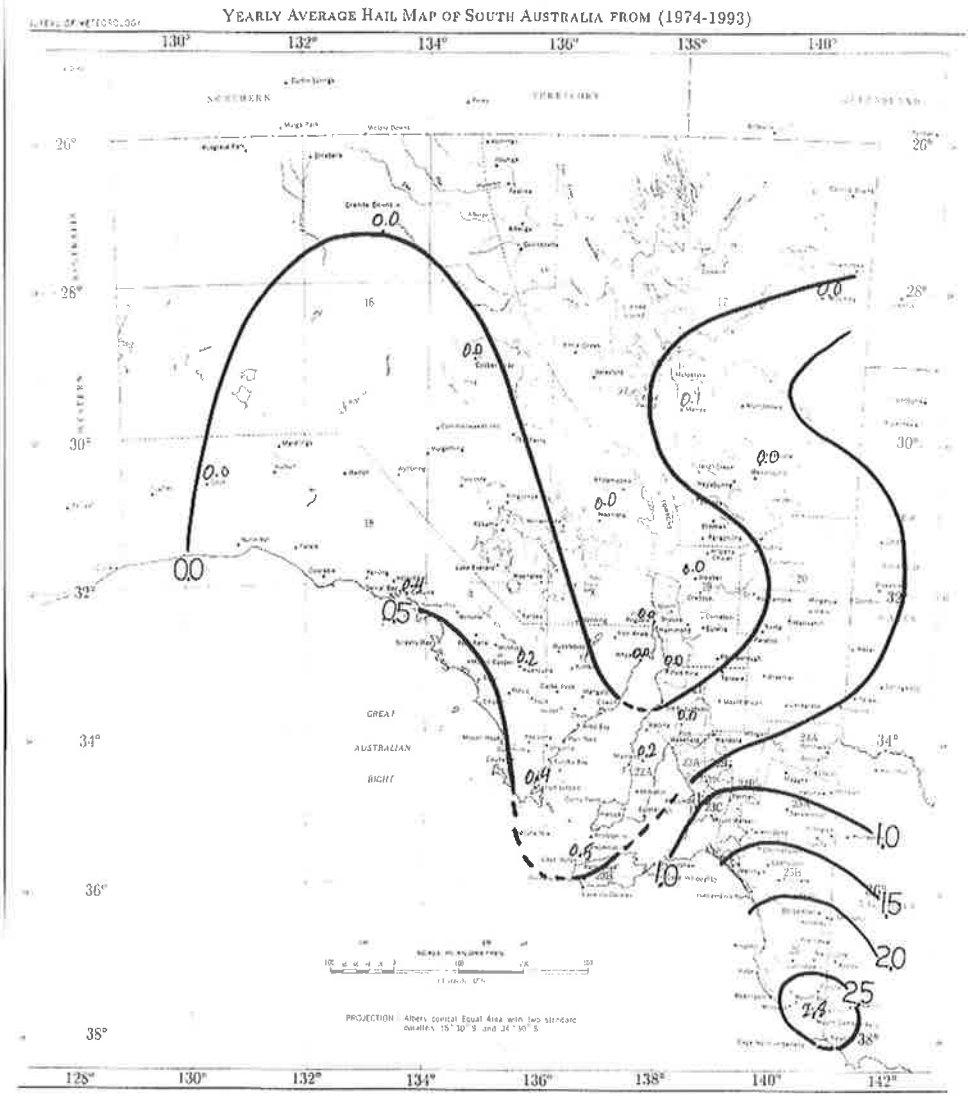

Figure 6.25: Yearly Average Hail Map of South Australia from 1974-1993.

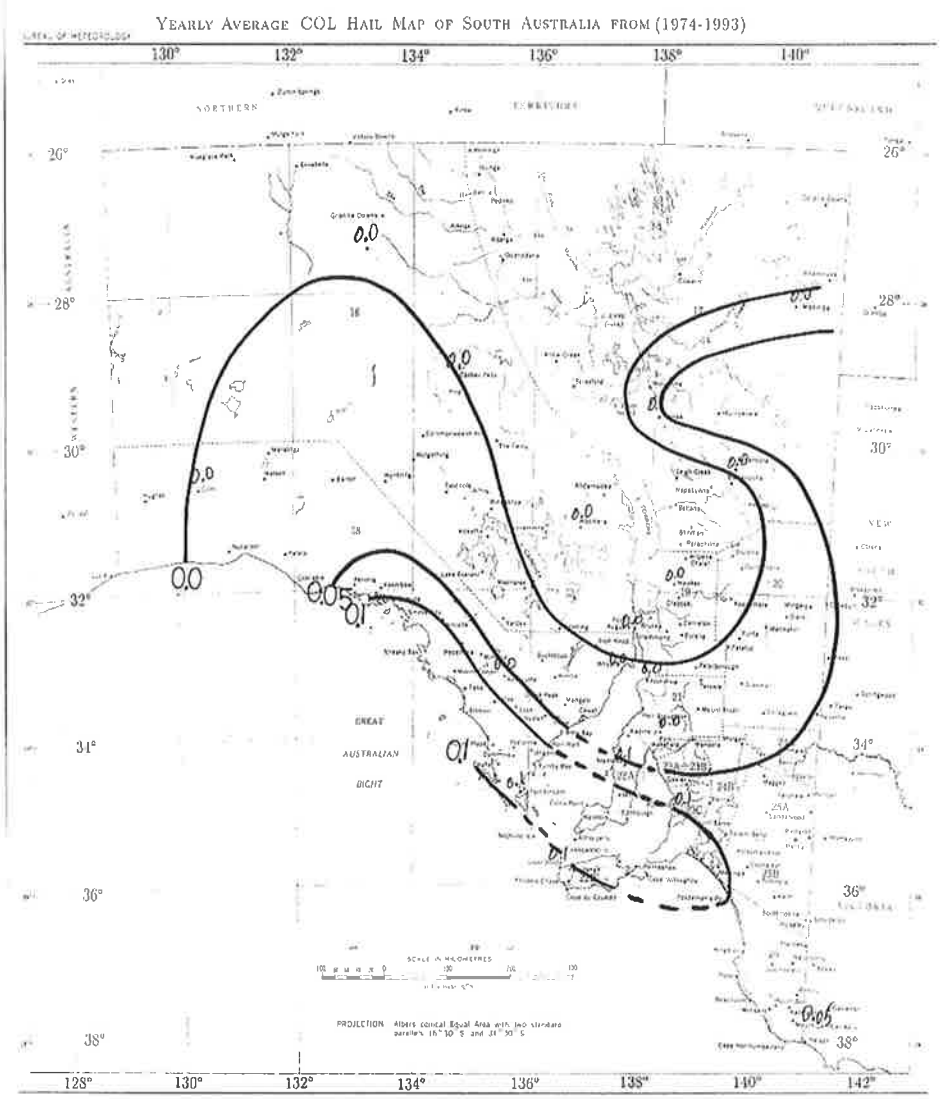

Figure 6.26: Yearly Average Cut-off Low Hail Map of South Australia from 1974-1993.

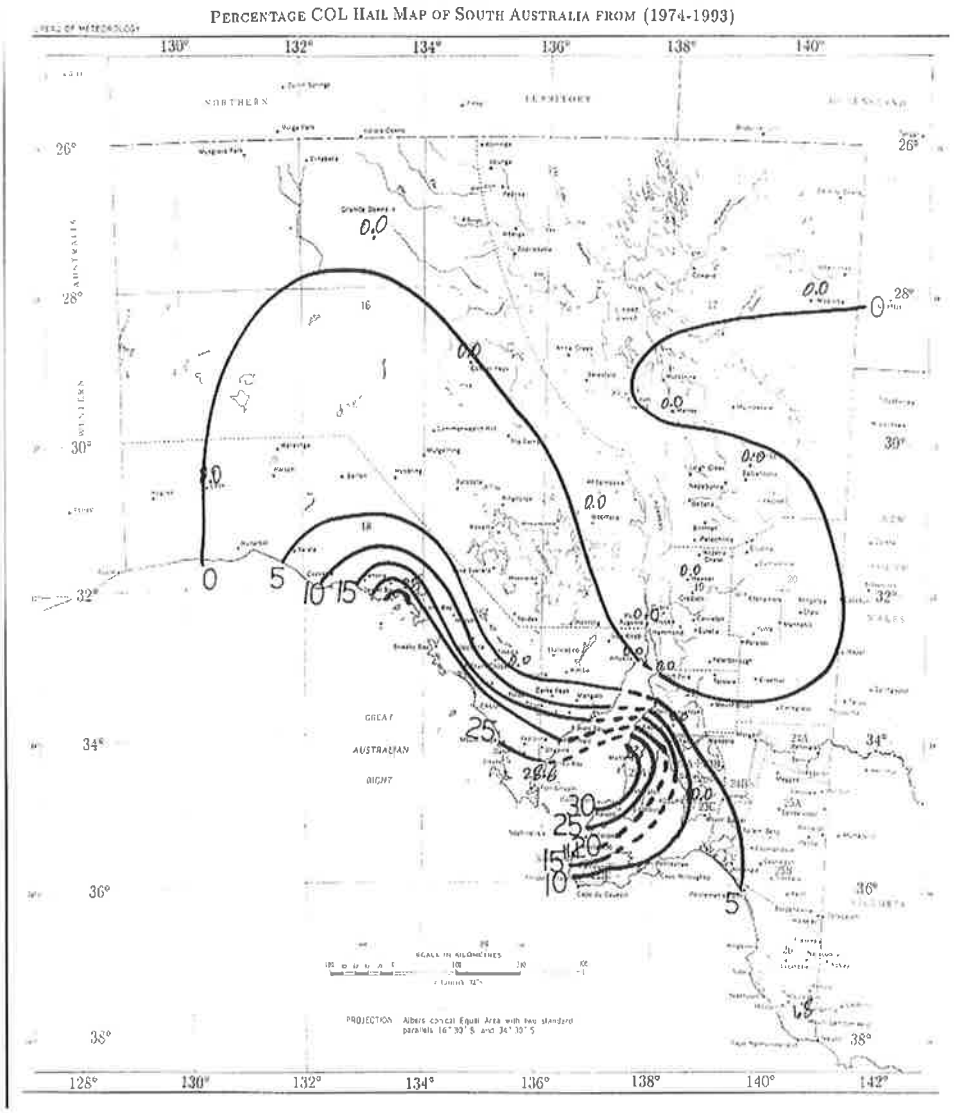

Figure 6.27: Percentage Cut-off Low Hail Map of South Australia from 1974-1993.

Chapter 7

Wind Profiler Observations of a Cut-off Low over South Australia

7.1 Introduction

Upper air weather analysis in the Australian region has been based on rawinsondes ascents and therefore is focused on synoptic scales. Satellite measurements, such as TOVS thermodynamic retrievals and cloud drift winds, have been assimilated into numerical analysis schemes and add significant mesoscale features. An emerging technology that provides high temporal and height resolution wind data is the radar wind profiler. Of particular note here is the NOAA demonstration network that has provided mesoscale data, both in analysis [*Spencer et al.*, 1996] or with improved numerical guidance.

The Bureau of Meteorology has been receiving real time data from a profiler in Darwin and occasionally from the University of Adelaide's research radar at Buckland Park. However, both of these are research radars. The Bureau has been evaluating an operational prototype wind profiler at Mt Gambier in 1998.

The purpose of this investigation is to take some research data from the Adelaide profiler and analyse the data using tools that will be available to the forecaster. It also illustrates some of the potential and helps develop operational techniques to utilize the profiler data. This elucidates the mesoscale structure embedded within cut-off lows. It is this mesoscale structure that is most closely associated with weather elements.

To date, much of the published profiler-based studies of mid-latitude systems have focused on fronts. Examples of these include the detailed structure of a front near the frontal head [*Shapiro et al.*, 1985], observations of Australian fronts linked to the Cold Fronts Program conceptual models [*Wilson and Stern,* 1985; *Ray and Wilson*, 1985; *Ray et al.*, 1985; *Ray et al.*, 1989; *May et al.*, 1990], upper level fronts [*Larsen and Röttger* , 1982], and the structure of upper level baroclinic waves and jet streaks [*Neiman et al.*, 1991]. Until recently, relatively few papers have focused on forecast applications, with the notable exception of *Beckman* [1990] where profiler and satellite data were used to distinguish mesoscale development and assess the departure of systems from numerical forecasts, and the diagnostic study of *Spencer et al.*, [1996]. These profiler studies of mid-latitude storm systems highlight mesoscale structure.

Wind profilers are becoming operational instruments (e.g. NOAA demonstration network). Even single instrument provides unique mesoscale data that effect subsequent weather evolution, which is often associated with mesoscale structure. This study focuses on cut-off lows, fronts, and troughs which are often associated with severe weather [e.g. *Mills & Russell*, 1992].

7.2 Data Sources

In order to study cut-off low systems as by the wind profiler data, operational analyses from 1991-1995 were examined and 7 well defined cases of cut-off lows were found. Of these, 3 significant cases were selected for detailed study as they had reasonably complete data. This will be discussed in chronological order. The operational parameters of the Buckland Park radar in Doppler (DBS) and spaced antenna (SA) modes were as summarized in Table 3.1.

In order to study the synoptic characteristics of the cut-off lows, the operational 3-hourly MSL charts (except 1500 UTC) as well as 12-hourly upper air charts (i.e. 850 hPa, 700 hPa, 500 hPa and 300 hPa) of the South Australian Regional Forecasting Centre (SARFC) were examined for the relevant periods. These analyses were supplemented by three-hourly GMS Infrared satellite images over South Australia. Twelve-hourly radiosonde data from Adelaide Airport (34.58S, 138.32E) for the period of study were used to derive the temperature profiles and virtual potential temperature profiles.

7.3 Case Study I: 6-9 October 1992

A cut-off low over South Australia from 6th to 9th of October 1992 has been studied in this section from two points of view, focussing firstly on the synoptic behavior and then on the mesoscale characteristic.

In relevant figures of this chapter triangles are used to show the positions of minor troughs (T) and minor ridges (R).

7.3.1 Synoptic Discussion

Although the surface cut-off low seems to have originated from the north-western part of the Australian continent the upper air charts show (Figures 3&4, *AppendixB*), it is actually a high-latitude type. That is, it is an extratropical cyclone. It was located at 31.5S, 131.6E just off the shore of the Australian Bight at 1800 UTC 06 October (Figure 1a, *Appendix B*). At this time it was moving southwards at about $5\,m\,s^{-1}$. The vertical axis of the system was inclined towards the west, up to the tropopause. The vortex has closed contours at $850\,hPa$ and $700\,hPa$ (Figures $3A1\,\&\,3A2$, *Appendix B*). There was strong warm advection in the front and strong cold advection at the rear of the upper low producing a strong baroclinic zone over the surface level of the cut-off low (Figures $3A1$ *to* $3A3$, *Appendix B*).

On the satellite imagery, there are three almost parallel strips of clouds of which two were associated with the north-westerly flow and the third southeasterly (Figure 7.1). The eastern band (labeled C) is warm and moist and related to the jet-stream and consisted of mainly high clouds. The band labeled B is the warm conveyor belt (WCB) with high wet-bulb potential temperature (θ_w) or moist isentropes [*Harrold*, 1973] and extended from northwest to southeast and turned anticyclonically at the poleward end. The band labeled A is associated with air of the cold conveyor belt (CCB) [*Carlson*, 1980] with low θ_w and consists of mainly low and middle type of clouds.

There are many minor troughs and minor ridges as a wave train is embedded within the WCB cloud band of the cut-off low system. These minor troughs are similar to the wide precipitation bands analyzed by *Sanders and Bosart* [1985]. These minor troughs and ridges are seen in the satellite image (Figure 7.1). The wave train is clearly seen in the reanalysis of the MSLP charts (Figure 7.2). The minor troughs (demarcated by T) in Figure 7.2 are almost coincident with the

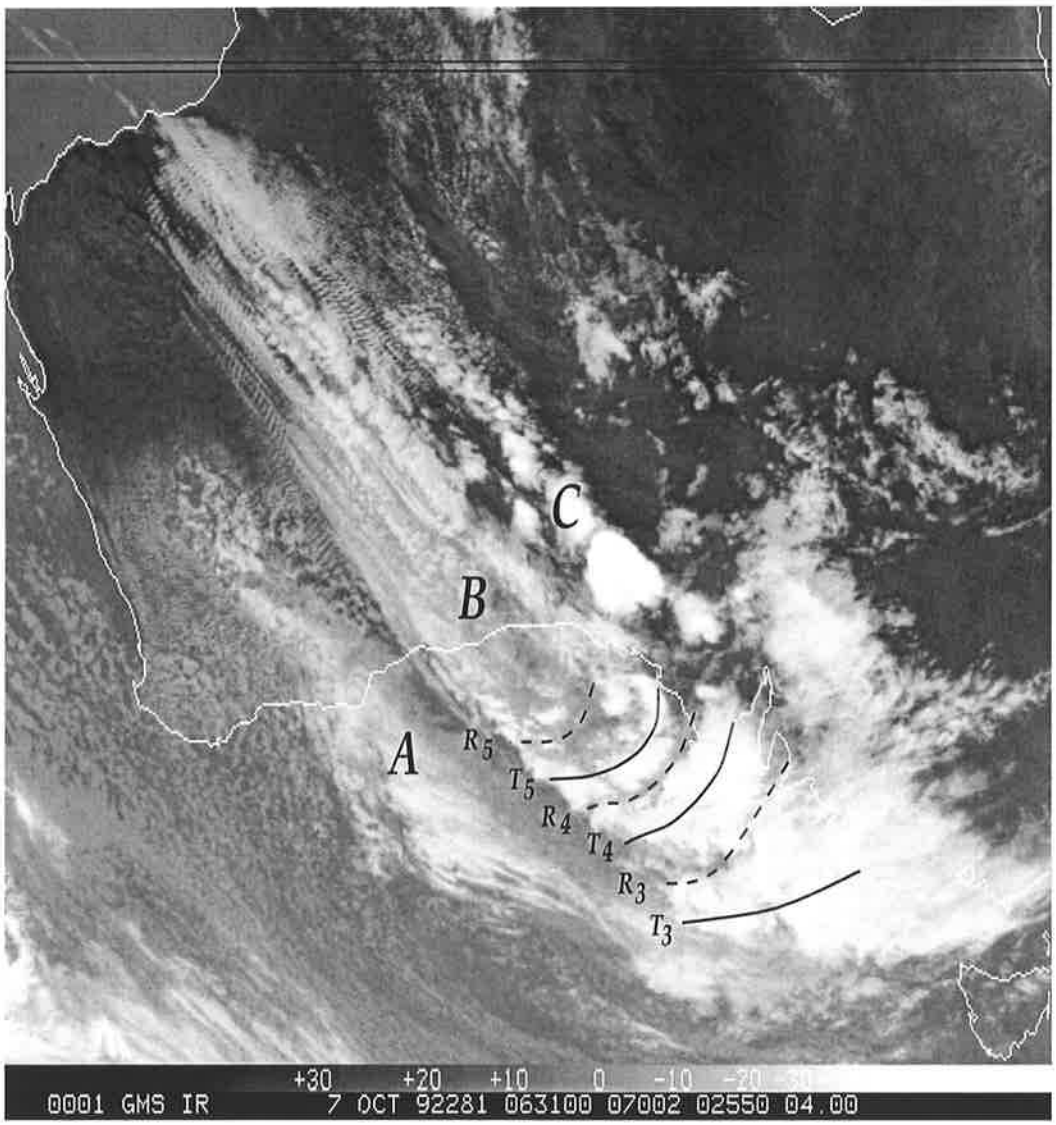

Figure 7.1: The GMS Infrared satellite imagery for 0631 UTC 07 October 1992. The letters A, B and C denotes the cloud band strips. The almost parallel lines demarcate the minor troughs (T) and minor ridges (R).

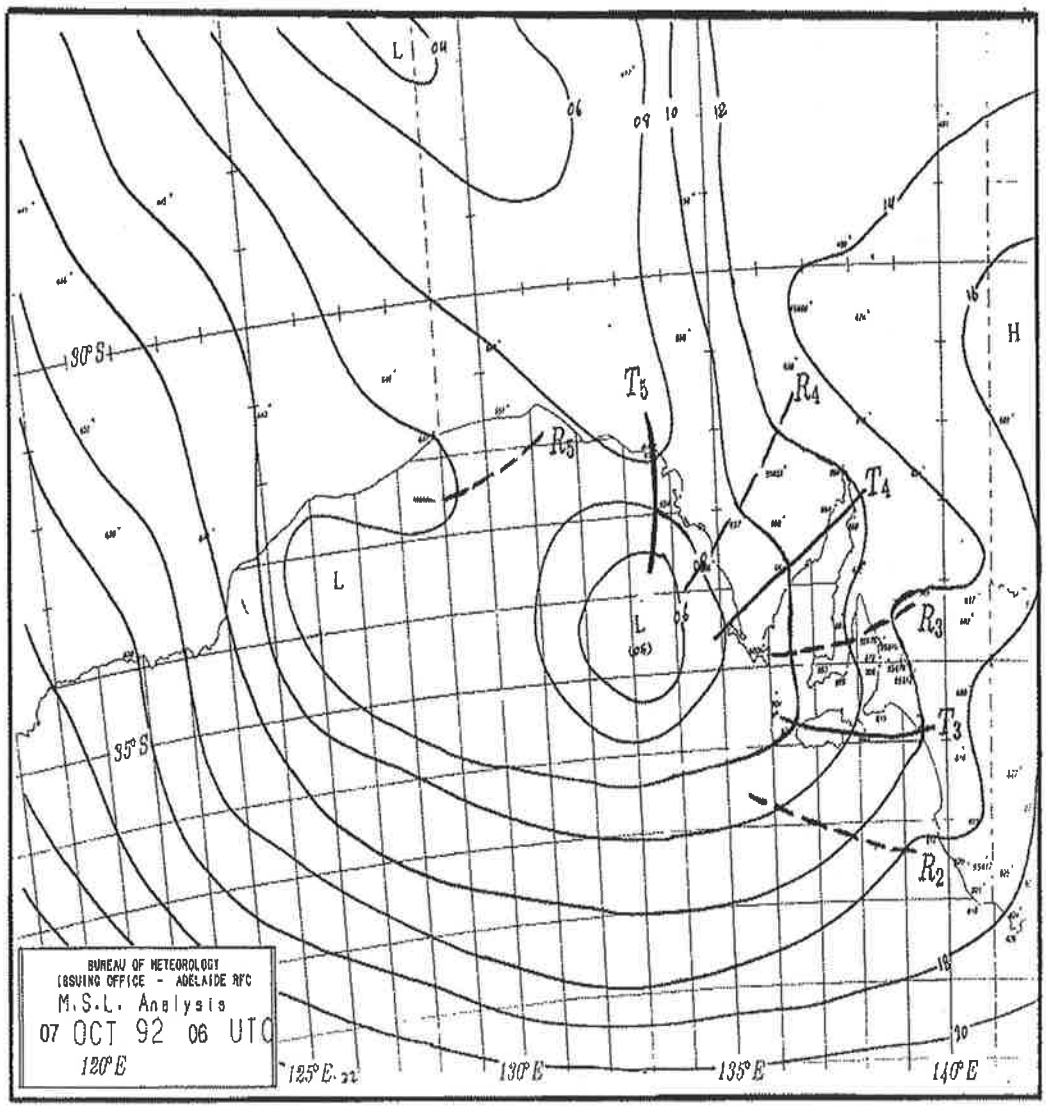

Figure 7.2: MSLP chart for 0600 UTC 06 October 1992. The minor troughs are shown by solid lines and minor ridges are shown be dashed lines appropriate to the above satellite image. The isobar intervals are 2 hPa.

minor cloud bands in the satellite image of Figure 7.1. Similarly, minor ridges (demarcated by R) in Figure 7.2 are almost coincident with the cloudless bands or shallow clouds of Figure 7.1. These series of minor troughs and ridges can be followed in the preceeding MSLP charts (Figures 1 and 2, *Appendix B*).

A jet-stream with a core speed of more than 70 $\mathrm{m\,s^{-1}}$, shown on the 300 hPa chart in Figure $3A4$, *AppendixB* is located on the northern side of the system over the closed 500 hPa contour. The isolated clouds over central Australia on the satellite image of 1831 UTC 06 October 1992 (*Appendix B*) is stretched towards southeast by this jet-stream. This band of cloud (labeled C in Figure 7.1) is clearly seen on image of 1831 UTC 07 October (*Appendix B*).

The front edge of the south-easterly cloud band (CCB) was coincident with the upper cold pool (CP) at 700 hPa and 500 hPa in Figures $3A2$ & $3A3$. This band gradually rotates clockwise (cyclonically), around the upper closed low over a surface weak low. The surface cut-off low was stretched horizontally to produce an elongated low with two centres, one of which is the main one and the other weaker and located underneath the rounded cloud at the western edge of CCB (Figures 1&2, *AppendixB*). This center is weak and nearly barotropic. In contrast, the main center is in a baroclinically favourable environment with respect to the upper low, and growing. Consequently, the rounded edge cloud which is visible on the satellite images is superimposed on this weak, barotropic low and weakening further.

The warm air wraps around, producing a main ridge to the eastern portion of the weak low. This in turn gradually separates the smaller vortex from the main parent low.

The trailing vortex of the surface cut-off low (WCB) passed over the profiler at about 0000 UTC 08 October for about 12 hours (demarcated MT & ST in

Figure 7.2), while the main center remained well south at about (39°S, 135°50′E). Although, at this stage there was no closed low analysed on the MSLP synoptic charts, the profiler horizontal wind data verified the existence and the passage of the system which was clearly shown on the satellite images (*Appendix B*). This is one of the capabilities of the profilers to show the existence of mesoscale vortices.

As Figures 3 & 4, *Appendix B* shows, on the lower tropospheric charts, there was a cold advection[1] ahead and warm advection in the rear of the east cloud band (labeled C in 7.1), producing the reverse solonoids and hence, slowing down its movement and consequently, merging with the WCB band (labeled B).

At the next stage the edge vortex was being weakened and filled out whilst another vortex was being generated at the triple point (defined as: where, CCB intersects WCB marking the cold front, the warm front and the occluded front). This process of filling up the tip vortex and regeneration of a new vortex is clearly shown on satellite imagery of 1231 UTC 08 October and 1831 UTC 08 October (*Appendix B*), respectively. The sequence of dissipation and regeneration of new vortex seems to be continued as long as there is baroclinicity and feeding the system. This is happening while the vertical axis of the main system is tilted backward (i.e. westwards) causing the positive absolute vorticity advection over the surface cut-off low. Should the vertical axis turns forward (i.e. towards east), the negative absolute vorticity advection superimposes over the surface cut-off low and the whole system fills out. To illustrate the cloud bands and also the dissipation and regeneration of new vortex, all satellite images are shown in Appendix B.

To determine the minor waves on the surface charts, the MSLP charts and

[1]Normally, advections on the isobaric charts are determined from the intersections of isotherms and contour lines and also the strength of advection is proportional to the intersecting angle.

upper air charts (i.e. $850\,hPa$, $700\,hPa$, $500\,hPa$ and $300\,hPa$) have been reanalysed with more detail for this case study period. Surface data over the land, in which there are sufficient data available, clearly shows the existence of the short waves, as are seen in the surface reanalysis charts of Figures 7.2 and also Figures 1 & 2, *Appendix B.*

7.3.2 Mesoscale Discussion

This section focuses on the mesoscale structure of the cut-off low, and in particular on the presence of short-waves on the main trough and the weather associated with them.

In the case of the closed low (e.g. cut-off low), it may be expected that there is upward vertical motion everywhere within the low. However, as the wind profiler hourly-averaged vertical velocity data illustrate (Figure 7.3) there are sequences of upward and downward motion during the passage of the cut-off low.

These are caused by small waves embedded within the cut-off low. These small waves produce minor troughs and minor ridges which are responsible for the aforementioned updrafts and downdrafts, respectively. Although the horizontal wind velocity measurements of the profiler start from on average $2\,km$, the waves are visible in the horizontal wind time-height cross-section (Figure 7.4).

Normally, during the synoptic analysis of the system, most of the shallow waves are smoothed out. However, they can be easily distinguished by the profiler vertical velocity analysis.

A word of caution is needed when considering vertical velocities. When there is precipitation, the wind profiler may detect echoes from the precipitation as well as the clear air and consequently, the vertical velocity is biased [*Atlas,* 1973; *Fukao et al.*, 1985; *Wakasugi et al.*, 1986; *Wakasugi et al.*, 1987; *Steiner and Waldvogel,*

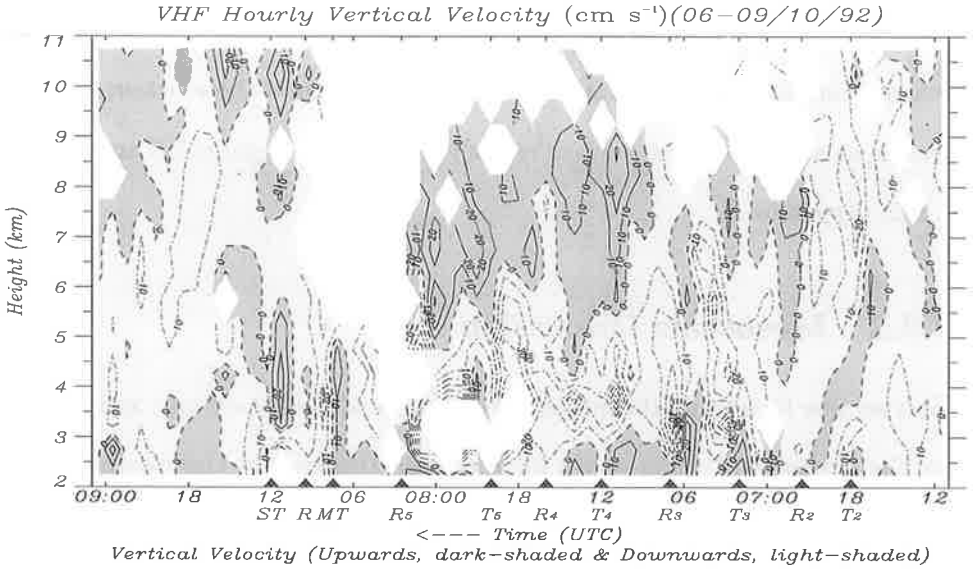

Figure 7.3: VHF hourly vertical velocity ($cm\,s^{-1}$), Upwards (solid, dark-shaded), Downwards (dash-dotted, light-shaded), for 6-9/10/1992. The triangles show the positions of minor troughs (T) and minor ridges (R).

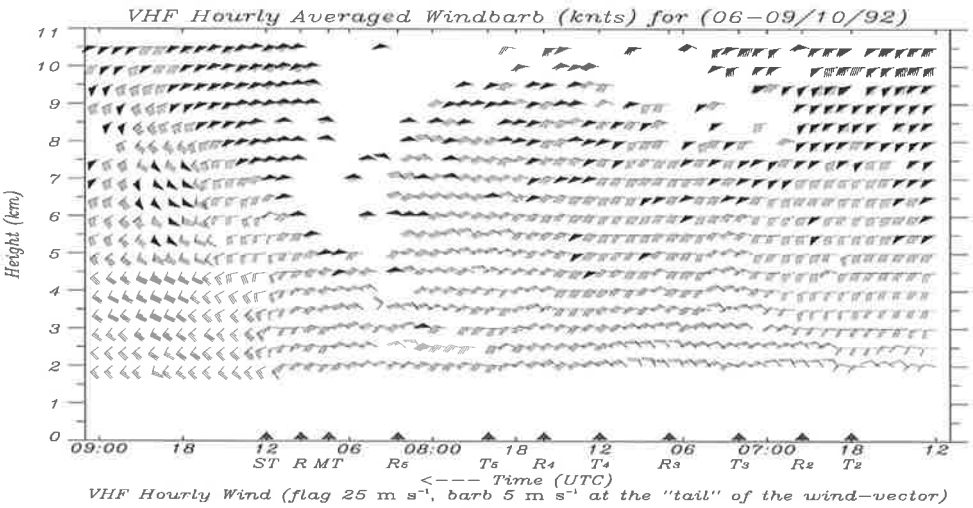

Figure 7.4: Reverse time-height cross-section of the profiler spaced-antenna wind field, displayed as windbarbs (flag $25 m\,s^{-1}$, barb $5 m\,s^{-1}$and half-barb $2.5 m\,s^{-1}$at the "tail" of the wind -vector) for 6-9/10/1992.

1987; *Gossard,* 1988; *Gossard et al.,* 1990; *Sato et al.*, 1990; *Rajopadhyaya et al.,* 1993]. These precipitation echoes can be used to retrieve raindrop and ice size distributions, but it is difficult to do this in real-time because of computational constraints.

Comparison of the time-height cross-section of one hourly averaged vertical velocity of the profiler (Figure 7.3) with the MSLP charts reveals the link between the series of minor ridges and troughs with the vertical motions measured by the Buckland Park wind profiler so that, ridges produce downward motion and troughs produce upward motion.

There is a minor trough (Figure 1a, *Appendix B*) at about 1800 UTC 06/10/92 (T_2) with updrafts to about 7km. A minor downdraft which is seen at T_3 in Figure 7.3 seems to occur as a result of precipitation echoes. A minor ridge (Figure 1b, *Appendix B*), with the downdraft associated with it to high levels passed at about 2130 UTC (R_2). An intense trough (Figure 1d, *Appendix B*) passed over the profiler at about 0200 UTC 07 October (T_3) with again apparent downdrafts from rain droplets at about 3 km. This trough continues to about 0600 UTC. A strong ridge (Figure 1e&1f, *Appendix B*) followed this trough (R_3) at about 0700 UTC. A trough (Figure 1g, *Appendix B*) with the contamination from precipitation in the lower troposphere passed over at about 1200 UTC on the same day (T_4), followed by a ridge (R_4) about 4 hours later (Figure 1h, *Appendix B*). At about 4 hours later (Figure 2i, *Appendix B*) a trough (T_5), preceding a ridge (Figure 2j & 2k, *Appendix B*) at about 0230 UTC 08 October (R_5), passed through. The passage of the main trough (Figure 2l, *Appendix B*) started from 0700 UTC 08 October onwards (MT) associated with the heavy rain, with a break from a minor ridge (R) about 2 hours later (Figure 2m, *Appendix B*). Finally, a secondary trough (ST) with high vertical velocity marks the passage of the cut-off low by about

1200 UTC 08 October 1992 (Figure 2*n*, *Appendix B*).

The minor waves are separated by periods ranging from a couple of hours to a few hours. Obviously, the longer the wavelength, the larger the duration of the waves.

A time-height cross-section of the one-hourly averaged profiler horizontal wind, Figure 7.4, shows the larger duration waves very well. Passage of the trailing vortex of the cut-off low was illustrated on profiler horizontal wind data in Figure 7.4. As it is shown the wind directions are changing cyclonically as a result of the passage of the main trough (*MT*) and secondary trough (*ST*). This is illustrated clearly in Figure 7.5, where the wind directions change from southerly to northerly component.

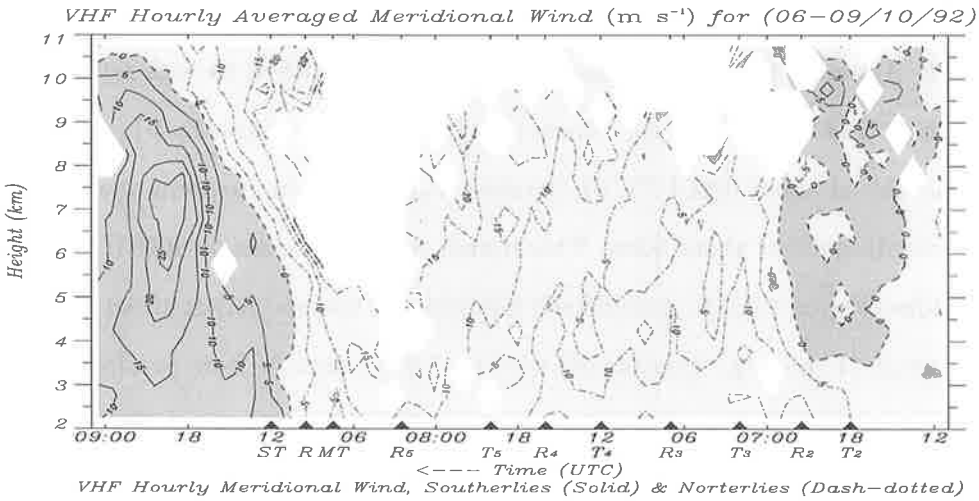

Figure 7.5: Profiler hourly-averaged meridional wind ($m\ s^{-1}$) for 6-9/10/1992. Southerly components are in solid or dark-shaded and northerly components are in dash-dotted or light-shaded.

If the high level clouds warrant, satellite images can clearly show the existence of short waves within the main cloud bands. The existence of minor troughs and ridges on the satellite images are exhibited by strips of bright and dark regions,

respectively (Figures 5 to 15, *Appendix B*). As an example, at 0631 UTC image of 07 October, Figure 7.1, the sequence of waves can easily be distinguished with the help of surface analysis and profiler data.

Figure 7.6 shows that the CCB cloud band which has easterly direction has not passed over the profiler, as there is no easterly component of wind. It is located south of Adelaide over the Ocean. The average zonal wind confirms the passage of only WCB over the profiler.

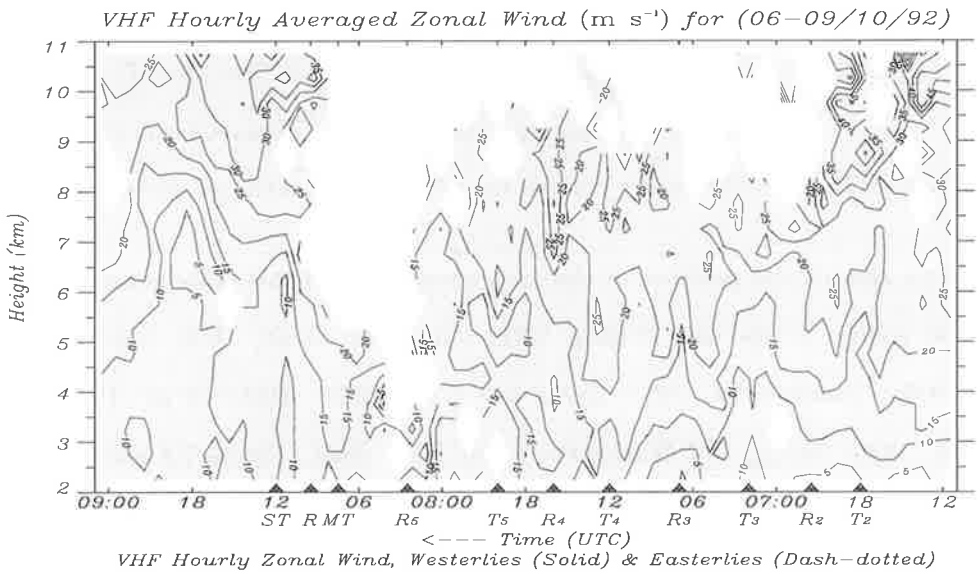

Figure 7.6: Profiler hourly zonal wind ($m\ s^{-1}$) for 6-9/10/1992 with westerly components, solid and easterly components, dash-dotted.

The location of a jet-stream equatorward of the cut-off low is very important for the development of the cyclone. An isotach analysis of the wind profiler (Figure 7.7) shows the existence of a jet-stream with the core speed of more than $50\,m\,s^{-1}$ meandering around the cut-off low and extending down as low as about $5\,km$. This jet-stream is also illustrated on $300\,hPa$ charts of figures $3A4$ & $3B4$ & $4C4$ & $4D4$.

Enhancement(s) of the returned power or signal-to-noise ratio of the profiler

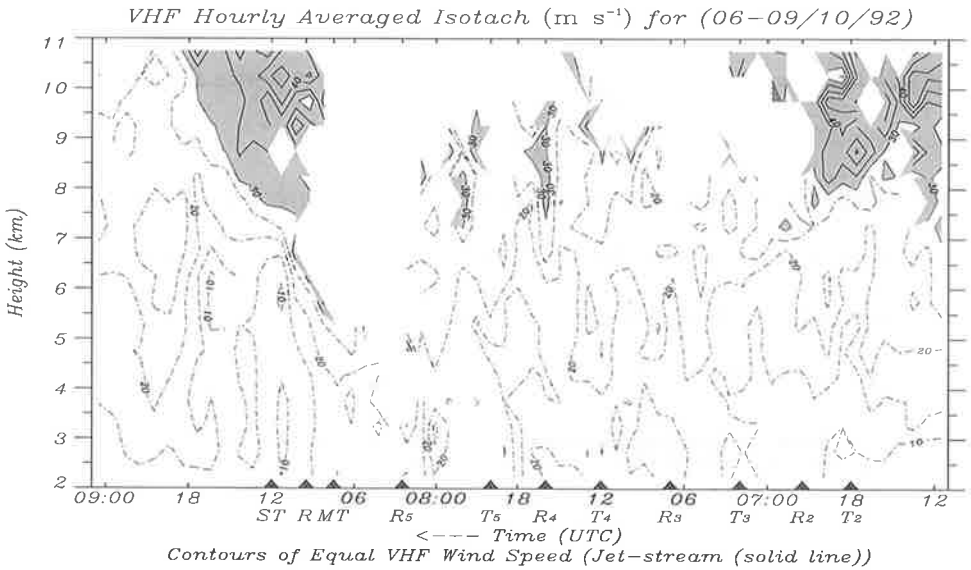

Figure 7.7: Profiler hourly isotach for 6-9/10/1992, with jet-stream level, solid.

data reveals the position of the tropopause or multiple tropopauses in a vertical column [*Gage and Balsley,* 1978; *Gage and Green*, 1979; *Gage and Green*, 1982a; *Riddle et al.*, 1983; *Green and Gage,* 1984; *Riddle et al.*, 1984; *Gage et al.*, 1986; *Sweezy and Westwater*, 1986; *Low,* 1996]. Figure 7.8 shows both, the profiler estimates of the tropopause height and rawinsonde tropopause measurements are consistent. The reduction in the height of the tropopause is one of the characteristics of a cut-off low. This is illustrated in Figure 7.8. As it is shown, the tropopause declines to about 8 *km* over the cut-off low vortex to exhibit the "tropopause funnel" in Figure 7.8.

7.3.3 Retrieval of Horizontal Temperature Gradients and Advections

Vertical wind shears measured by the Buckland Park VHF Doppler wind profiler were used in conjunction with the geostrophic thermal wind equation to retrieve

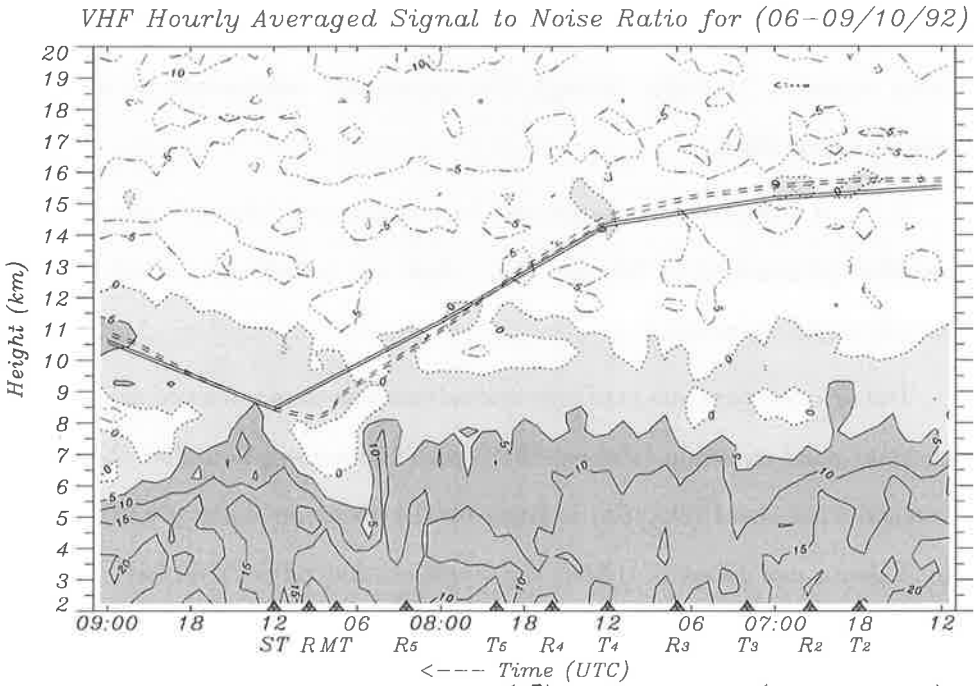

Figure 7.8: Profiler hourly Signal to Noise Ratio for 6-9/10/1992, positive, solid and negative, dash-dot-dot-dotted, as well as Tropopause (rawinsonde, double-solid & profiler, double-dashed).

the horizontal thermal gradients and associated advections for our three cases studies. The single station thermal retrieval technique has been utilized for many years using twice-daily rawinsonde wind measurements [*Oliver and Oliver*, 1945; *Saucier*, 1955] but not with the vertical and temporal resolution offered by wind profilers. In quasi-balanced flow regimes, this simple thermal retrieval technique can aid the operational community by monitoring baroclinic features and associated temperature advections on an hourly basis, rather than on a 12-hourly[2] basis currently available through the operational rawinsonde network [*Neiman and Shapiro*, 1989].

It is in regions of concentrated baroclinity and thermal advections where weather phenomena of interest (i.e. clear air turbulence, clouds and precipitation) most often occur.

Isobaric temperature gradients and advections were retrieved using the geostrophic thermal wind equation [*Holton*, 1979] with the assumption that the geostrophic vertical wind shear ($\partial v_g/\partial p$) is given by the observed shear ($\partial v/\partial p$). According to *Neiman and Shapiro*, [1989], the single-station retrieval isobaric temperature gradient $\nabla_r T$ can be expressed as

$$\nabla_r T(z,t) = \frac{f\overline{p}}{R}\widehat{k} \times \frac{\overrightarrow{V}[p(z+\Delta z,t),t] - \overrightarrow{V}[p(z-\Delta z,t),t]}{p(z+\Delta z,t) - p(z-\Delta z,t)} \qquad (7.1)$$

where $\overrightarrow{V} = \widehat{i}u + \widehat{j}v$ and the profiler winds measured in height coordinates were expressed as a function of pressure using the standard atmosphere (*Appendix A*), R is the gas constant ($287\,J\,kg^{-1}\,K^{-1}$); f the Coriolis parameter at -35 degrees latitude ($\sim -8.36504e-05\,s^{-1}$), $\overline{p} = [p(z+\Delta z,t) + p(z-\Delta z,t)]/2$, the mean-layer pressure; $\widehat{i}$, $\widehat{j}$ and $\widehat{k}$ are unit vectors along zonal, meridional and vertical

[2]Sometimes, 24-hourly.

directions, respectively; $\nabla_r T = \widehat{i}\partial T_r/\partial x + \widehat{j}\partial T_r/\partial y$; and Δz is one vertical grid length ($500\,m$). The magnitude of the baroclinity at height z and time t is obtained from the x and y components of the retrieved temperature gradient, such that

$$|\nabla_r T(z,t)| = \left\{ [\frac{\Delta T}{\Delta x}(z,t)_r]^2 + [\frac{\Delta T}{\Delta y}(z,t)_r]^2 \right\}^{1/2}. \tag{7.2}$$

Temperature advection profiles were calculated from the retrieved temperature gradient profiles and the wind profiler mean-layer winds. The mean-layer wind velocity is

$$\overrightarrow{\overline{V}} = \frac{\overrightarrow{V}[p(z+\Delta z,t),t] + \overrightarrow{V}[p(z-\Delta z,t),t]}{2}. \tag{7.3}$$

The temperature advection were derived as

$$\overrightarrow{\overline{V}}.\nabla_r T(z,t) = \left[\overline{u}(z,t)\frac{\Delta T}{\Delta x}(z,t)_r + \overline{v}(z,t)\frac{\Delta T}{\Delta y}(z,t)_r \right]. \tag{7.4}$$

The time-height cross-section of the derived temperature gradient displayed in Figure 7.9, and the derived temperature advection in Figure 7.10 match very well with the upper air charts and shows the thermal troughs and ridges. As Figures 7.9 shows there are relatively higher temperature gradients ahead of the minor troughs. Derived temperature gradient and advection are useful means for diagnosis of weather systems [*Neiman and Shapiro*, 1989] as well as the prediction of the thermal structure of the atmosphere as compared with the radar values.

As the temporal resolution of the rawinsonde data of the closest station to the profiler (i.e. Adelaide Airport) is 12-hourly, the time-height cross-section of temperature in Figure 7.11 and the time-height virtual isentropic cross-sectional

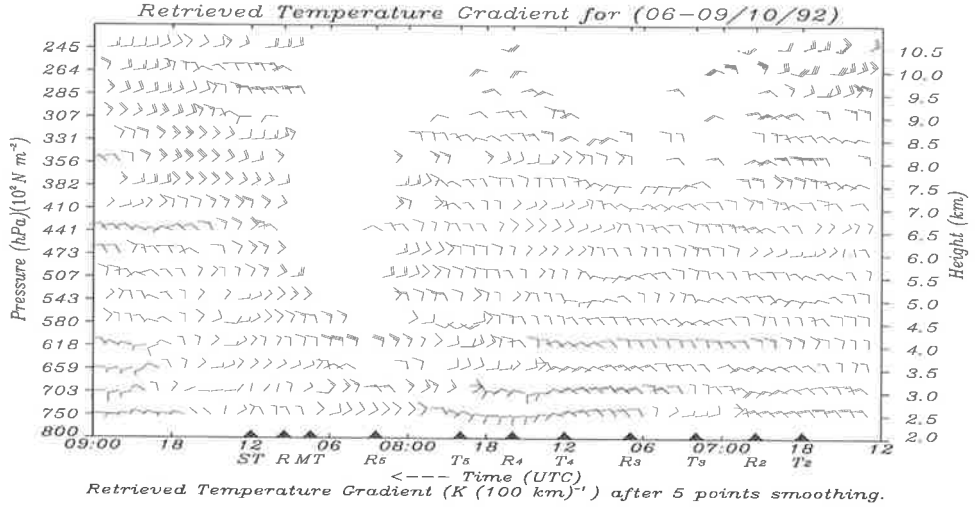

Figure 7.9: Time-height analysis of horizontal temperature gradients ($°C(100\ km)^{-1}$) retrieved from the Buckland Park wind profiler vertical wind shears between 1200 UTC 06 October and 0000 UTC 09 October 1992. Flag, $5°C(100\ km)^{-1}$); barb, $1°C(100\ km)^{-1}$); and half-barb, $0.5°C(100\ km)^{-1}$). The convention for designating the direction of $\nabla_r T$ and horizontal wind is identical.

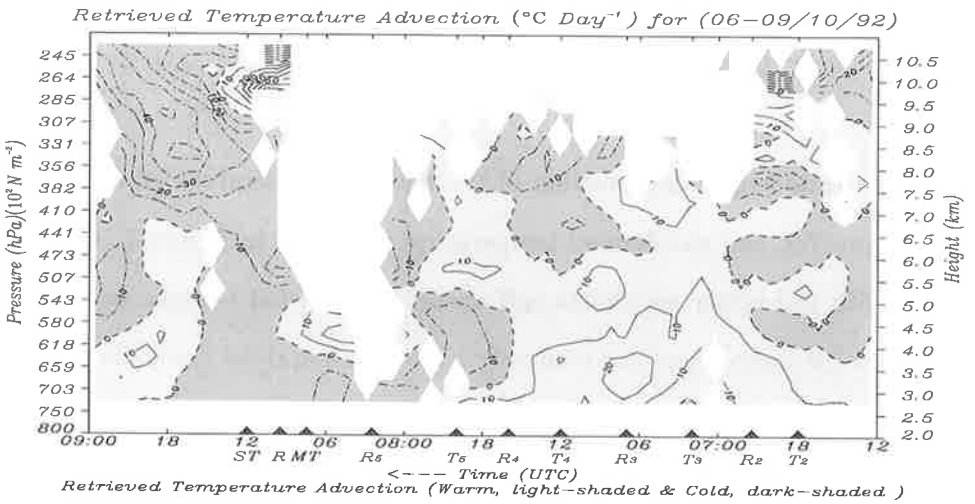

Figure 7.10: Time-height analysis of horizontal temperature advection ($°C\,day^{-1}$) retrieved from the Buckland Park wind profiler vertical wind shears between 1200 UTC 06 October and 0000 isUTC 09 October 1992. Solid contours (light-dashed) indicate warm advection; dash-dotted contours (dark-dashed) indicate cold advection; dashed lines indicate neutral temperature advection.

analysis in Figure 7.12, for the period of study, do show the differences in the thermal structure of the atmosphere.

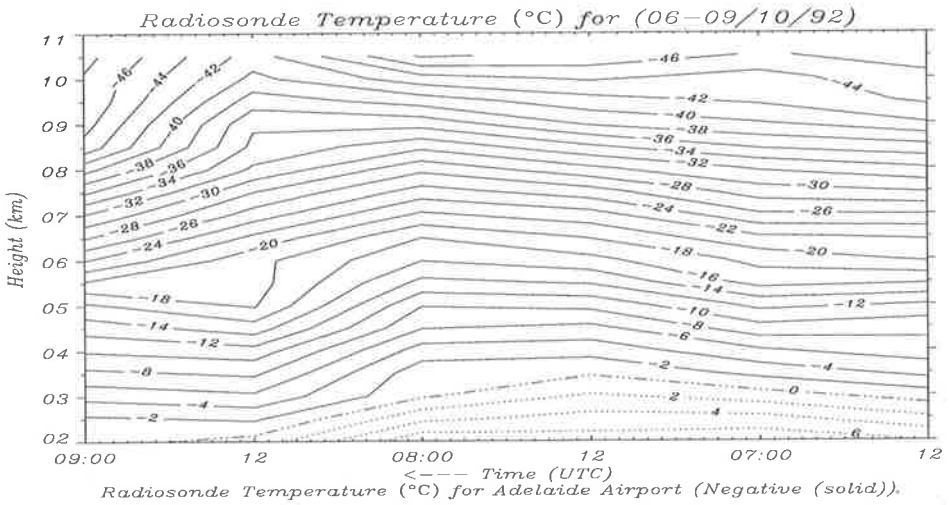

Figure 7.11: Time-height cross-section of Adelaide Airport temperature (°C) between 1200 UTC 06 October and 0000 UTC 09 October 1992.

The strong temperature gradient and undulations in Figure 7.12 show the strong baroclinity during the passage of the main trough and secondary trough between 0600-1200 *UTC* 08 October 1992 at lower troposphere inclining backwards higher up at upper troposphere.

7.4 Case Study II: 25-27 July 1995

This case study is about "comma cloud" (section 5.3.4) while, the main band (WCB) has passed through the profiler at the time of observation. The radar configuration figures are the same as Table 3.1.

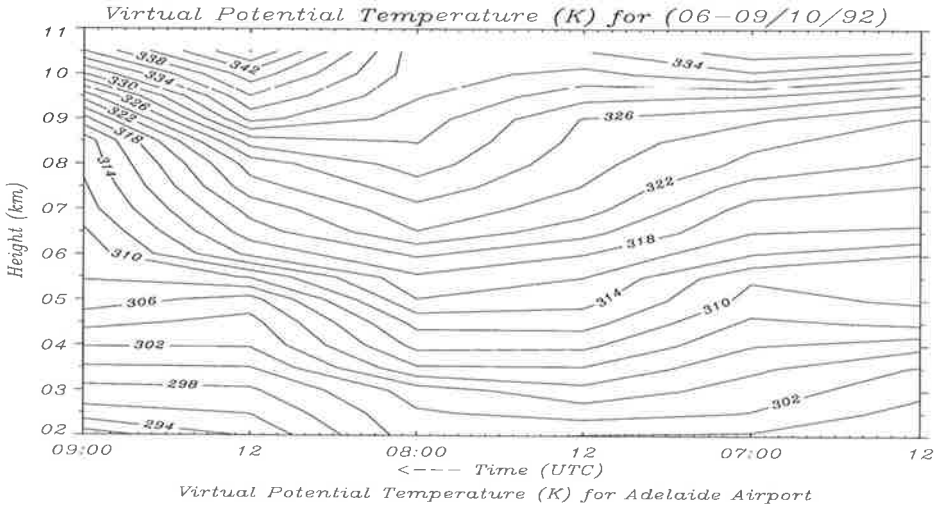

Figure 7.12: Time-height analysis of Adelaide Airport virtual potential temperature (K) between 1200 UTC 06 October and 0000 UTC 09 October 1992.

7.4.1 Synoptic Discussion

The surface cut-off low originated from the southwest was of the high latitude type or more simply, an extratropical cyclone. Superimposing the upper air charts [3] (Figure 2, *Appendix C*) on top of the surface low, the axis of the system is aligned verticaly while, on 26th July the axis inclined towards east advecting negative absolute vorticity and consequently, weakening and filling up the system. As the upper air charts show (Figure 2, *Appendix C*), the system is baroclinic with warm advection in the front and cold advection at the rear.

As the satellite imagery (Figure 7.13) shows the comma cloud consists of ribbons of convective clouds. These ribbons of convective clouds are "minor troughs" and in-between are "minor ridges" with lower level clouds or sometimes clear sky.

The detailed analysis of the surface chart of the same time, Figure 7.14, verifies

[3] Unfortunately, at that time the Bureau of Meteorology had been launching radiosonde once a day (0000 *UTC*) as a result, upper air charts for 1200 *UTC* can not be presented.

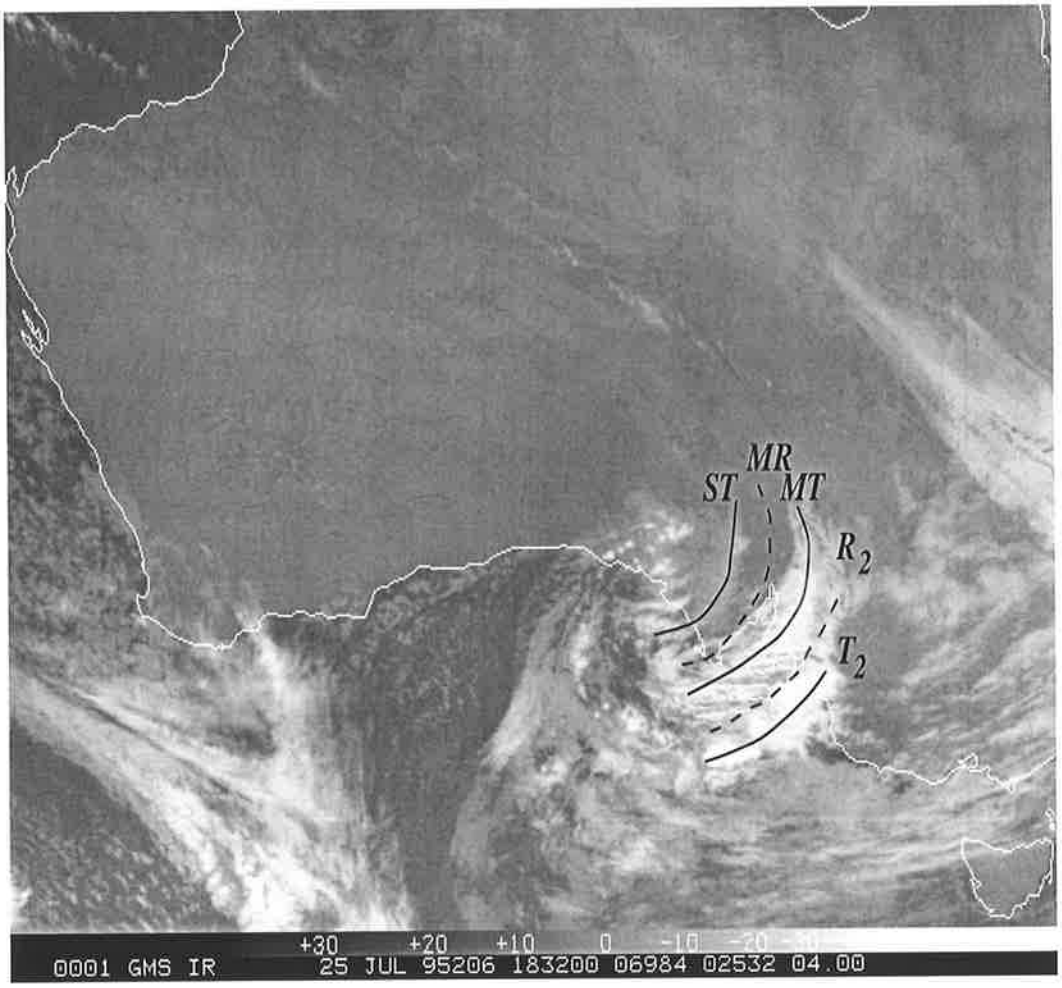

Figure 7.13: The GMS Infrared satellite imagery for 1832 UTC 25 July 1995. The almost parallel lines demarcate the minor troughs (T) and minor ridges (R).

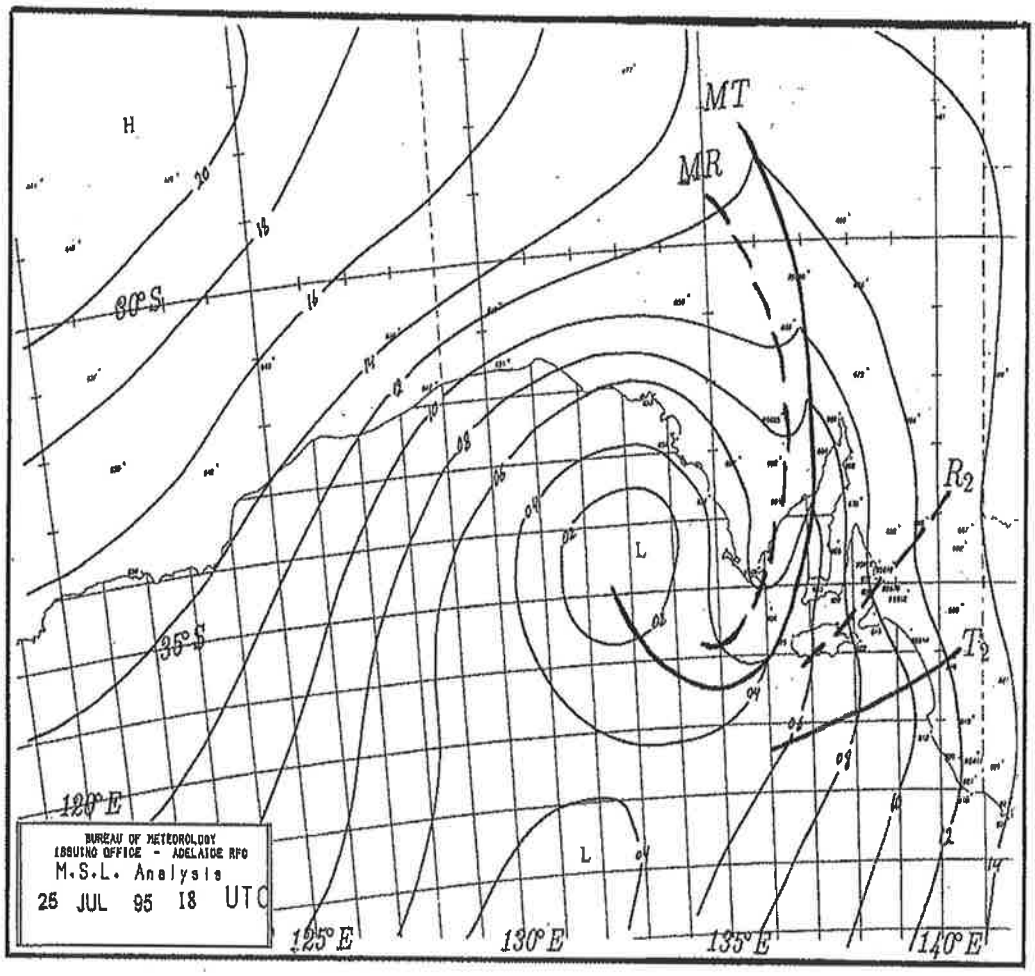

Figure 7.14: MSLP chart for 1800 UTC 25 July 1995. The minor troughs are shown by solid lines and minor ridges are shown be dashed lines appropriate to the above satellite image. The isobar intervals are 2 hPa.

the existence of such features. These features are followed in the preceding and proceeding charts (Figures 1a-h, *AppendixC*). Although Figures 7.2 and 7.14 look the same, the satellite imageries, Figures 7.1 and 7.13 illustrate the differences. The first two are strips of minor troughs and ridges in the WCB while, ribbons of troughs and ridges as a wave in the comma cloud can be seen in the last two.

7.4.2 Mesoscale Discussion

This section focuses on mesoscale the structure of the comma cloud of the cut-off low and in particular on the ribbons of clouds called troughs and ridges as waves and also the weather associated with them.

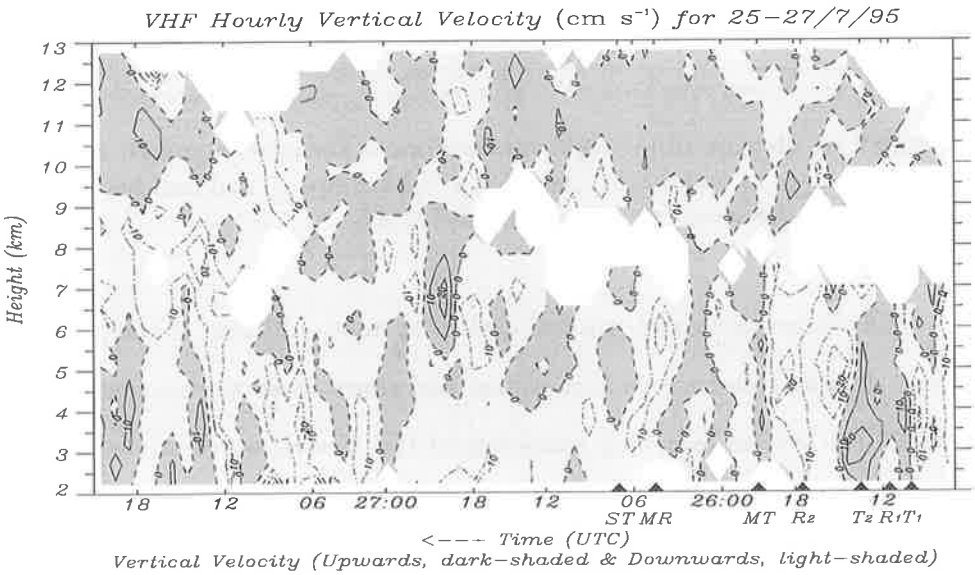

Figure 7.15: VHF hourly vertical velocity (cms^{-1}), Upwards (solid, dark-shaded), Downwards (dash-dotted, light-shaded), for 25-27/7/1995.

Profiler hourly vertical velocity (Figure 7.15) shows the existence of sequences of upward and downward motion within the center of the low and the comma cloud. These upward and downward motions are produced by troughs and ridges, respectively. Comparison of MSLP charts (Figure 1a-h) with vertical velocity

(Figure 7.15), with time adjustments reveals the existence of a wave. Considering the effects of precipitation on detected echoes by VHF radar, these fluctuations of vertical velocity illustrate the positions of troughs and ridges.

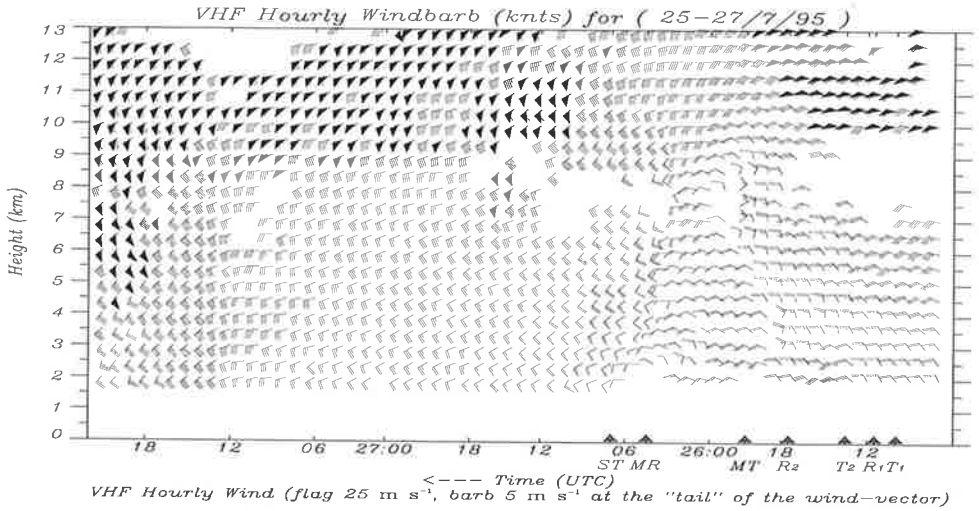

Figure 7.16: Reverse time-height cross-section of the profiler spaced-antenna wind field, displayed as windbarbs (flag $25 m s^{-1}$, barb $5 m s^{-1}$and half-barb $2.5 m s^{-1}$at the "tail" of the wind -vector) for 25-27/7/1995.

There is another extra-tropical cyclone system southwest of the comma cloud which had an influence on this system and slows down the movement and also pushes the system over land southwest of the Australian Continent. The main trough of comma cloud passed over the profiler from about 2030 UTC 25 July 1995 to 0430 UTC 26 July 1995. In Figure 7.15, the rain echoes can be seen at about 2200 UTC 25 July and 0200 UTC 26 July.

The passage of stronger waves especially the main trough is illustrated by profiler spaced antenna (SA) horizontal wind (Figure 7.16) with marked cyclonic shear associated with the passage of the trough and marked anticyclonic shear associated with the passage of the ridge. As Figure 7.16 shows, the disturbance caused by the main band extended upto about $10km$ height. The horizontal wind

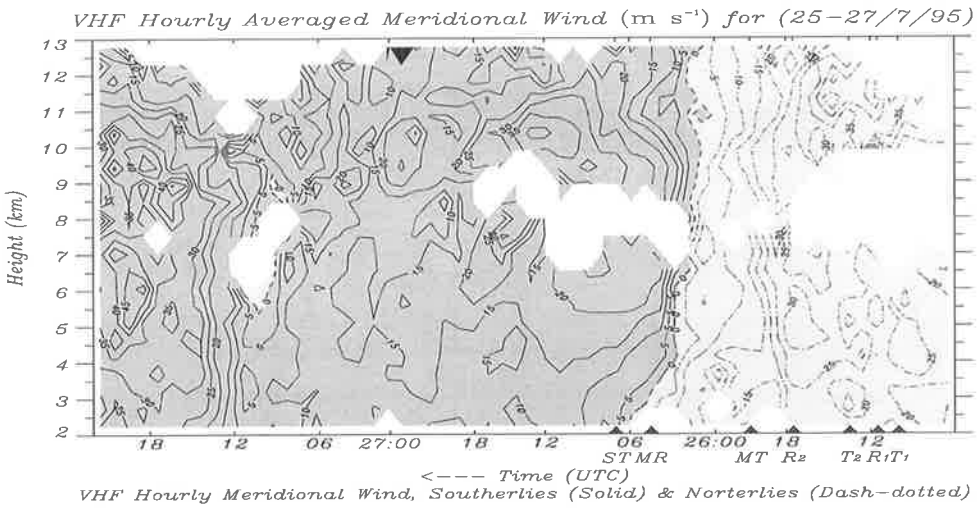

Figure 7.17: Profiler hourly meridional wind ($m\,s^{-1}$) for 25-27/7/1995. Southerly components are in solid and northerly components are in dash-dotted.

shear is also shown in profiler's meridional component of wind (Figure 7.17 with a sharp change in direction at the passage of the secondary trough (ST).

The existence of a jet-stream with the core speed of more than 60 $m\ s^{-1}$ is meandering equatorward of the cut-off low and shown on $300hPa$ upper air charts (Figures $2A_4$ & $2B_4$, *Appendix C)* is verified from the profiler's horizontal wind (Figure 7.18). As the core of the jet-stream did not pass over the profiler, the wind speeds are much lower than that shown on the 300 hPa charts. The height of the jet detectable by isotach analysis is about 10 km as shown in Figure 7.18.

Finally, the decline of the tropopause over the cut-off low is shown by enhancements of the returned power of the profiler echoes [*Gage and Balsley,* 1978; *Gage and Green*, 1979; *Gage and Green*, 1982a; *Riddle et al.*, 1983; *Green and Gage,* 1984; *Riddle et al.*, 1984; *Gage et al.*, 1986; *Sweezy and Westwater*, 1986; *Low,* 1996]. This feature of the tropopause funnel is shown by a double-dashed line on the profiler image (Figure 7.19) with the rawinsonde tropopause of Adelaide Airport superimposed by double solid lines. As it is shown in the Figure

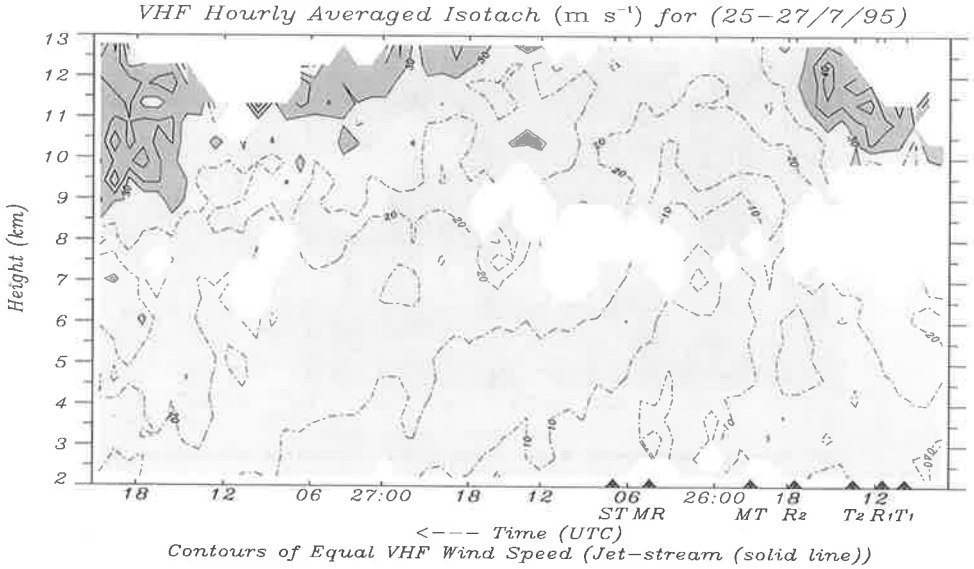

Figure 7.18: Profiler hourly isotach, equal wind speed for 25/27/7/1995, with jet-stream level, solid.

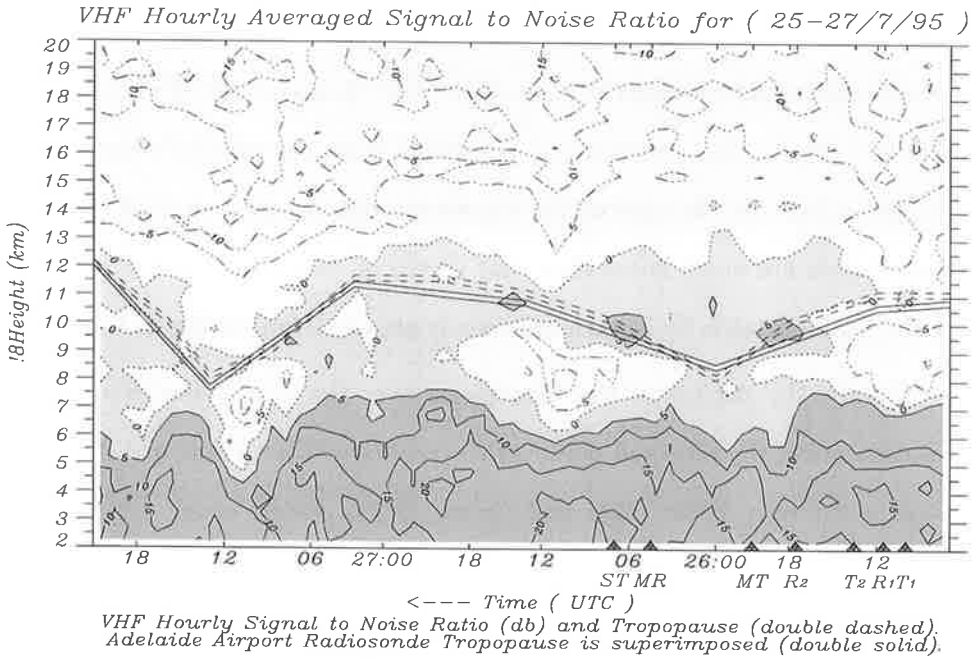

Figure 7.19: Profiler hourly Signal to Noise Ratio for 25-27/7/1995, positive, solid and negative, dash-dot-dot-dotted, as well as Tropopause, double-solid.

7.19, the tropopauses match each other illustrating the tropopause funnel over cut-off low. The secondary tropopause inclination shown in the Figure 7.19 at about 1400 *UTC* 27 July 1995 is due to the passage of the system which was located southwest of the comma cloud of the cut-off low.

7.4.3 Retrieval of Horizontal Temperature Gradients and Advections

The algorithm of derivation of temperature gradient and temperature advection for a single station is discussed in section 7.3.3.

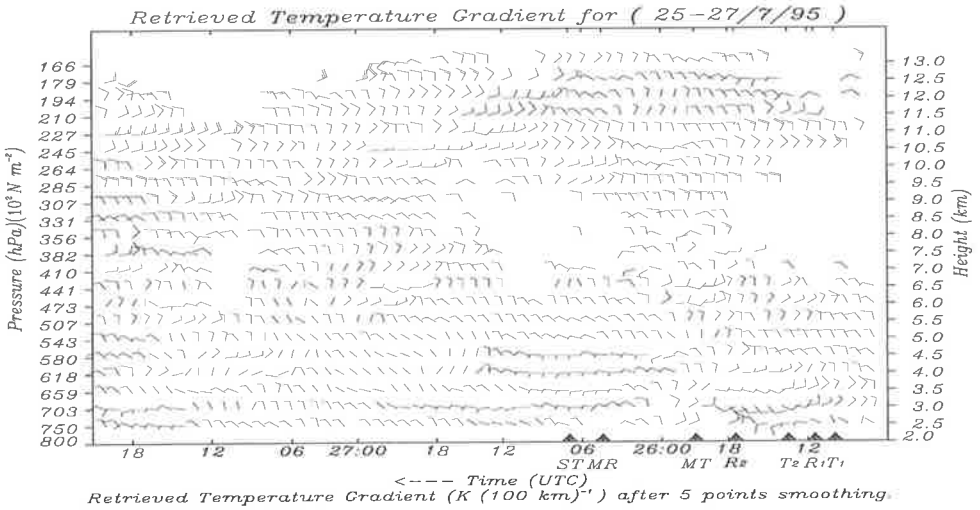

Figure 7.20: Time-height analysis of horizontal temperature gradients (°C$(100\ km)^{-1}$) retrieved from the Buckland Park wind profiler vertical wind shears between 1200 UTC 06 October and 0000 UTC 09 October 1992. Flag, 5°C$(100\ km)^{-1}$); barb, 1°C$(100\ km)^{-1}$); and half-barb, 0.5°C$(100\ km)^{-1}$). The convention for designating the direction of $\nabla_r T$ and horizontal wind is identical.

Time-height cross-section of the derived temperature gradient in Figure 7.20, and the derived temperature advection in Figure 7.21 match very well with the upper air charts and show the thermal troughs and ridges. Comparing Figures 7.20 and 7.16 shows the coincidence of the thermal trough and contour trough.

This can be followed through upper air charts in Figure 2, *Appendix C* showing that the system of comma cloud is barotropic at almost all levels. Derived temperature gradient and advection from a single station do show the thermal structure of the atmosphere [*Neiman and Shapiro,* 1989].

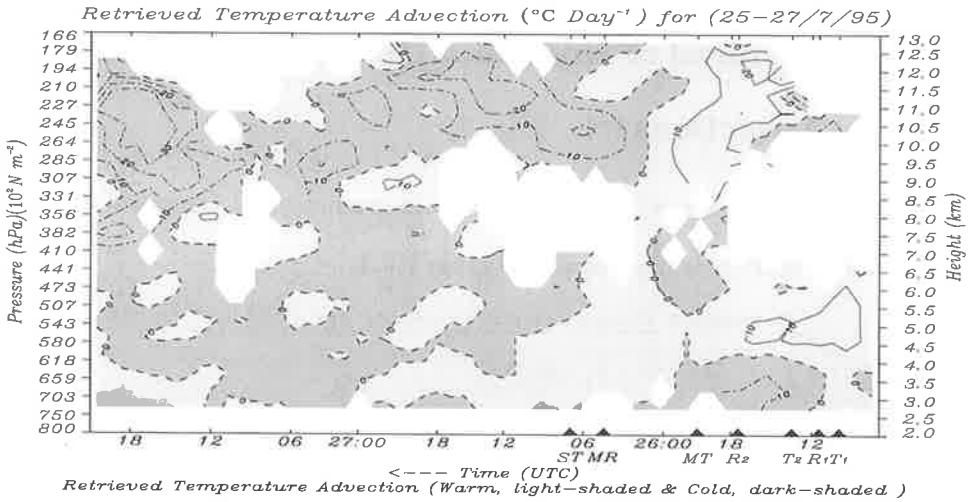

Figure 7.21: Time-height analysis of horizontal temperature advection ($^{\circ}$C day^{-1}) retrieved from the Buckland Park wind profiler vertical wind shears between 1200 UTC 06 October and 0000 isUTC 09 October 1992. Solid contours (light-dashed) indicate warm advection; dash-dotted contours (dark-dashed) indicate cold advection; dashed lines indicate neutral temperature advection.

As the temporal resolution of the rawinsonde data of the closest station to the profiler (i.e. Adelaide Airport) is 12 hourly the time-height cross-section of temperature in Figure 7.22 and the time-height virtual isentropic cross-sectional analysis in Figure 7.23, for the period of study, do show the anomaly in isotherms during the passage of comma-cloud.

The absence of a strong temperature gradient in Figure 7.23 verifies that the system of comma-cloud is barotropic during the passage of the main trough and the secondary trough between 1200 *UTC* 25 July 1995 - 0600 *UTC* 26 July 1995 at almost all levels.

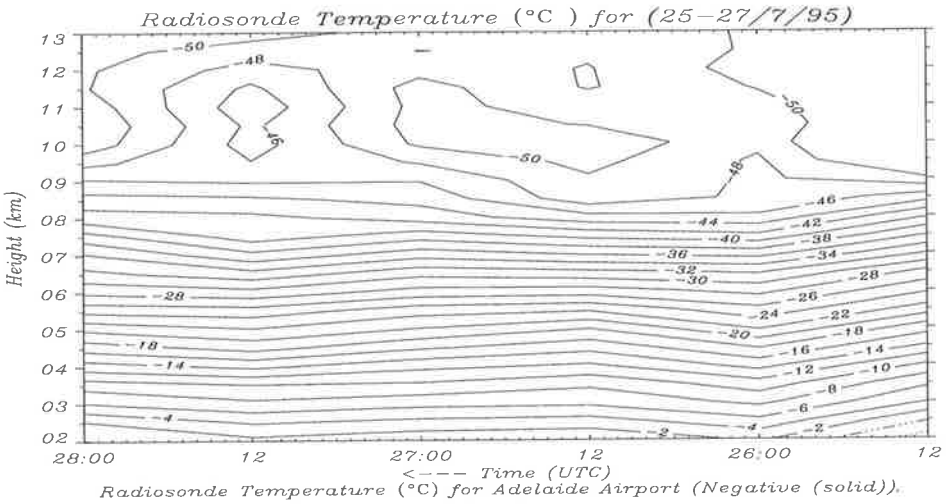

Figure 7.22: Time-height cross-section of Adelaide Airport temperature (°C) between 1200 UTC 06 October and 0000 UTC 09 October 1992.

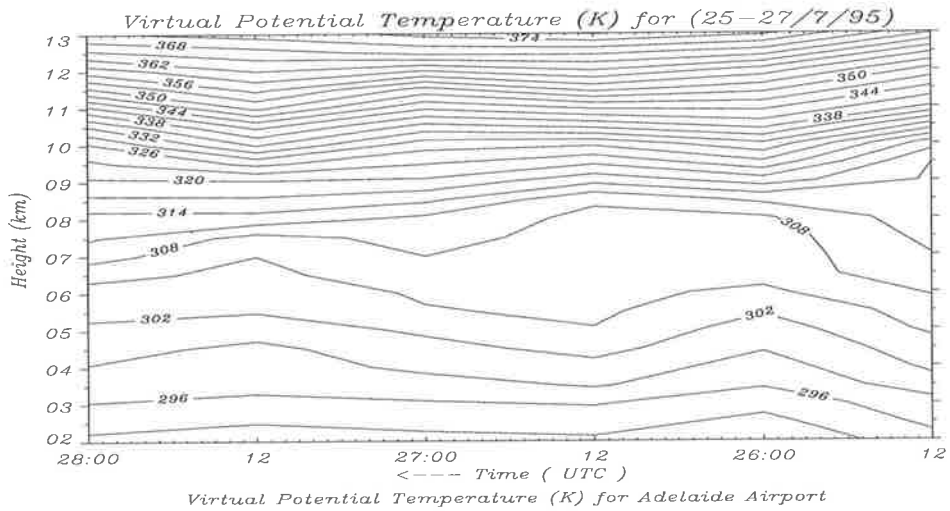

Figure 7.23: Time-height analysis of Adelaide Airport virtual potential temperature (K) between 1200 UTC 06 October and 0000 UTC 09 October 1992.

7.5 Case Study III: 29 September-02 October 1995

The larger velocity is measurable (Equation 2.14) when The higher the pulse repetition frequency (PRF) is used. Limitations of the previous studies were on the highest velocity with lower PRF. In order to detect higher velocities, the "Configuration Parameters" of the transmitting and receiving system of profiler were changed for the preceding case study. For Doppler mode, the PRF was doubled (i.e. from $4096\,Hz$ to $8192\,Hz$) and also the number of data points was doubled (i.e. from 256 to 512 points). The higher the PRF, the lower the maximum range that can be observed (Equation 2.6). As a result, the maximum height decreased to $14.5\,km$ (i.e. twenty six in $500\,m$ intervals). The data acquired from this experiment were Fourier transformed and the signal power, noise power and velocity for further analysis were extracted from the spectrum.

The cut-off low was analysed in a similar manner to the preceding case studies. The results are very similar to the previous cases, and consequently, only a brief discussion is presented here.

As the satellite imagery (Figure 7.24) and detailed analysis of MSLP chart (Figure 7.25) show, the system supports the idea of short waves as minor troughs and minor ridges embedded within the cut-off low.

The horizontal time-height cross-section of the profiler's wind (Figure 7.27) clearly shows the passage of the minor troughs and minor ridges with matching vertical velocity fluctuations. As this figure shows, the main trough with the depth distinguishable up to about $11\,km$ height, passed over the profiler at about $0000\,UTC$ 30 September 1995. There are data missing at $0400\,UTC$-$06\,UTC$ 30 September and $0500\,UTC$-$0700\,UTC$ 01 October 1995 due to the downloading of

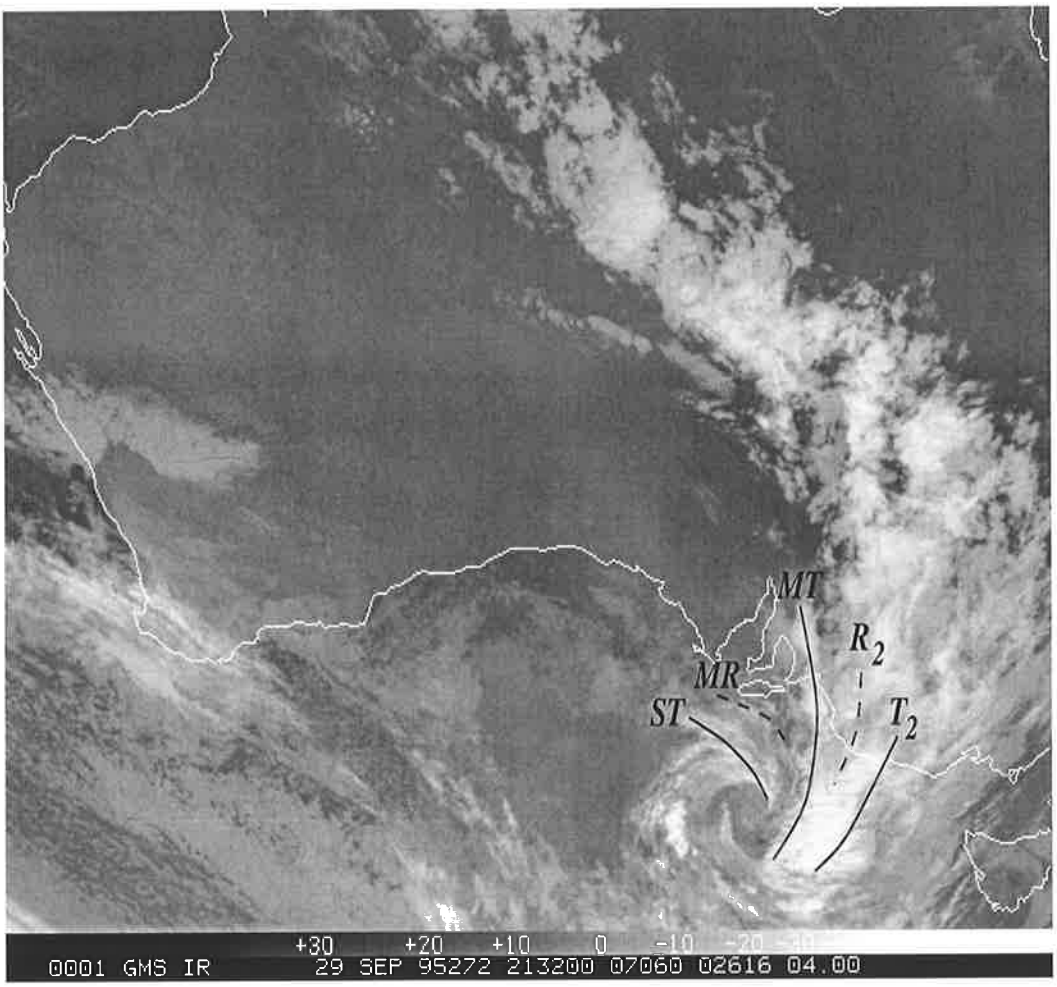

Figure 7.24: The GMS Infrared satellite imagery for 2132 UTC 29 September 1995. Lines show the minor troughs (T) and minor ridges (R).

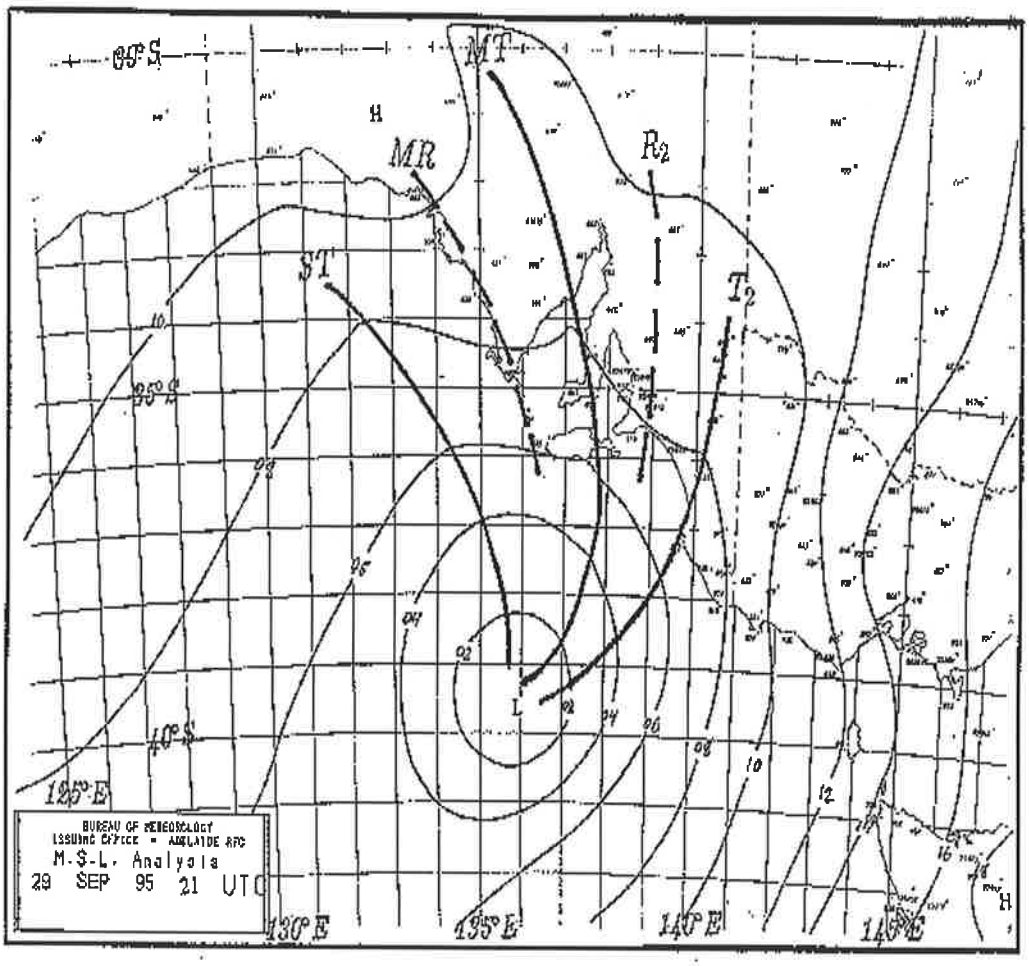

Figure 7.25: MSLP chart for 2100 UTC 29 September 1995. The minor troughs are shown by solid lines and minor ridges are shown be dashed lines appropriate to the above satellite image. The isobar intervals are 2 hPa.

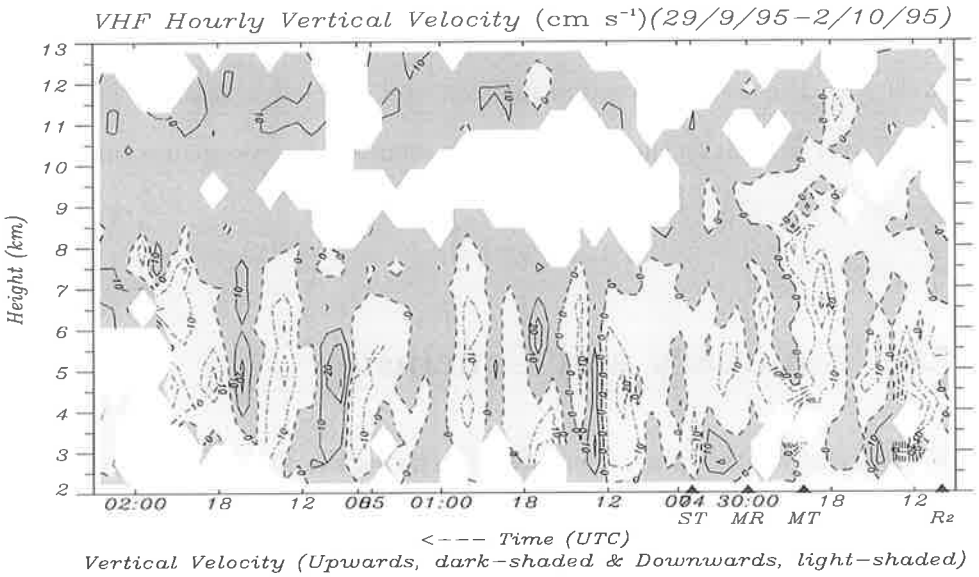

Figure 7.26: VHF hourly vertical velocity (cms^{-1}), Upwards (solid, dark-shaded), Downwards (dash-dotted, light-shaded), for 29/9-2/10/1995.

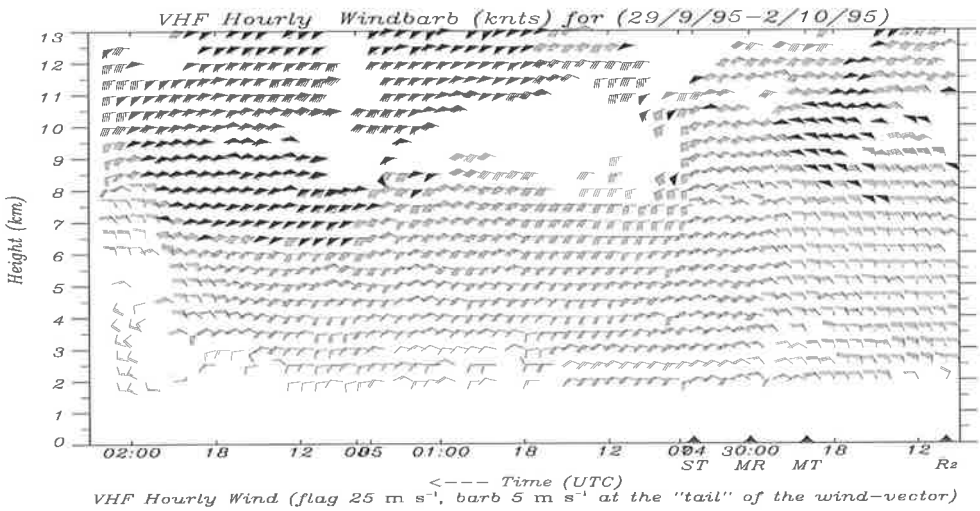

Figure 7.27: Reverse time-height cross-section of the profiler spaced-antenna wind field, displayed as windbarbs (flag $25ms^{-1}$, barb $5ms^{-1}$and half-barb $2.5ms^{-1}$at the "tail" of the wind -vector) for 29/9-2/10/1995.

the raw data from the computer.

The thermal structure of the system shows a strong baroclinity at almost all levels with the warm advection in front and cold advection at the rear of the cut-off low. Similar to the other two case studies, the tropopause funnel was also seen over this cut-off low.

7.6 Summary and Conclusion

Of the severe weather phenomena over Australia, the cut-off low systems and their impacts on the environment and economy are the important features. Three examples of cut-off low systems were studied in this chapter using the data obtained with the VHF radar wind profiler and using meteorological charts from the Bureau of Meteorology, as well as satellite imagery. These case studies were chosen because they illustrated different aspects of the synoptic and mesoscale features associated with the cut-off lows. All three cases were from high latitude origin type cut-off low system and strongly baroclinic with the warm advection at the front and cold advection at the rear of the system. Case I concentrated on a cut-off low which passed south of the radar site and the features of the "warm conveyor belt" were particularly evident. Case II was chosen because the center of the low passed nearby the radar site and the "comma cloud" passed over the profiler. The comma cloud consisted of ribbons of convective clouds caused by "minor troughs" and also "minor ridges" in between troughs. Finally, the cut-off low studied in case III showed many of the features of case I and case II and was discussed here in less detail. The retrieval single-station temperature gradients and advections were also investigated.

A common feature of these and the other cut-off low systems studied was the

presence of the minor troughs and minor ridges. These manifested themselves in the cloud patterns and MSLP charts. The minor troughs were similar to the "wide precipitation bands" found by *Sanders and Bosart* [1985]. The passage of these ridges and trough lines were evident in the radar horizontal wind and vertical wind data, especially at low level heights. These undulations were particularly evident in the retrieval of temperature gradients (e.g. 7.20).

These studies involved synoptic-scale discussion and meso-scale discussion. The retrieved single-station temperature gradient and temperature advection were also investigated. These studies were consistent with the finding of *Browning* [1990] that says, *where a velocity maximum in the polar air approaches a cold front, it may generate a comma cloud pattern entirely within the cold air* (i.e. the second case study) *or a wave on the cold frontal cloud band* (i.e. the first case study).

The strength of the backscattered signal observed by the radar was used to derive tropopause heights. These case studies illustrated very well the capability of radars to trace the height of that tropopause and to see the decrease and then increase in height as the cut-off low passed nearby. This is the so called tropopause funnel.

The key point about these studies is that without the high time and spatial resolution provided by the radar it would not be possible to see synoptic and mesoscale features in such detail. A limitation of the studies here has been the absence of wind data from below $2\,km$. The recent development of a VHF boundary layer radar will help to overcome this deficiency.

Chapter 8

Summary and Conclusion

8.1 Summary

In the past two decades radars have become powerful tools for studying the properties of the atmosphere. These systems might replace existing wind measuring instruments and methods.

This thesis has been concerned with the theory and application of VHF wind profilers to studies of the cut-off low phenomenon over Australia. Since the vertical motion of the air is an important factor in meteorology in general and the evolution of a cut-off low in particular, we have concentrated on the vertical motion of the air.

The overview and background for the work presented in this thesis was provided in chapter 1. A brief description of the atmosphere was provided in terms of profiles of the temperature structure. The physics and thermodynamics of the atmosphere were presented. Different types of observation systems for measuring the meteorological parameters at the ground surface and the upper-air levels were discussed.

In the atmosphere the presence of turbulence will cause the refractive index to fluctuate around its mean value, both in time and in space. These fluctuations will, in principle, produce scattering of radio waves, which are observable with a radar sensitive enough to detect very weak echoes.

The general overview on coherent radar techniques with special emphasis to mesosphere, stratosphere, troposphere (MST) radar operating in the VHF band, was given in chapter 2. Some basic introduction to Doppler radar measurements and the radar equations were followed by the data analysis in terms of the correlation and spectrum analysis. The techniques for the measurement of wind velocities, namely, the different modes of Doppler methods as well as the spaced antenna (SA) method were also surveyed. A brief discussion about comparisons of spaced antenna method with other wind measurements brought the chapter to a close.

Chapter 3 describes the Buckland Park VHF radar, which is capable of a variety of applications in atmospheric research and meteorology. The hardware and operating parametres are discussed as well as aspects and properties of the Co-Co antenna array.

All phenomena happening within a cut-off low such as: heavy precipitation, flooding, thunderstorm and lightning are due to the vertical motion of the air. The long term averaging of vertical velocity of a site is essential for the evaluation of the radar system behaviour. Wind profiling Doppler radars have been designed to measure the radial component of motion in the atmosphere along the radar beam. One possible complicating factor that can affect the accuracy of average vertical wind measurements arises from slight tilts of the vertical beam resulting from the slope of the ground under the transmitting antenna or phasing errors between antennas. Small inaccuracies in the vertical beam direction can

fold a fraction of horizontal wind into vertical velocities and severely contaminate the measurements. However, a beam tilt of a few hundredths of a degree does not appreciatively affect instantaneous velocity values. In order to evaluate the vertical beam tilt, three different methods were applied: (i) The height measurements of ground and the antenna level by using the visible hose and water, (ii) determination of gradient of a plain surface fitted to the surface data and (iii) correlation of $\overline{w}$ with $\overline{u}$ using the five years of available data from 1991 to 1995 ($\simeq$ 5405 hours). Zenith angle of 0.18° and azimuth angle of 210°, which were consistent for three different methods, were derived for the Buckland Park Co-Co transmitting antenna array slope.

The mechanism of the apparent mean vertical velocity being weighted toward downward motion in a gravity wave [*Nastrom and VanZandt*, 1994] and determination of this bias in long term vertical velocity is also of interest. In order to evaluate the mean vertical velocity of air at the Buckland Park site, the available data for 5 years (i.e. 1991-1995) were corrected against the zenith angle and azimuth angle relationships discussed in chapter 4 and then averaged at different heights. The long term mean vertical velocity, $\overline{w}$, was found to be about $-4\,cm\,s^{-1}$ at mid-troposphere, tending towards $0\,cm\,s^{-1}$ near tropopause and possessing slightly positive characteristics farther away. The results for the Buckland Park site were quite consistent with the *Nastrom and VanZandt* [1994] for Flatland VHF radar.

In chapter 5 discussion about cyclones in general, and organization of clouds and precipitation at the warm conveyor belt (WCB) and cold conveyor belt (CCB) in particular, were presented. A very brief discussion about comma cloud was also presented. Some aspects of clouds and precipitation over Australia were discussed. The chapter came to an end with the typical synoptic structure of

cut-off low.

The climatology of cut-off lows over South Australia is important in meteorology by informing forecasters about the frequency and potential of cut-off low for their impacts on the environment. An investigation of 20 years (1974-1993) of Australian continental charts revealed aspects and characteristics of cut-off lows such as: origins, monthly and yearly frequency, their tracks and their speeds. These issues were discussed in chapter 6. In order to investigate the impacts of cut-off lows over South Australia, 20 years (1974-1993) of 3-hourly synoptic data from 25 major South Australian stations were analysed for precipitation, thunderstorm, shower and hail.

The synoptic and mesoscale discussion of three distinct case studies were presented in chapter 7. In the synoptic analysis the minor troughs and minor ridges were found to be embedded in the WCB and comma cloud. In mesoscale analysis three components of velocities and signal to noise ratio (SNR) were investigated. The vertical thermal structure of cut-off low were investigated through the retrieval of single-station horizontal temperature gradients and temperature advections, as well as the upper air charts. The three dimensional structure of cut-off low systems were discussed in this chapter.

8.2 Conclusion

The cut-off low phenomenon over Australia was investigated in this thesis. In order to eliminate the contamination of vertical velocity from folding of a fraction of horizontal velocity into it due to a very slight tilt in vertical beam from zenith, the slope of the beam was found through three different methods with the consistent results of zenith angle of 0.180° and azimuth angle of 210°. The

long term vertical velocity over the Buckland Park VHF wind profiler site was investigated after the data were corrected against the slight tilt of beam. The results were found to be consistent with *Nastrom and VanZandt* [1994].

The climatology of cut-off lows over South Australia through 20 years (1974-1993) of data analysis revealed some of its aspects and characteristics in the region. The fact that more than 15% of precipitation and thunderstorm activity and 8% of shower activity in Adelaide is due to cut-off lows, makes the cut-off low very important for the economy of the region.

The synoptic scale and mesoscale investigation of three distinct case studies of cut-off lows clearly showed the presence of the minor troughs and minor ridges in the WCB and comma cloud. These results were consistent with *Browning* [1990]. These waves manifested themselves in the cloud patterns and mean sea level pressure charts, as well as VHF radar data analysis. The minor troughs were found to be similar to the "wide precipitation bands" found by *Sanders and Bosart* [1985].

8.3 Suggestions for Further Work

The work presented in this thesis provides a thorough investigation of a number of cut-off lows using the VHF wind profiler of the time at Buckland Park. At the time, there were only three receivers and it was impossible to use the high gain of the receivers because of the saturation from Co-Co antenna receiver. Consequently, missing data were inevitable. The new RDAS (radar data acquisition system) having 6 receivers allows us to minimize missing data. Further investigation using the new RDAS as a campaign with Bureau of Meteorology for a pre-prepared cut-off low will undoubtedly, improve the results of this work. It is

worth mentioning that having the Buckland Park field station equipped with the weather elements recording facilities such as: anemograph, thermograph, barograph, pluviograph or ombrograph or recording rain gauge and rain-intensity gauge, will upgrade the investigations.

Another limitation of the studies presented in this thesis has been the absence of wind data from below 2 km. The recent development of a VHF boundary layer radar will help to overcome this deficiency.

During the massive analysis of Buckland Park VHF radar data for different case studies in order to choose the optimum ones, the author came across some odd aspects of atmosphere. These are presented in Appendix D. As was discussed, the importance of the work to meteorology is evident and there are also some particular applications to aviation from the point of view of efficiency of flights and economy. A thorough investigation for each aspect shown is suggested for further work.

Appendix A

Spaced Antenna Technique

The spaced antenna (SA) technique dates back to the early ionospheric measurements of velocity (e.g. *Briggs et al.*, [1950]). The principles of the measurement of horizontal velocities with SA method are described in detail by *Briggs* [1977] and the theoretical details are presented by *Briggs* [1984] and *Schminder and Kurschner* [1984] and recently reviewed by *Briggs* [1993]. The vertical velocity is still measured by the Doppler method with vertical beams. *Briggs* [1980] and *May* [1990] have shown that the DBS and SA method are basically equivalent. They demonstrated that although the mathematics of the data analysis are quite different, both techniques use the amplitudes and phases of radar returns from different angles for their derivatives. *Royrvik* [1983] concluded that a smaller and less sensitive radar system benefits most by using the SA technique, while a large antenna system is not very efficient in the SA mode and is used to better advantage in DBS mode.

The SA technique is based on correlation techniques. In this technique the electromagnetic pulses are continuously transmitted to the atmosphere vertically. The returned echoes are received by at least three sets of antennas located tri-

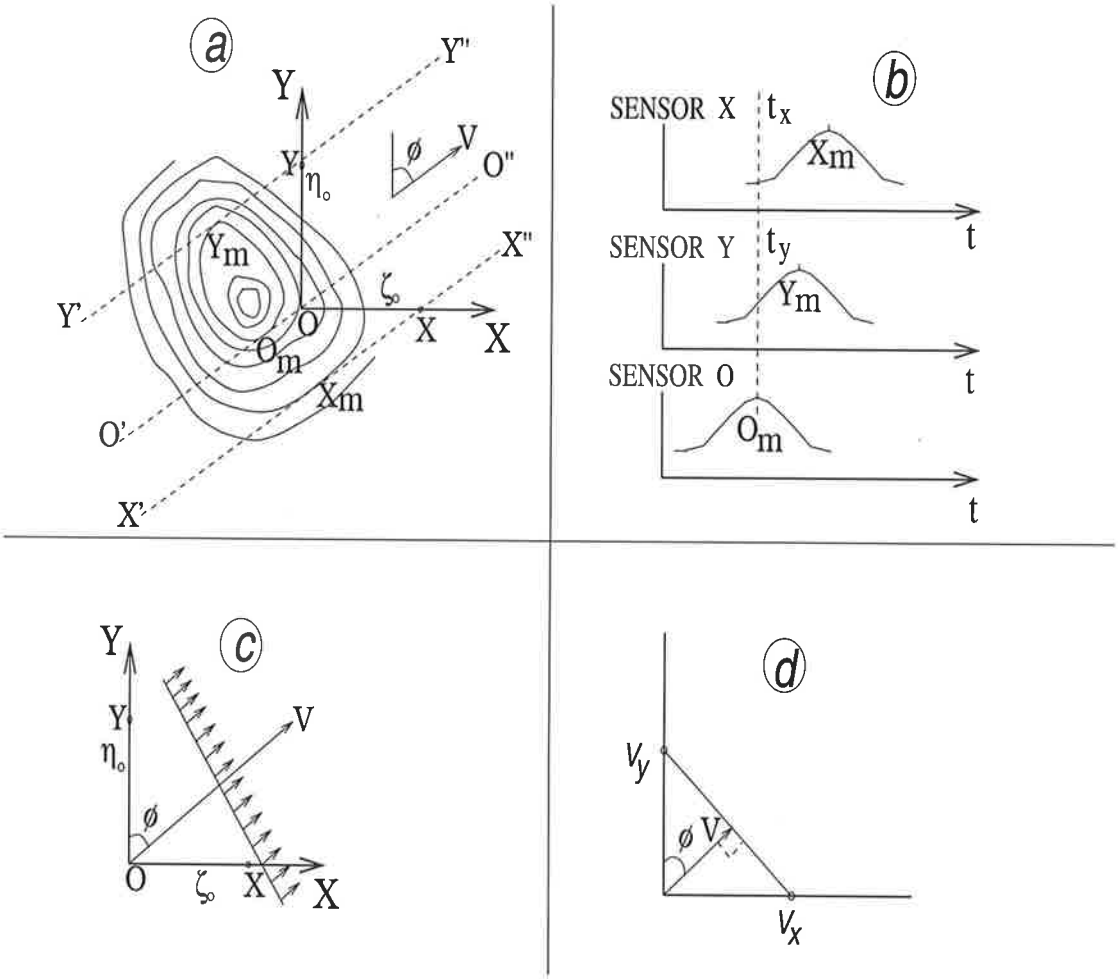

Figure A.1: A typical "hill" moving with a speed V in a direction which makes an angle ϕ with the y-axis (a). The records obtained might look something like those of (b). A simple representation of the diffraction pattern (c) by a line of maximum which is perpendicular to the velocity vector V. A geometrical construction to obtain velocity from its components (d). (adapted from *Briggs* [1984]).

angularly, called Yagi arrays. The initial assumption of the analysis is that the atmospheric irregularities have a certain shape and random nature and move with a constant speed in a fixed direction. It is worthwhile to represent a pattern by contour lines of an arbitrarily measured real quantity. It is assumed that pattern contains irregular "hills" or "ridges" and "valleys" or "troughs". Figure A.1(a) shows a typical "hill" moving with a speed V in a direction which makes an angle ϕ with the y-axis.

Suppose the measured quantity is recorded as a function of time by three sensors located at O, X and Y. The sensors form a right angled triangle with separation ζ_o and η_o in the x and y-direction, respectively. The sensor at O records a "section" through the "hill" along the dotted line $O'O''$ parallel to the direction of movement. Similarly, the sensors at X and Y record along $X'X''$ and $Y'Y''$, respectively.

The records obtained might look something like those of Figure A.1(b). The maximum corresponds to the points marked X_m, O_m and Y_m in Figure A.1(a). To a good approximation, the "line of maximum" (i.e. $X_mO_mY_m$) may be taken as straight, if the "hill"is large compared to the separation of the sensors O, X and Y. Furthermore, it tends to be perpendicular to the direction of the motion of the pattern. Hence, the diagram of Figure A.1(a) can be replaced by the much simpler one of Figure A.1(c). From this diagram the time differences t_x of Figure A.1(b), can be calculated as:

$$t_x = \frac{\zeta_0 sin\phi}{V} \tag{A.1}$$

and

$$t_y = \frac{\eta_0 cos\phi}{V} \tag{A.2}$$

recalling, $V_x = \zeta_0/t_x$ and $V_y = \eta_0/t_y$, then:

$$V_x = \frac{V}{sin\phi} \tag{A.3}$$

and

$$V_y = \frac{V}{cos\phi} \tag{A.4}$$

which clearly shows that V_x and V_y are not components of V. The V can be obtained from V_x and V_y in Figure A.1(d) as:

$$V = \frac{V_x V_y}{\sqrt{V_x^2 + V_y^2}}. \tag{A.5}$$

By using the average time displacements in the above equations, the average velocities which are generally called "apparent velocities" can be estimated.

Cross-correlation of the signals at each antenna allows measurement of the time delays between antennas, which can be used to calculate the "apparent" velocity of the scatterers. Application of the full correlation analysis (FCA), corrects for the effects of turbulence to produce the "true" velocity [*Briggs,* 1968a; *Briggs*, 1968b]. *Hocking et al.,* [1988] reviewed all the applications, and *Larsen and Rottger* [1988] described the possibilities for utilizing the spaced antenna method for wind profiling. For detailed description of FCA, readers are addressed to *Briggs* [1984].

The spacing of antenna in SA systems, is important corresponding to the choice of zenith angle in DBS system. The antenna spacing should be comparable to the mean pattern scale, which presents some difficulties since pattern scale varies in altitude and time, whereas, antenna spacing is usually fixed. Optimum spacing must be determined experimentally, although studies show that tropo-

spheric and lower stratospheric VHF pattern scales of around $50\,m$ are typical [*Vincent et al.*, 1987; *Van Baelen et al.*, 1990]. The observed pattern scale is also dependent on the beamwidth of the transmitting antenna. Errors in wind estimations of SA technique were discussed by *May* [1988] considering the statistical variation in derived parameters and *Holdsworth and Reid* [1995a] by modeling the effects of sampling rate and antenna spacing.

Vincent et al., [1987] quoted precisions of about $1\,m\,s^{-1}$ in hourly average independent FCA derived wind analysis during quiet periods, demonstrating the ability to be reproduced.

The application of the SA method has both advantages and disadvantages compared with other methods. Aspect sensitivity argues in favor of the SA method since it uses vertical-beam antenna and, as a result, an increase in the signal-to-noise ratio (SNR). Antenna sidelobe effects are also less important. However, a beamwidth of at least a few degrees must be used. A VHF or UHF spaced antenna system can also be used in the interferometer mode, which yields additional information about the spatial structure of waves and turbulence.

The data are usually analysed by correlation techniques in the time domain, motivated by the original idea that the time displacements for the pairs of antennas would indicate horizontal motions [*Briggs et al.*, 1950]. However, *Costa and Fougere* [1988] and *Liu et al.*, [1990] have pointed out that an essentially equivalent analysis can be carried out in the frequency domain. The conversion of the equations of correlation analysis from the time domain to the frequency domain can only be carried out explicitly if a functional form for the correlation function is assumed, and if the form is such that the required Fourier transforms can be evaluated analytically [*Briggs and Vincen*t, 1992].

The application of either the spaced antenna and / or the Doppler method has

advantages and limitations, and there obviously is a trade-off between accuracy, simplicity and cost-effectiveness in the planning and operating of a VHF / UHF radar system.

A.1 The Standard Atmosphere

A hypothetical vertical distribution of atmospheric temperature, pressure, and density which, by international agreement, is taken to be representative of the standard atmosphere for different purposes. The air is assumed to obey the perfect gas law and the hydrostatic equation, which, taken together, relate temperature, pressure, and density variations in the vertical. It is further assumed that air contains no water vapour, and that the acceleration of gravity does not change with height. This last assumption is equivalent to adopting a particular unit of geopotential height in place of a unit of geometric height for representing the measure of vertical displacement.

The current standard atmosphere which has been adopted by the International Civil Aeronautical Organization (ICAO), is taking the place of the U.S. Standard Atmosphere. The parametric assumption and physical constants used in preparing the ICAO Standard Atmosphere are as follows:

- Zero pressure-altitude corresponds to that pressure which will support a column of mercury $760\,mm$ high. This pressure is taken to be 1.013250×10^{6} *dynes* cm^{-2}, or $101325\,Nm^{-2}$ or $1013.250\,hPa$ (and is known as one *standard atmosphere* or one *atmosphere*).

- The gas constant for dry air is $2.8704\times10^{6} erg\,g^{-1}\,K^{-1}$ or $287.04\,J\,kg^{-1}\,K^{-1}$.

- The ice point at one standard atmosphere pressure is $273.16\,K^{-1}$.

- The acceleration of gravity is $980.665\,cm\,s^{-2}$ or $9.80665\,m\,s^{-2}$.
- The temperature at zero pressure altitude is 15 $^{\circ}C$ or 288.16 K.
- The density at zero pressure altitude is $1.2250\,kg\,m^{-3}$.
- The lapse rate of temperature in the troposphere is 6.5 $^{\circ}C\,km^{-1}$.
- The pressure altitude of the tropopause is 11 km.
- The temperature at the tropopause is – 56.5 $^{\circ}C$.
- The lapse rate from 11 km to 25 km is 0 $^{\circ}C\,km^{-1}$.
- The lapse rate from 25 km to 47 km is + 3.0 $^{\circ}C\,km^{-1}$; temperature at 47 km is + 9.5 $^{\circ}C$.
- The lapse rate from 47 km to 53 km is 0 $^{\circ}C\,km^{-1}$.
- The lapse rate from 53 km to 75 km is – 3.9 $^{\circ}C\,km^{-1}$; temperature at 75 km is – 76.3 $^{\circ}C$.
- The lapse rate from 75 km to 90 km is 0 $^{\circ}C\,km^{-1}$.
- The lapse rate from 90 km to 126 km is + 3.5 $^{\circ}C\,km^{-1}$; temperature at 126 km is + 49.7 $^{\circ}C$ (molecular-scale temperatures).
- The lapse rate from 126 km to 175 km is + 10.0 $^{\circ}C\,km^{-1}$; temperature at 175 km is 539.7 $^{\circ}C$ (molecular-scale temperatures).
- The lapse rate from 175 km to 500 km is + 5.8 $^{\circ}C\,km^{-1}$; temperature at 500 km is 2424.7 $^{\circ}C$ (molecular-scale temperatures).

The U.S. Extension to the ICAO Standard Atmosphere is essentially a recomputation of the above data from the surface to 300 km.

A.2 Thermodynamics of the atmosphere

Motion in the atmosphere, thermodynamics, potential temperature, equivalent potential temperature are important features for which it is appropriate to introduce their definitions and terminologies.

A.2.1 First Law of Thermodynamics

The conservation of energy for a thermodynamic system, which states that the heat added to or subtracted from a system must equal the change in the internal energy plus the work done by the system. This is the first law of thermodynamics. The law is defined mathematically as:

$$dH = du + dw \tag{A.6}$$

where,

dH = an infinitesimal amount of heat added per unit mass,

du = change in internal energy per unit mass,

$dw = pd\alpha$, work done by a unit mass of the system.

Substituting for dw, the Equation A.6 becomes:

$$dH = du + pd\alpha. \tag{A.7}$$

It may be shown that internal energy is a function of temperature for ideal gases, which satisfy an equation of state:

$$p\alpha = R_d T \tag{A.8}$$

or

$$p = \rho R_d T \tag{A.9}$$

where,

$\alpha = V/M$ is the specific volume of mixture of atmospheric gases,

$\rho = M/V$ is the specific mass of mixture of atmospheric gases,

$R_d = 287.04\, J\, kg^{-1}\, K^{-1}$ is the gas constant for dry air.

If the volume is kept constant, the Equation A.7 implies that the heat added becomes internal energy. The added internal energy is:

$$du = c_v dT \tag{A.10}$$

where, dT is the change of temperature and c_v is the specific heat at constant volume (*i.e.* $c_v = (dH/dT)_{\alpha=const.}$). For actual gases, c_v slowly varies with temperature. However, for the atmospheric range of temperature, c_{vd} is considered to be approximately constant.

Substituting in Equation A.7, the first law of thermodynamics becomes:

$$dH = c_v dT + p d\alpha. \tag{A.11}$$

Differentiating the Equation of state, $p\alpha = RT$, giving:

$$p d\alpha + \alpha dp = R dT. \tag{A.12}$$

Substituting for $pd\alpha$ into Equation A.11, yields:

$$dH = (c_v + R) dT - \alpha dp. \tag{A.13}$$

For an isobaric process $dp = 0$, and Equation A.13 becomes:

$$\left(\frac{dH}{dT}\right)_{p=const} = c_v + R. \tag{A.14}$$

According to the definition of the specific heat at constant pressure, $(dH/dT)_{p=const} = c_p$ so, the Equation A.14 becomes:

$$c_p = c_v + R. \tag{A.15}$$

Utilizing Equation A.15, the alternative form of the first law of thermodynamics becomes:

$$dH = c_p dT - \alpha dp. \tag{A.16}$$

A.2.2 Potential Temperature

An adiabatic process is defined as a thermodynamic change of state of a system in which there is no transfer of heat or mass across the boundaries of the system. Replacing dH equal to zero and substituting from Equation of state (*i.e.* A.8) for α in Equation A.16 for dry air, gives:

$$c_{pd}\frac{dT}{T} - R_d\frac{dp}{p} = 0 \tag{A.17}$$

where, $c_{pd} = 1005.7 \pm 2.5\, J\, kg^{-1}\, K^{-1}$ [*Bolton*, 1980], is the specific heat for dry air at constant pressure. Integrating (A.17) from an initial state (p, T) to a final state (p_s, T_s), gives Poisson's equation relating temperature and pressure for an

adiabatic process in dry air:

$$\frac{T_s}{T} = \left(\frac{p_s}{p}\right)^{R/c_{pd}} . \tag{A.18}$$

As the *potential temperature*, θ, is the temperature a parcel of dry air would have if brought adiabatically from its initial state to the (arbitrarily selected) standard pressure of $1000\,hPa$, (A.18) follows that:

$$\theta = T\left(\frac{p_s}{p}\right)^{R/c_{pd}} . \tag{A.19}$$

Introducing a non-dimensional term, k_d, for dry air as, $k_d = R_d/c_{pd} = 0.2854 \pm 0.0007$ [*Bolton*, 1980], the Equation A.19 yields:

$$\theta = T\left(\frac{p_s}{p}\right)^{k_d} \qquad or \qquad \theta = T\left(\frac{1000}{p}\right)^{0.2854} . \tag{A.20}$$

It is evident from the definition that potential temperature will be constant during an adiabatic process in dry air, and hence, is superior to the temperature, T.

Appendix B

Charts and Images For Case Study I

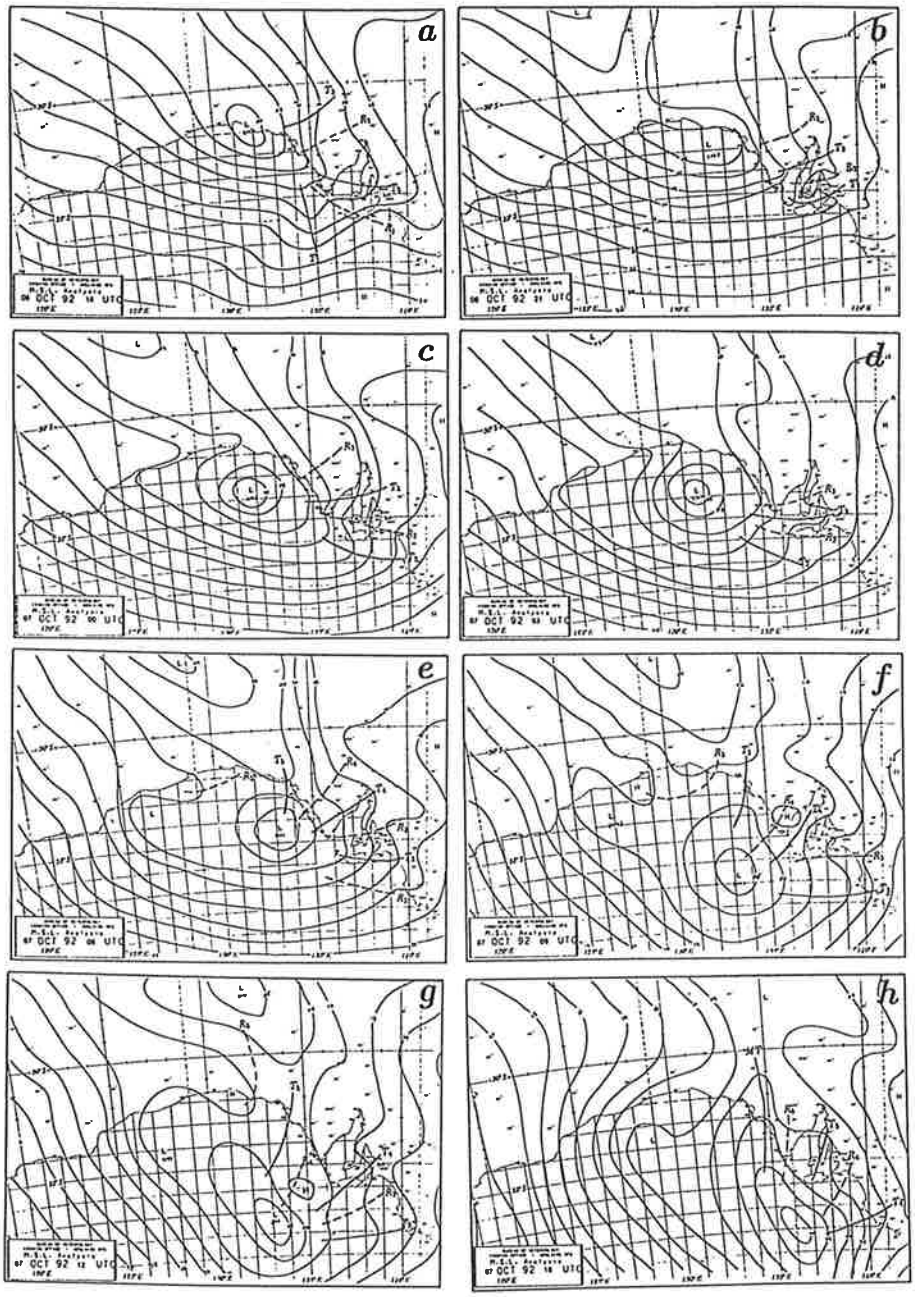

Figure B.1: MSLP surface charts from 1800UTC 06 October 1992 (a) to 1800UTC 07 October 1992 (h). Isobars are drawn in 2 hPa intervals. Minor troughs (T) and minor ridges (R) are also shown.

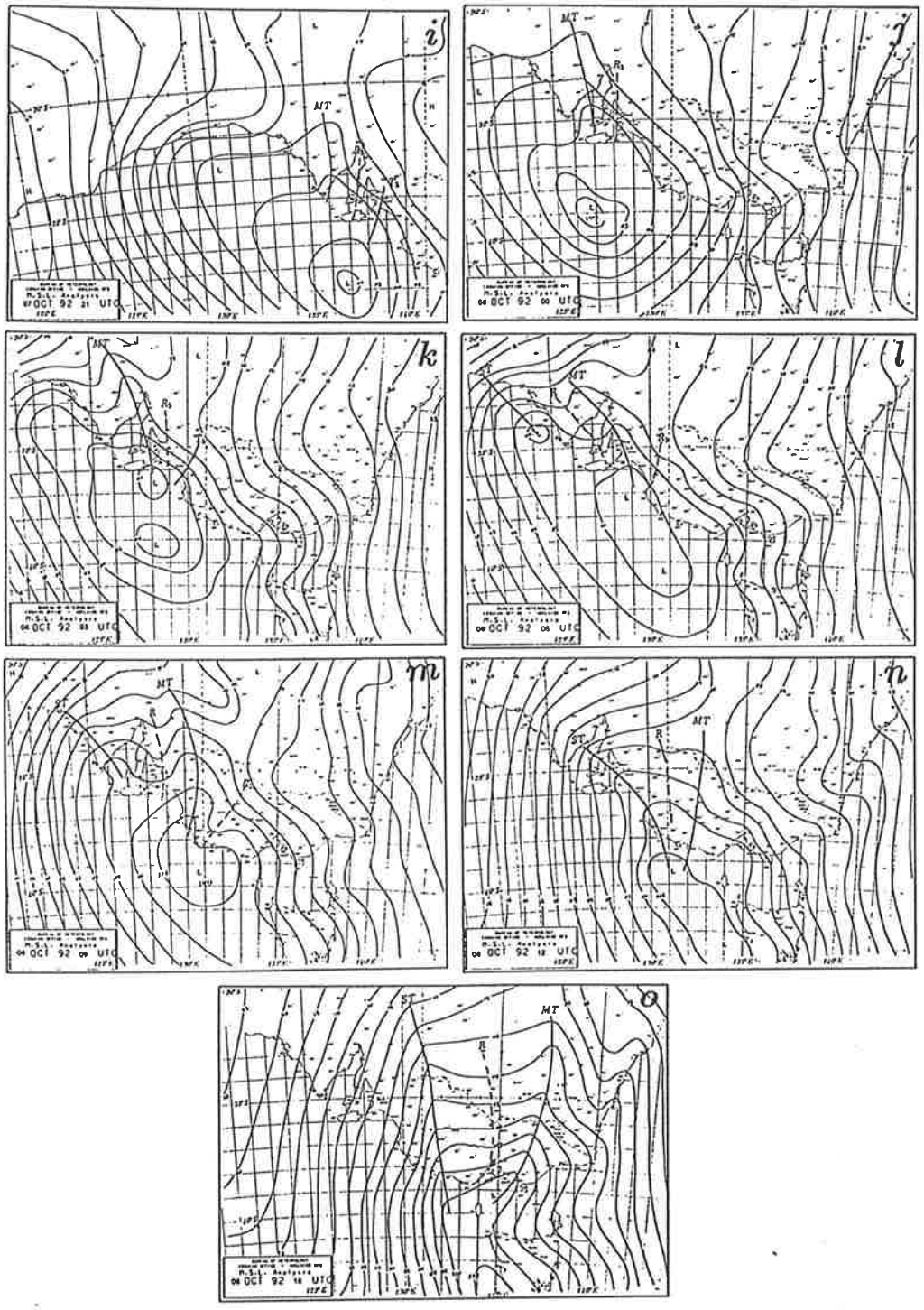

Figure B.2: MSLP surface charts from 2100 UTC 07 October 1992 (ai) to 1800 UTC 08 October 1992 (o). Isobars are drawn in 2 hPa intervals. Minor troughs (T) and minor ridges (R) are also shown.

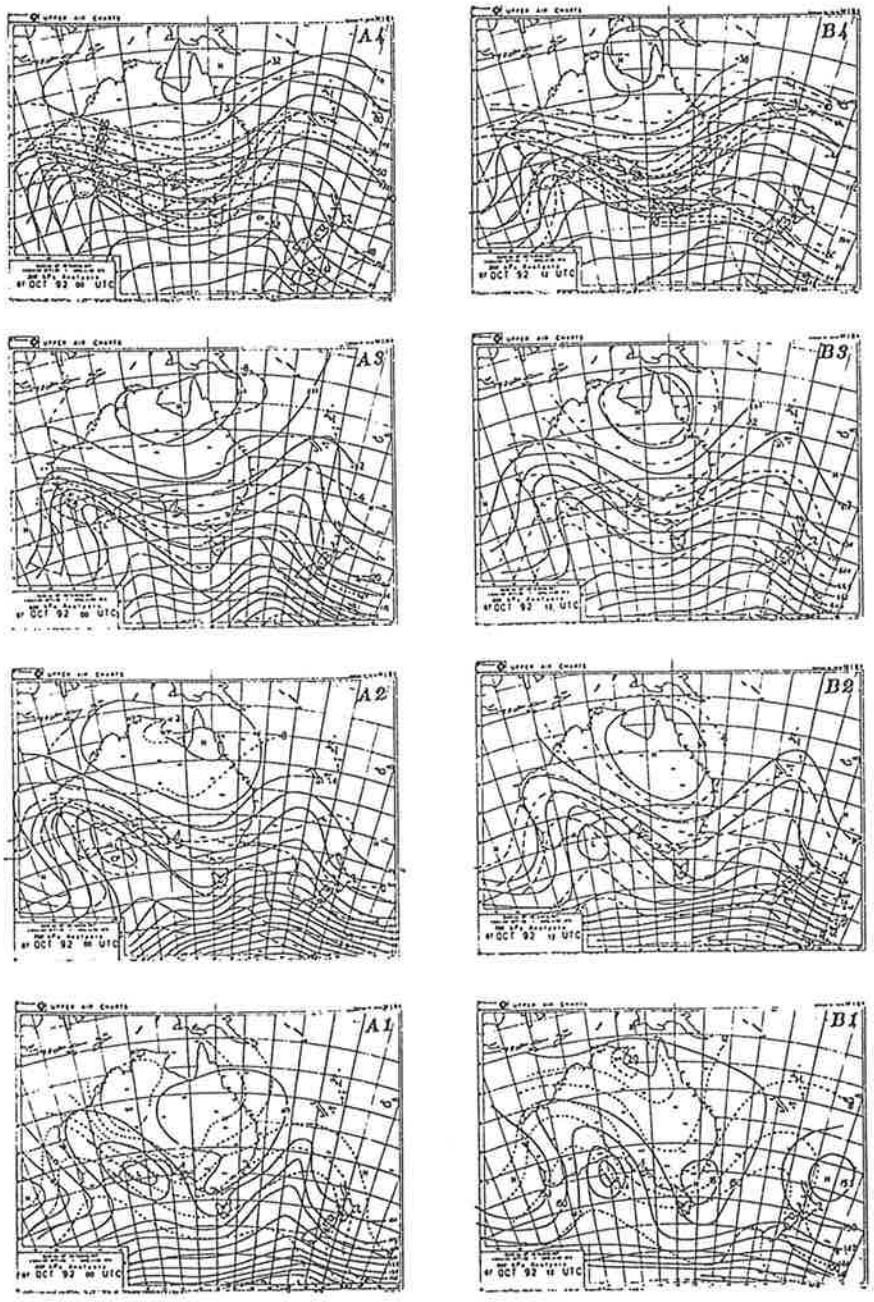

Figure B.3: Upper air charts for 0000 UTC ($A_1 - A_4$) and 1200 UTC ($B_1 - B_4$) 07 October 1992. Levels begin from 850 hPa (bottom) up to 300 hPa (top). Isotherms are drawn in 4°C intervals.

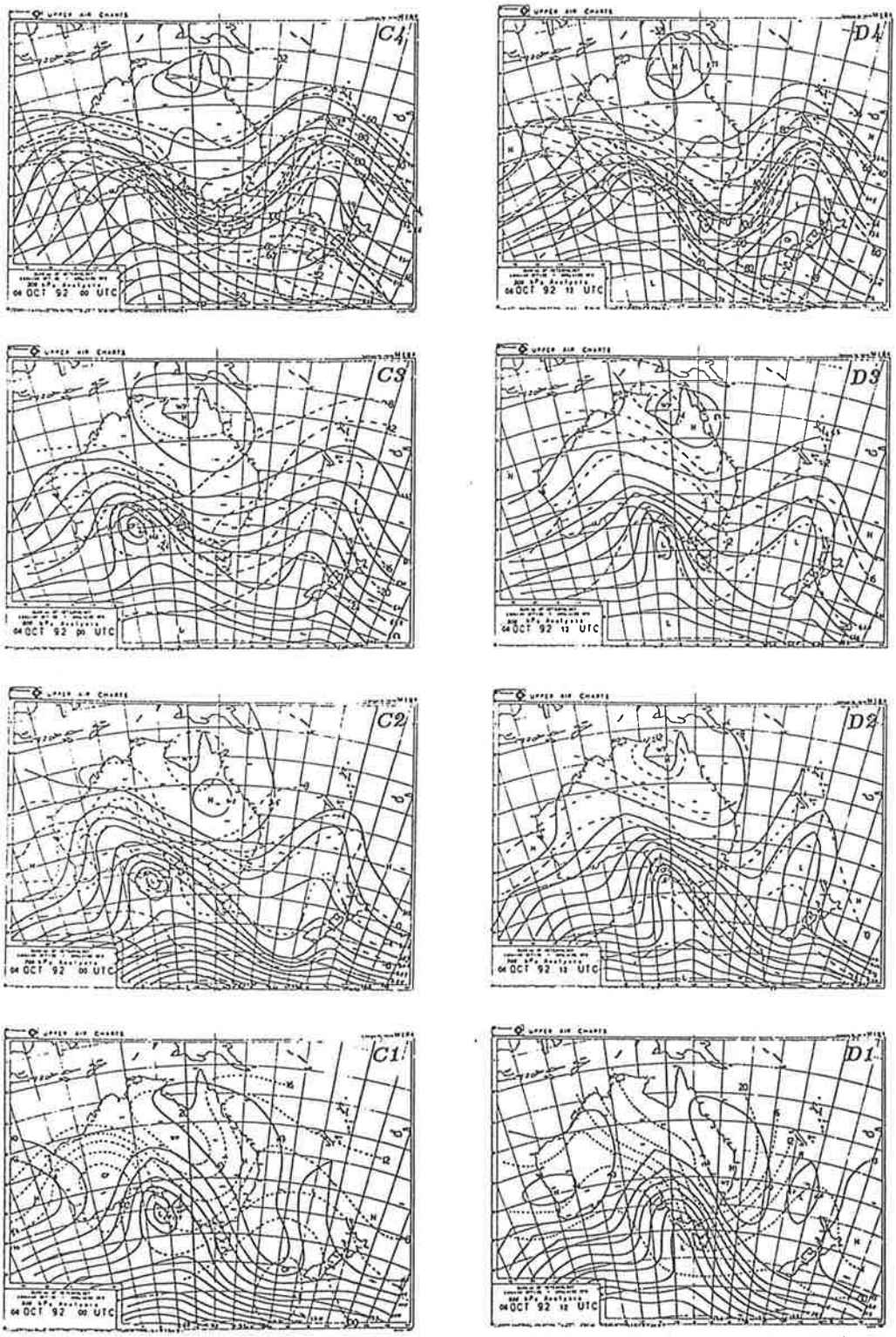

Figure B.4: Upper air charts for 0000 UTC ($C_1 - C_4$) and 1200 UTC ($D_1 - D_4$) 08 October 1992. Levels begin from 850 hPa (bottom) up to 300 hPa (top). Isotherms are drawn in $4°C$ intervals.

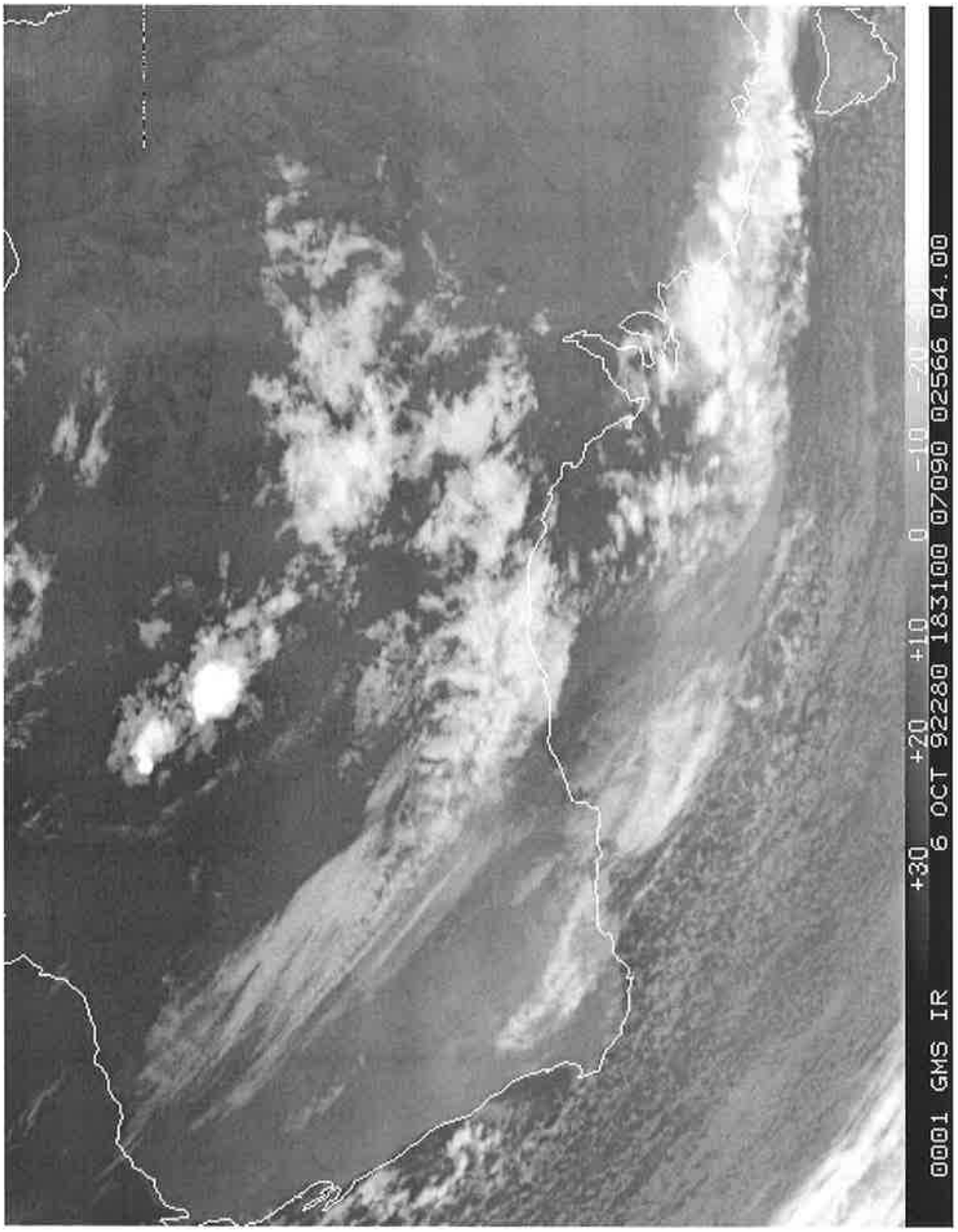

Figure B.5: GMS infrared satellite imagery for 1831 UTC 06 October 1992.

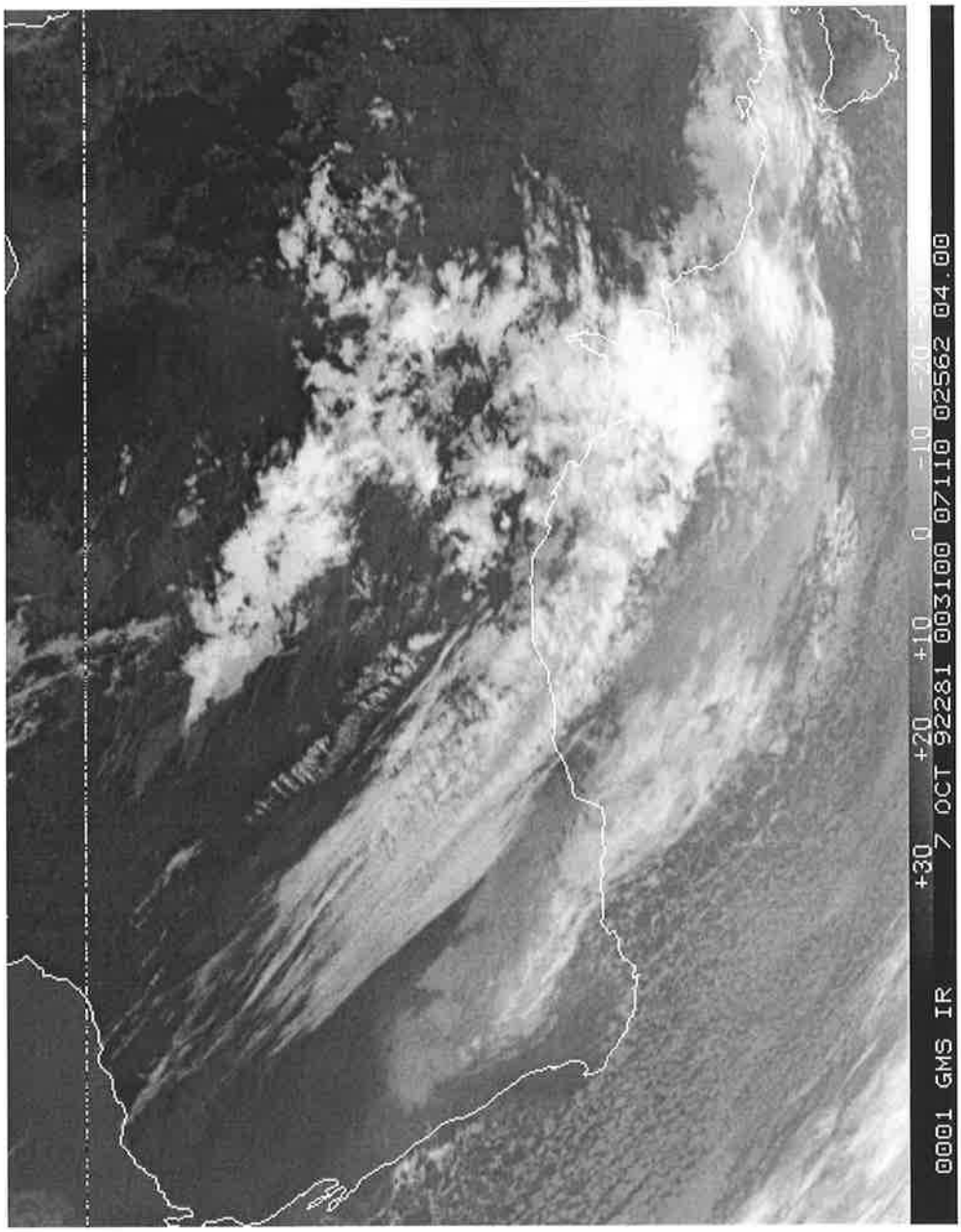

Figure B.6: GMS infrared satellite imagery for 0031 UTC 07 October 1992.

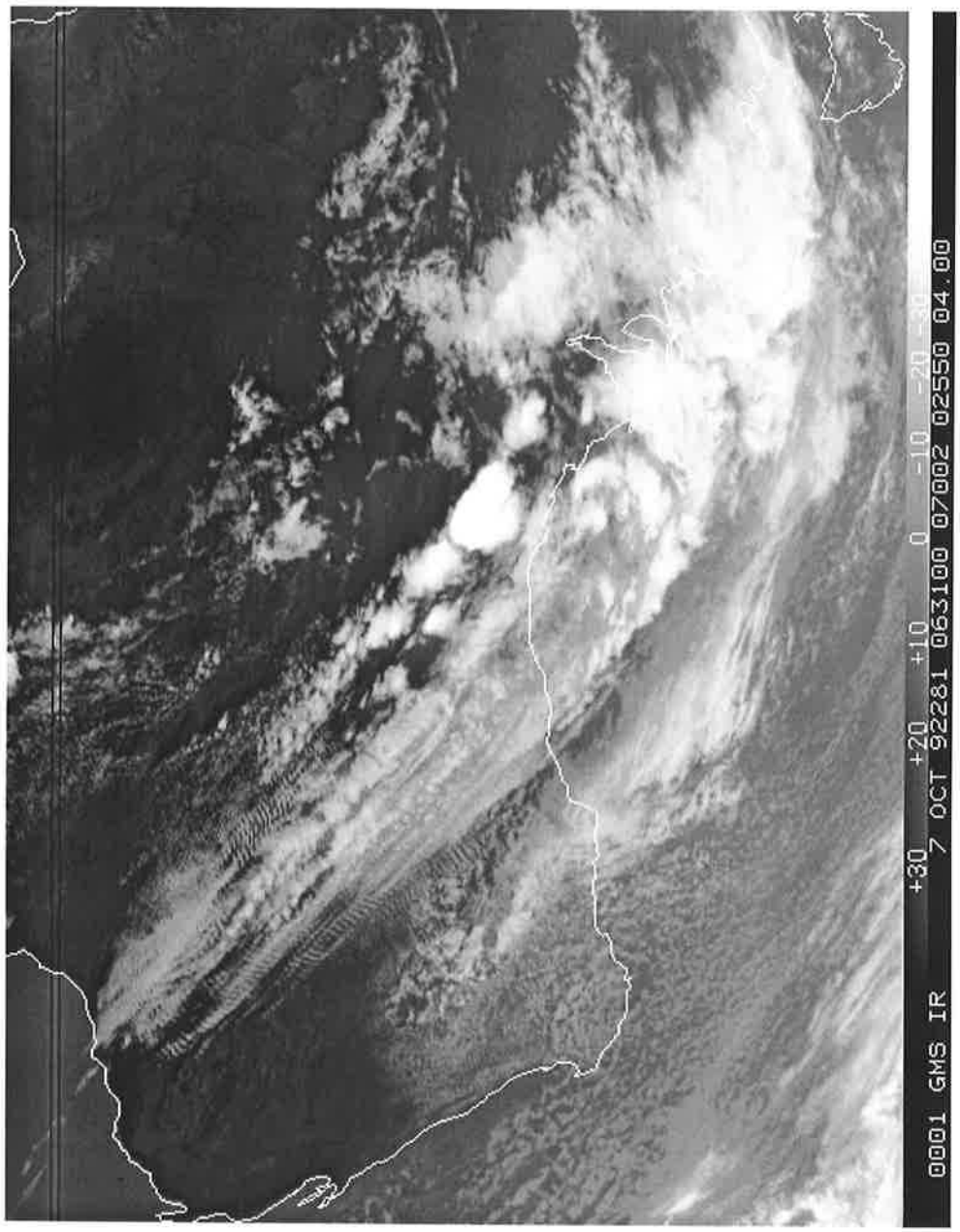

Figure B.7: GMS infrared satellite imagery for 0631 UTC 07 October 1992.

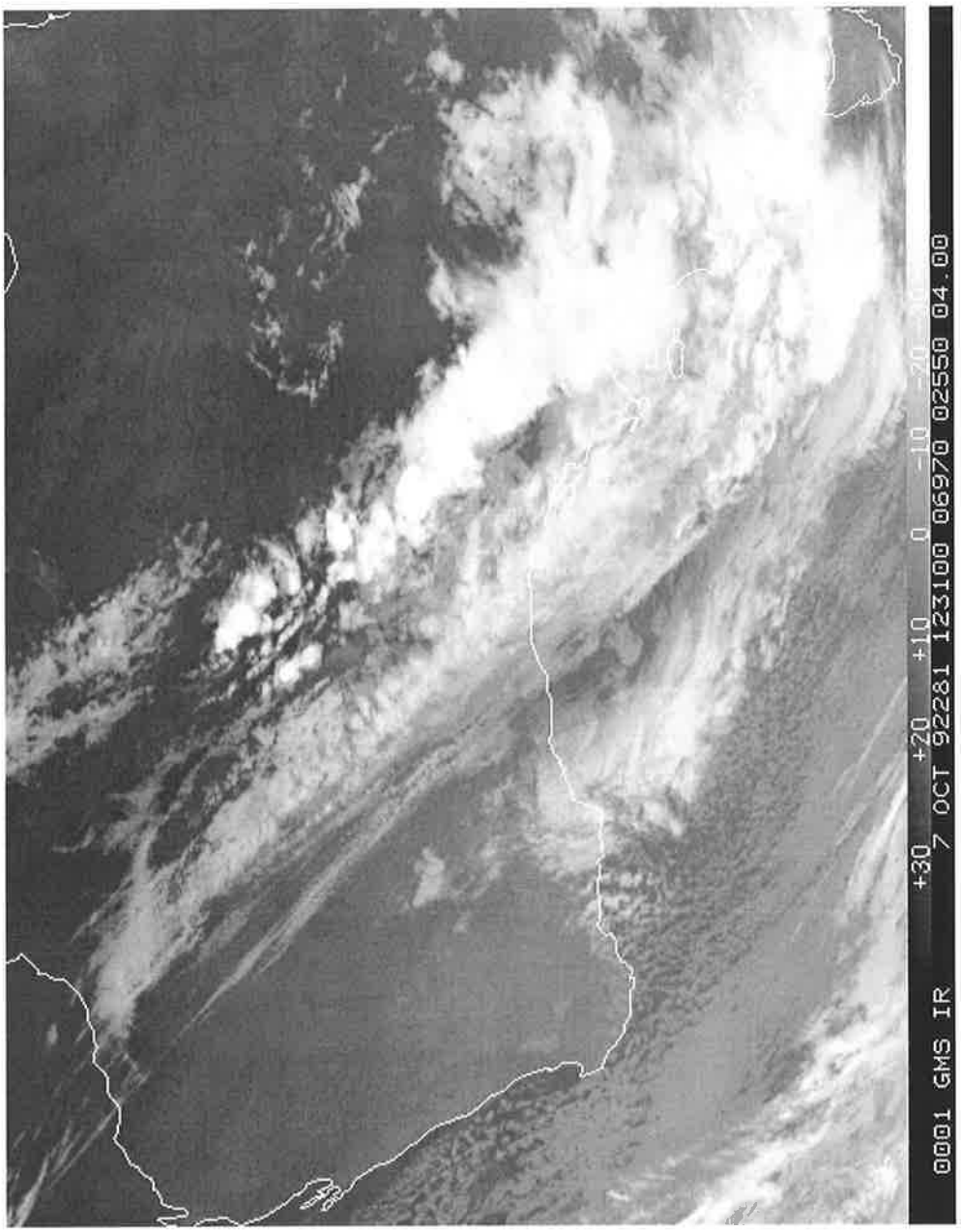

Figure B.8: GMS infrared satellite imagery for 1231 UTC 07 October 1992.

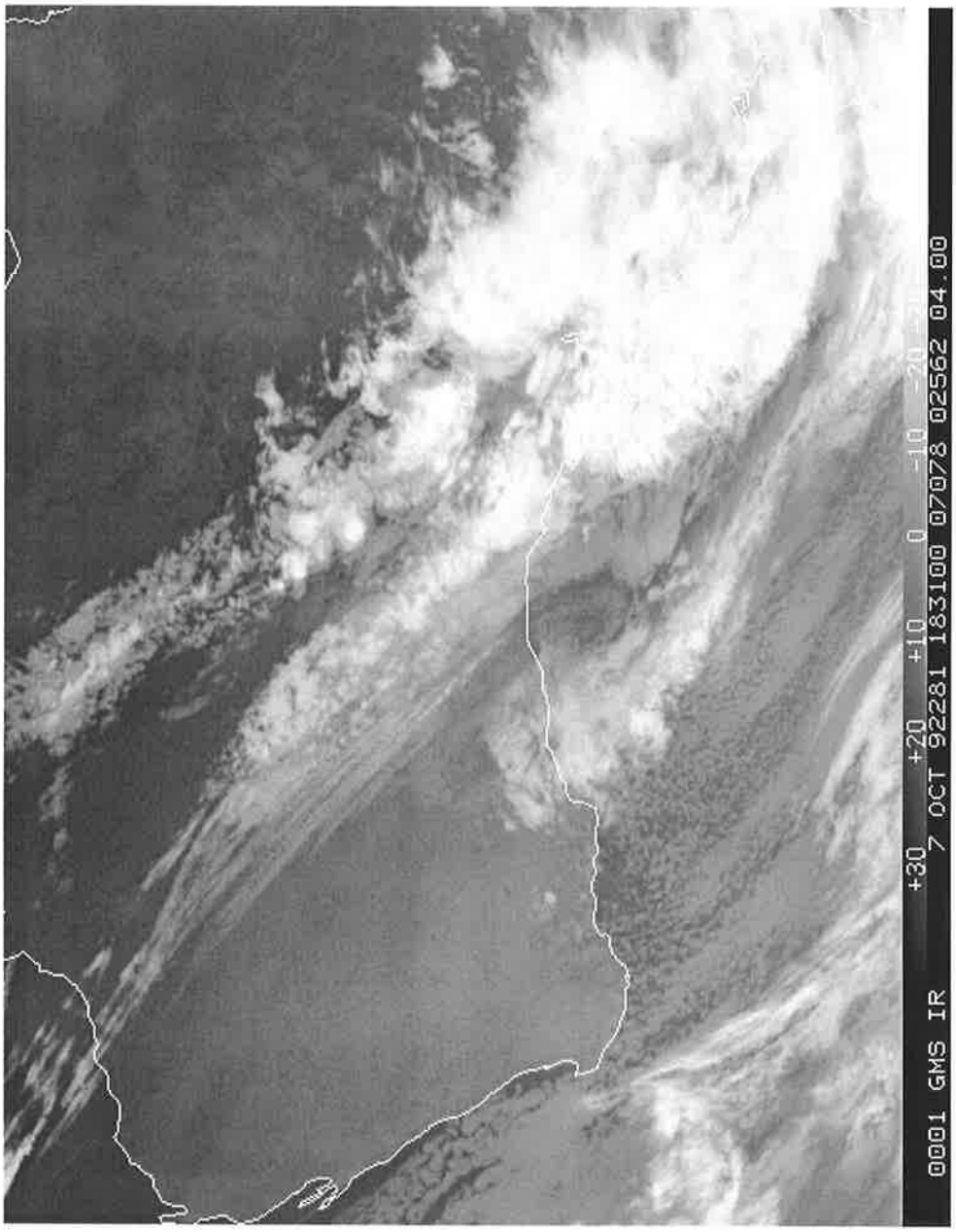

Figure B.9: GMS infrared satellite imagery for 1831 UTC 07 October 1992.

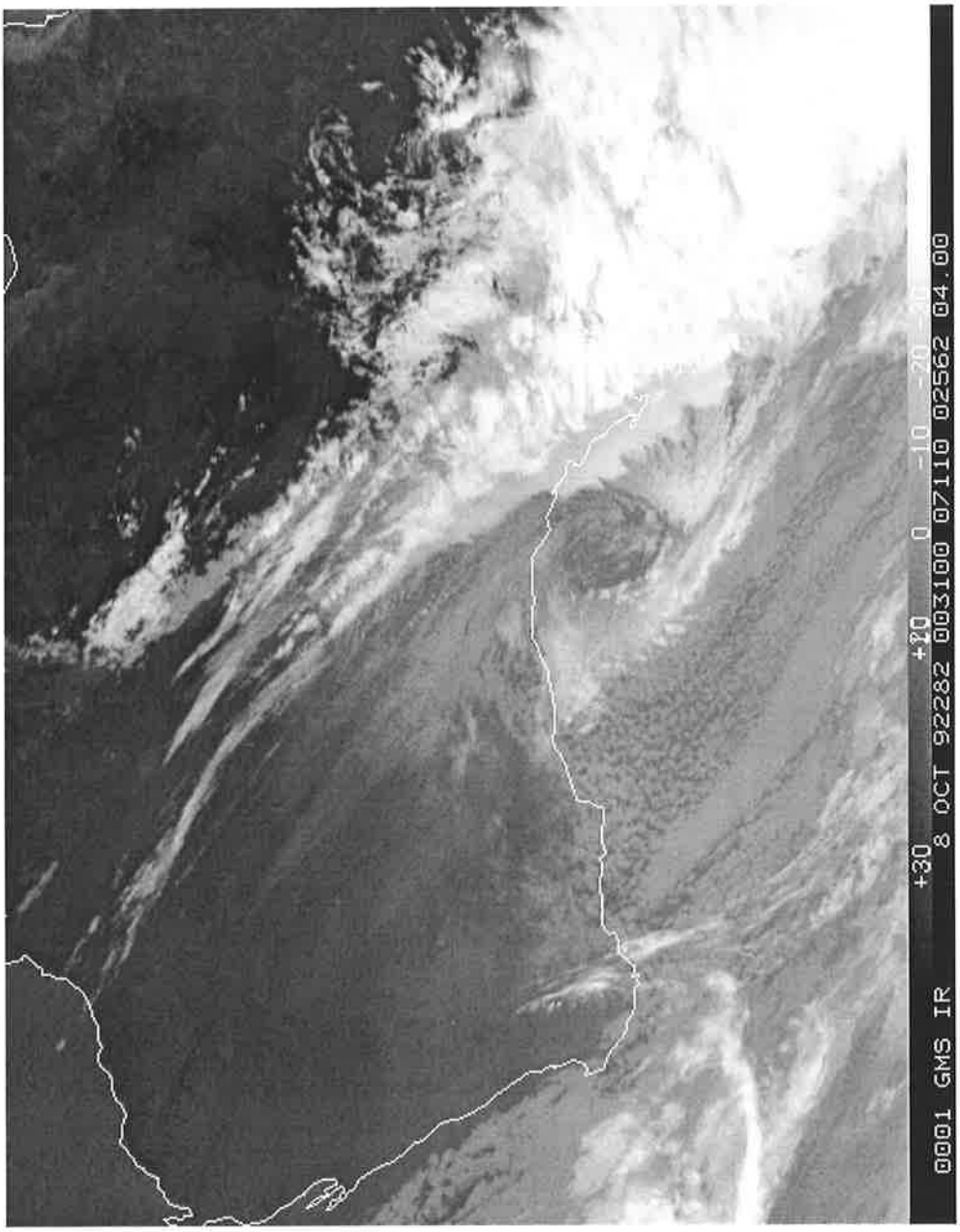

Figure B.10: GMS infrared satellite imagery for 0031 UTC 08 October 1992.

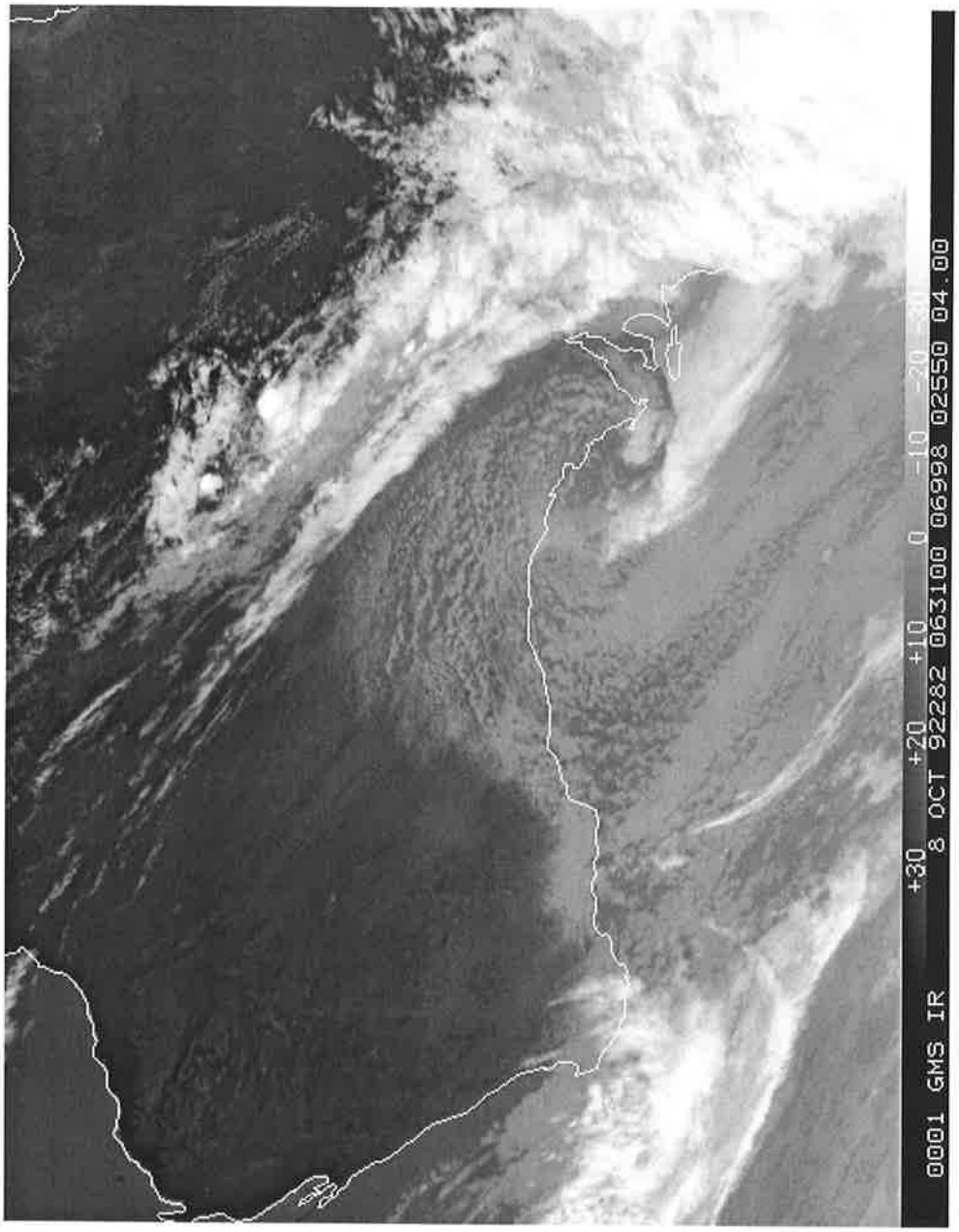

Figure B.11: GMS infrared satellite imagery for 0631 UTC 08 October 1992.

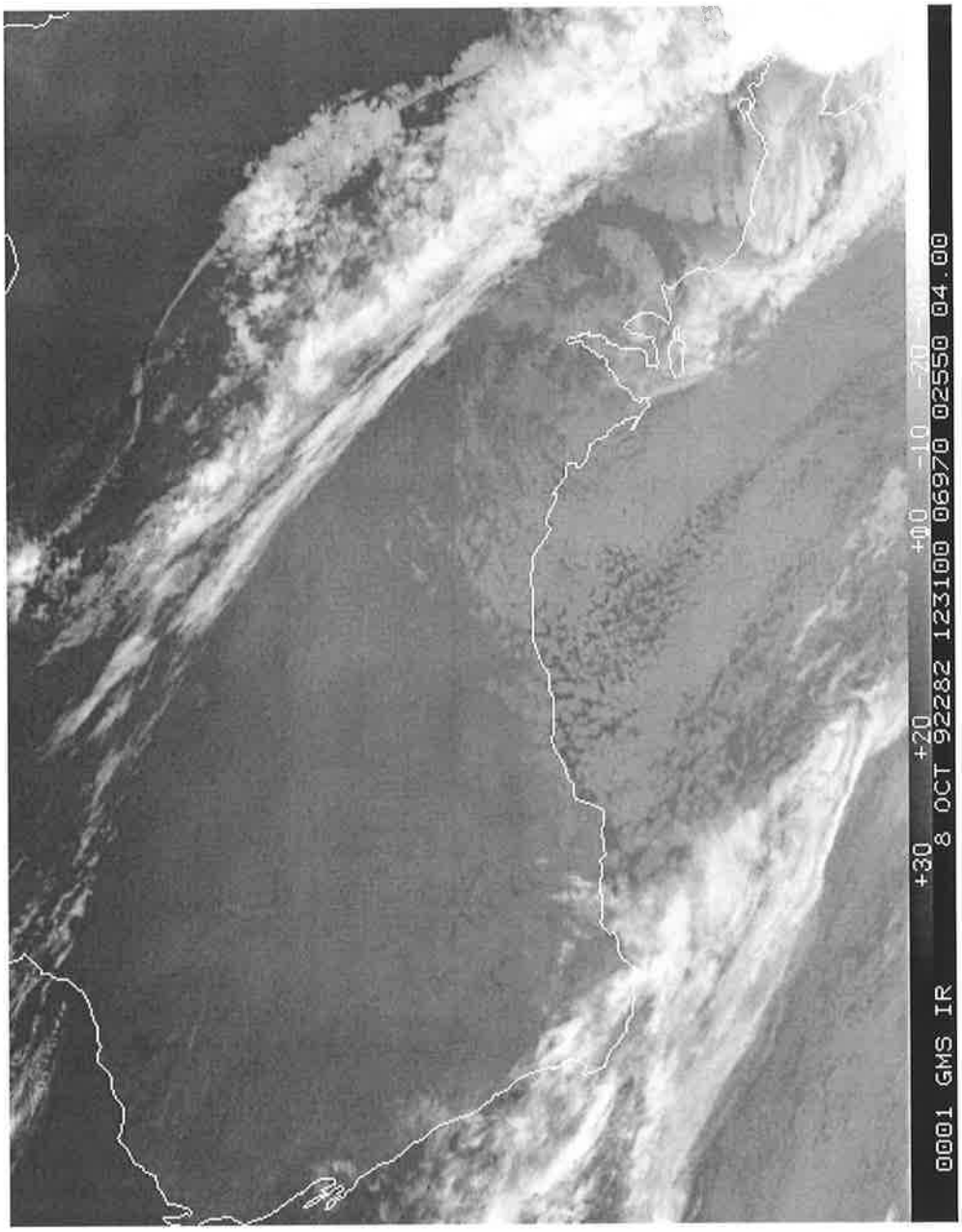

Figure B.12: GMS infrared satellite imagery for 1231 UTC 08 October 1992.

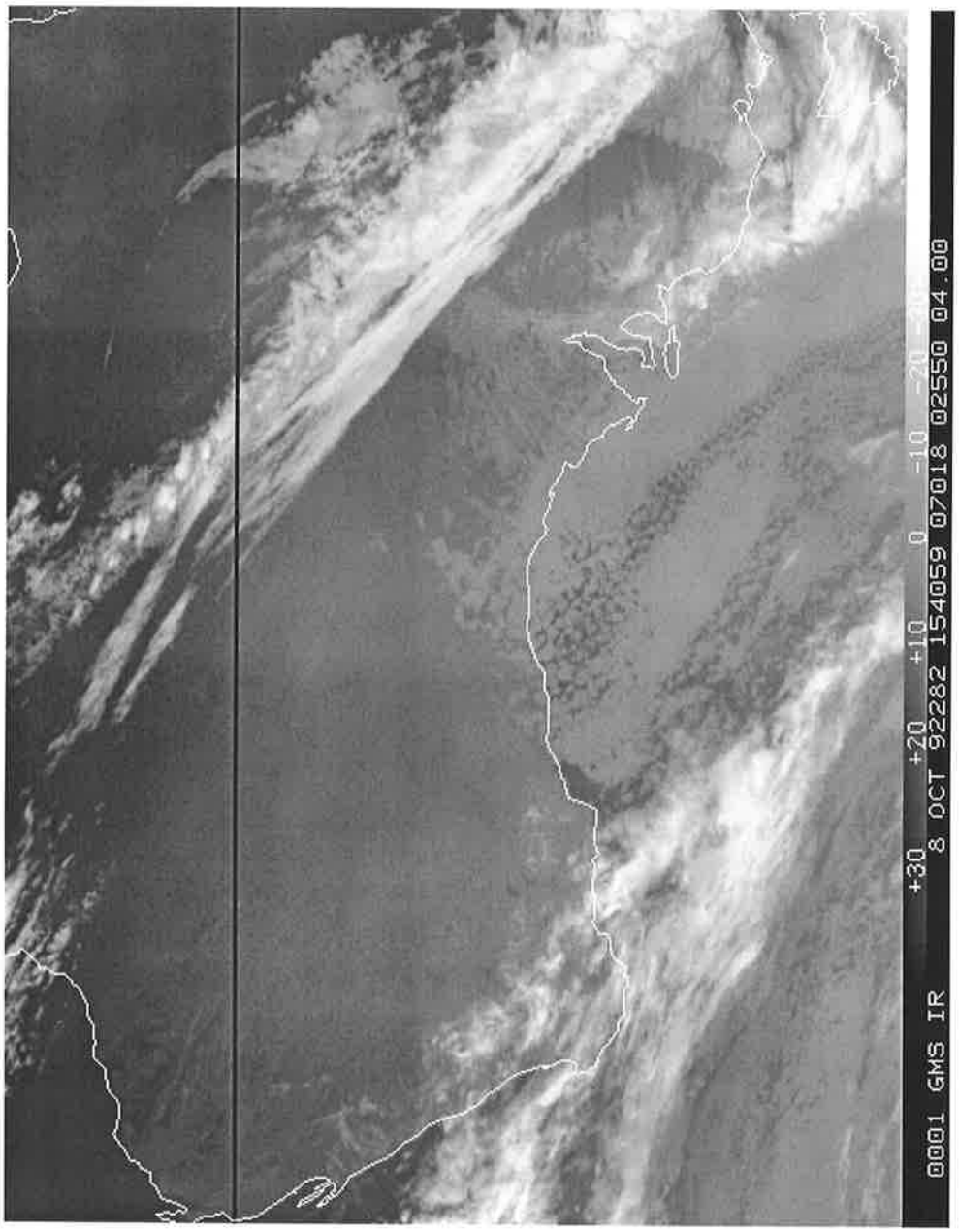

Figure B.13: GMS infrared satellite imagery for 1540 UTC 08 October 1992.

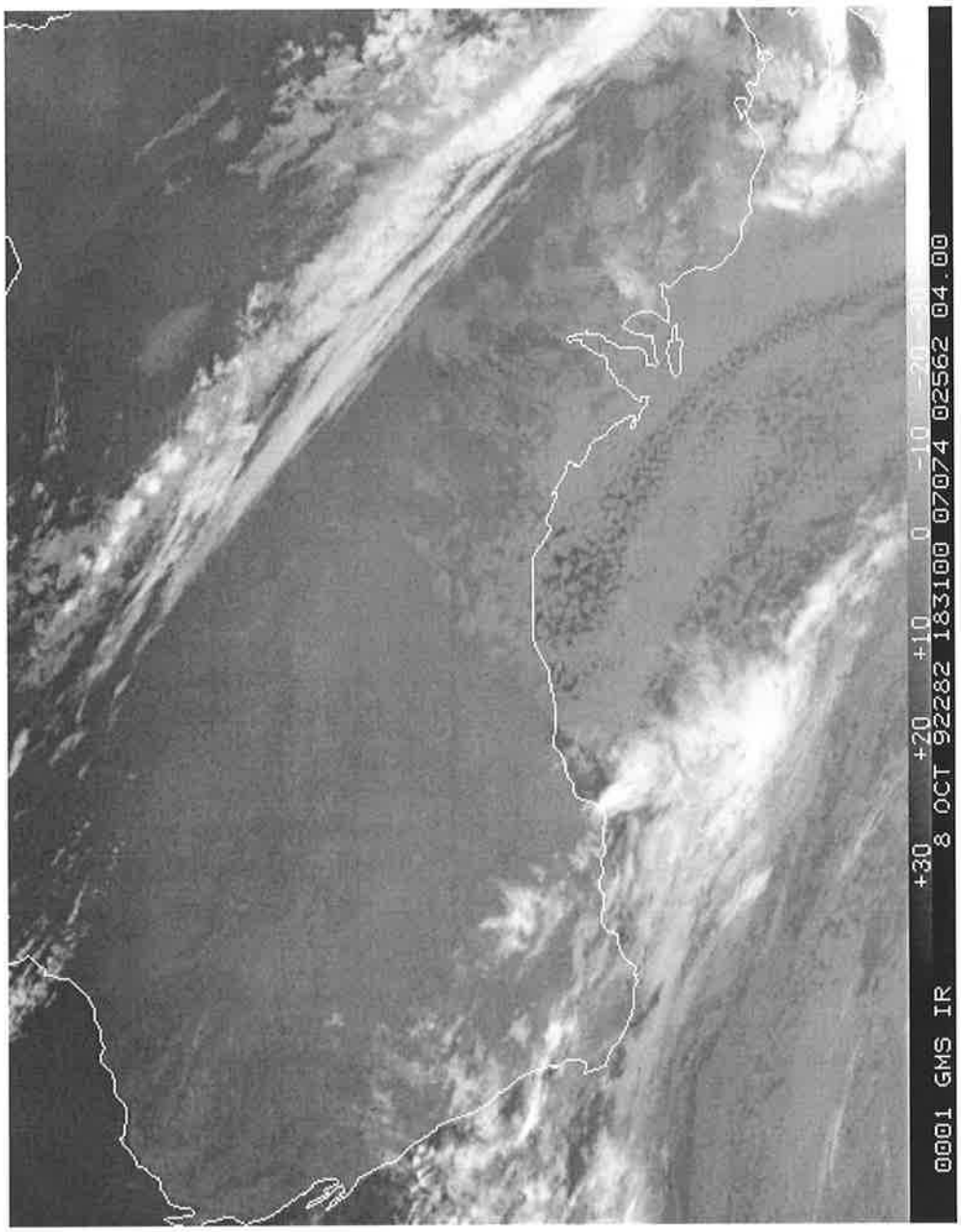

Figure B.14: GMS infrared satellite imagery for 1831 UTC 08 October 1992.

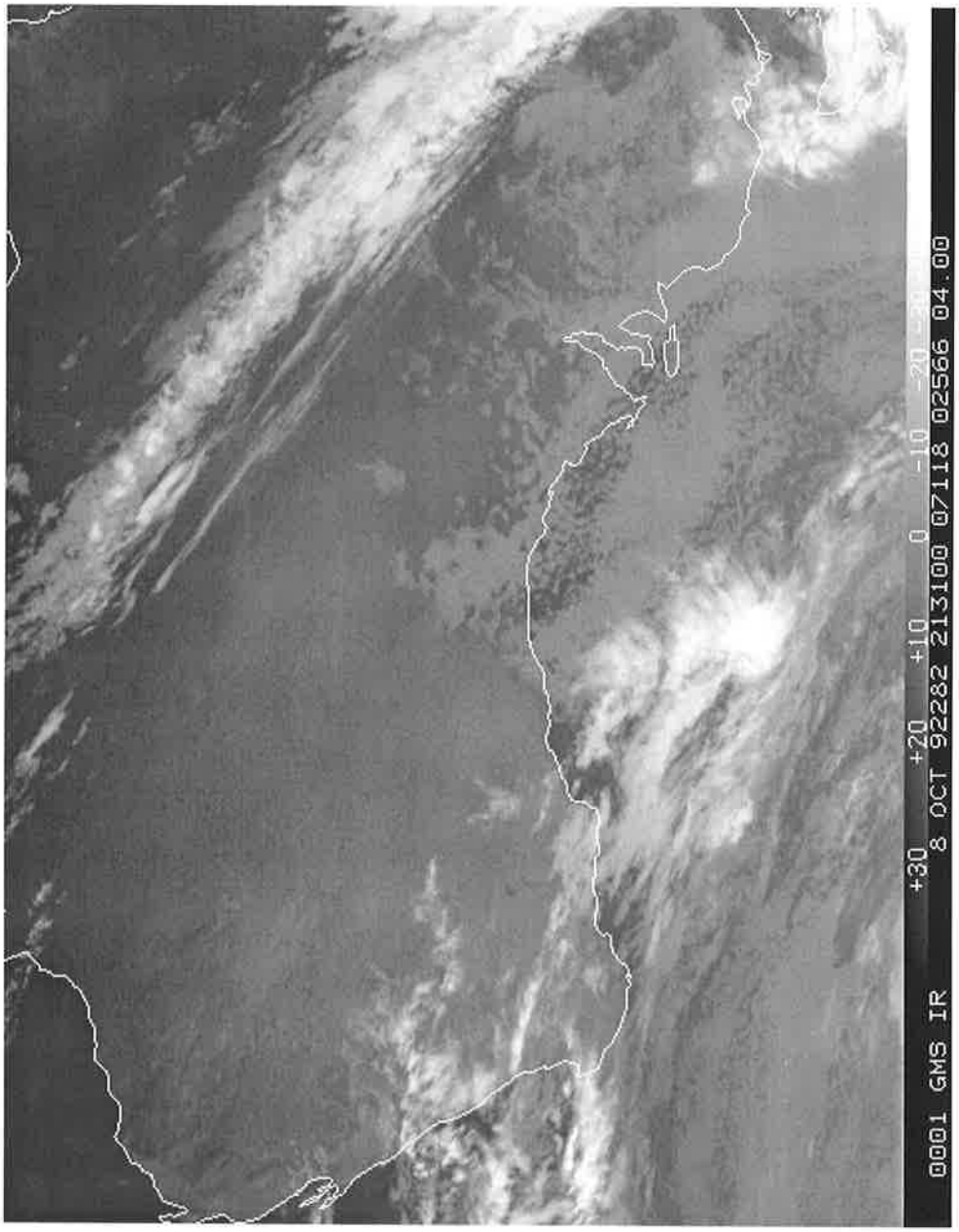

Figure B.15: GMS infrared satellite imagery for 2131 UTC 08 October 1992.

Appendix C

Charts and Images For Case Study II

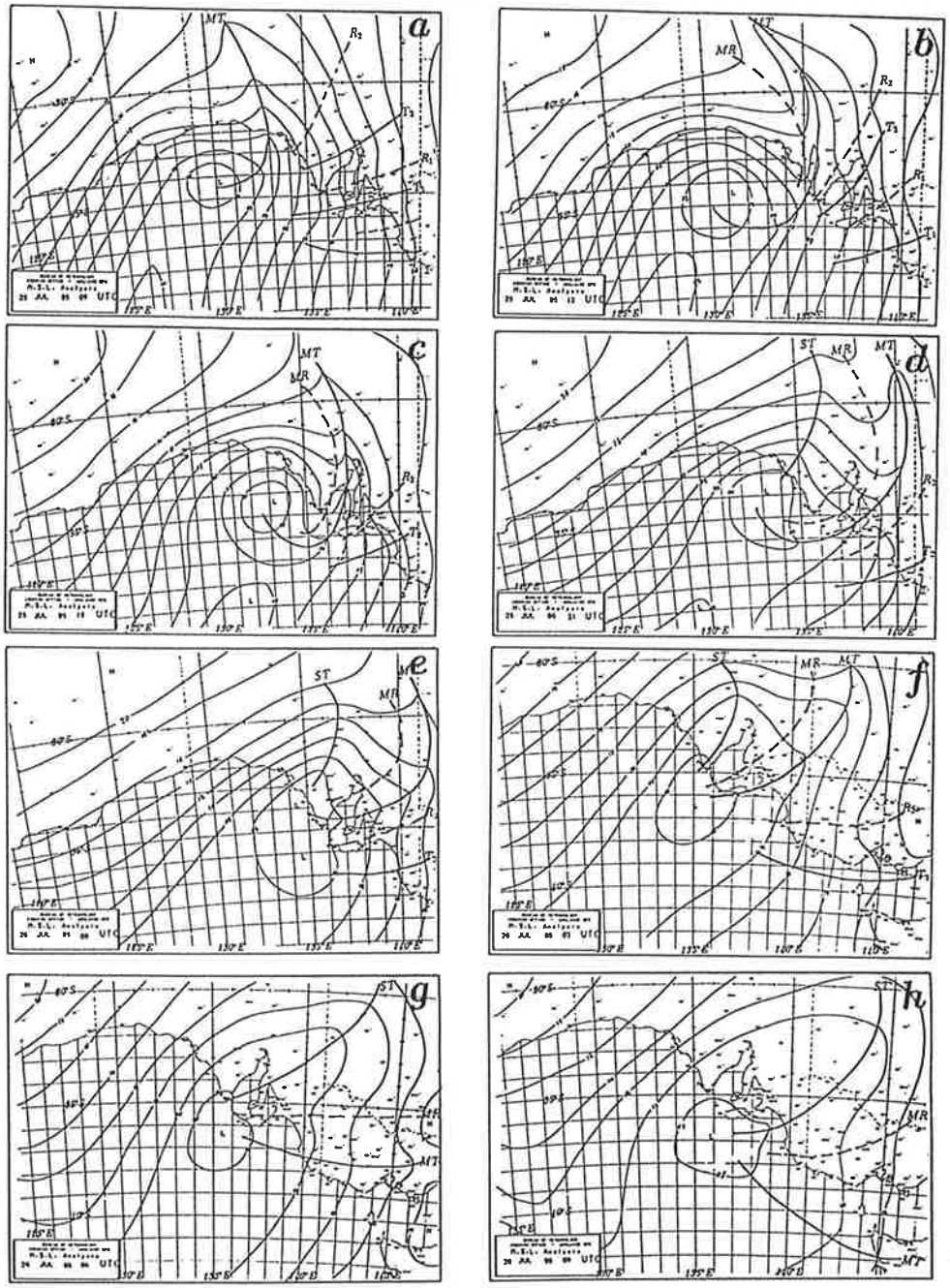

Figure C.1: MSLP surface charts from 0900 UTC 25 July 1995 (a) to 0900 UTC 26 July 1995 (h). Isobars are drawn in 2 hPa intervals. Minor troughs (T) and minor ridges (R) are also shown.

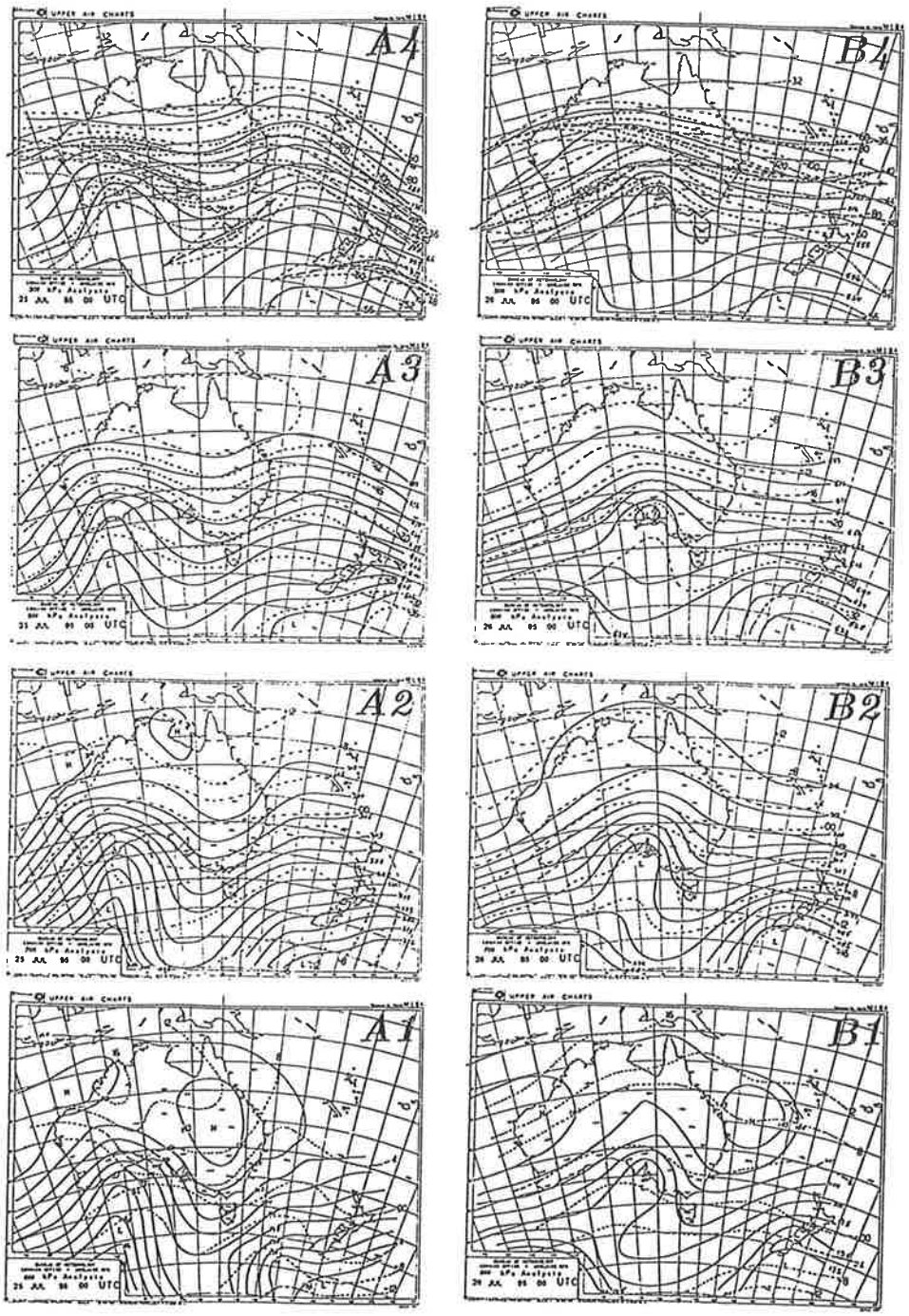

Figure C.2: Upper air charts for 0000 UTC 25 July 1995 ($A_1 - A_4$) and 0000 UTC 26 July 1995 ($B_1 - B_4$). Levels begin from 850 hPa (bottom) up to 300 hPa (top). Isotherms are drawn in 4°C intervals.

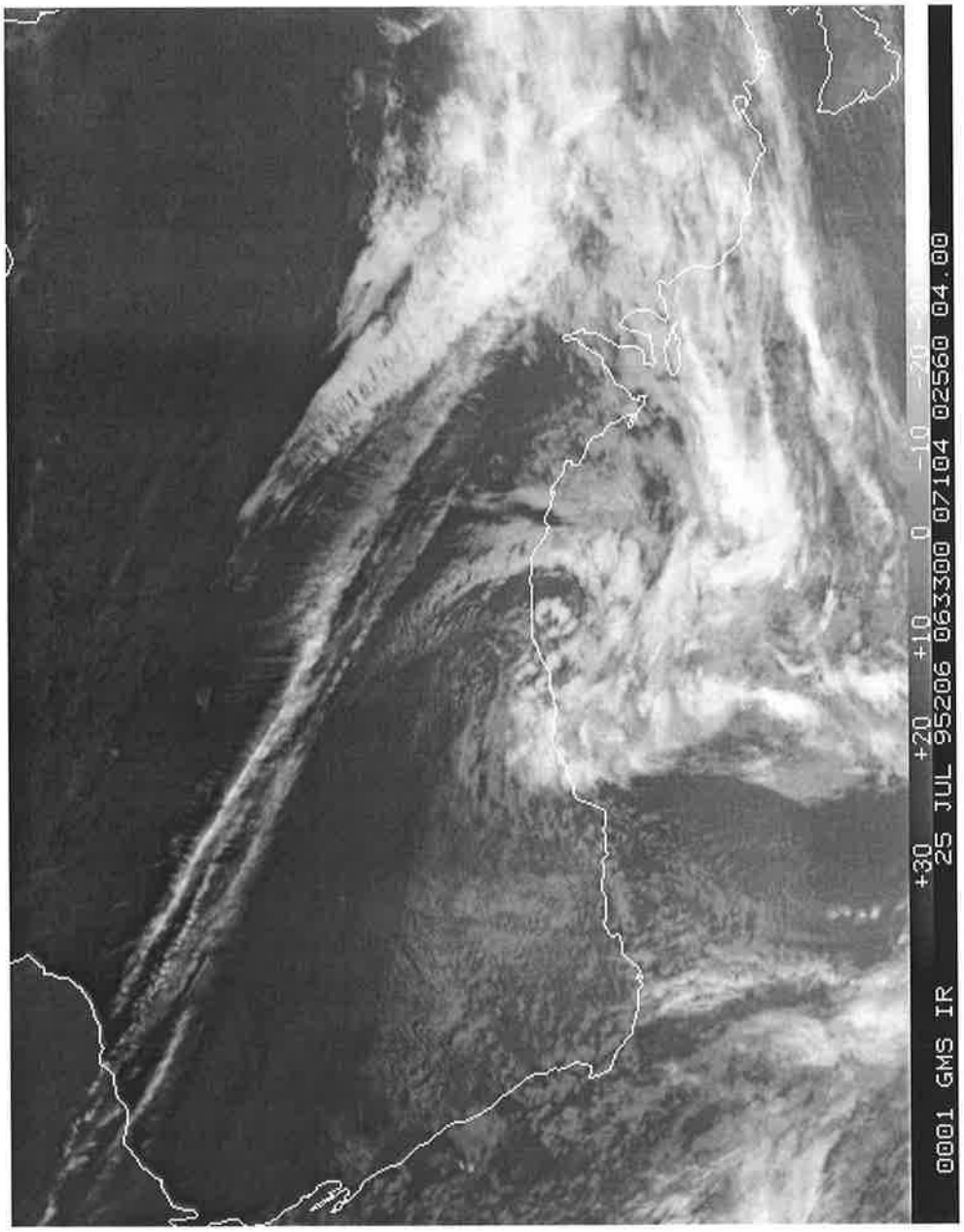

Figure C.3: GMS infrared satellite imagery for 0633 UTC 25 July 1995.

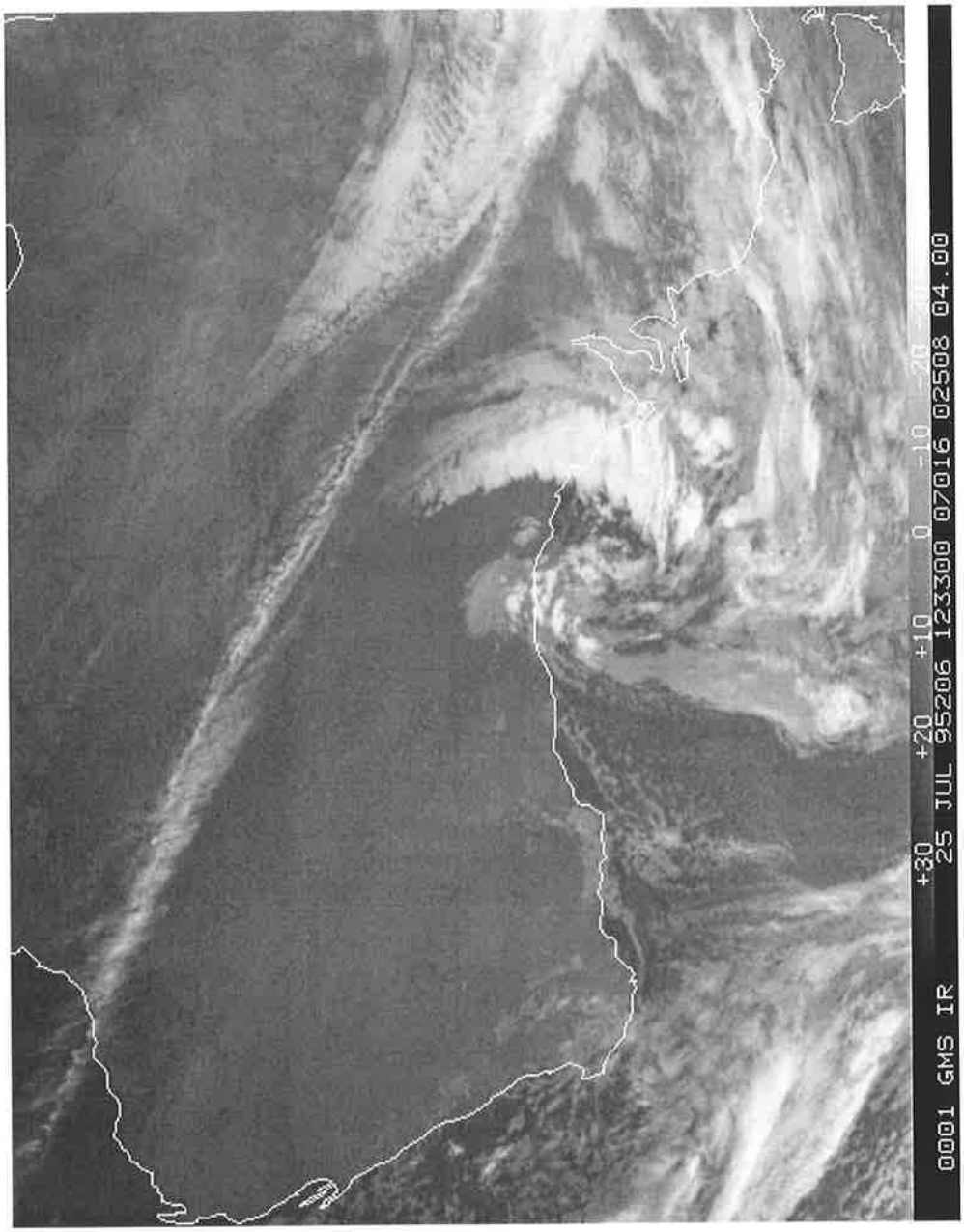

Figure C.4: GMS infrared satellite imagery for 1233 UTC 25 July 1995.

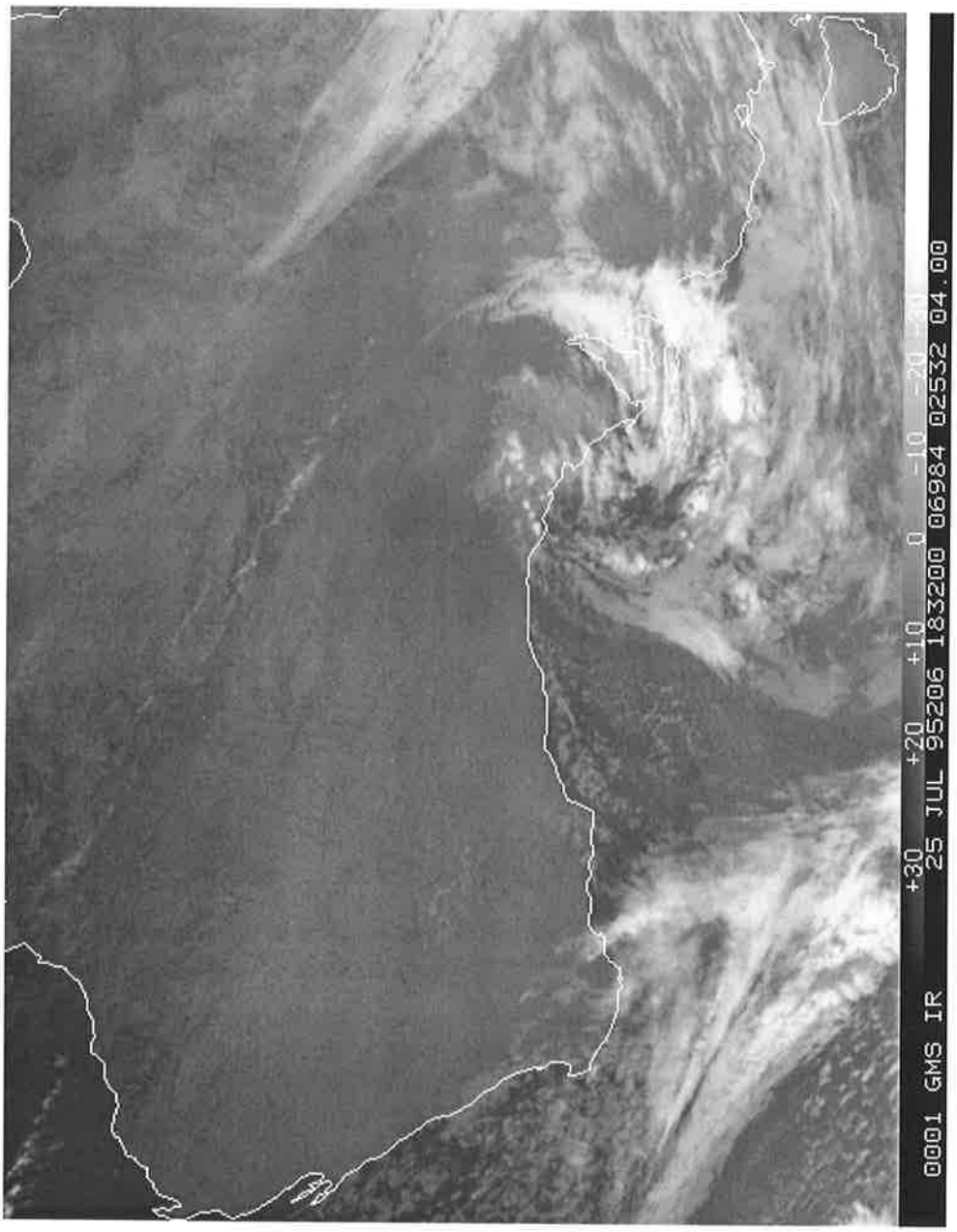

Figure C.5: GMS infrared satellite imagery for 1833 UTC 25 July 1995.

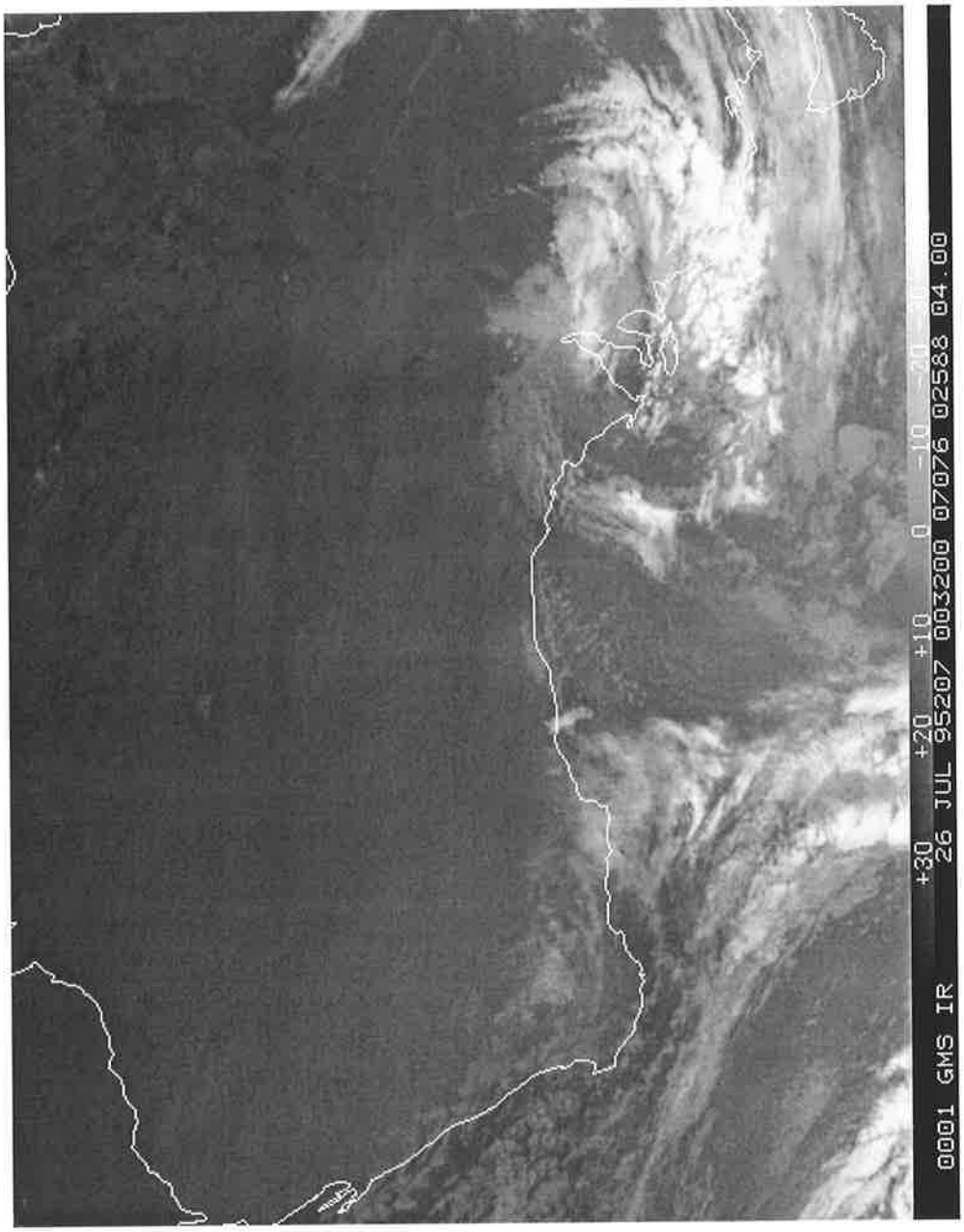

Figure C.6: GMS infrared satellite imagery for 0032 UTC 26 July 1995.

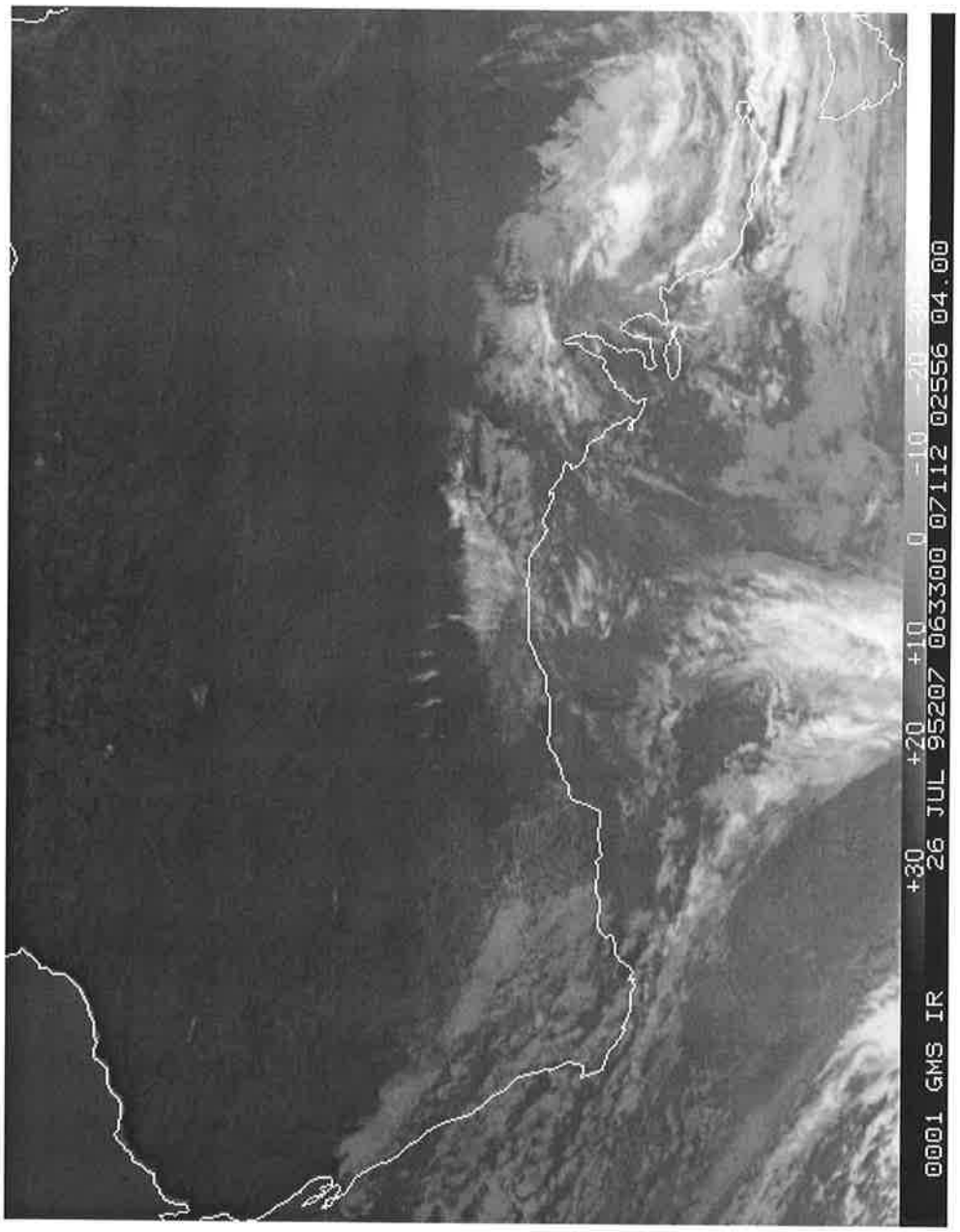

Figure C.7: GMS infrared satellite imagery for 0633 UTC 26 July 1995.

Appendix D

Unique Features Observed by Wind Profiler

Wind profilers are capable of depicting the unique and very important features of the atmosphere from the viewpoint of "nowacasting", "analysis" of meteorological charts, "forecasting", and "aviation". These features could not be depicted otherwise with the normal meteorological facilities at forecasting centers.

The ability to take measurements with a very high temporal and spatial resolution is one of the special characteristics of wind profilers. They are relatively inexpensive and cost effective and can operate at remote areas unattended for long periods.

During the massive analysis of Buckland Park VHF radar data for different case studies, the author came across some odd aspects of the atmosphere and decided that, it would not be good to represent only selective ones with a limited discussion.

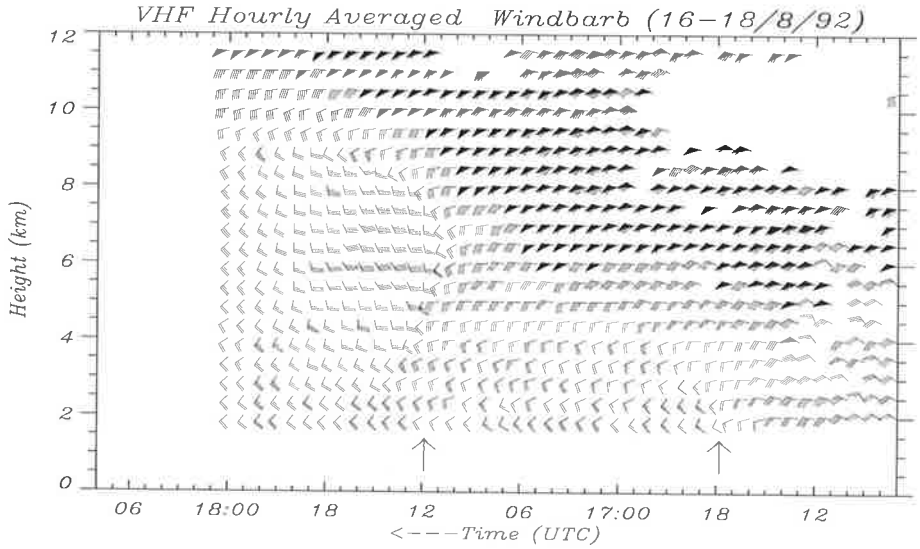

Figure D.1: VHF hourly averaged windbarbs (*knts*) on 16th and 17th August 1992, showing a split sharp trough. The lower portion of the trough is moving ahead of the main trough by almost a day. The position of troughs is shown by vertical arrows.

D.1 Split Trough

A splitted trough is shown in Figure D.1. The upper portion of trough is sharper than the lower part (location is shown by vertical arrows). The lower portion is moving ahead (time scale is backward!) of the main trough by almost a day. These features might cause confusion for the forecasters.

D.2 Vortex aloft

A vortex at high altitudes without showing any sign or trace at low altitudes is shown in Figure D.2. The vortex which is centered at about 11 km height at about 14:00 UTC 27th May 1993, is characterized by two distinctive troughs. One of the troughs is elongated eastward and slightly upward while the other, stretched westward and downward to about 5 km. The center position of the

vortex relative to the ground is shown by vertical arrows. There is no indication of either the vortex or the trough below 5 km height.

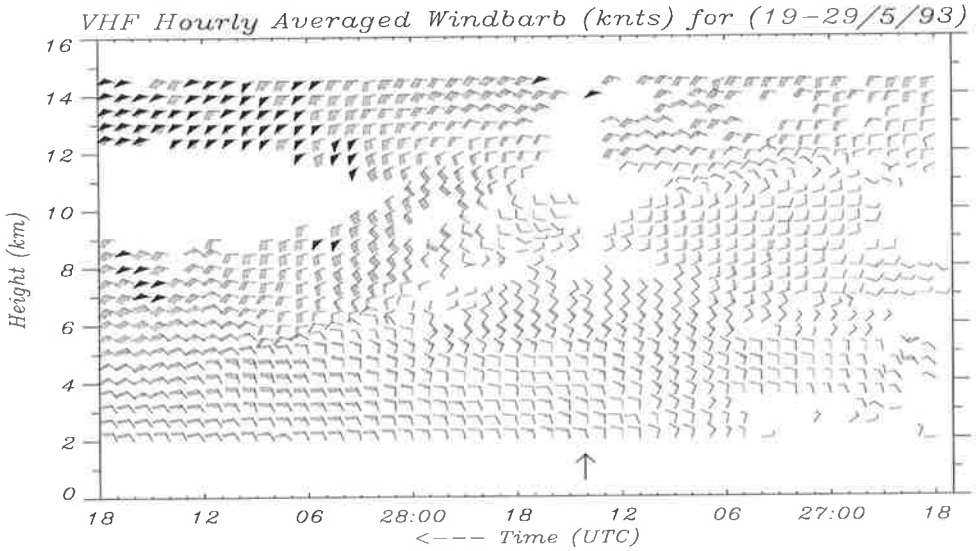

Figure D.2: VHF hourly averaged windbarbs (*knts*) showing a vortex at about 11 km at 14:00 UTC with two elongated troughs.

D.3 Eastward Oriented Trough

Figure D.3 shows two cases of eastward oriented troughs one of which, is extended from low levels up to about 11 km height while, the other extended from low levels to about 5 km with relatively shallow slope.

Figure D.4 illustrates an eastward oriented trough expanding up to about 10 km height.

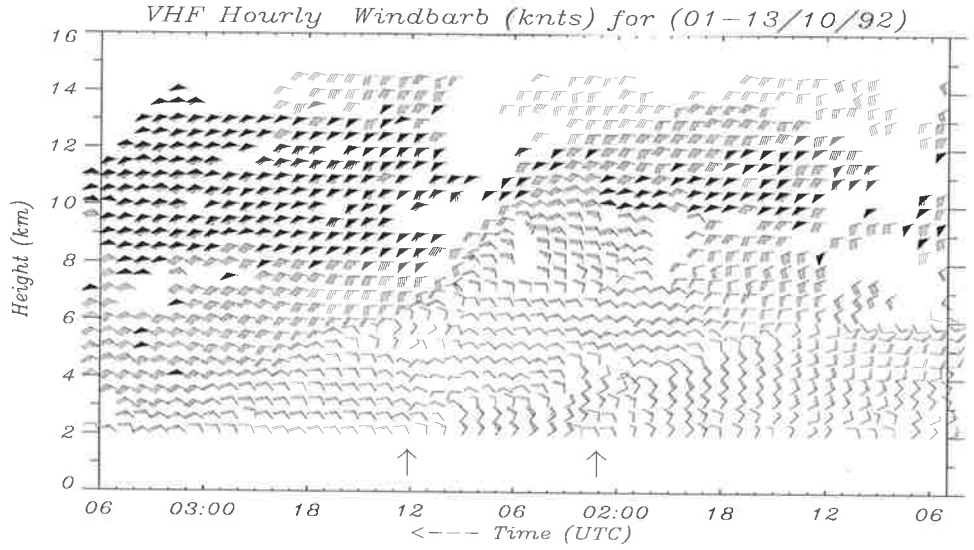

Figure D.3: VHF hourly averaged windbarbs (*knts*) showing two troughs extending eastward and upward.

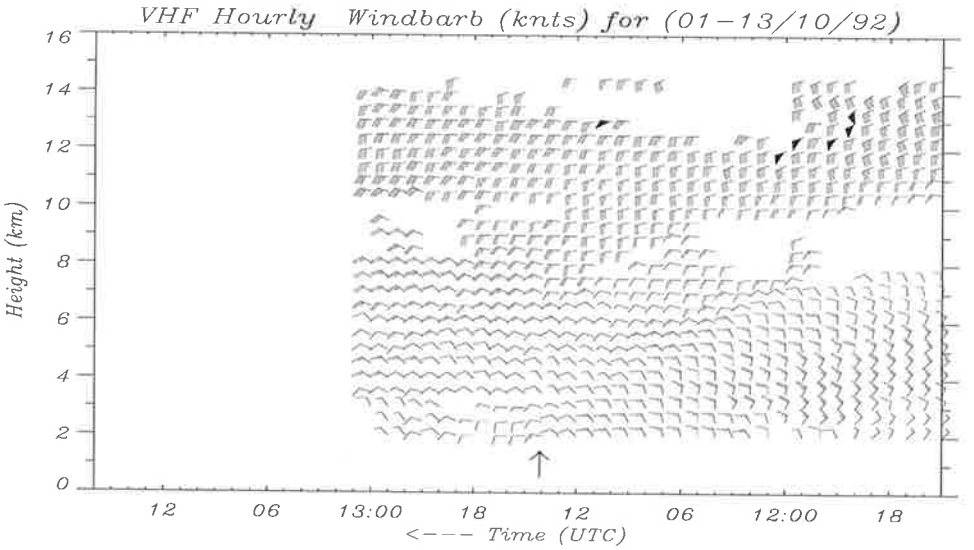

Figure D.4: VHF hourly averaged windbarbs (*knts*) showing an eastward oriented trough.

D.4 Westward Oriented Trough

The westward oriented trough is well shown in Figure D.5 & D.6. In both figures the trough is clearly marked and extended from low levels westward and upward up to about 8 km height with relatively sharp slope.

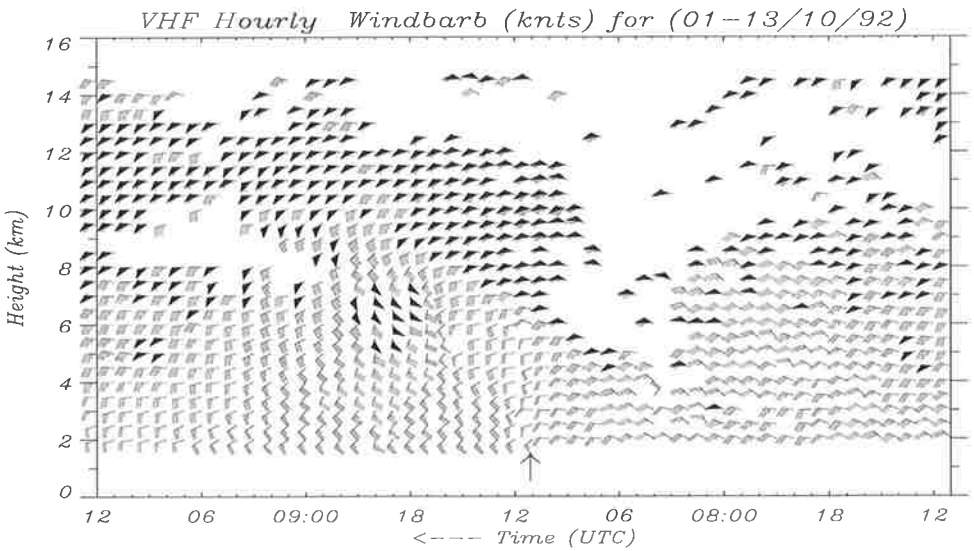

Figure D.5: VHF hourly averaged windbarbs (*knts*) showing the westward oriented trough.

D.5 Upper Shallow Trough

Shallow troughs are clearly detectable by a wind profiler. Figure D.7 shows a shallow trough at high altitudes from 8 km to about 11 km without showing any trace of a trough at low levels.

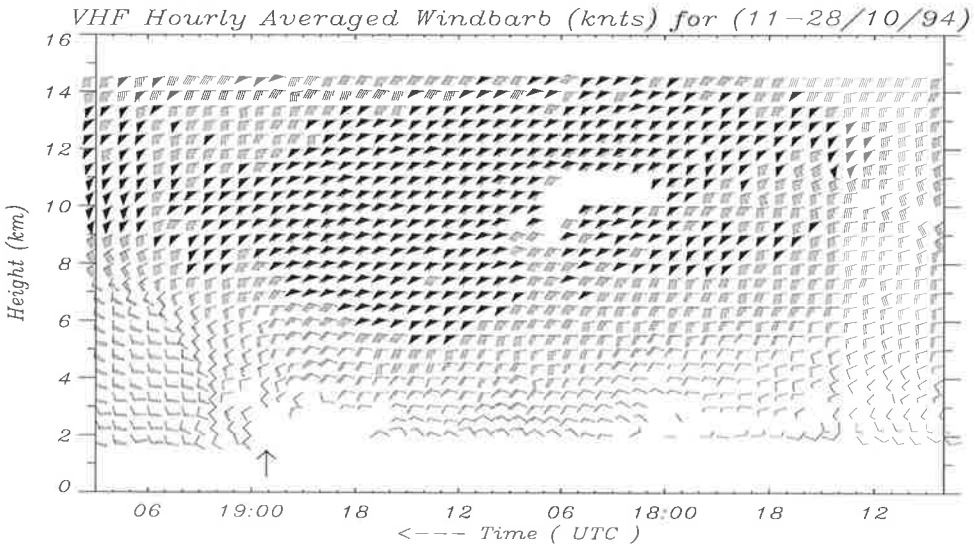

Figure D.6: VHF hourly averaged windbarbs (*knts*) showing the westward oriented trough.

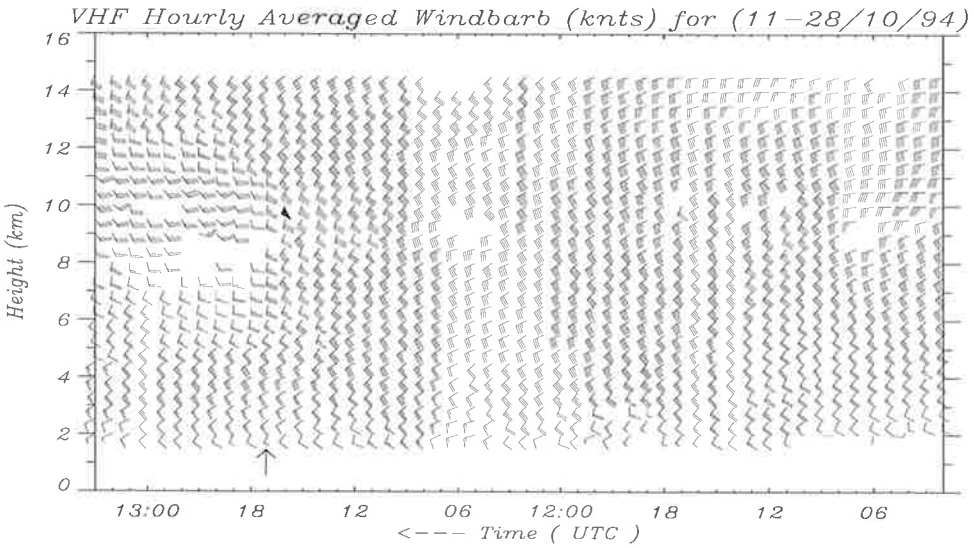

Figure D.7: VHF hourly averaged windbarbs (*knts*) showing a shallow trough at high altitudes (from 8 km to about 11 km).

D.6 Upper Deep Trough

Figure D.8 manifests a sharp and deep trough aloft starting from about $4\,km$, extending to about $11\,km$ height, being very sharp at about $9\,km$. Below this, there is no evidence of trough. This figure also shows a classic ridge around 06 UTC 11 October 1992.

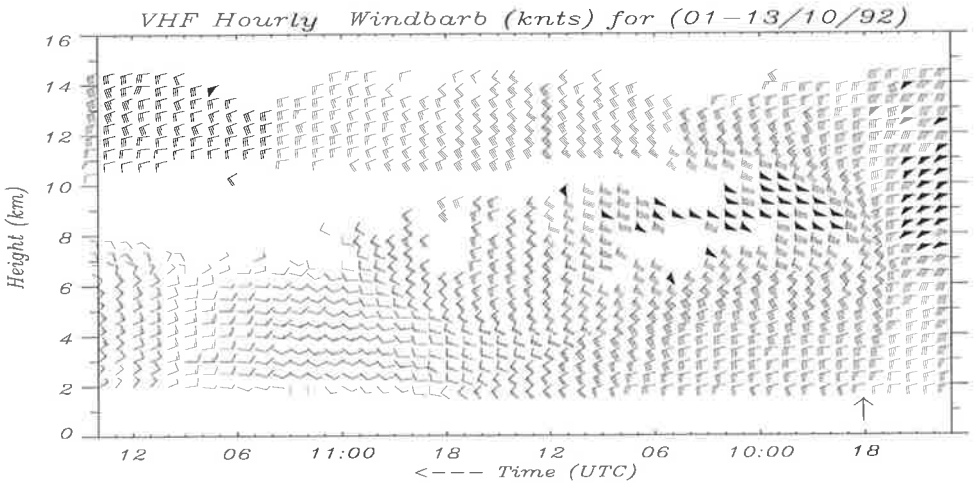

Figure D.8: VHF hourly averaged windbarbs (*knts*) showing a deep trough extending from $4\,km$ to $9\,km$ height. Position of a ridge is also shown to be at about 06 UTC 11th October 1992.

Figure D.9 illustrates another deep and sharp trough at higher altitudes. The trough starts from $2.5\,km$ with the distinct clockwise break in wind direction upto about $8\,km$.

An spectacular elongated trough is demonstrated in Figure D.10 in which, the length from nose of trough (relevant position is shown by an arrow) to tail is about 2 days. The trough is extended from low levels to as high as about $12\,km$ height.

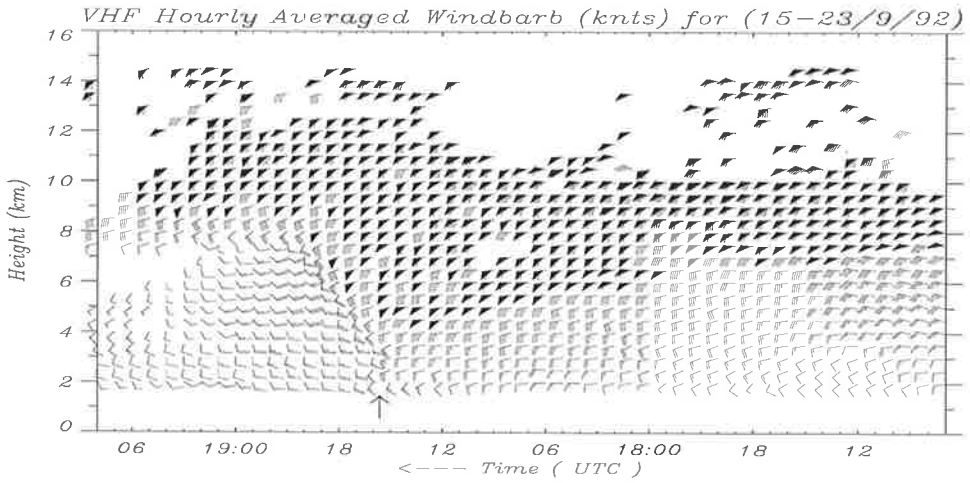

Figure D.9: VHF hourly averaged windbarbs (*knts*) showing a deep trough aloft extending from 2.5 *km* to about 8 *km* height. The position of trough is shown by a vertical arrow.

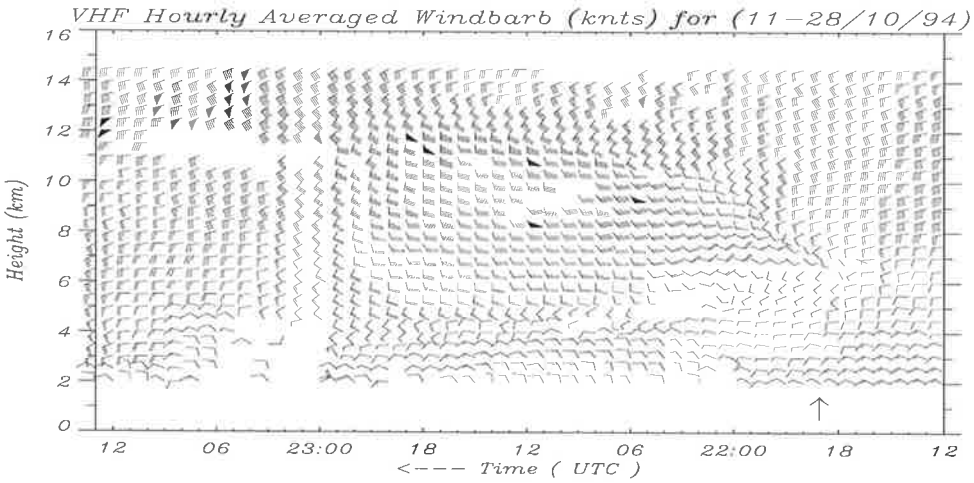

Figure D.10: VHF hourly averaged windbarbs (*knts*) illustrating an elongated trough with the length of about 2 days extending from low levels to about 12 *km* height.

D.7 Disturbance Aloft

A clear disturbance is shown in Figure D.11 at high levels ($\sim 7\ km$) without any indication of such a disturbance underneath. This anomaly is confined at a very shallow layer. The appropriate position is shown by a vertical arrow.

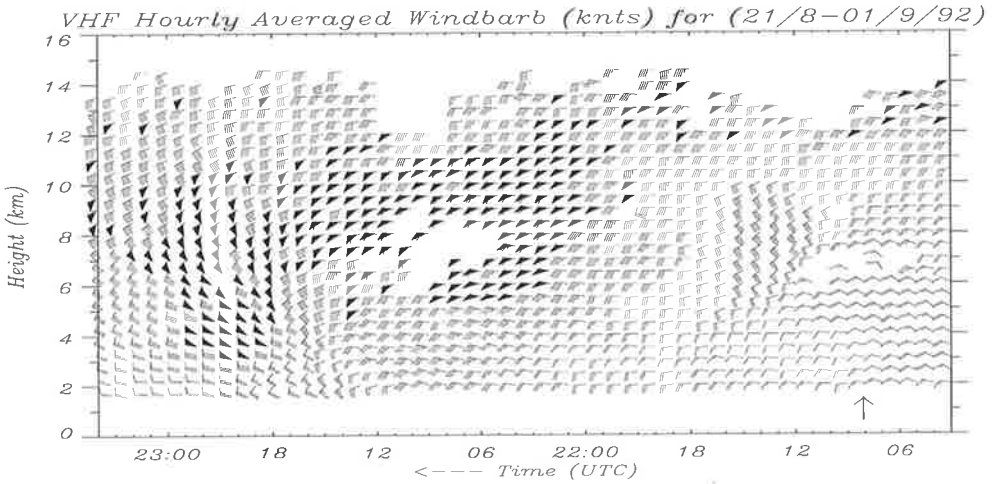

Figure D.11: VHF hourly averaged windbarbs (*knts*) reveals the existence of a shallow disturbance aloft at about 7 *km* height. The relevant position is shown by a vertical arrow.

D.8 Expansion of Polar Front Jet-stream to Low Levels

The Polar Front Jet-streams (PFJ) while meandering about the troughs or Cut-off Lows, sometimes, expand to low levels as well, producing a potential danger for aviation if they occur close to airports. Figure D.12 clearly shows an expansion of a PFJ as low as about 3 *km*. In this figure, a narrow vertical trough is also evident. The positions are marked by vertical arrows. The appearance of PFJ

to low levels can also be easily detected from Figures D.1, D.5, D.6, D.9, D.11, D.14 & D.15.

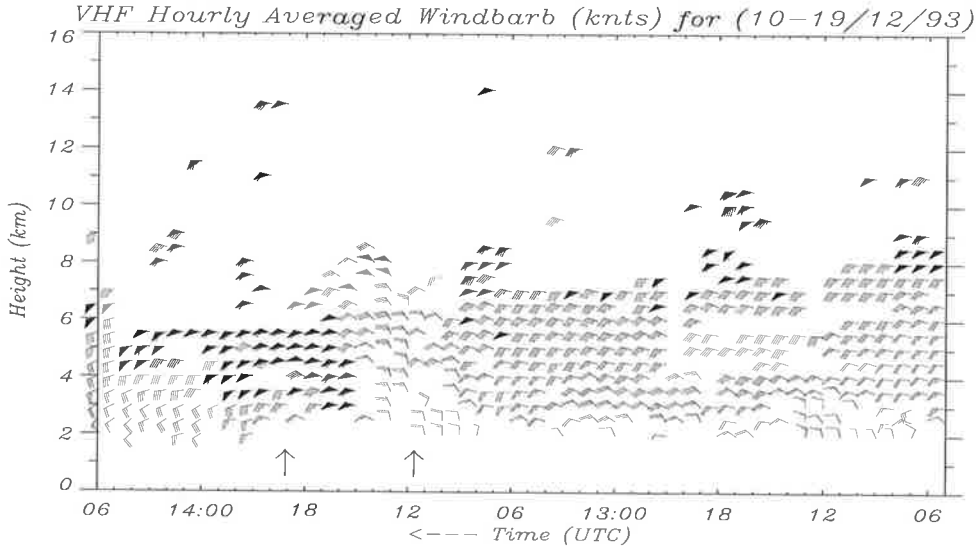

Figure D.12: VHF hourly averaged windbarbs (*knts*) showing the expansion of the Polar Front Jet-stream (PFJ) to low levels. The position of a narrow vertical trough is also shown by a vertical arrow.

D.9 Easterly Shallow Layer Aloft

An easterly layer at higher altitudes is shown in Figure D.13. Above and below this layer wind components show westerly directions. This layer can be very important for aviation from economic point of interest. The layer shown, is as deep as about 3 km (i.e. from 8 km to 11 km) and as long as about 2 days.

D.10 Multiple Troughs

Figure D.14 proclaims an odd multiple trough, one of which extends eastward and slightly upward with low slope while, the other extends straight upward. The

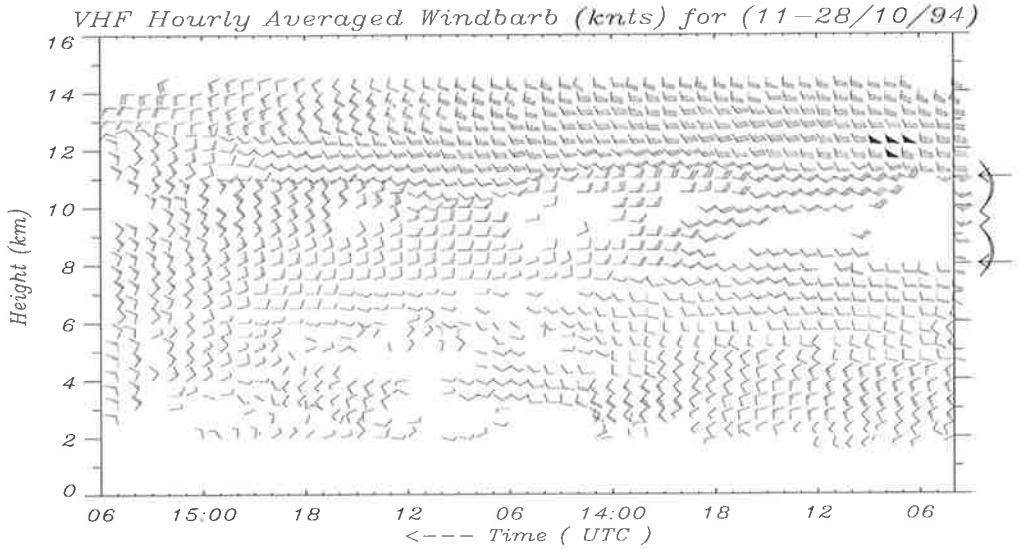

Figure D.13: VHF hourly averaged windbarbs (*knts*) reveal an easterly layer about 8 to 11 *km* deep and about 2 days long.

positions of troughs are shown by vertical arrows.

D.11 Short Waves

Short waves can be easily detected from the profilers' data, as is shown in Figure D.15. The position of a short wave with a ridge and a trough is shown by arrows in this figure.

D.12 Comments

The unique features which are demonstrated in this chapter, reveal the existence and importance of such phenomena. Some of these features are associated with the weather and some are not. Besides being helpful in the analysis of meteorological charts, these aspects of the atmosphere have interests in nowacasting,

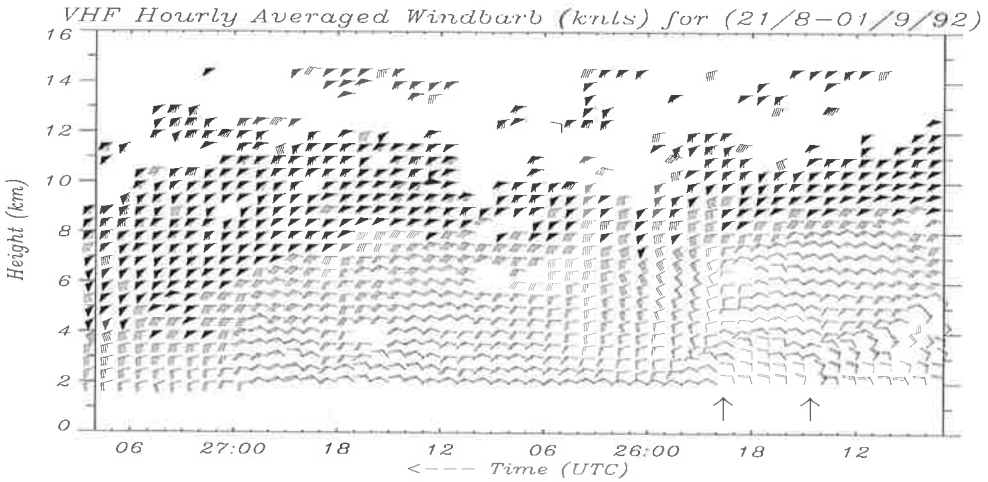

Figure D.14: VHF hourly averaged windbarbs (*knts*) manifest a multiple trough aloft. The positions are shown by vertical arrows.

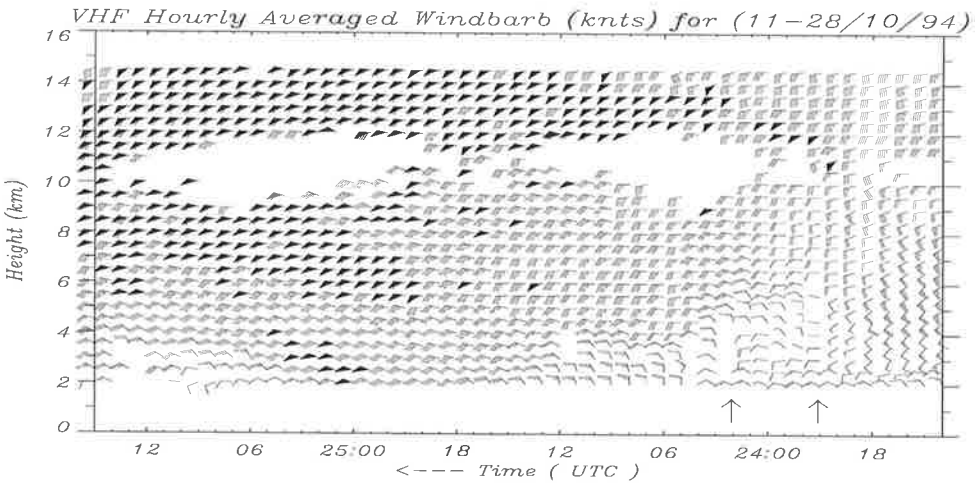

Figure D.15: VHF hourly averaged windbarbs (*knts*) reveals the existence of a short wave at lower troposphere. The positions of a ridge and a trough is shown by vertical arrows.

forecasting and more importantly, in aviation. Being alert to the existence of these kinds of phenomena and ultimately, prediction of the aspects caused by them, can indobtably, save lives and properties as well as resources.

A network installation of these inexpensive profilers will inevitably reveal a clearer image in the lower range of the meso-scale structure of the atmosphere.

These dynamic pictures of the atmosphere produced by the wind profilers may in turn, be able to prevent and/or explain some of the mystery accidents of aviation.

Bibliography

Atlas, D. R., Srivastava, R. C., & Sekon, R. S. (1973), 'Doppler radar characteristics of precipitation at vertical incidence', *Rev. Geophys. Space Phys.* **11**, 1–35.

Balsley, B. B. (1981), 'The MST technique—a brief review', *J. Atmos. Terr. Phys.* **43**, 495–509.

Balsley, B. B., & Ecklund, W. L. (1972), 'A portable coaxial collinear antenna', *IEEE Transactions on Antennas and propagation.* **20**, 513–516.

Balsley, B. B. & Gage, K. S. (1980), 'The MST radar technique: Potential for middle atmospheric studies', *Pure Appl. Geophys.* **118**, 452–493.

Balsley, B. B., Ecklund, W. L., Carter, D. A., Riddle, A. C. & Gage, K. S. (1988), 'Average vertical motions in the tropical atmosphere by a radar wind profiler on Pohnpei (7° N latitude, 157° E longitude).', *J. Atmos. Sci.* **45**, 396–405.

Battan, L. J. (1973), *Radar Observations of the Atmosphere*, University of Chicago Press, Chicago, Illinois.

Beckman, S. K. (1990), 'Operational use of profiler data and satellite imagery to evaluate the NMC numerical models in predicting heavy snow', *Weather and Forecasting,* **5**, 259–277.

Betts, A. K., & Dugan, F. J. (1973), 'Empirical formula for saturation pseudo-adiabats and saturation equivalent potential temperature', *J. Appl. Meteor.*, **12**, 731–732.

Betts, A. K., & Miller, R. D. (1975), 'VIMHEX 1972 rawinsonde data', *Dept. of Atmospheric Science, Colorado State University.* 178 pp.

Bilbro, J., Fichtl, G., Fitzjarrald, D., Kraus, M. & Lee, R. (1984), 'Airborne Doppler lidar wind field measurements', *Bull. Amer. Meteor. Soc.* **65**, 348–359.

Bjerknes, J., & Solberg, H. (1922), 'Life cycle of cyclones and the polar front theory of atmospheric circulation', *Geofys. Publ.* **3**, No. 1, 1–18.

Bjerknes, J., & Holmboe, J. (1944), 'On the theory of cyclones', *J. Meteor.* **1**, 1–22.

Bolton, D. (1980), 'The computation of equivalent potential temperature', *Mon. Wea. Rev.* **108**, 1046–1053.

Bowhill, S. A. (1983), 'Review of correlation techniques', *Handbook for the Middle Atmosphere Program* **9**, 521–526. SCOSTEP Secretariat, University of Illinois, Urbana, Illinois.

Bracewell, R. N. (1986), *The Fourier transform and its applications*, 2nd edn, McGraw-Hill, Singapore.

Briggs, B. H. (1968*a*), 'On the analysis of moving patterns in geophysics—I. Correlation analysis', *J. Atmos. Terr. Phys.* **30**, 1777–1788.

Briggs, B. H. (1968*b*), 'On the analysis of moving patterns in geophysics—II. Dispersion analysis', *J. Atmos. Terr. Phys.* **30**, 1789–1794.

Briggs, B. H. (1977), 'The analysis of moving patterns by correlation methods. Rep. ADP 148, Dept. of Physics, University of Adelaide, Australia. (Chapter 21a)'

Briggs, B. H. (1977), 'Ionospheric drifts', *J. Atmos. Terr. Phys.,* **39**, 1023–1033.

Briggs, B. H. (1980), 'Radar observations of atmospheric winds and turbulence: A comparison of techniques', *J. Atmos. Terr. Phys.* **42**, 823–833.

Briggs, B. H. (1984), 'The analysis of spaced sensor records by correlation techniques', *Handbook for the Middle Atmosphere Program* **13**, 166–186. SCOSTEP Secretariat, University of Illinois, Urbana, Illinois.

Briggs, B. H. (1993), 'Observations of atmospheric dynamics using radar techniques', *Aust. J. Phys.* **46**, 127–147.

Briggs, B. H., Phillips, G. J., & Shinn, D. H. (1950), 'The analysis of observations on spaced-receivers of the fading of radio signals', *Proc. Phys. Soc. London.* **B63**, Part 2, 106–121. (Chapter 21a)

Briggs, B. H., Elford, W. G., Felgate, D. G., Golley, M. G., Rossiter, D. E., & Smith, J. W. (1969), 'Buckland Park aerial array', *Nature (London)* **223**, 1321–1325.

Briggs, B. H., & Vincent, R. A. (1992), 'Spaced antenna analysis in the frequency domain', *Radio Sci.* **27**(2), 117–129.

Browning, K. A. (1986), 'Conceptual models of precipitation systems', *Weather and Forecasting,* **1**, 23–41.

Browning, K. A. (1990), Organisation of clouds and precipitation in extratropical cyclones, *in* C. W. Newton & E. O. Holopanen, eds, 'Extratropical cyclones.

The Erik Palmen Memorial Volume', American Meteorological Society, pp. 129–165.

Browning, K. A., & Harrold, T. W. (1970), 'Air motion and precipitation growth at a cold front', *Quart. J. Roy. Meteor. Soc.* **96**, 369–389.

Browning, K. A. & Szejwach, G. (1994), 'Developments in observational systems for weather forecasting', *Meteorol. App.* **1**, 3–22.

Brunt, D. (1930), 'The present position of theories of the origin of cyclonic depressions', *Quart. J. Roy. Meteor. Soc.* **56**, 345–350.

Carlson, T. N. (1980), 'Airflow through midlatitude cyclones and the comma cloud pattern', *Mon. Wea. Rev.* **108**, 1498–1509.

Carlson, T. N. (1987), 'Cloud configuration in relation to relative isentropic motion', *Satellite and Radar Imagery Interpretation* (preprint vol., workshop at U.K. Meteorological Office), M. Bader and T. Waters, Eds. EUMETSAT, Darmstadt, FRG, 43–61.

Cervera, M. A. (1996), *Meteor observations with a narrow beam VHF radar.* Ph.D. thesis, Univ. of Adelaide, Adelaide, Aust.

Cervera, M. A. & Reid, I. M. (1995) , 'Comparison of simultaneous wind measurements using colocated VHF meteor radar and MF spaced antenna radar systems', *Radio Sci.* **30**, 1245–1261.

Charney J. G., & Stern, M. E. (1962), 'On the stability of internal baroclinic jets in a rotating atmosphere', *J. Atmos. Sci.* **19**, 159–172.

Clark, W. L., Green, J. L. & Warnock, J. M. (1986), The use of vertical beam clear-air Doppler radar to measure horizontal divergence of the wind field,

in 'Preprints, 23rd Radar Meteorology Conference, Snowmass', American Meteorological Society, pp. 38–40.

Costa, E., & Fougere, P. F. (1988), 'Cross-spectral analysis of spaced-receiver measurements', *Radio Sci.* **23**(2), 129–139.

Doviak, R. J. & Zrnić, D. S. (1984), *Doppler Radar and Weather Observations*, Academic Press, Orlando, Florida.

Eckermann, S. D., & Vincent, R. A. (1992), 'VHF radar observations of gravity-wave production by cold fronts over Southern Australia', *J. Atmos. Sci.* **50**, 785–805.

Ertel, H. (1942), 'Ein Neuer hydrodynamischer Wirbelsatz', *Meteor. Zeits.* **59**, 271–281.

Flock, W. L. & Balsley, B. B. (1967), 'VHF radar returns from the D-region of the equatorial ionosphere', *J. Geophys. Res.,* **72**(21), 5537–5541.

Frederiksen, J. S., & Frederiksen, C. S. (1993), 'Southern Hemisphere storm tracks, blocking, and low-frequency anomalies in a primitive equation model', *J. Atmos. Sci.* **50**, 3148–3163.

Frisch, A. S., Weber, B. L., Strauch, R. G., Merritt, D. A. & Moran, K. P. (1986), 'The altitude coverage of the Colorado wind profilers at 50, 405 and 915 MHz', *J. Atmos. Oceanic Technol.* **3**, 680–692.

Fujita, T. T. (1981), 'Tornadoes and downbursts in the context of generalized planetary scales', *J. Atmos. Sci.* **38**, 1512–1534.

Fujita, T. T. (1986), Mesoscale Classifications, *in* P. S. Ray, ed., 'Mesoscale Meteorology and Forecasting', American Meteorological Society, Boston, chapter 2, pp. 18–35.

Fukao, S., Sato, T., Yamasaki, N., Harper, R. M. & Kato, S. (1982), 'Winds measured by a UHF Doppler radar and rawinsondes: Comparisons made on twenty-six days (August–September 1977) at Arecibo, Puerto Rico', *J. Appl. Meteor.* **21**, 1357–1363.

Fukao, S., Wakasugi, K., Sato, T., Morimoto, S., Tsuda, T., Hirota, I., Kimura, I., & Kato, S. (1985), 'Direct measurement of air and precipitation particle motion by VHF Doppler radar', *Nature* **316**, 712–714.

Gage, K. S. (1990), 'Radar observations of the free atmosphere: Structureand dynamics', *Radar in Meteorology.* David Atlas, Ed.,*Amer. Meteor. Soc.*, 535–564.

Gage, K. S., & Balsley, B. B. (1978) , 'Doppler radar probing of the clear atmosphere', *Bull. Amer. Meteor. Soc.* **59**, 1074–1093.

Gage, K. S., & Green, J. L. (1978), 'Evidence for specular reflection from monostatic VHF radar observations of the stratosphere', *Radio Science.* **13**, 991–1001.

Gage, K. S. & Green, J. L. (1979), 'Tropopause detection by partial specular reflection with Very-High-Frequency radar', *Science* **203**, 1238–1240.

Gage, K. S. & Balsley, B. B. (1980) , 'On the scattering and reflection mechanisms contributing to clear air radar echoes from the troposphere, stratosphere, and mesosphere', *Radio Sci.* **15**, 243–257.

Gage, K. S. & VanZandt, T. E. (1981), 'Wind measurement techniques available for the middle atmosphere program', *J. Geophys. Res.* **86**, 9591–9598.

Gage, K. S. & Green, J. L. (1982*a*), 'An objective method for the determination of tropopause height from VHF radar observations', *J. Appl. Meteor.* **21**, 1150–1154.

Gage, K. S., Mc Afee, D. A., Ecklund, W. L., Riddle, A. C. & Balsley, B. B. (1986), 'Objective tropopause height determination using low-resolution VHF radar observations', *J. Atmos. Oceanic Technol.* **3**, 248–254.

Gage, K. S., Ecklund, W. L., Riddle, A. C., Reid, G. C. & Balsley, B. B. (1991), 'Long-term mean vertical motions over the tropical Pacific: Wind-profiling Doppler radar measurements', *Science,* **254**, 1771–1773.

Gardner, F. F., & Pawsey, J. L. (1953), 'Study of the ionospheric D-region using partial reflections', *J. Atmos. Terr. Phys.* **3**, 321–344.

Garratt, J. R., Physick, W. L., Smith, R. K., & Troup, A. J. (1985), 'The Australian summertime cool change. Part II: Mesoscale aspects', *Mon. Wea. Rev.* **113**, 202–223.

Golden, J. H., Serafin, R., Lally, V. & Facundo, J. (1986), Atmospheric Sounding Systems, *in* P. S. Ray, ed., 'Mesoscale Meteorology and Forecasting', American Meteorological Society, Boston, chapter 4, pp. 50–70.

Gossard, E. E. (1988), 'Measuring drop-size distributions in clouds with a clear-air-sensing Doppler radar', *J. Atmos. and Oceanic Technol.* **5**, 640–649.

Gossard, E. E. & Strauch, R. G. (1983), *Radar observations of clear air and clouds*, Elsevier Science Publishing, New York.

Gossard, E. E., Strauch, R. G., & Rogers, R. R. (1990), 'Evolution of dropsize distributions in liquid precipitation observed by ground-based Doppler radar', *J. Atmos. and Oceanic Technol.* **7**, 815–828.

Green, J. L. & Gage, K. S. (1984), 'Comparison of tropopause altitude determination by the Platteville radar, Sunset radar and the NWS radiosonde', *Handbook for the Middle Atmosphere Program* **14**, 58–61. SCOSTEP Secretariat, University of Illinois, Urbana, Illinois.

Gregory, J. B. (1956), 'Ionospheric reflections from heights below the E-region', *Aust. J. Phys.* **9**, 324–342.

Griffiths, M., Reeder, M. J., Low, D. J., & Vincent, R. A. (1998), 'Observations of a cut-off low over southern Australia', *Q. J. R. Meteorol. Soc.* **124**, 1109–1132.

Harrold, T. W. (1973), 'Mechanisms influencing the distribution of precipitation within baroclinic disturbances', *Quart. J. Roy. Meteor. Soc.* **99**, 232–251.

Hemler, M. G. (1987), 'Doppler wind profiler examination of cloud edges', M.S. thesis, Dept. of Meteor., Pennsylvania State University.

Heymsfield, G. M. (1979), 'Doppler radar study of a warm frontal region', *J. Atmos. Sci.* **36**, 2093–2107.

Hines, C. O., Adams, G. W., Brosnahan, J. W., Djuth, F. T., Sulzer, M. P., Tepley., & Van Baelen J. S. (1993), 'Multi-instrument observations of mesospheric motions over Arecibo: Comparison and interpretations', *J. Atmos. Terr. Phys.* **55**, 241–287.

Hobbs, P. V., Matejka, T. J., Herzegh, P. H., Locatelli, J. D., & Houze Jr, R. A. (1980), 'The mesoscale and microscale structure and organization of cloud and precipitation in midlatitude cyclones. Part I: A case study of a cold front', *J. Atmos. Sci.* **37**, 568–596.

Hocking, W. K. (1983*a*), 'On the extraction of atmospheric turbulence parameters from radar backscatter Doppler spectra–I. theory', *J. Atmos. Terr. Phys.* **45**, 89–102.

Hocking, W. K. (1983*b*), 'Mesospheric turbulence intensities measured with a HF radar at 35°*S*–II', *J. Atmos. Terr. Phys.* **45**, 103–114.

Hocking, W. K., May, P., & Röttger, J. (1988), 'Interpretation, reliability and accuracies of parameters deduced by the spaced antenna method in middle atmosphere applications', *Pure Appl. Geophys.* (Chapter 21a)

Hogg, D. C., Decker, M. T., Guiraud, F. O., Earnshaw, K. B., Merritt, D. A., Moran, K. P., Sweezy, W. B., Strauch, R. G., Westwater, E. R. & Little, C. G. (1983), 'An automatic profiler of the temperature, wind, and humidity in the troposphere', *J. Climate Appl. Meteor.* **22**, 807–831.

Holdsworth, D. A. & Reid, I. M. (1995*a*), 'A simple model of atmospheric radar backscatter: Description and application to the full correlation analysis of spaced sensor data', *Radio Sci.* **30**, 1263–1280.

Holdsworth, D. A. & Reid, I. M. (1995*b*), 'Spaced antenna analysis of atmospheric radar backscatter model data', *Radio Sci.* **30**, 1417–1433.

Holland, G. J., Lynch, A. H. & Leslie, L. M. (1987), 'Australian East-Coast cyclones. Part I: Synoptic overview and case study', *Mon. Wea. Rev.* **115**, 3024–3036.

Holton, J. R. (1972), *An Introduction to Dynamic Meteorology*, 1st edn Academic press, New York.

Holton, J. R. (1979), *An Introduction to Dynamic Meteorology*, 2nd edn Academic press, New York, 391pp.

Holton, J. R. (1992), *An Introduction to Dynamic Meteorology*, 3rd edn, Academic Press, New York.

Homer W. H. (1970), *Radar Meteorology,* 3rd edn, Radar Meteorology Laboratory, Rosenstiel School of Marine and Atmospheric Sciences, University of Miami.

Hopkins, L. C. & Holland, G. J. (1997), 'Australian heavy-rain days and associated east coast cyclones: 1958-1992', *Journal of Climate* **10**, 621–635.

Hoskins, B. J. (1990), Theory of extratropical cyclones, *in* C. W. Newton & E. O. Holopanen, eds, 'Extratropical cyclones. The Erik Palmen Memorial Volume', American Meteorological Society, pp. 63–80.

Hubert, L. F. (1979), Wind derivation from geostationary satellites, *in* J. S. Winston, ed.; 'Quantitative Meteorological Data From Satellites', WMO Technical Note 166, pp. 33–59.

Hubert, L. F. & Whitney, Jr., L. F. (1971), 'Wind estimation from geostationary satellite pictures', *Mon. Wea. Rev.* **99**, 665–672.

Huaman, M. M. & Balsley, B. B. (1996), 'Long-term average vertical motions observed by VHF wind profilers: The effect of slight antenna-pointing inaccuracies', *J. Atmos. Oceanic. Technol.* **13**, 560–569.

Huschke, R. E. (1970), 'Glossary of meteorology', *Amer. Meteor. Soc.* 45 Beacon St. Boston, Mass. 02108.

Johnson, D. R., & Downey, W. K. (1976), 'The absolute angular momentum budget of an extratropical cyclone: Quasi-Lagrangian diagnostics 3', *Mon. Wea. Rev.* **104**, 3–14.

Keifer, P. J., Kinney, G. F., & Stuart, M. C. (1954), 'Principles of Engineering thermodynamics', *John Wiley & Sons, Inc., New York.*

Krishnamurti, T. N. (1968), 'A study of a developing wave cyclone', *Mon. Wea. Rev.* **96**, 208–217.

Kudeki, E., Rastogi, P. K., & Surucu, F. (1993), 'Systematic errors in radar wind estimation: Implications for comparative measurements', *Radio Sci.* **28**, 169–180.

Kutzbach, G. (1979), 'The thermal theory of cyclones', *Amer. Meteor. Soc.* 255pp.

Larsen, M. F. (1983*a*), 'The MST radar technique: Requirements for operational weather forecasting. Invited review', *URSI/MAP Workshop on Technical Aspects of MST Radar. Also Handbook for MAP,* S. A. Bowhill and B. Edwards, Eds., **9**, 3-11. [Published by SCOSTEP Secretariat, University of Illinois, Urbana.] (Chapter 21a:1983a)

Larsen, M. F. (1983*b*), 'Can a VHF Doppler radar provide synoptic wind data? A comparison of 30 days of radar and radiosonde data.' Preprints, *Fifth Symp. on Meteorological Observations and Instrumentation*, Toronto, Amer. Meteor. Soc., 183–190. Also *Mon. Wea. Rev.* **111**, 2047–2057. (Chapter 21a:1983b)

Larsen, M. F., & Röttger, J. R. (1982), 'VHF and UHF Doppler radars as tools for synoptic research',. *Bull. Amer. Meteor. Soc.* **63**, 996–1007.

Larsen, M. F., & Röttger, J. (1988), 'The spaced antenna technique for radar wind profiling. *J. Atmos. Oceanic Technol.* (Chapter 21a)

Larsen, M. F., & Röttger, J. (1991), 'VHF radar measurements of reflectivity layer tilted angles and associated vertical-beam radial velocity corrections. *J. Atmos. Oceanic Technol.* **8**(4), 477–490.

Ligda, M. G. H. (1951), Radar storm observations, *in* 'Compendium of Meteorology', American Meteorological Society, Boston, pp. 1265–1282.

Liu, C. H., Pan, C. J., & Franke, S. J. (1990), 'A model for spaced antenna observational mode for MST radars', *Radio Sci.* **29**(4), 551–563.

Low, D. J. (1996), *Studies of the lower atmosphere with a VHF wind profiler* Ph.D. thesis, Univ. of Adelaide, Adelaide, Aust.

Matuura, N., Masuda, Y., Inuki, H., Kato, S., Fukao, S., Sato, T. & Tsuda, T. (1986), 'Radio acoustic measurement of temperature profile in the troposphere and stratosphere', *Nature* **323**, 426–428.

May, P. T. (1986), 'VHF radar studies of the troposphere', Ph. D. Thesis, The University of Adelaide.

May, P. T. (1988), 'Statistical errors in the determination of wind velocities by the spaced antenna technique', *J. Atmos. Terr. Phys.* **50**, 21–32.

May, P. T. (1990), 'Spaced antenna versus Doppler radars: A comparison of techniques revisited', *J. Atmos. Terr. Phys.* **25**, 1111–1119.

May, P. T. (1996), 'The organization of convection in the rainbands of tropical cyclone Laurence', *Mon. Wea. Rev.* **124**, 807–815.

May, P. T. & Strauch, R. G. (1989) , 'An examination of wind profiler signal processing algorithms', *J. Atmos. Oceanic Technol.* **6**, 731–735.

May, P. T., Moran, K. P. & Strauch, R. G. (1989*a*), 'The accuracy of RASS temperature measurements', *J. Appl. Meteor.* **28**, 1329–1335.

May, P. T., Sato, T., Yamamoto, M., Kato, S., Tsuda, T. & Fukao, S. (1989*b*), 'Errors in the determination of wind speed by Doppler radar', *J. Atmos. Oceanic Technol.* **6**, 235–242.

May, P. T., Wilson, K. J. & Ryan, B. F. (1990), 'VHF radar studies of cold fronts traversing southern Australia', *Beitr. Phys. Atmosph.* **63**, 257–269.

May, P. T., Holland, G. J., & Ecklud, W. L. (1994), 'Wind profiler observations of tropical storm Flo at Saipan', *Weather and Forecasting.* **9**, 410–426.

McAfee, J. R., Gage, K. S., & Strauch, R. G. (1993), 'A comparison of vertical velocities measured by the 50 MHz and 404 MHz profilers at Platteville, Colorado.' Preprints, *26th Conf. on Radar Meteorology,* Norman, Amer. Meteor. Soc., 561–563

Mills, G. A. (1989), 'Dynamics of a rapid cloud band development over south-eastern Australia', *Mon. Wea. Rev.* **117**, 1402–1422.

Mills, G. A. & Seaman, R. S. (1990) , 'The BMRC limited area data assimilation system', *Mon. Wea. Rev.* **118**, 1217–1237.

Mills, G. A. & Russell, I. (1992), 'The April 1990 floods of eastern Australia: Synoptic description and assesment of regional NWP guidance', *Wea. Forecasting* **7**, 636–668.

Mills, G. A. & Wu, B.-J. (1995), 'The "Cudlee Creek" flash-flood—an example of synoptic scale forcing of a mesoscale event', *Aust. Meteor. Mag.* **44**, 201–218.

Nastrom, G. D., VanZandt, T. E., Clark, W. L., Warnock, J. M., Green, J. L., & Gage, K. S. (1990*a*), 'Diagnosis of a downward bias in the vertical motions seen by VHF clear-air Doppler radars', *Eos.* **71**, 28 (abstract only).

Nastrom, G. D., Gage, K. S. & Ecklund, W. L. (1990b), 'Uncertainties in estimates of the mean vertical velocity from MST radar observations', *Radio Sci.* **25**, 933–940.

Nastrom, G. D. & VanZandt, T. E. (1994), 'Mean vertical motions seen by radar wind profilers', *J. Appl. Meteor.* **33**, 984–995.

Nastrom, G. D., & VanZandt, T. E. (1996), 'Biases due to gravity wave in wind profiler measurements of winds', *J. Appl. Meteor.* **35**, 243–257.

Neiman, P. J., & Shapiro, M. A. (1989), 'Retrieving horizontal temperature gradients and advections from single-station wind profiler observations', *Weather and Forecasting* **4**, 222–233.

Neiman, P. J., May, P. T., Stankov, B. B., & Shapiro, M. A. (1991), 'Radio acoustic sounding system observations of an arctic front', *J. Appl. Meteor.* **30**, 881–892.

Newton, C. W. (1990), Erik Palmen's contributions to the development of cyclone concepts, *in* C. W. Newton & E. O. Holopanen, eds, 'Extratropical cyclones.

The Erik Palmen Memorial Volume', American Meteorological Society, pp. 1–18.

Oliver, V. J., & Oliver, M. B. (1945), *Handbook of Meteorology,* McGraw-Hill, 858–879.

Orlanski, I. (1975), 'A rational subdivision of scales for atmospheric processes', *Bull. Amer. Meteor. Soc.* **56**, 527–530.

Palmen E. (1951), 'The aerology of extratropical disturbances', *Compendium of Meteorology*, T. F. Malone, Ed. American Meteorological Society, 599–620.

Palmer, R. D., Larsen, M. F., Woodman, R. F., Fukao, S., Yamamoto, M., Tsuda, T., & Kato, S. (1991), 'VHF radar interferometry measurements of vertical velocity and the effect of tilted refractivity surfaces on standard Doppler measurements', *Radio Sci.* **26**, 417–427.

Pauley, P. M., Creasey, R. L., Clark, W. L., & Nastrom, G. D. (1994), 'Comparisons of horizontal winds measured by opposing beams with the Flatland ST radar and between Flatland measurments and NMC analyses', *J. Atmos. Oceanic. Technol.* **11**, 256–274.

Petterssen, S. (1956), *Weather Analysis and Forecasting,* 2nd ed., Vol. 1. McGraw-Hill, 428pp.

Rajopadhyaya, D. K. (1994), Meteorological studies using a VHF radar, PhD thesis, University of Adelaide, South Australia.

Rajopadhyaya, D. K., May, P. T., & Vincent, R. A. (1993), 'A general approach to the retrieval of raindrop size distributions from wind profiler Doppler spectra: Modeling results', *J. Atmos. and Oceanic Tech.* **10**, 710–717.

Rastogi, P. K. & Holt, O. (1981), 'On detecting reflections in presence of scattering from amplitude statistics with application to D region partial reflection', *Radio Sci.* **16**, 1431–1443.

Rastogi, P. K. & Röttger, J. (1982), 'VHF radar observations of coherent reflections in the vicinity of the tropopause', *J. Atmos. Terr. Phys.* **44**, 461–469.

Reed, R. J. (1979), 'Cyclogenesis in polar air stream', *Mon. Wea. Rev.* **107**, 38–52.

Reed, R. J. (1990), Advances in knowledge and understanding of extratropical cyclones during the past quarter century: An overview, *in* C. W. Newton & E. O. Holopanen, eds, 'Extratropical cyclones. The Erik Palmen Memorial Volume', American Meteorological Society, pp. 27–45.

Reid, I. M. (1988), 'MF Doppler and spaced antenna radar measurements of upper middle atmosphere winds', *J. Atmos. Terr. Phys.* **50**, 117–134.

Riddle, A. C., Gage, K. S. & Balsley, B. B. (1983), An algorithm to monitor continuously the tropopause height using a VHF radar, *in* 'Preprints, 21st Radar Meteorology Conference, Edmonton', American Meteorological Society, pp. 153–157.

Riddle, A. C., Gage, K. S. & Balsley, B. B. (1984), 'Practical use of a tropopause height determination algorithm on an MST radar data set', *Handbook for the Middle Atmosphere Program* **14**, 69–73. SCOSTEP Secretariat, University of Illinois, Urbana, Illinois.

Riehl, H. (1990), General circulation studies in Chicago from the 1940s into the 1950s, *in* C. W. Newton & E. O. Holopanen, eds, 'Extratropical cyclones.

The Erik Palmen Memorial Volume', American Meteorological Society, pp. 19–26.

Rossby, C. G. (1940), 'Planetary flow patterns in the atmosphere', *Quart. J. Roy. Meteor. Soc.* **66**, Suppl., 68–87.

Rossby, C. G. (1941), 'The scientific basis of modern meteorology', *Climate and Man, Yearbook of Agriculture. U.S. Gov't Printing Office*, 599–655.

Röttger, J. (1980*a*), 'Reflection and scattering of VHF radar signals from atmospheric refractivity structures', *Radio Sci.* **15**, 259–276.

Röttger, J. (1984), 'The MST radar technique', *Handbook for the Middle Atmosphere Program* **13**, 187–232. SCOSTEP Secretariat, University of Illinois, Urbana, Illinois.

Röttger, J. (1989), 'The interpretation of MST radar echoes: The present knowledge of the scattering/reflection and the irregularity generation mechanism', in*Handbook for MAP*, SCOSTEP Sec., Univ. of Ill., Urbana. **28**, 66–72.

Röttger, J. & Liu, C. H. (1978) , 'Partial reflection and scattering of VHF radar signals from the clear atmosphere', *Geophys. Res. Lett.* **5**, 357–360.

Röttger, J., & Vincent, R. A. (1978), 'VHF radar studies of tropospheric velocities and irregularities using spaced antenna techniques', *Geophys. Res. Lett.* **5**(11), 917–920.

Röttger, J. & Czechowsky, P. (1980), Tropospheric and stratospheric wind measurements with the spaced antenna drifts technique and the Doppler beam swinging technique using a VHF radar, *in* 'Preprints, 19th Radar Meteorology Conference, Miami', American Meteorological Society, pp. 577–584.

Röttger, J. & Larsen, M. F. (1990), UHF/VHF radar techniques for atmospheric research and wind profiler applications, *in* D. Atlas, ed., 'Radar in Meteorology', American Meteorological Society, Boston, chapter 21a, pp. 235–281.

Royrvik, O. (1983), 'Spaced antenna drifts at Jicamarca, mesospheric measurements', *Radio Sci.* **18**, 461–476.

Ryan, B. F. (1982), 'A perspective of research into cold fronts and associated mesoscale phenomena into the 1980's', *Aust. Meteor. Mag.* **30**, 123–131.

Ryan, B. F. & Meadows, J. (1979), 'A relative-flow isentropic analysis of a cut-off low', *Aust. Meteor. Mag.* **27**, 43–57.

Ryan, B. F. & Wilson, K. J. (1985) , 'The Australian summertime cool change. Part III: Subsynoptic and mesoscale models', *Mon. Wea. Rev.* **113**, 224–240.

Ryan, B. F., Wilson, K. J., Garratt, J. R. & Smith, R. K. (1985), 'Cold Fronts Research Programme: Progress, future plans and research directions', *Bull. Amer. Meteor. Soc.* **66**, 1116–1122.

Ryan, B. F., Wilson, K. J. & Zipser, E. J. (1989), 'Modification of the thermodynamic structure of the lower troposphere by the evaporation of precipitation ahead of a cold front', *Mon. Wea. Rev.* **117**, 138–153.

Sanders, F. (1987), 'Skill of NMC operational dynamical models in prediction of explosive cyclogenesis', *Weather and Forecasting.* **2**, 322–336.

Sanders, F., & Gyakum, J. R. (1980), 'Synoptic-dynamic climatology of the "bomb"', *Mon. Wea. Rev.* **108**, 1589–1606.

Sanders, F., & Bosart, L. F. (1985), 'Mesoscale structure in the megalopolitan snowstorm of 11–12 February 1983. Part I: Frontogenetical forcing and symmetric instability', *J. Atmos. Sci.* **42**, 1050–1061.

Sato, T. (1988), 'Radar principles', *Lecture notes: International School on atmospheric radars.*ed. S. Fukao, Kyoto.

Sato, T. (1989), 'Radar principles', *Handbook for the Middle Atmosphere Program* **30**, 19–53. SCOSTEP Secretariat, University of Illinois, Urbana, Illinois.

Sato, T., Doji, H., Iwai, H., & Kimura, I. (1990), 'Computer processing for deriving drop-size distributions and vertical air velocities from VHF Doppler radar spectra', *Radio Sci.* **25**, 961–973.

Saucier, W. J. (1955), '*Principles of Meteorological Analysis.*', The University of Chicago Press, 438 pp.

Schminder, R., & Kürscher, D. (1984), 'D1 LF wind measurements in the 90 to 100 *km* height range', *Handbook for MAP,* R. A. Vincent, Ed., **13**, 248. [Published by SCOSTEP Secretariat, University of Illinois, Urbana.] (Chapter 21a)

Shapiro, M. A., Hampel, T., & Van De Kamp, D. W. (1984), 'Radar wind profiler observations of fronts and jet streams', *Mon. Wea. Rev.* **112**, 1263–1266.

Shapiro, M. A., Hampel, T., Rotzoll, D., & Mosher, F. (1985), 'The frontal hydraulic head: A micro-scale (1km) triggering mechanism for mesoconvective weather systems', *Mon. Wea. Rev.* **113**, 1166–1183.

Sheppard, E. L., Larsen, M. F., Palmer, R. D., Fukao, S., Yamamoto, Y., Tsuda, T. & Kato, S. (1993), 'A statistical comparison of spaced antenna and spatial interferometry wind estimation', *Radio Sci.* **28**, 585–593.

Shimomai, T., & Balsley, B. B. (1998), 'On the latitudinal variability of short-term vertical motions observed by the VHF and UHF wind profilers', *Handbook for the Fourth International Symposium on Tropospheric Profiling: Needs and Technologies.* The University of Colorado, Snowmass, Colorado **2**, 300–301.

Simpson, R. H. (1978), 'On the computation of equivalent potential temperature', *Mon. Wea. Rev.* **106**, 124–130.

Skolnik, M. I. (1990), *Radar Handbook*, 2nd edn, McGraw-Hill.

Smith, R. K., Ryan, B. F., Troup, A. J. & Wilson, K. J. (1982), 'Cold fronts research: The Australian summertime "cool change"', *Bull. Amer. Meteor. Soc.* **63**, 1028–1034.

Smith, R. K. & Reeder, M. J. (1988) , 'On the movement and low-level structure of cold fronts', *Mon. Wea. Rev.* **116**, 1927–1944.

Smith, R. K., Reeder, M. J., Tapper, N. J. & Christie, D. R. (1995), 'Central Australian cold fronts', *Mon. Wea. Rev.* **123**, 16–38.

Spencer, N. W. (1976), 'Experimental programs',*Handbook for MAP* (chapter 3), [Published by SCOSTEP Secretariat, University of Illinois, Urbana.] 19–38.

Spencer, P. L., Carr, F. H., & Doswell III, C. A. (1996), 'Diagnosis of an amplifying and decaying baroclinic wave using wind profiler data', *Mon. Wea. Rev.* **124**, 209–223.

Steiner, M., & Waldvogel, A. (1987), 'Peaks in raindrop size distributions ', *J. Atmos. Sci.* **44**, 3127–3133.

Strauch, R. G. (1983), 'Techniques for measurement of horizontal and vertical velocities: Optimum pointing angle', *Handbook for the Middle Atmosphere Program* **9**, 232–234. SCOSTEP Secretariat, University of Illinois, Urbana, Illinois.

Sulzer, M. P. & Woodman, R. F. (1985), 'Pulse compression hardware decoding techniques for mst radars', *Radio Sci.* **20**, 1146–.

Sutcliffe, R. C. (1947), 'A contribution to the problem of development', *Quart. J. Roy. Meteor. Soc.* **73**, 370–383.

Sweezy, W. B. & Westwater, E. R. (1986), 'A comparison of methods for determining tropopause height from VHF radar observations', *J. Atmos. Oceanic Technol.* **3**, 324–332.

Swords, S. S. (1986), 'Technical history of the beginnings of radar.' P. Peregrinus Ltd, IEEE History of Techn. Ser. 6, London .

Tatarskii, V. I. (1971), *The effects of the turbulent atmosphere on wave propagation*, U.S. Department of Commerce, Springfield, Virginia. Translated from the Russian , Israel Prog. for Sci. Translations.

Tsuda, T., May, P. T., Sato, T., Kato, S. & Fukao, S. (1988), 'Simultaneous observations of reflection echoes and refractive index gradient in the troposphere and lower stratosphere', *Radio Sci.* **23**, 655–665.

Uccellini, L. W. (1990), Processes contributing to the rapid development of extratropical cyclones, *in* C. W. Newton & E. O. Holopanen, eds, 'Extratropical

cyclones. The Erik Palmen Memorial Volume', American Meteorological Socicty, pp. 81–105.

Väisälä (1988), Wind Profiling: The history, principles, and applications of clear-air Doppler radar, Technical report, Tycho Technology, Inc., P.O. Box 1716, Boulder, Colorado 80306, U.S.A.

Van Baelen, J. S., Tsuda, T., Richmond, A. D., Avery, S. K., Kato, S., Fukao, S. & Yamamoto, M. (1990), 'Comparison of VHF Doppler beam swinging and spaced antenna observations with the MU radar: First results', *Radio Sci.* **25**, 629–640.

Vandepeer, B. G. W. (1993), 'A new MF Doppler radar for upper atmospheric research,' Ph.D. thesis, Univ. of Adelaide, Adelaide, Aust.

Vandepeer, B. G. W. & Reid, I. M. (1995), 'On the spaced antenna and imaging Doppler interferometer techniques', *Radio Sci.* **30**, 885–901.

Vincent, R. A. (1984), 'Relationship of spaced antenna and Doppler techniques for velocity measurement', *Handbook for MAP,* ed. S. A. Bowhill and B. Edwards. **14**, 126–130.

Vincent, R. A., Stubbs, T. J., Pearson, P. H. O., Lloyd, K. H. & Low, C. H. (1977), 'A comparison of partial reflection drifts with winds determined by rocket techniques–1', *J. Atmos. Terr. Phys.* **39**, 813–821.

Vincent, R. A. & Röttger, J. (1980), 'Spaced antenna VHF radar observations of tropospheric velocities and irregularities', *Radio Sci.* **15**, 319–335.

Vincent, R. A., Elford, W. G., & Briggs, B. H. (1982), 'A VHF radar for atmospheric studies', *The Australian Physicist* **19**, 70–73.

Vincent, R. A., May, P. T., Hocking, W. K., Elford, W. G., Candy, B. H. & Briggs, B. H. (1987), 'First results with the Adelaide VHF radar: Spaced antenna studies of tropospheric winds', *J. Atmos. Terr. Phys.* **49**, 353–366.

Wakasugi, K., Mizutani, A., & Matsuo, M. (1986), 'A direct method for deriving drop-size distribution and vertical air velocities from VHF Doppler radar spectra', *J. Atmos. and Oceanic Technol.* **3**, 623–629.

Wakasugi, K., Mizutani, A., & Matsuo, M. (1987), 'Further discussion on deriving drop-size distribution and vertical air velocities directly from VHF Doppler radar spectra', *J. Atmos. and Oceanic Technol.* **4**, 170–179.

Weber, B. L., Wuertz, D. B., Law, D. C., Frisch, A. S., & Brown, J. M. (1992), 'Effects of small-scale vertical motion on radar measurements of wind and temperature profiles', *J. Atmos. Oceanic Technol.* **9**, 193–209.

Wheeler, H. A. (1956), 'A vertical antenna made of transposed sections of coaxial cable', *IRE Conv. Rec.* **4**, 160–164.

Wilson, D. A., & Miller, L. J. (1972), 'Atmospheric motion by Doppler radar', *Remote Sensing of the Atmosphere,* V. E. Derr, Ed., 27pp. (Chapter 21a, 27a).

Wilson, K. J. & Stern, H. (1985), 'The Australian summertime cool change. Part I: Synoptic and subsynoptic scale aspects', *Mon. Wea. Rev.* **113**, 177–201.

Wilson, K. J., Barrell, S. L. & Del Beato, R. (1987), 'An approach to verifying prognoses of line phenomena and its application to fronts over southeastern Australia', *Mon. Wea. Rev.* **115**, 1339–1371.

Woodman, R. F. (1980), 'High-altitude resolution stratospheric measurements with the Arecibo 430-MHz radar', *Radio Sci.* **15**(2), 417–422.

Woodman, R. F. (1985), 'Spectral moment estimation in MST radars', *Radio Sci.* **20**, 1185–1195.

Woodman, R. F. & Guillén, A. (1974), 'Radar observations of winds and turbulence in the stratosphere and mesosphere', *J. Atmos. Sci.* **31**, 493–505.

Zrnić, D. S. (1979), 'Estimation of spectral moments for weather echoes', *IEEE Transactions: Geosciences and Electronics* **GE-17**, 113–128.

Addendum

To the thesis submitted for the degree of

DOCTOR OF PHILOSOPHY

BY

Alireza Kazempour, M.Sc.

Page 92 at the end of section 4.1.3 should be added:

- It should be noted that the bistatic radar geometry used for the spaced antenna measurements will influence the results. Because of the separation between the transmitting and receiving antenna, the radial velocity measured from the Doppler shift of reflections received on the large array will not be the same as the radial velocity associated with the horizontal velocity measured from the spaced antenna signals. The difference between these two angles will decrease with increasing observation height. An approximate calculation based on the geometry specified in Figure 3.2 and Table 3.1, confirms such an offset to be the correct order of magnitude.

At the end of the section 5.2 should be added:

- The paper by *Hoskins et al* [1985] has been enormously influential on the use and significance of isentropic potential vorticity maps in the area of cut-off low. However, as archived data were used for analysis of cut-off lows in this thesis, the isentropic potential vorticity maps were not available for further analysis.

Page 126 after the first paragraph should be added:

- Modern theories and observations explicitly recognize that cyclogenesis arises from the interaction between finite-amplitude disturbances such as an upper-level short-wave trough and a pre-existing baroclinic zone or front. Nowadays, such disturbances are identified with cyclonic P anomalies. *Hoskins et al* [1985] discuss the sequence of events that follow from the advection of an upper-level cyclonic P anomaly over a low-level cyclonic P anomaly.

Page 126 last sentence should be replaced by:

- Generally, the maximum (non-convective) ascent occurs in the warm conveyor belt on the eastern and poleward sides of a cut-off low [*Hoskins et al*, 1985].

Section 6.1 after the second paragraph should be added:

- To make the definition of cut-off low more concrete, the cut-off low is identified as a pressure minima or geopotential minima in this thesis. Although, the Geostrophic relative vorticity, ζ_g , minima and satellite imagery have got advantages *(M.R. Sinclair*, [1994], *M.R. Sinclair*, [1995], *M.R. Sinclair*, [1996]) we have used the traditional methods with excluding the stationary or quasi-stationary heat-lows and orographic troughs (lee troughs) from data to eliminate bias. Furthermore, a similar derivation of cut-off low statistics was made for higher levels of 700 *hPa*, 500 *hPa* and 300 *hPa* to eliminate the shallow topographic perturbations and low level pressure reductions to mean sea level (MSL) charts.

Bibliography should be added:

- Hoskins, B.J., McIntyre, M.E. and Robertson, A.W. (1985), "On the use and significance of isentropic potential vorticity maps", *Quart. J. R. Met.* Soc., **111**, 877-946.

- Sinclair, M.R. (1994), "An objective cyclone climatology for the Southern Hemisphere", *Mon. Wea. Rev.*, **122**, 2239-2256.

- Sinclair, M.R. (1995), "A climatology of cyclogenesis for the Southern Hemisphere", *Mon. Wea. Rev.*, **123**, 1601-1619.

- Sinclair, M.R. (1996), "Reply to Rao and Gan (1996)", *Mon. Wea. Rev.*, **124**, 2615-2618.